UNIVERSITÄT HAMBURG
DEPARTMENT PHYSIK

Search for Supersymmetry in τ Final States at ATLAS and Constraints on New Physics Using Electroweak Precision Data

Dissertation zur Erlangung des Doktorgrades
des Department Physik
der Universität Hamburg

vorgelegt von
Dipl.-Phys. Dörthe Kennedy geb. Ludwig
aus Berlin

Hamburg
Juni 2012

Gutachter der Dissertation	Prof. Dr. Johannes Haller Prof. Dr. Klaus Desch
Gutachter der Disputation	Prof. Dr. Johannes Haller Prof. Dr. Peter Schleper
Datum der Disputation	12. Juli 2012
Vorsitzende des Prüfungsausschusses	Prof. Dr. Caren Hagner
Vorsitzender des Promotionsausschusses	Prof. Dr. Peter Hauschildt
Leiterin des Departments Physik	Prof. Dr. Daniela Pfannkuche
Dekan der MIN-Fakultät	Prof. Dr. Heinrich Graener

“Everybody is a genius.
But if you judge a fish by its ability to climb a tree,
it will live its whole life believing that it is stupid.”
Albert Einstein

Abstract

In this thesis, various models beyond the Standard Model (SM) offering different solutions to some of the shortcomings of the SM are studied: Supersymmetry, the two Higgs doublet model, and models with warped extra dimensions. A search for events with large missing transverse momentum, jets, and at least two τ leptons using $2\,\mathrm{fb}^{-1}$ of proton-proton collision data recorded at $\sqrt{s} = 7\,\mathrm{TeV}$ with the ATLAS detector at the Large Hadron Collider is performed. No excess above the SM background expectation is observed and a 95 % CL upper limit on the visible cross section for new phenomena is set. A 95 % CL lower limit of 32 TeV is set on the Gauge Mediated Supersymmetry Breaking scale Λ independent of the ratio of $\tan\beta$. These limits provide the most stringent tests to date in a large part of the considered parameter space.

By using the results of the oblique vacuum polarization parameters from a fit to the electroweak precision data indirect constraints on model parameters are set. While in the two Higgs doublet model as well as in models with warped extra dimensions a heavy Higgs boson is compatible with the electroweak precision data, models with warped extra dimensions featuring custodial symmetry cannot accommodate a heavy Higgs.

Zusammenfassung

In dieser Arbeit werden verschiedene Modelle untersucht, die das Standard Modell (SM) erweitern und unterschiedliche Lösungen für einige der Probleme des SM aufzeigen. Diese Modelle sind Supersymmetrie, das zwei Higgs Duplett Modell und Modelle mit *warped* Extradimensionen. Es wurde eine Suche nach Ereignissen mit viel fehlender transversaler Energie, Jets und mindestens zwei Tauleptonen durchgeführt. Sie basiert auf $2\,\mathrm{fb}^{-1}$ Proton-Proton Kollisionsdaten, die am LHC mit dem ATLAS Detektor bei einer Schwerpunktsenergie von $\sqrt{s} = 7\,\mathrm{TeV}$ aufgezeichnet wurden. Im Vergleich zur SM-Erwartung wurde kein Überschuss an Ereignissen gefunden. Eine obere Grenze des effektiven Wirkungsquerschnitt für Physik jenseits des SM wurde bestimmt. Dabei ist der effektive Wirkungsquerschnitt definiert durch das Produkt des Wirkungsquerschnitts, des Verzweigungsverhältnisses, der Detektorakzeptanz und der Selektionseffizienz. Außerdem wurde eine untere Grenze auf die Brechungsskala von supersymmetrischen Modellen gesetzt, bei denen die Brechung durch eine Eichwechselwirkung übertragen wird. Für einen großen Teil des Parameterraums stellen diese Grenzen die schärfsten derzeit verfügbaren Grenzen für diese Art der Suchen dar.

Unter Zuhilfenahme der *oblique* Parameter und der Verwendung von Fitresultaten dieser Parameter an elektroschwache Präzisionsdaten lassen sich Modellparameter von Neuer Physik indirekt einschränken. Während im zwei Higgs Duplett Modell und in einfachen Modellen mit *warped* Extradimensionen schwere Higgs Bosonen erlaubt sind, ist dies innerhalb von Modellen mit *warped* Extradimensionen mit zusätzlicher *custodial* Symmetrie nicht möglich.

Contents

List of Figures

List of Tables

1. Introduction

The main goals of the two multi-purpose experiments ATLAS and CMS at the Large Hadron Collider (LHC) are the study of electroweak symmetry breaking and the search for physics beyond the Standard Model (SM). Among the many proposed extensions of the SM, Supersymmetry (SUSY) is considered a key candidate because it solves several shortcomings of the SM in an elegant way. For example, SUSY may provide a dark matter candidate and allows the unification of the coupling constants at a GUT scale. Since supersymmetric particles should have the same mass as their superpartners but have not yet been observed, SUSY is a broken symmetry. However, the breaking mechanism is unknown. It is usually assumed that the breaking takes place at a high energy scale and the SUSY breaking is then communicated to the visible sector via mechanisms such as gravity mediation, gauge mediation or anomaly mediation. The mass spectrum of the SUSY particles and the phenomenology are largely determined by the mediation mechanism, in particular by the nature of the lightest supersymmetric particle (LSP) which is stable if R-parity is assumed to be conserved.

In this thesis Gauge Mediated Supersymmetry Breaking (GMSB) models are investigated. They provide a possible mechanism to communicate SUSY breaking to the visible sector through an ordinary gauge interaction. In these models, the LSP is the gravitino, while the next-to-lightest supersymmetric particle (NLSP) is either a neutralino or a slepton. In the case of a $\widetilde{\tau}$ NLSP, events with large missing transverse momentum from the escaping gravitino, highly energetic jets from squark or gluino decays and up to four τ leptons from the production and decay of the $\widetilde{\tau}$ NLSP are expected in pp-collisions at the LHC providing a powerful channel to probe the GMSB theory. Before the operation of the LHC started, Monte Carlo (MC) studies were done to estimate the discovery potential of the ATLAS detector for these type of models. In case of discovery, the invariant ditau mass distribution could be used to extract information concerning the masses of the SUSY particles involved.

A search for supersymmetric events with large missing transverse momentum, jets, and at least two τ leptons was performed using $2.05\,\mathrm{fb}^{-1}$ of LHC proton-proton-collision data recorded in 2011 with the ATLAS detector at a center-of-mass energy of $\sqrt{s} = 7\,\mathrm{TeV}$. No excess above the SM expectation was observed and the results are interpreted in the context of GMSB. Limits on the number of signal events from new physics models as well as on the (visible) cross section, and the GMSB breaking scale parameter are set. The visible cross section is defined by the product of the cross section, the branching fraction, the detector acceptance, and the event selection efficiency.

However, SUSY is not the only possibility to extend the SM. Various other models can provide solutions for some of the SM shortcomings. As examples, the two Higgs doublet model (2HDM) and models with warped extra dimensions (WED) are studied in this thesis using the results of the oblique corrections obtained from a fit to electroweak precision data. Their prediction depends on the Higgs boson and the top mass for the SM and on the model parameters for the SM extension. The investigated models in many cases allow for a heavier Higgs boson as

the contribution to the oblique parameters from the Higgs boson and from the new physics model could cancel each other.

This thesis is organized as follows: Chapter 2 introduces the SM and some of its shortcomings motivating the need for an extension. It also presents some of these potential extensions, i.e. SUSY and in particular GMSB, 2HDM and WED models. In the third chapter, the constraints on the 2HDM and models with WED are discussed, following the presentation of the recent publication in [1]. Chapter 4 focuses on the ATLAS detector which is the experimental basis for the data analysis performed. Afterwards, in chapter 5, further details regarding the data taking and the simulated event samples used are given. In chapter 6, the various reconstruction algorithms for identifying electrons, muons, τ candidates, jets, and $E_{\mathrm{T}}^{\mathrm{miss}}$ are described. In chapter 7, a MC study that was performed prior to LHC data taking to estimate the discovery potential of GMSB models is presented. Chapter 8 focuses on the aforementioned search for GMSB events featuring τ final states. The interpretation of the results is given in chapter 9. This analysis and its results have also been recently published in [2, 3] which are used as a guideline.

2. Standard Model of Particle Physics and Beyond the Standard Model Physics

The Standard Model (SM) of particle physics summarizes the current knowledge of the fundamental particles and their interactions except gravity. It can explain many observed phenomena and make predictions that have been confirmed by different experiments. This chapter gives an overview of the SM including the Higgs mechanism. By discussing the shortcomings of the SM the need for an extension of the SM is motivated.

Even though the SM is unable to explain various aspects of nature, it is considered to be incomplete rather than incorrect. A common assumption is that the SM is a low energy limit of a more general theory. The most favored and popular of these theories is Supersymmetry (SUSY) which suggests a supersymmetric partner to every SM particle. Since no such particle has been previously discovered SUSY breaking is assumed. The Minimal Supersymmetric Standard Model (MSSM) and the *Gauge Mediated Supersymmetry Breaking* (GMSB) model, a particular kind of a SUSY breaking model, are introduced in the following.

If SUSY is not found in the expected mass range at the LHC other models might be an alternative. The two Higgs doublet model (2HDM) and extra dimension models are presented as possible alternatives following the descriptions in [1] and references therein.

2.1. Standard Model

The SM [4] describes all known elementary particles and their fundamental interactions: the strong, the weak, and the electromagnetic interaction, excluding gravity. It is based on a relativistic quantum field theory. There are twelve elementary particles, leptons and quarks. They are fermions, carrying spin $1/2$, representing the basic constituents of matter. Three of the leptons are electrically charged while three are the uncharged neutrinos. They participate in the electroweak interaction. The six quarks also interact strongly. Leptons and quarks are arranged in three families, each family containing one charged lepton, one neutrino, and one up- and one down-type quark. Table 2.1 lists a few fundamental properties of the fermions. The masses of these particles are free parameters of the SM and are determined experimentally. The particles appear left- or right-handed, except for the neutrinos which are only left-handed as they are assumed to be massless in the SM. However, the observation of neutrino oscillations has shown that the weak eigenstates are a mixture of mass eigenstates.

The three SM interactions can be mathematically described by the local symmetry group

$$SU(3)_C \otimes SU(2)_L \otimes U(1)_Y, \tag{2.1}$$

where C denotes the color charge of the strong interaction, L indicates the left-handedness of the weak current, and Y is the weak hypercharge. The description of the forces is formulated

Quarks			Leptons		
	Mass [MeV]	Charge [e]		Mass [MeV]	Charge [e]
down	4.1-5.8	$-1/3$	e	0.511	-1
up	1.7-3.3	$2/3$	ν_e	-	0
strange	101^{+29}_{-21}	$-1/3$	μ	105.7	-1
charm	1270^{+70}_{-90}	$2/3$	ν_μ	-	0
bottom	4190^{+180}_{-60}	$-1/3$	τ	1777	-1
top	$(173.18\pm0.94)\cdot10^3$	$2/3$	ν_τ	-	0

Table 2.1.: Fundamental properties of the elementary fermions described by the SM. The quark masses are given in the $\overline{\text{MS}}$ scheme [5, 6]. The neutrino masses are not specifically known. Further details in the context of neutrino mixing may be found in [5] and the references therein.

within the Lagrangian formalism using the Lagrangian density $\mathscr{L}$. The interactions are mediated by gauge bosons: gluons (strong), photons (electromagnetic), and the W and Z bosons (weak).

The interactions between gluons and quarks are described by Quantum Chromodynamics [7]. The massless gluons carry a color and an anticolor similar to quarks. One of the nine possible combinations results in a colorless state not realized in nature. Therefore, gluons are arranged in an $SU(3)_C$ octet. They are not affected by the breaking of the $SU(2)_L$ symmetry (see below). As leptons are color-singlets they do not interact strongly.

The coupling strength of the strong interaction α_S varies depending on the momentum transfer Q^2. If the momentum transfer is small the coupling strength is high and vice versa. Consequently, quarks are *asymptotically free* [8, 9] for very large values of Q^2, while at very low values of Q^2 the *confinement* of quarks allows them to only occur in color-neutral quark compositions, either quark-antiquark-pairs (*mesons*) or three quark configurations (*baryons*). This can be imagined as the field between a quark and an antiquark reinforcing with distance due to the self-coupling of the gluons.

Protons are the most relevant examples of baryons. Naively, a proton consists of three valence quarks: two up quarks and one down quark. Experimentally, it has been found that additionally gluons are present which further produce sea-quarks when splitting into quark–anti-quark pairs. The HERA experiments measured the structure of the proton described by the momentum fraction x carried by the partons. The result, the parton density function (PDF) of the proton, is shown in Fig. 2.1 at momentum transfers of $Q^2 = 10\,\text{GeV}^2$ and $Q^2 = 10000\,\text{GeV}^2$. It can be seen that with increasing Q^2, occurring at higher center-of-mass energies, the gluons and sea-quarks become more relevant.

Based on the knowledge of the proton structure, the cross sections for many processes expected at the LHC have been determined. Figure 2.2 shows a few selected processes, comparing them for LHC and Tevatron as a function of the center-of-mass energy. Since the hard scattering during a collision at the LHC in general involves only two partons which carry only part of the proton momentum, the effective center-of-mass energy will be lower than that of the proton

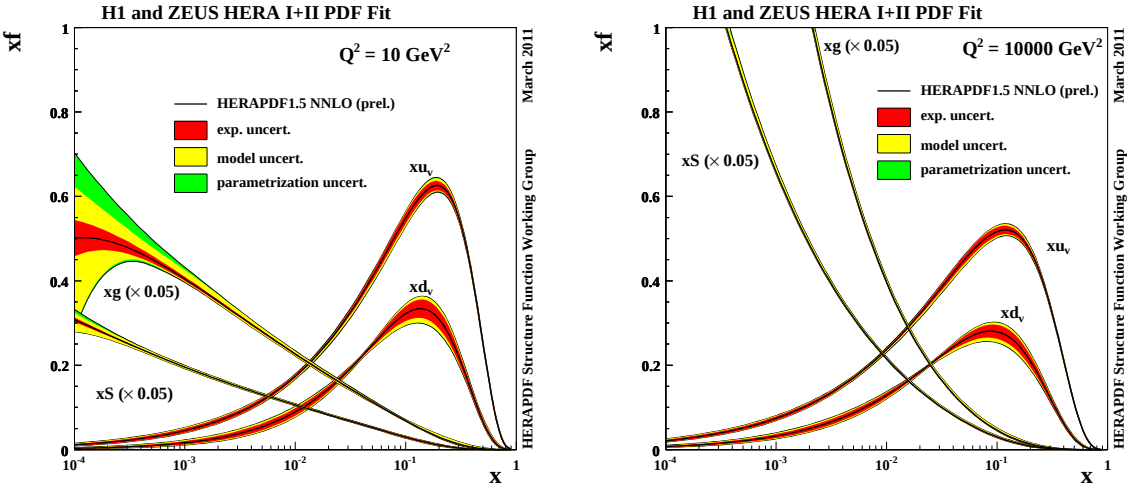

(a) (b)

Figure 2.1.: The parton density function for the valence quarks u_v and d_v, gluons g, and sea quarks S within the proton for (a) $Q^2 = 10\,\mathrm{GeV}^2$ and (b) $Q^2 = 10000\,\mathrm{GeV}^2$ [10]. It has been determined by combining ZEUS and H1 measurements.

system. While the total inelastic cross section is around $\mathcal{O}(100\,\mathrm{mb})$, the cross section of many SUSY scenarios is often ten orders of magnitude smaller and only a few pb.

The aforementioned hypercharge Y establishes a correlation between the electric charge Q and the third component of the weak isospin T_3 (Gell-Mann-Nishijima relation)

$$Q = T_3 + \frac{Y}{2}\,. \tag{2.2}$$

The gauge bosons of the electroweak interaction are represented by massless fields, a $SU(2)$ triplet $W_\mu^{1,2,3}$ and a $U(1)$ singlet B_μ. The electroweak symmetry breaking introduces the mixing of these weak eigenstates to the mass eigenstates representing the physical observable fields of the massless photon and the massive W and Z boson ($\mathcal{O}(100\,\mathrm{GeV})$). The physical fields of the charged $W^\pm$ bosons are a mixing of two fields $W_{1,2}^\mu$ with a weak isospin $T = 1$ and $T_3 = \pm 1$ resulting from the $SU(2)$ gauge invariance

$$W^{(\pm)\mu} = \frac{1}{\sqrt{2}}\left(W_1^\mu \pm i W_2^\mu\right)\,. \tag{2.3}$$

The corresponding third field of the triplet W_3^μ with a weak isospin of $\mathrm{T} = 1$ and $\mathrm{T_3} = 0$ mixes with the weak isospin singlet B^μ ($\mathrm{T} = \mathrm{T_3} = 0$) forming the physical fields Z^μ and A^μ of the Z boson and the photon, respectively

$$\begin{pmatrix} A^\mu \\ Z^\mu \end{pmatrix} = \begin{pmatrix} \cos\theta_W & \sin\theta_W \\ -\sin\theta_W & \cos\theta_W \end{pmatrix} \begin{pmatrix} B^\mu \\ W_3^\mu \end{pmatrix}, \tag{2.4}$$

where θ_W is the weak mixing angle that links the masses of the weak gauge bosons. It is defined through the couplings g' and g of $SU(2)_L \times U(1)_Y$ as

$$\cos\theta_W = \frac{g}{\sqrt{g^2 + g'^2}}, \qquad \sin\theta_W = \frac{g'}{\sqrt{g^2 + g'^2}}, \qquad M_\mathrm{Z} = \frac{M_\mathrm{W}}{\cos\theta_W}\,. \tag{2.5}$$

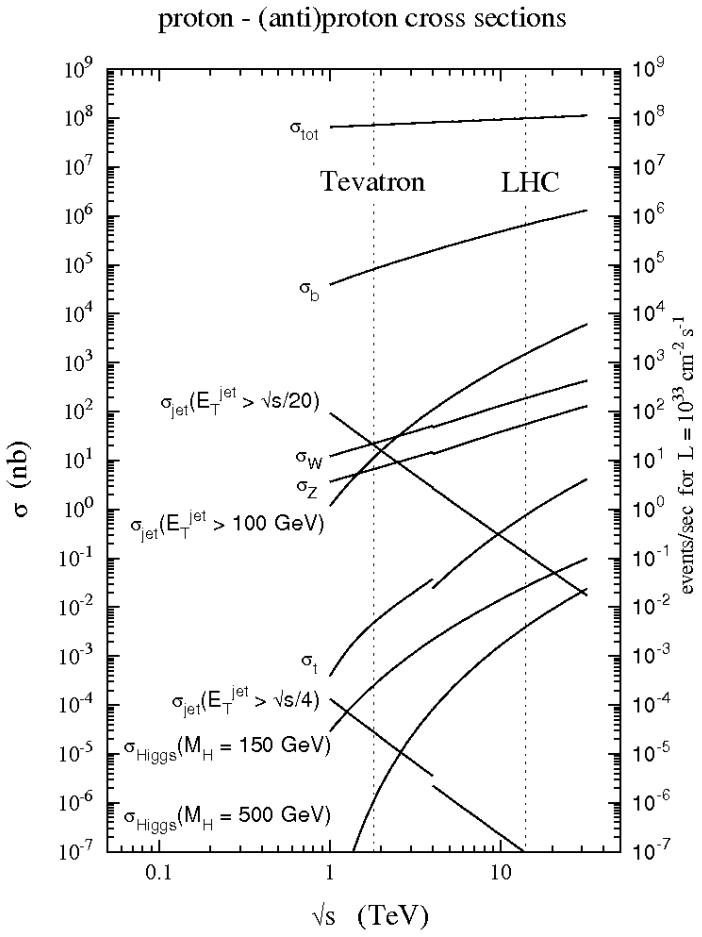

Figure 2.2.: The cross section for proton-proton collisions at the LHC and proton-antiproton collisions at the Tevatron as a function of the center-of-mass energy [11].

In addition, the couplings are defined through the electric charge

$$e = g \sin\theta_W = g' \cos\theta_W \,. \tag{2.6}$$

The fields W^μ of $SU(2)$, and therefore the gauge bosons $W^\pm$, solely couple to the left-handed states of all particles. As the field B^μ couples to left- as well as right-handed fermions the photon and the Z boson do as well.

The quark states listed in Tab. 2.1 are the mass eigenstates which are different from the weak eigenstates. Three of the weak eigenstates are a mixing of the strong ones. By convention, the down type mix according to the *Cabibbo-Kobayashi-Maskawa-Matrix* (CKM-Matrix) [12, 13]:

$$\begin{pmatrix} \mathrm{d}' \\ \mathrm{s}' \\ \mathrm{b}' \end{pmatrix} = \begin{pmatrix} V_{\mathrm{ud}} & V_{\mathrm{us}} & V_{\mathrm{ub}} \\ V_{\mathrm{cd}} & V_{\mathrm{cs}} & V_{\mathrm{cb}} \\ V_{\mathrm{td}} & V_{\mathrm{ts}} & V_{\mathrm{tb}} \end{pmatrix} \begin{pmatrix} \mathrm{d} \\ \mathrm{s} \\ \mathrm{b} \end{pmatrix} \tag{2.7}$$

The diagonal elements are highly dominant while the other elements are considerably smaller, resulting in a strongly suppressed mixing of the first and third quark family. The CKM-

Matrix is unitary and is determined by four parameters: three mixing angles and one complex CP-violating phase. This phase is the only source of CP-violation in the SM [13].

Experimentally, it is known that the weak gauge bosons as well as the fundamental fermions are massive particles. However, introducing mass terms to the Lagrangian breaks local gauge invariance. Therefore, a scalar field has been introduced coupling to the massive fermions and gauge bosons by spontaneous electroweak symmetry breaking. The *Higgs field* [14] is described by a complex scalar isospin doublet with four degrees of freedom

$$\phi = \begin{pmatrix} \phi^+ \\ \phi^0 \end{pmatrix} , \tag{2.8}$$

where '+' and '0' indicate electric charge. Its potential is $SU(2)_L$ symmetric

$$V(\phi) = \mu^2 |\phi|^2 + \lambda |\phi|^4 . \tag{2.9}$$

Assuming $\mu^2 < 0$ and $\lambda > 0$, the minimum of the potential is not at $\phi = 0$ and the vacuum expectation value is non zero

$$|\phi_0| = \sqrt{\frac{-\mu^2}{\lambda}} = v \quad \text{with } v = 246\,\text{GeV} . \tag{2.10}$$

This configuration is still $SU(2)_L$ symmetric while choosing any specific ground state breaks the electroweak symmetry $SU(2)_L \otimes U(1)_Y$ to the electromagnetic $U(1)_{\text{EM}}$. Three of the four degrees of freedom yield the masses of the weak gauge bosons

$$M_W = \frac{1}{2} g' v , \quad M_Z = \frac{1}{2} v \sqrt{g^2 + g'^2} , \quad M_\gamma = 0 . \tag{2.11}$$

Since the fourth degree of freedom is not absorbed by the photon it results in a physical, neutral *Higgs boson* whose couplings to the fermions are proportional to their masses

$$m_f = \frac{1}{\sqrt{2}} v \lambda_f , \tag{2.12}$$

where λ_f is the coupling constant. The Higgs boson mass is also given by the vacuum expectation value

$$M_H = \sqrt{2\lambda} v . \tag{2.13}$$

Even though in the SM only one Higgs field is assumed, this is not a necessity. Various extensions of the SM, introduce a second doublet, e.g. SUSY and the two Higgs doublet model (cf. Secs. 2.3 and 2.4).

The Higgs boson is the only particle of the SM which has not yet been observed. While the top mass could be precisely predicted prior to its discovery this is not possible for the Higgs mass. The reason is that the radiative correction of the self energy of the weak gauge bosons depends quadratically on the top mass whereas their dependence on the Higgs mass is only logarithmically. Nonetheless, a global fit of the electroweak precision data [1, 15] allows to determine the most probable value for the Higgs mass. It has been found to be $94^{+25}_{-22}\,\text{GeV}$ at 68% confidence level (CL) [16]. Figure 2.3 shows the corresponding $\Delta\chi^2$ scan as a function of M_H. Further details concerning this fit can be found in Ch. 3. Also indicated in Fig. 2.3 are the mass regions that were excluded by the different direct searches. LEP set a mass

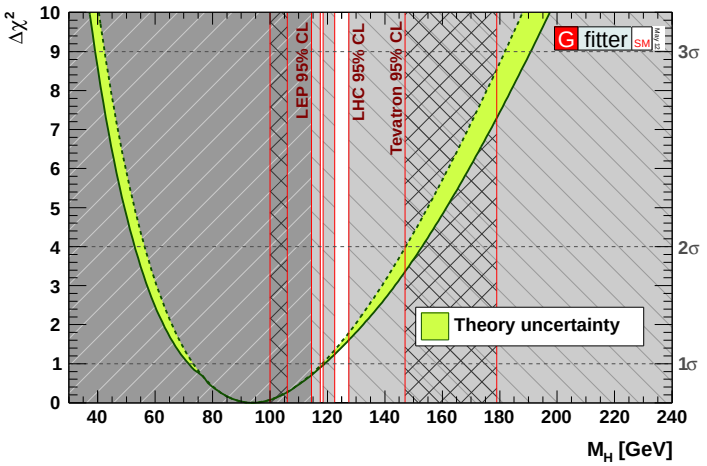

Figure 2.3.: $\Delta\chi^2$ as a function of M_H for the standard fit [16]. The solid (dashed) line gives the results when including (ignoring) theoretical errors. The gray regions show which mass range could be excluded by LEP, Tevatron, and LHC through direct Higgs searches.

constraint of $M_H \geq 114\,\text{GeV}$ [17]. The combination of the two Tevatron experiments using up to $8.6\,\text{fb}^{-1}$ of proton-antiproton collision data led to the exclusion of $156\,\text{GeV} < M_H < 177\,\text{GeV}$ at 95 % CL [18]. ATLAS and CMS have analyzed up to $4.9\,\text{fb}^{-1}$ of proton-proton collision data. In their searches, they have included the decays $H \to WW$, $H \to ZZ$, $H \to \tau\tau$, $H \to bb$, and $H \to \gamma\gamma$. While CMS excludes the mass range $127\,\text{GeV} < M_H < 600\,\text{GeV}$ and $129\,\text{GeV} < M_H < 525\,\text{GeV}$ at 95 % CL and 99 % CL, respectively, an excess at $M_H \approx 124\,\text{GeV}$ has been found with a local significance of $3.1\,\sigma$ [19]. At the same time, ATLAS excludes the mass ranges $110\,\text{GeV} < M_H < 117.5\,\text{GeV}$, $118.5\,\text{GeV} < M_H < 122.5\,\text{GeV}$, $129\,\text{GeV} < M_H < 539\,\text{GeV}$ at 95 % CL and $130\,\text{GeV} < M_H < 486\,\text{GeV}$ at 99 % CL. Similar to CMS, an excess at $M_H \approx 126\,\text{GeV}$ with a local significance of $2.5\,\sigma$ has been found [20].

2.2. Shortcomings of the Standard Model

The SM describes the known particle spectrum and their interactions. Despite its success, the SM raises some questions without providing answers. The nature of these problems ranges from cosmological measurements to purely theoretical issues.

Dark Matter and Matter-Antimatter-Asymmetry

It is known from cosmological observations, that the matter described by the SM makes up only approximately 5 % of the universe [21]. A large part (22 %) supposedly consists of neutral, only weakly interacting *dark matter*. There are various hypotheses on dark matter based on the mass and velocity of the particles: hot dark matter, warm dark matter, and cold dark matter. The most popular choice is cold dark matter as it explains the structure of the universe. However, the only uncharged massive stable particles of the SM are neutrinos but due to their velocity they can only be considered hot dark matter candidates. If they were

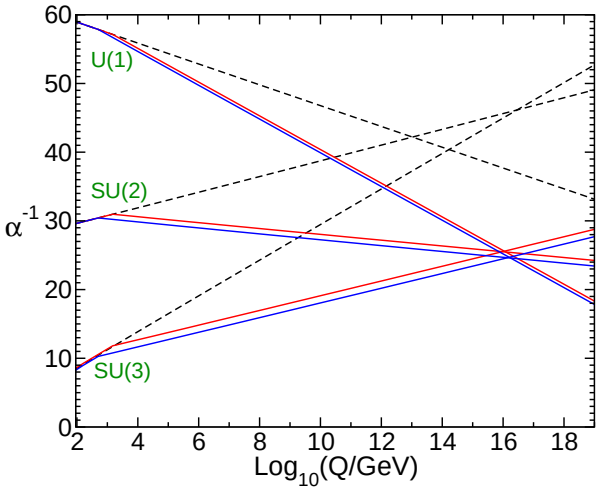

Figure 2.4.: Two-loop renormalization group evolution of the inverse gauge couplings $\alpha_a^{-1}(Q)$ in the SM (dashed lines) and the MSSM (solid lines) [25]. In the MSSM case, the sparticle masses are treated as a common threshold varied between 500 GeV (blue) and 1.5 TeV (red), and $\alpha_S(M_Z)$ is varied between 0.117 and 0.121.

dark matter candidates they would have caused a more homogeneous structure of the universe than as it is observed today. On the other hand, various SUSY models introduce potential heavier candidates to account for the relic density. Very little is known about the remaining 73 % fraction of the universe, called *dark energy*.

As mentioned above, the only source of CP-violation in the SM is the complex phase of the CKM-Matrix. However, it is insufficient to entirely explain the observed matter-antimatter asymmetry of the universe [22–24].

Unification of the Coupling Constants

A nice feature of a model beyond the SM would be if at sufficiently high energies, all forces are unified and their couplings are identical. When extrapolating the coupling constants from the electroweak scale to the Grand Unified Theory (GUT) scale ($\mathcal{O}(10^{16}\,\text{GeV})$) they should intersect. In the SM there is no such intersection for all three couplings as illustrated by the black, dashed lines in Fig. 2.4. SUSY is one of the models that would alter the running of the couplings in such a way that one intersection of all coupling constants is created resolving this problem. This is also shown in Fig. 2.4 for two different SUSY particle, *sparticle*, mass scales.

Hierarchy Problem of the Higgs Mass

Assuming the existence of the Higgs in the SM, its mass underlies sizeable quantum corrections from loops of every massive SM particle, especially the top quark. The Higgs boson mass is the sum of the bare Higgs mass and those corrections. If $-\lambda_f H \bar{f} f$ is the coupling of the Higgs

field to the fermion in the Lagrangian, the contribution to the Higgs mass reads

$$\Delta M_H^2 = -\frac{|\lambda_f|^2}{8\pi^2}\left(\Lambda_{\mathrm{UV}}^2 - 3m_f \ln\left(\frac{\Lambda_{\mathrm{UV}}}{m_f}\right) + ...\right), \tag{2.14}$$

whereas m_f is the fermion mass. Λ_{UV}^2 denotes an ultraviolet momentum cutoff. It is interpreted as the scale where new physics enters. If it is chosen to coincide with the Planck scale the Higgs mass is several orders of magnitude too large. An incredibly high degree of fine-tuning of the radiative corrections needs to occur to still yield the assumed Higgs mass of $\mathcal{O}(100\,\mathrm{GeV})$. By introducing SUSY, additional bosons would be introduced and contribute to the corrections mentioned in Eq. (2.14). As bosons are scalars, they would cancel the fermion terms, reducing the necessary degree of fine-tuning.

Gravity

The SM does not include any description of gravity. Attempts to incorporate the theory of general relativity into the SM have not been successful so far. While at the electroweak scale gravitational effects are negligible, they become relevant at the Planck scale ($10^{19}\,\mathrm{GeV}$) and are of equal strength as the other forces. Again, SUSY might provide a solution to this problem if it is introduced as a local gauge symmetry. As supersymmetric transformations include space-time, gravity would automatically be a part of supersymmetric models.

2.3. Supersymmetry

As explained above, SUSY [26–30] provides solutions to various problems occurring in the SM. It establishes a symmetry between fermions and bosons. For every SM fermion, a supersymmetric boson is introduced and vice versa. The irreducible representation of the SUSY algebra is achieved with *supermultiplets* containing both the fermionic and the bosonic states of the superpartners, where the number of degrees of freedom is identical for fermions and bosons. This is done by combining one Weyl fermion with its two helicity states and two scalars into one supermultiplet. Except for their spin, superpartners have identical quantum numbers, e.g. they possess the same mass, electric charge, and weak isospin.

In the SM, the baryon number B and lepton number L are conserved since no possible renormalizable Lagrangian terms can introduce such violation. In SUSY, the most general gauge-invariant renormalizable superpotential contains such terms, inducing the rapid proton decay. Since this decay has not been confirmed experimentally, these terms need to be suppressed. Therefore, an additional multiplicative quantum number, called *R-parity*, is defined

$$R = (-1)^{2S+3(B-L)}, \tag{2.15}$$

where S is the spin. Employing this definition leads to $R = 1$ ($R = -1$) for all SM particles (SUSY sparticles). Assuming exact R-parity conservation [31, 32] implies several significant consequences:

- Only an even number of sparticles is allowed in one vertex.

Name	Spin	Gauge eigenstates	Mass eigenstates
Squarks	0	$\widetilde{u}_L, \widetilde{u}_R, \widetilde{d}_L, \widetilde{d}_R$	identical
		$\widetilde{c}_L, \widetilde{c}_R, \widetilde{s}_L, \widetilde{s}_R$	identical
		$\widetilde{t}_L, \widetilde{t}_R, \widetilde{b}_L, \widetilde{b}_R,$	$\widetilde{t}_1, \widetilde{t}_2, \widetilde{b}_1, \widetilde{b}_2$
Sleptons	0	$\widetilde{e}_L, \widetilde{e}_R, \widetilde{\nu}_e$	identical
		$\widetilde{\mu}_L, \widetilde{\mu}_R, \widetilde{\nu}_\mu$	identical
		$\widetilde{\tau}_L, \widetilde{\tau}_R, \widetilde{\nu}_\tau$	$\widetilde{\tau}_1, \widetilde{\tau}_2, \widetilde{\nu}_\tau$
Higgs bosons	0	$H_u^0, H_d^0, H_u^+, H_d^-$	$h^0, H^0, A^0, H^\pm$
Neutralinos	1/2	$\widetilde{B}^0, \widetilde{W}^0, \widetilde{H}_u^0, \widetilde{H}_d^0$	$\widetilde{\chi}_1^0, \widetilde{\chi}_2^0, \widetilde{\chi}_3^0, \widetilde{\chi}_4^0$
Charginos	1/2	$\widetilde{W}^\pm, \widetilde{H}_u^+, \widetilde{H}_d^-$	$\widetilde{\chi}_1^\pm, \widetilde{\chi}_2^\pm$
Gluino	1/2	$\widetilde{g}$	identical
Gravitino	3/2	$\widetilde{G}$	identical

Table 2.2.: Supersymmetric particle spectrum in the MSSM [25].

- At colliders, such as the LHC, sparticles can only be produced in pairs, resulting in two decay chains.
- Eventually, every sparticle decays into the lightest supersymmetric particle (LSP) or an odd number of LSPs, producing various SM particles in the process.
- The LSP is stable. Inside a detector, it behaves similarly to neutrinos. Since it is only weakly interacting the typical signature is a noticeable amount of missing transverse momentum $E_{\mathrm{T}}^{\mathrm{miss}}$. If the LSP is neutral and has no color, it can be considered a viable dark matter candidate.

The phenomenology of R-parity violating models [33] is quite different because the LSP decays into SM particles. R-parity breaking terms appear naturally in the Lagrangian. For R-parity violating models, they are not explicitly removed as it is done for R-parity conserving models. To avoid the rapid proton decay in these models one of the coupling constants is set to a small value. Throughout this thesis, R-parity conservation is assumed.

2.3.1. The MSSM

The MSSM is the simplest supersymmetric extension of the SM. Its particle content is summarized in Tab. 2.2. As the left- and right-handed states transform differently under the gauge group individual sparticles are introduced for left- and right-handed fermions. These left- and right-handed supersymmetric states do not refer to their own helicity but rather to that of their SM partner. They are arranged in *chiral* supermultiplets. The fermion superpartners are called squarks $\widetilde{q}$ and sleptons $\widetilde{\ell}$, $\widetilde{\nu}$ while the gauginos are named gluino, wino, zino, and photino. The gravitino $\widetilde{G}$ is the only particle possessing a spin of 3/2. The gauge interactions and couplings of the sparticles are the same as those of their SM partners.

In the SM, the electroweak symmetry is broken by introducing the Higgs mechanism and one Higgs doublet to give mass to all SM fermions. In the MSSM, two doublets are needed. One of the two Higgs supermultiplets possesses the Yukawa coupling needed to give mass to the up-type quarks (with the electroweak hypercharge being $Y = 1/2$) while the Yukawa coupling of the other doublet ($Y = -1/2$) is appropriate to give mass to the down-type quarks and the charged leptons. The individual vacuum expectation values of the two superfields are denoted v_u and v_d. Their ratio, $\tan\beta = v_u/v_d$, is an important free parameter of the theory. These two doublets have eight degrees of freedom. Three are absorbed by the gauge bosons of the weak interaction, just as in the SM, leaving five physical Higgs bosons (cf. Tab. 2.2).

The superpartners of the SM gauge bosons, arranged in gauge supermultiplets, are not the mass eigenstates of the MSSM. A mixing of the gauginos occurs. The neutral superpartners of the gauge boson fields, bino and wino, mix with the neutral Higgsinos to form the four mass eigenstates, called *neutralinos* $\widetilde{\chi}^0$, while the charged gauginos and Higgsinos mix to form the mass eigenstates of the *charginos* $\widetilde{\chi}^{\pm}$. In addition, mixing occurs in the third squark and slepton family whereas the mixing is larger with increasing tanβ values.

2.3.2. SUSY-Breaking

SUSY must be a broken symmetry since no supersymmetric particles have been observed so far and the masses of the superpartners are obviously different from those of their SM partners. It needs to occur at a scale sufficiently low for SUSY to still be able to provide a solution to the hierarchy problem. Otherwise, the loop corrections to the Higgs do not cancel each other.

Since the MSSM Lagrangian does not contain any terms that might induce spontaneous SUSY breaking, the MSSM is extended, and it is assumed that the breaking occurs in a hidden sector that does not couple directly to the visible sector of the MSSM supermultiplets. The breaking is added to the Lagrangian as *soft breaking* terms

$$\mathscr{L} = \mathscr{L}_{\mathrm{SUSY}} + \mathscr{L}_{soft}\,, \tag{2.16}$$

whereas $\mathscr{L}_{\mathrm{SUSY}}$ contains all gauge and Yukawa couplings and $\mathscr{L}_{soft}$ contains all violating terms. These soft breaking terms arise indirectly or radiatively.

The breaking is communicated from the hidden to the visible sector either through gravity or electroweak and QCD gauge interactions. In the general MSSM, 105 free parameters are added to the 19 of the SM. Assuming a specific breaking mechanism reduces the number of free parameters that determine the masses of all particles and their mixing. All the branching ratios are calculable, fixing the resulting phenomenology. The two most prominent examples for specific SUSY breaking mechanisms are *Minimal Supergravity* (mSUGRA) [34–38] and GMSB [39–44].

In mSUGRA, it is assumed that SUSY is a local symmetry with five free parameters. At the GUT scale all scalar particles (all gauginos) are assumed to have the same mass m_0 ($m_{1/2}$). This is illustrated in Fig. 2.5. Other free parameters are the Higgs-sfermion-sfermion-coupling A, tanβ, and the sign of the Higgsino mass term μ. The minimal GMSB model has six free parameters and is discussed in detail in the next section.

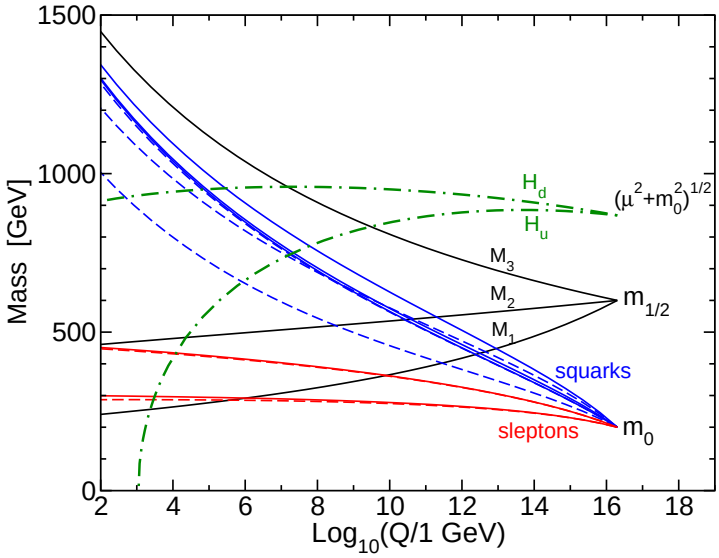

Figure 2.5.: Evolution of scalar and gaugino mass parameters in the MSSM with mSUGRA boundary conditions imposed at $Q_0 = 2 \cdot 10^{16}\,\mathrm{GeV}$ [25]. The mSUGRA parameters are set to $m_0 = 200\,\mathrm{GeV}$, $m_{1/2} = 600\,\mathrm{GeV}$, $A = 600\,\mathrm{GeV}$, $\tan\beta = 10$, $\mathrm{sgn}\,\mu = +$. The parameter $\mu^2 + m_{H_u}^2$ runs negative, provoking electroweak symmetry breaking.

2.3.3. Gauge Mediated Supersymmetry Breaking

In GMSB models, SUSY breaking is communicated from the hidden sector to the visible sector through a flavor-blind SM gauge interaction via messenger fields at a scale M_{mess}, which is small compared to the Planck mass. The soft breaking terms of the MSSM arise from loop diagrams of these messenger particles. The messenger fields form complete representations of $SU(5)$ and therefore preserve the unification of the coupling constants. The breaking might also be communicated through gravity, but its impact is small compared to the gauge interactions. At M_{mess} the masses are the same for each generation preventing the occurrence of flavor changing neutral currents. Squarks, sleptons, and gauginos obtain their masses radiatively from the gauge interactions with the massive messenger fields in such a way that the superpartner masses are proportional to the breaking scale. The free parameters in GMSB models are the following:

Λ: the SUSY breaking mass scale; typically it has values of (10-100) TeV and sets the overall mass scale for all MSSM superpartners, which depend linearly on Λ. The gauge interactions communicating the breaking are proportional to the gauge couplings times Λ.

M_{mess}: the messenger mass scale; it has to be larger than Λ in order to prevent color and charge breaking in the messenger sector. Sparticle masses depend logarithmically on M_{mess}.

N_5: the number of equivalent messenger fields; the gaugino masses depend linearly on N_5 while the sfermion masses are proportional to $\sqrt{N_5}$. This influences significantly which particle is the next-to-lightest supersymmetric particle (NLSP). If N_5 is too large the gauge couplings diverge before unifying at the GUT scale.

$\tan\beta$: the ratio of the two Higgs doublet vacuum expectation values at the electroweak scale mentioned above.

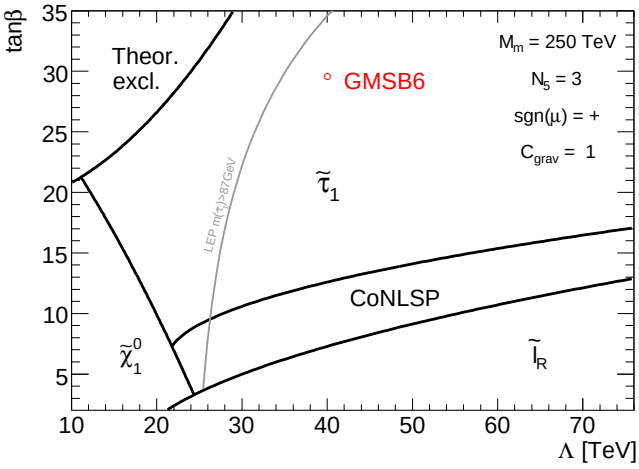

Figure 2.6.: Type of NLSP in the GMSB parameter space of Λ and $\tan\beta$.

sgn $\mu = \pm$: the sign of the Higgsino mass term appearing in the neutralino and chargino mass matrices and in the superpotential.

$C_{\text{grav}} \geq 1$: the scale factor for the gravitino mass; it determines the lifetime of the NLSP. For $C_{\text{grav}} = 1$, the NLSP decays promptly ($c\tau_{\text{NLSP}} < 0.1\,\text{mm}$).

In GMSB scenarios, the gravitino is always the LSP. Due to its very small mass of $\mathcal{O}(\text{eV})$, the NLSP is the only sparticle decaying into the LSP. Therefore, the nature of the NLSP, depending mainly on N_5, $\tan\beta$, and Λ, strongly influences the phenomenology of the scenario:

- For N_5 =1 and small to medium values of $\tan\beta$, the NLSP is the lightest neutralino $\widetilde{\chi}_1^0$ which decays into a photon and a gravitino. Since $\tan\beta$ determines the mixing of the $\widetilde{\tau}$, the $\widetilde{\tau}_1$ is the NLSP for higher values of $\tan\beta$.
- For $N_5 \geq 2$, the NLSP is a $\widetilde{\tau}_1$ or a right-handed slepton $(\widetilde{\text{e}}_R, \widetilde{\mu}_R)$ in a wide range of the parameter space as shown in Fig. 2.6 for the example of $N_5 = 3$. The NLSP is the $\widetilde{\tau}_1$ $(\widetilde{\text{e}}_R, \widetilde{\mu}_R)$ for large (small) values of $\tan\beta$ while for medium $\tan\beta$ values the $\widetilde{\tau}_1$ and the right-handed sleptons are almost degenerate in mass[1].

The region of small Λ and large $\tan\beta$ is theoretically excluded since it leads to tachyonic states.

In the LHC data analysis presented in this thesis, final states with τ leptons are studied as expected for GMSB scenarios with a $\widetilde{\tau}_1$ NLSP. A typical GMSB scenario is given by the ATLAS benchmark scenario GMSB6[2] [2,46] with the following parameter values: $\Lambda = 40\,\text{TeV}$, $M_{\text{mess}} = 250\,\text{TeV}$, $N_5 = 3$, $\tan\beta = 30$, $\text{sgn}\,\mu = +$ and $C_{\text{grav}} = 1$. GMSB6 is chosen because it features a promptly decaying $\widetilde{\tau}_1$ as NLSP leading to τ final states. Its kinematic properties are representative for a wide range of the GMSB parameter space offering moderately large inclusive τ production cross sections while not yet being excluded by former experiments.

[1] This *CoNLSP*-region is defined as the region where the mass difference of the $\widetilde{\tau}_1$ and the right-handed sleptons $(\widetilde{\text{e}}_R, \widetilde{\mu}_R)$ is smaller than the τ mass [45].

[2] Due to the development of the data analysis, GMSB6 was renamed to GMSB4030 corresponding to the Λ and $\tan\beta$ values of this benchmark point. Both names can be used interchangeably.

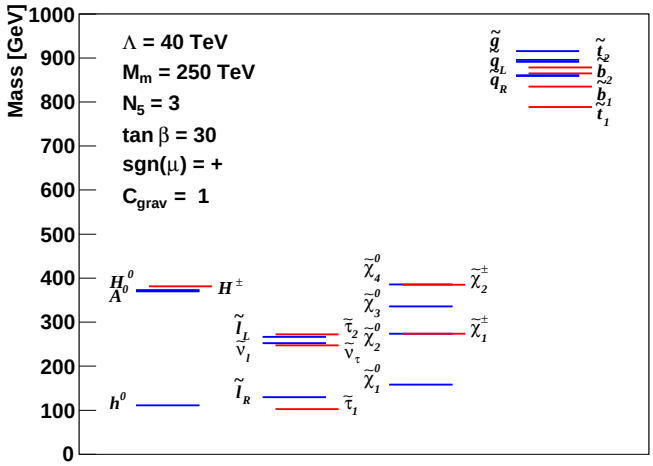

Figure 2.7.: Mass spectrum of one GMSB benchmark point.

Additionally, it respects the current constraints from SM measurements as $b \to s\gamma$ and $(g_\mu - 2)/2$ and is similar to other benchmark points used in the literature, e. g. G2a [47] or SPS7 [48]. In comparison to G2a and SPS7, the value of tanβ is much higher to ensure that the NLSP is the $\widetilde{\tau}_1$. The mass spectrum in the GMSB6 scenario is shown in Fig. 2.7. Detailed numbers are given in the appendix (cf. Tab C.1). Apart from the quasi-massless gravitino (2.4 eV, not shown), it features squarks and gluinos with masses around (800-900) GeV, while the sleptons and gauginos have lower masses around (100-400) GeV. The $\widetilde{\tau}_1$ NLSP has a mass of $m_{\widetilde{\tau}_1} = 102.8\,\text{GeV}$.

At the LHC, squarks and gluinos might be produced via gluon-gluon and gluon-quark fusion or through strong quark-antiquark annihilation and quark-quark scattering. The tree-level Feynman diagrams for these processes are shown in Fig. 2.8. An additional production process might be electroweak gaugino production, but its cross section is assumed to be much lower, provided that the sparticle masses are within the reach of the LHC. These sparticles decay directly or through cascades into the NLSP, which subsequently decays to the LSP. The decays of the lightest neutralino and the right-handed slepton at the end of the decay chain are dominant

$$\widetilde{\chi}^0_{1,2} \to \widetilde{\tau}_1\,\tau \to \tau\,\tau\,\widetilde{G}\,, \tag{2.17}$$

$$\widetilde{\ell}_R \to \ell\,\widetilde{\tau}_1\,\tau \to \ell\,\tau\,\tau\,\widetilde{G}\,. \tag{2.18}$$

The decay of a chargino is not as frequent and produces only one τ and a ν_τ

$$\widetilde{\chi}^\pm_1 \to \widetilde{\tau}_1\,\nu_\tau \to \tau\,\nu_\tau\,\widetilde{G}\,. \tag{2.19}$$

These decays result in events containing a minimum of two and up to four τ leptons. The event signature is also characterized by multiple jets from squark or gluino decays and E_T^miss from the escaping LSP.

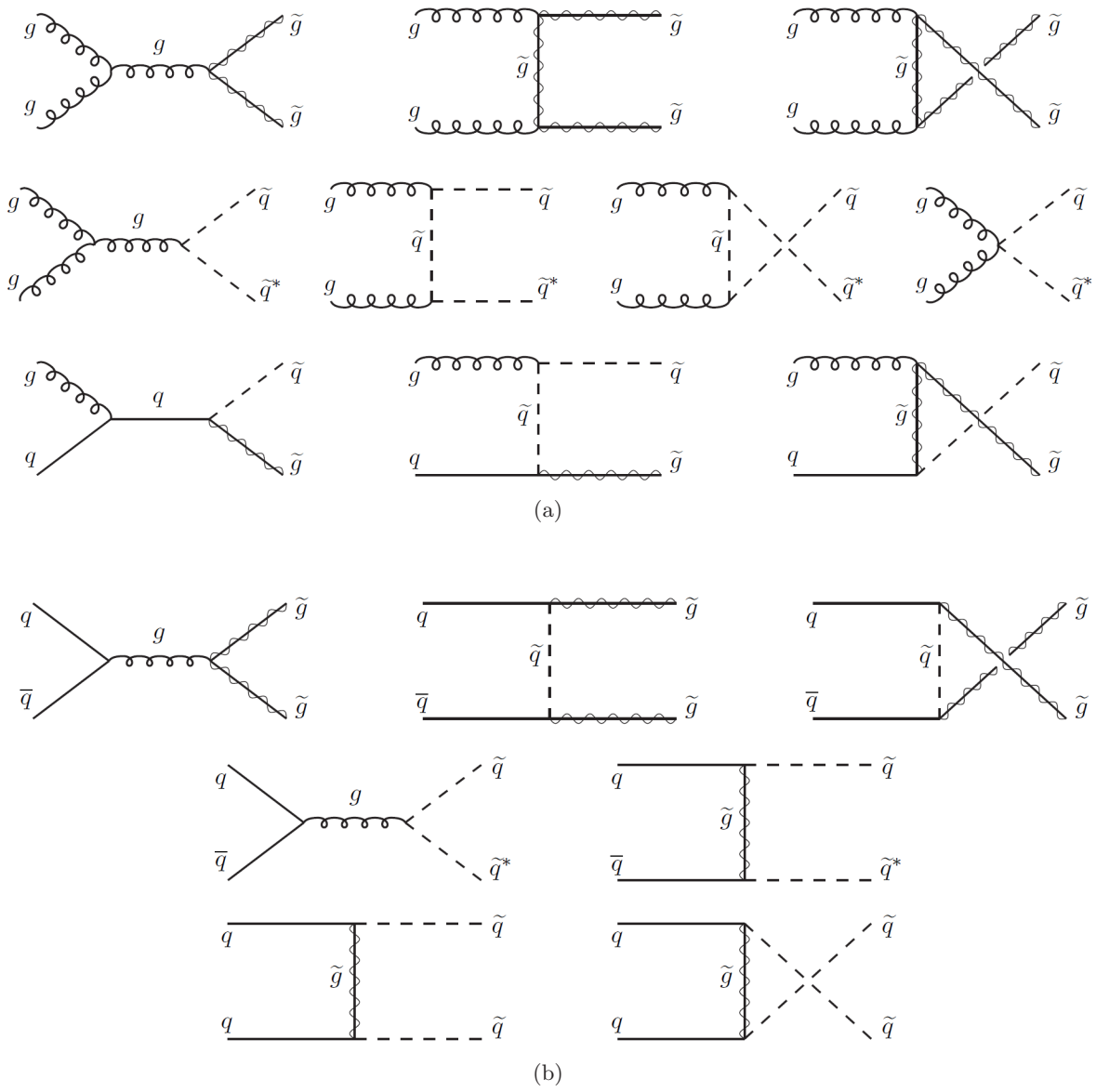

Figure 2.8.: Feynman diagrams for gluino and squark production at hadron colliders from (a) gluon-gluon and gluon-quark fusion and (b) from strong quark-antiquark annihilation and quark-quark scattering [25].

2.4. Two Higgs Doublet Model

Two Higgs doublet models (2HDM) [49] are simple extensions to the SM Higgs sector, which introduce one additional $SU(2)_L \times U(1)_Y$ Higgs doublet with hypercharge $Y = 1$. As mentioned above, two Higgs doublets lead to five physical Higgs boson states, of which three h^0, H^0, A^0, are electrically neutral, and the remaining two $H^\pm$, are electrically charged. Of the neutral states, h^0 and H^0 are scalars and A^0 is pseudoscalar. The free parameters of the 2HDM are the Higgs boson masses $M_{h^0} M_{H^0}$, M_{A^0} and $M_{H^\pm}$, as well as $\tan\beta = v_2/v_1$, occurring in the mixing of charged and neutral Higgs fields, and the angle α, governing the mixing of the neutral CP-even Higgs fields. In the most general 2HDM, $\tan\beta$ and, hence, the corresponding Higgs couplings and mass matrix elements depend on the choice of the basis for the Higgs fields [50, 51].

Models with two Higgs doublets intrinsically fulfill the empirical equality $M_W^2 \approx M_Z^2 \cos^2\theta_W$. They also increase the maximum allowed mass of the lightest neutral Higgs boson for electroweak baryogenesis scenarios to values not yet excluded by LEP [52] and allow for CP-violation in the Higgs sector. Flavor changing neutral currents can be suppressed with an appropriate choice of the Higgs-to-fermion couplings [53, 54]. For example, in the Type-I 2HDM this is achieved by letting only one Higgs doublet couple to the fermion sector. In the Type-II 2HDM [55], one Higgs doublet couples to the up-type quarks and leptons only, while the other one couples to the down-type fermions. The Type-II 2HDM resembles the Higgs sector of the MSSM. It fixes the basis of the Higgs fields and promotes tanβ to a physical parameter.

2.5. Extra Dimension Models

The hierarchy problem, the very large difference between the Planck and the electroweak scale, is one of the known shortcomings of the SM (cf. Sec 2.2). A prominent class of new physics models addresses the hierarchy problem through the existence of extra spatial dimensions, e.g. large [56, 57], universal [58], or warped extra dimension [59] models. The latter are introduced below and discussed within the context of the oblique parameters in Secs. 3.3.3 and 3.3.4.

2.5.1. Warped Extra Dimensions

Randall and Sundrum (RS) proposed a single, small and non-factorisable extra space dimension accessible to gravity only [59]. The geometry of this model is determined by the extra dimension confined by two three-branes, one of them containing the SM fields. The model assumes only one fundamental mass scale: the ultraviolet (UV) Planck scale. The effective four-dimensional Planck scale is determined by a higher dimensional Planck scale and the geometry of the extra dimension. The generation of the weak scale on the infrared (IR) brane from the UV brane is achieved by introducing a *warp factor* $\mathrm{e}^{-2kr\phi}$ altering the four-dimensional Minkowski metric

$$ds^2 = \mathrm{e}^{-2kr\phi}\eta_{\mu\nu}dx^\mu dx^\nu + r^2 d\phi^2\,, \tag{2.20}$$

where k and r are the dimensional curvature of the five-dimensional space-time and the compactification radius, respectively. k and $1/r$ are scales of the order of the Planck scale chosen to fulfill $kr \approx 12$. x^μ are the coordinates for the familiar four-dimensions, and $0 \leq \phi \leq \pi$ is the coordinate for the extra dimension, a S^1/Z_2 orbifold, whose size is determined by the compactification radius. As can be seen from Eq. 2.20, the warp factor is an exponential function of the compactification radius of the extra dimension

$$\epsilon = \frac{\Lambda_{\mathrm{IR}}}{\Lambda_{\mathrm{UV}}} \equiv \mathrm{e}^{-kr\pi} \approx 10^{-16}\,, \tag{2.21}$$

where the Planck or UV brane is at $\phi = 0$ and the TeV or IR brane is at $\phi = \pi$. It is small and thus precludes the extra dimension to be observed at low-scale gravity experiments. It is considered to be the source of the observed large hierarchy between the Planck and the electroweak scale in four space-time dimensions.

Due to the propagation of gravity in the higher-dimensional bulk, the RS model features a fundamental *Kaluza-Klein* (KK) *tower* of massive spin-2 graviton excitations. These excitations couple strongly to the SM particles and would thus manifest themselves in the form of TeV scale resonances of pairs of jets, leptons, photons, and gauge bosons in collider experiments. The scale can be reduced if either a heavy Higgs is allowed or an ultraviolet cut-off below the Planck scale is introduced. The simplest RS models contain only the SM particles and their KK excitations. These models are characterized by only two new parameters, one of which is the order-one logarithm of the warp factor, $L = kr\pi$. The inverse warp factor sets the scale of the other free parameter, $M_{\mathrm{KK}} = ke^{-L} = \mathcal{O}(\mathrm{TeV})$. It is also the mass scale for the low-lying KK excitations of the SM fields.

In the minimal RS model, all SM fields are confined to one brane, while only gravity propagates in the five-dimensional warped bulk. Since in this model the unification of the gauge couplings cannot be described by an effective field theory [60] and the flavor hierarchy is not addressed, alternatives have been developed. In a first extension, the SM gauge bosons are allowed to propagate into the bulk. In following variations also the SM fermions are allowed to propagate into the bulk corresponding to the 0^{th} mode of the five-dimensional fields. Each SM fermion is accompanied by two towers of heavy KK states. M_{KK} then determines the lowest KK excitations of the SM fields in the bulk. The masses of the first KK gluon and photon excitations are approximately $2.5 \cdot M_{\mathrm{KK}}$.

In this scenario, the oblique parameter T (cf. Sec. 3.3.1) can still adopt rather large values which in return forces M_{KK} to adapt rather high values to still be compatible with the electroweak precision data. This led to the development of alternative scenarios, one described below.

2.5.2. Warped Extra Dimensions with Custodial Symmetry

In an alternative approach to the above mentioned extensions of the minimal RS model, *custodial isospin gauge symmetry* [61] is introduced in the bulk, thereby extending the hypercharge group. Thus, the electroweak gauge symmetry is enhanced to $SU(2)_L \times SU(2)_R \times U(1)_{B-L}$ yielding a $SU(3)_C \times SU(2)_L \times SU(2)_R \times U(1)_{B-L}$ gauge symmetry in the bulk of the extra dimension. $SU(2)_R$ is then broken to $U(1)_R$ on the Planck brane, resulting in a spontaneous breaking of $U(1)_R \times U(1)_{B_L}$ to $U(1)_Y$ on the UV brane, while keeping the IR brane $SU(2)_R$

symmetric. Consequently, the right-handed fermionic fields are promoted to doublets of this symmetry. In addition, to ensure a small overlap of light fermion fields with the Higgs on the IR brane they are localized near the UV brane. The gauge sector does not contribute to custodial $SU(2)$ breaking as it would be the case in the absence of $SU(2)_R$ [61].

3. Constraints on New Physics using the Electroweak Precision Data

Gfitter is a generic fitting package. It allows to test the compatibility between theoretical predictions and experimental data. Model parameters can be determined, as well as the overall goodness of the fit can be tested. Unknown model parameters can be constrained by the use of multi-parameter fits. By exploiting contributions from radiative corrections, physics at a much higher energy scale than the masses of the particles directly involved in the experimental reactions may be probed [1]. Hence, Gfitter may be used to confront the predictions of the oblique parameters [62] for beyond the SM (BSM) physics models with the fit results of the electroweak precision data thereby constraining the model parameters.

This chapter outlines briefly the underlying statistical aspects of Gfitter while following the original introduction in [15]. The work on the statistical framework, on the electroweak fit, and on the determination of the oblique parameters was not subject of this work. Their description can be found in [1, 15, 63] and references therein. A few selected concepts and results are presented here for illustration purposes and completeness only, closely following the presentations in [1, 63].

However, during the work on this thesis, various BSM physics models (cf. Secs. 2.4 and 2.5.1) have been tested using the results on the oblique parameters. The results for the 2HDM, and two extra dimension models will be discussed. The description here follows their recent publication in [1]. They represent the status prior to data taking at the LHC in 2011 and do not yet include the direct Higgs searches performed by ATLAS and CMS.

3.1. The Statistics Framework Gfitter

Gfitter relies on a Frequentist interpretation of results where the underlying statistical method is the minimization of a test statistics. Likelihood functions are used to measure the agreement between data and theoretical predictions. They lead to the definition of confidence intervals (CI) and p-values which are derived through the use of toy Monte Carlo (MC) simulation. The p-value is defined as the probability to wrongly exclude the model tested and is therefore an exclusion probability whereas CIs are a measure for the inclusion probability[1]. The minimization of the test statistics by default is done via TMINUIT [64]. Additionally, more involved global minima finders are available through the TMVA [65] package incorporated into ROOT [66], i.e. Genetic Algorithm and Simulated Annealing. During the implementation phase of the framework and while fixing the statistical methods to be used, Gfitter has profited from the experience that was gained during the development of CKMFitter [67].

[1] A short introduction to p-values and confidence levels can be found in the Appendix (cf. Sec. A.)

Statistical Methods

For a set of $N_{\rm exp}$ measurements $(x_{\rm exp})_{i=1,..,N_{\rm exp}}$ exists a corresponding set of theoretical expressions $(x_{\rm theo})_{i=1,..,N_{\rm exp}}$. The theoretical expressions are functions of a set of $N_{\rm mod}$ model parameters $(y_{\rm mod})_{j=1,..,N_{\rm mod}}$ where the model parameters $y_{\rm mod}$ are either unconstrained parameters of the theory like the Higgs boson mass, theoretical parameters that are precisely measured like the Z boson mass, or theoretical uncertainties like higher order QCD corrections. The test statistics of least-squares is defined as

$$\chi^2(y_{\rm mod}) \equiv -2\ln\mathcal{L}(y_{\rm mod})\,, \tag{3.1}$$

where the likelihood function $\mathcal{L}$ is a product of the experimental likelihood $\mathcal{L}_{\rm exp}$, measuring the agreement between the theoretical predictions and their measurements, and the theoretical likelihood $\mathcal{L}_{\rm theo}$, expressing prior knowledge of the model parameters

$$\mathcal{L}(y_{\rm mod}) = \mathcal{L}_{\rm exp}(x_{\rm theo}(y_{\rm mod}) - x_{\rm exp}) \cdot \mathcal{L}_{\rm theo}(y_{\rm mod})\,. \tag{3.2}$$

The theoretical likelihood is a product of individual likelihood components, one for each model parameter. When performing the fit, the model parameters are allowed to vary within predefined ranges $[\bar{y}_{\rm mod} - \sigma_{\rm theo}, \bar{y}_{\rm mod} + \sigma_{\rm theo}]$, where $\bar{y}_{\rm mod}$ is the best guess value and $\sigma_{\rm theo}$ is the theoretical systematic uncertainty. As long as $y_{\rm mod}$ adopts a value within this allowed range, the corresponding likelihood does not contribute to the χ^2. This approach is called the Rfit scheme [67, 68]. Thus, all allowed model parameter values are treated equally irrespective of their closeness to the assumed central value.

The experimental likelihood is a product of individual likelihood components accounting for each relevant observable. In the simplest case, they are independent Gaussian functions. Most of the time however, they are correlated featuring systematic and theoretical uncertainties in addition to the statistical ones. The systematic uncertainties are added in quadrature while theoretical uncertainties are treated according to the Rfit scheme [67, 68].

The combined likelihood function of a single parameter for a given set of $y_{\rm mod}$ parameters can be expressed by

$$-2\ln\mathcal{L}(y_{\rm mod}) = \begin{cases} 0\,, & \text{if: } -\sigma^-_{\rm theo} \le f(y_{\rm mod}) - x_0 \le \sigma^+_{\rm theo}\,, \\ \left(\frac{f(y_{\rm mod}) - \left(x_0 + \sigma^+_{\rm theo}\right)}{\sigma^+_{\rm Gauss}}\right)^2\,, & \text{if: } f(y_{\rm mod}) - x_0 > \sigma^+_{\rm theo}\,, \\ \left(\frac{f(y_{\rm mod}) - \left(x_0 - \sigma^-_{\rm theo}\right)}{\sigma^-_{\rm Gauss}}\right)^2\,, & \text{if: } x_0 - f(y_{\rm mod}) > \sigma^-_{\rm theo}\,, \end{cases} \tag{3.3}$$

where x_0 is the central measured value of the parameter, $\sigma^+_{\rm Gauss}(\sigma^-_{\rm Gauss})$ are positive (negative) Gaussian errors, $\sigma^+_{\rm theo}(\sigma^-_{\rm theo})$ are positive (negative) theoretical errors, and $f(y_{\rm mod})$ are the theoretical predictions of the $y_{\rm mod}$ parameters. The sum over all likelihood contributions for each individual observable (cf. Eq. (3.3)) defines the final test statistics of the global fit where correlations between measurements are properly treated by the likelihood functions. The rescaling mechanism introduced in Gfitter allows the introduction of dependencies among parameters [15].

In case the SM is assumed to be correct, the overall agreement between the data and the theory is not questioned and rather the degree of agreement between the data and different SM parameter sets is of interest. Therefore, the offset corrected test statistics is defined

$$\Delta\chi^2(y_{\mathrm{mod}}) = \chi^2(y_{\mathrm{mod}}) - \chi^2_{\mathrm{min};\hat{y}_{\mathrm{mod}}}\,, \tag{3.4}$$

where $\chi^2(y_{\mathrm{mod}})$ is the χ^2 of a given parameter set y_{mod} and $\chi^2_{\mathrm{min};\hat{y}_{\mathrm{mod}}}$ is the absolute minimum of the χ^2 function (cf. Eq. (3.1)). By construction, the minimum of $\Delta\chi^2(y_{\mathrm{mod}})$ is zero. This ensures that exclusion confidence levels (CL) equal to zero are obtained when the assumed model is correct. The CL is derived from the p-value

$$\mathrm{CL} = 1 - \mathrm{Prob}(\Delta\chi^2, n_{\mathrm{dof}})\,, \tag{3.5}$$

where n_{dof} is the number of degrees of freedom for the offset corrected $\Delta\chi^2$. The p-value is an estimator for the goodness-of-the-fit and for a Gaussian problem estimated by $\mathrm{Prob}(\Delta\chi^2, n_{\mathrm{dof}})$, which is a ROOT function. In a non-Gaussian case, the CL needs to be derived with toy MC instead. This method has been used to confirm the results for the global electroweak fit obtained through Eq. (3.5).

3.2. Electroweak SM Fit

The electroweak precision data can be used to constrain the parameters of the SM. In this chapter, the general idea of a SM fit to the electroweak precision data is briefly summarized. As an example result, the prediction of the Higgs boson mass is explained. The presentation in this chapter follows [1]. Further detailed results, e.g. the determination of the top quark and W boson mass, the strong coupling constant, and the effective weak mixing angle can be found in recent publications [1, 16, 63].

In the past, intensive studies have been performed including theoretical calculations of electroweak precision observables and the development of various software packages predicting these observables within the SM, e.g. GAPP [69–71], LEPTOP [72], TOPAZ0 [73, 74], and ZFITTER [75,76]. Global electroweak fits are also performed regularly by the LEP electroweak working group [77] and the Particle Data Group [5]. All this work has been of great advantage for the electroweak studies using Gfitter.

SM Predictions and Experimental Input

The relevant parameters to predict the SM observables are the masses of the elementary fermions m_f and bosons M_Z, M_W, M_H and the coupling constants of the electromagnetic α, weak G_F, and strong interaction α_S. The neutrino masses are set to zero. The number of unknown SM parameters is reduced by two through electroweak unification resulting in a mass-less photon and establishing a relation between the electroweak gauge bosons and their couplings. Further reduction can be achieved by fixing parameters whose uncertainties are negligible compared to the accuracy of the fit. Therefore, all SM predictions for the electroweak observables can be written as functions of the following seven floating fit parameters: M_Z, M_H, m_t, $\overline{m}_b$, $\overline{m}_c$, $\Delta\alpha^{(5)}_{\mathrm{had}}(M_Z^2)$, and $\alpha_s(M_Z^2)$. Further details on the theoretical predictions may be found in [1, 63] and references therein.

The *"standard"* fit includes the electroweak precision data measured at the Z-pole (Z resonance parameters, partial Z cross sections, neutral current couplings) and their experimental correlations [78]. Additionally, the W mass world average $M_W = 80.399 \pm 0.023\,\text{GeV}$ [79] and width $\Gamma_W = 2.098 \pm 0.048\,\text{GeV}$ [80] are used. Further, the average of the direct Tevatron top mass measurements $m_t = 173.18 \pm 0.56\,(\text{stat}) \pm 0.75\,(\text{syst})\,\text{GeV}$ [6] enters the fit[2]. The five lightest quark flavors contribute to the running of the electromagnetic coupling strength $\Delta\alpha^{(5)}_{\text{had}}(M_Z^2)$ at the Z pole through vacuum polarization. Its latest determination resulted in $\Delta\alpha^{(5)}_{\text{had}}(M_Z^2) = (2757 \pm 10) \cdot 10^{-10}$ [85][3].

In addition, the *"complete"* fit takes into account the direct Higgs searches from LEP [17], Tevatron [86, 87] and LHC (2010 data only) [88, 89]. The LHC data comprises the combined ATLAS results accounting for searches in six different channels and CMS results in the fully leptonic channel ($H \to WW \to \ell\nu\ell\nu$). Since both LHC results are dominated by statistical uncertainties the correlations due to common systematic uncertainties have been neglected. The latest results of the Higgs searches from the 2011 LHC run are summarized in Sec. 2.1. They are not included since the correlation between the ATLAS and CMS searches and the Tevatron results are not sufficiently known at this point.

Important Fit Results

The standard and complete fit converge at a global minimum of the test statistics of $\chi^2_{\text{min}} = 16.6$ and $\chi^2_{\text{min}} = 17.8$, respectively. To express the degree of compatibility of the SM with the data, taking into account the number of degrees of freedom, the naive p-values can be calculated, giving $\text{Prob}(\chi^2_{\text{min}}, 13) = 0.21$ and $\text{Prob}(\chi^2_{\text{min}}, 14) = 0.23$, respectively.

Figure 3.1 shows the profile curve of the $\Delta\chi^2$ test statistics for the standard fit. For each chosen Higgs mass value, the other free parameters of the fit are varied to return the minimum of the test statistics. For the Higgs mass, the absolute minima are found to be at

$$M_H = \begin{cases} 91^{+30}_{-23}\,\text{GeV} & \text{standard fit}\,, \\ 120^{+12}_{-5}\,\text{GeV} & \text{complete fit}\,, \end{cases} \tag{3.6}$$

with the 95 % (99 %) upper bounds of 163 GeV (194 GeV) and 143 GeV (149 GeV) for the standard and complete fit, respectively.

A two-dimensional scan of the Higgs mass versus the W mass is shown in Fig. 3.2. It shows the 68 %, 95 %, and 99 % CL allowed regions without the direct searches of the two observables in blue. They are in agreement with the world average of M_W shown as a green band. Once the direct M_W measurements are included, these regions are reduced mainly towards smaller Higgs masses (purple regions). In green, the allowed regions are shown when additionally including the direct Higgs searches.

[2] There are theoretical uncertainties from non-perturbative color-reconnection effects in the fragmentation process [81, 82] and from ambiguities in the top-mass definition [83, 84] affecting the top mass measurement. However, since their estimation is difficult and not sufficiently verified by experimental data they have not been included in the fit.

[3] In addition, a functional dependence of the central value on the strong coupling strength of $0.37 \cdot 10^{-4} \cdot (\alpha_S(M_Z^2) - 0.1193)/0.0028$ around the central value has been observed. This is incorporated into Gfitter through the rescaling mechanism mentioned above.

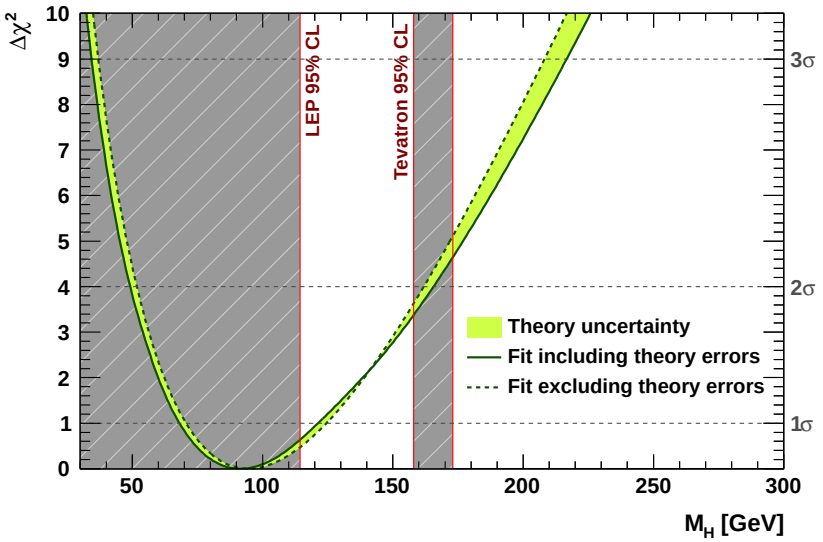

Figure 3.1.: Indirect determination of the Higgs boson mass [1]: $\Delta\chi^2$ as a function of M_H for the standard fit. The solid (dashed) lines give the results when including (ignoring) theoretical errors.

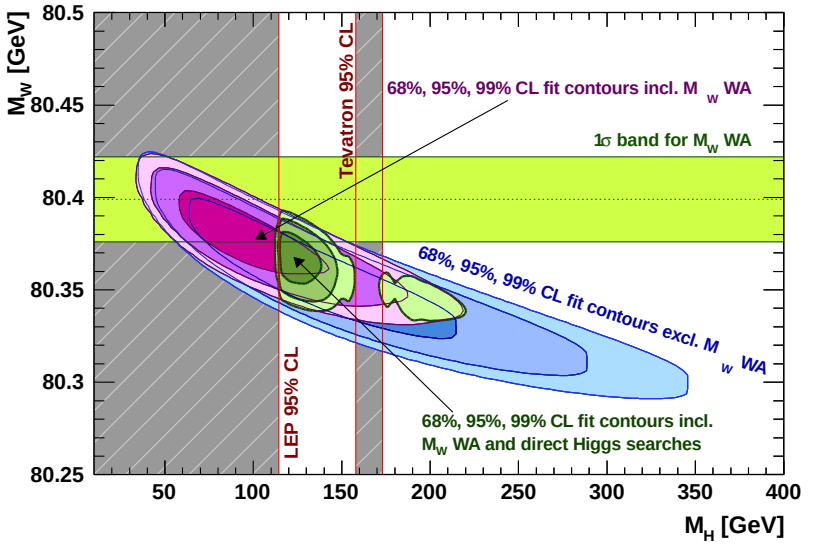

Figure 3.2.: Allowed contours of 68 %, 95 %, and 99 % CL obtained from scans of fits with fixed variable pairs M_W vs. M_H [1]. The largest/blue allowed regions are the results of the fit excluding the M_W measurement and any direct Higgs search information. The narrow/purple (narrowest/green) contours indicate the constraints obtained for a fit including the M_W measurement and the direct Higgs search results. The horizontal band represents the M_W world average experimental value with its 1σ uncertainty.

3.3. Constraints on New Physics Models

In the following, the concept of the oblique parameters will be introduced along with their implications for the SM and several BSM physics models, i.e. 2HDM and warped extra dimension models with and without custodial symmetry. The presentation follows again [1].

3.3.1. Oblique Parameters

Oblique parameters offer an interesting way to parametrize BSM model contributions to predictions of electroweak precision observables under the assumption that the new physics mass scale is higher than the mass scale accessible to direct production and new physics only contributes through vacuum polarization loops. Otherwise, if the new physics scale is not much larger than the electroweak scale additional parameters need to be introduced [90, 91]. They are set to zero in the presented analysis as they can only be independently determined if data taken at a higher center-of-mass energy than the Z-pole mass is included.

The two equivalent oblique parameter sets $\epsilon_1, \epsilon_2, \epsilon_3$ [92, 93] and S, T, U [62] are a representation of the three form-factors $\Delta\rho, \Delta\kappa, \Delta r$ absorbing the radiative corrections to the total Z coupling strength, the effective weak mixing angle, and the W mass, respectively. The S, T, U parameters used in the following can be derived from $\epsilon_1, \epsilon_2, \epsilon_3$. The $\epsilon_1, \epsilon_2, \epsilon_3$ parameters include SM contributions as well as BSM physics model contributions

$$\epsilon_1 = \Delta\rho\,, \tag{3.7}$$

$$\epsilon_2 = \cos^2\theta_W \Delta\rho + \frac{\sin^2\theta_G}{\cos^2\theta_W - \sin^2\theta_G}\Delta r - 2\sin^2\theta_G \Delta\kappa'\,, \tag{3.8}$$

$$\epsilon_3 = \cos^2\theta_W \Delta\rho + (\cos^2\theta_W - \sin^2\theta_G)\Delta\kappa'\,, \tag{3.9}$$

where $2\sin^2\theta_G = 1 - \sqrt{1 - \sqrt{8}\pi\alpha(M_Z^2)/(G_F M_Z^2)}$ and $\Delta\kappa'$ relates $\sin^2\theta^f_{eff}$ to $\sin^2\theta_G$ instead of $\sin^2\theta_W$. The quadratic top mass dependence present in all form factors has been removed explicitly from the parameters ϵ_2 and ϵ_3.

The SM contributions are dominated by top-quark and Higgs boson corrections and depend on fixed reference values of m_t and M_H defining a reference SM. For the definition of S, T, U, they are subtracted. Therefore, by construction S, T, U vanish for the reference SM (cf. Eq. (3.13)). Nonetheless, the difference between the experimental S, T, U parameters and a model prediction is independent of the reference. The S, T, U parameters are normalized and related to the ϵ-parameters

$$S = \quad \epsilon_3 \frac{4\sin^2\theta_G}{\alpha(M_Z^2)} - d_S\,, \tag{3.10}$$

$$T = \quad \epsilon_1 \frac{1}{\alpha(M_Z^2)} - d_T\,, \tag{3.11}$$

$$U = -\epsilon_2 \frac{4\sin^2\theta_G}{\alpha(M_Z^2)} - d_U\,, \tag{3.12}$$

where d_i are the SM predictions for the chosen M_H and m_t reference values of $M_{H,\mathrm{ref}} = 120\,\mathrm{GeV}$ and $m_{t,\mathrm{ref}} = 173\,\mathrm{GeV}$.

The S, T, U parameters allow for an easy comparison of the electroweak precision data and a BSM physics model. The prediction of an electroweak observable is given by

$$O = O_{\mathrm{SM,ref}}(M_{H,\mathrm{ref}}, m_{t,\mathrm{ref}}) + c_S S + c_T T + c_U U\,, \tag{3.13}$$

where $O_{\mathrm{SM,ref}}(M_{H,\mathrm{ref}}, m_{t,\mathrm{ref}})$ is the SM prediction of the observable in a reference SM, including all known two-loop and beyond two-loop electroweak corrections. The coefficients c_S, c_T, and c_U have been provided by [94]. S, T, U measure the deviations from electroweak radiative corrections that are expected in the reference SM:

***S*:** parametrizes the new physics contribution to neutral current processes at different energy scales.

***S* + *U*:** parametrizes the new physics contribution to charged current processes at different energy scales whereas U is only sensitive to M_W and Γ_W. In new physics models, it is usually very small and often set to zero.

***T*:** parametrizes the difference between neutral and charged current processes at low energies and is sensitive to weak isospin violation.

In case the Higgs mass and the top mass differ from the values chosen as reference, the S, T, U predictions do not only parametrize the BSM contribution but also SM contribution accounting for the difference to $\mathrm{SM_{ref}}$. The Higgs boson and top-quark mass dependence of this contribution can be approximated at one-loop level [62]

$$S \approx \frac{1}{12\pi}\ln\frac{M_H^2}{M_{H,\mathrm{ref}}^2} + \frac{1}{6\pi}\ln\frac{m_t^2}{m_{t,\mathrm{ref}}^2}\,, \tag{3.14}$$

$$T \approx -\frac{3}{16\pi\cos^2\theta_W}\ln\frac{M_H^2}{M_{H,\mathrm{ref}}^2} + \frac{3}{16\pi\sin^2\theta_W\cos^2\theta_W}\ln\frac{m_t^2 - m_{t,\mathrm{ref}}^2}{m_Z^2}\,, \tag{3.15}$$

$$U \approx \frac{1}{2\pi}\ln\frac{m_t^2}{m_{t,\mathrm{ref}}^2}\,. \tag{3.16}$$

As can easily be seen, these contributions to S, T, U vanish for the reference values.

The S, T, U parameters can be determined from a global electroweak fit according to Eq. 3.13. Except for the Higgs boson and top-quark mass for which the reference values are used ($M_{H,\mathrm{ref}} = 120\,\mathrm{GeV}$, $m_{t,\mathrm{ref}} = 173\,\mathrm{GeV}$) all parameters are allowed to vary freely in the fit. If U is set to zero the fit results for S and T are

$$S|_{U=0} = 0.06 \pm 0.09, \qquad T|_{U=0} = 0.10 \pm 0.08\,. \tag{3.17}$$

with a correlation coefficient of +0.88. The corresponding 68%, 95% and 99% CL allowed regions in the (S,T)-plane are shown by the blue ellipse in Fig. 3.3(a) along with the SM prediction (gray band). The width of the gray band is determined by the uncertainty on the top mass measurement while the allowed values for the Higgs mass determine the length, whereas the region excluded by the Tevatron experiment has been left out. As expected, the electroweak data prefer a light Higgs boson over a heavy one. By construction, $S = T = U = 0$ is predicted for the reference values.

Letting also U vary freely in the fit, results in

$$S = 0.03 \pm 0.10\,, \qquad T = 0.05 \pm 0.12\,, \qquad U = 0.07 \pm 0.11\,, \tag{3.18}$$

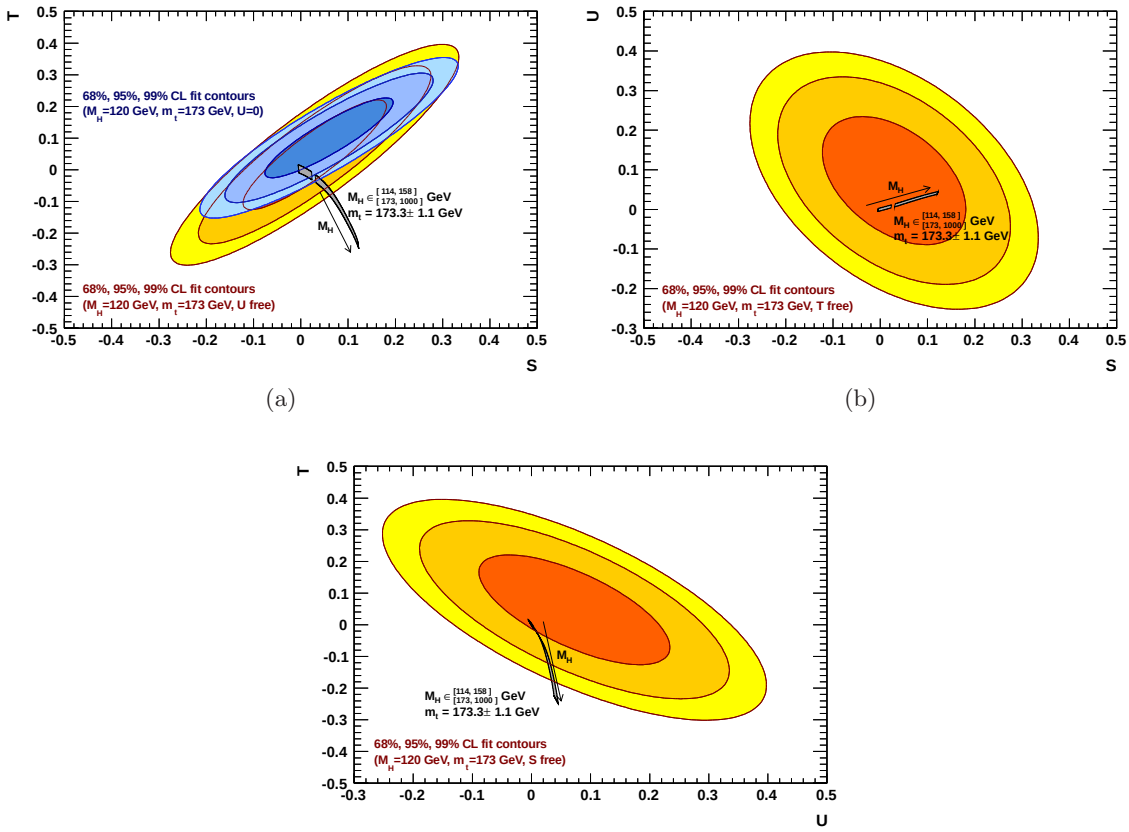

Figure 3.3.: Fit result of the oblique parameters [1]: Shown are the 68 %, 95 %, and 99 % CL allowed regions in the (a) (S,T)-, (b) (S,U)- and (c) (U,T)-planes together with the SM prediction. For the (S,T)-plane also the fit with $U = 0$ is shown. The gray/dark area illustrates the SM prediction for various values of M_H and m_t.

with correlation coefficients of +0.89, -0.45, and -0.69 between S and T, S and U, and T and U, respectively. All values are compatible with zero and therefore with the reference SM. S and T are less constrained when U is allowed to vary because the constraints from M_W and Γ_W are absorbed in the U parameter in this case. Figure 3.3 shows the corresponding 68 %, 95 %, and 99 % CL allowed regions in the (S,T)-, (S,U)-, and (U,T)-plane (orange ellipses).

Previous studies testing the compatibility of the SM and electroweak precision data have been performed by the LEP electroweak working group [77] and the particle data group [70]. They are in agreement with the above results.

3.3.2. Two Higgs Doublet Model

Adding an additional Higgs doublet, as described in Sec. 2.4, introduces additional Higgs bosons and couplings altering the predictions for the S, T, U parameters. For the study of the 2HDM oblique corrections, the type distinction between the different 2HDM models is

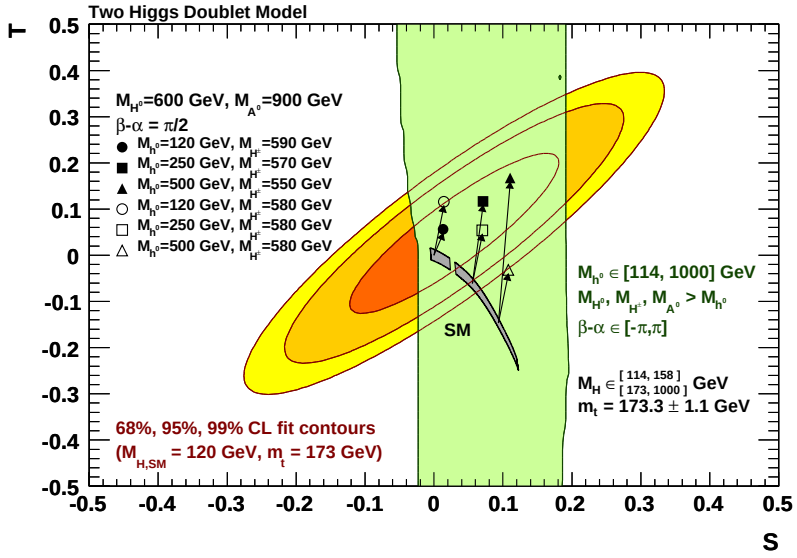

Figure 3.4.: Oblique parameters in the 2HDM. Shown are the S, T fit results (leaving U free) compared with predictions from the SM (gray) and 2HDM (light green). The 2HDM area is obtained with the use of the mass and mixing parameter ranges given on the plot. The symbols illustrate the 2HDM predictions for six example settings, compared to the corresponding SM predictions via the arrows.

irrelevant as they are defined according to the Yukawa couplings, which do not enter the oblique corrections at one-loop order. For the prediction of the S, T, U parameters in the 2HDM, the formulas[4] of Refs. [95–97] are used

$$\begin{aligned} S = \frac{1}{\pi M_Z^2}\{&\sin^2(\beta-\alpha)\mathcal{B}_{22}(M_Z^2, M_{H^0}^2, M_{A^0}^2) - \mathcal{B}_{22}(M_Z^2, M_{H^\pm}^2, M_{H^\pm}^2) \\ &+ \cos^2(\beta-\alpha)[\mathcal{B}_{22}(M_Z^2, M_{h^0}^2, M_{A^0}^2) + \mathcal{B}_{22}(M_Z^2, M_Z^2, M_{H^0}^2) - \mathcal{B}_{22}(M_Z^2, M_Z^2, M_{h^0}^2) \\ &- M_Z^2\mathcal{B}_0(M_Z^2, M_Z^2, M_{H^0}^2) + M_Z^2\mathcal{B}_0(M_Z^2, M_Z^2, M_{h^0}^2)]\} \end{aligned} \tag{3.19}$$

$$\begin{aligned} T = \frac{1}{16\pi M_W^2 s_w^2}\{&F(M_{H^\pm}^2, M_{A^0}^2) + \sin^2(\beta-\alpha)[F(M_{H^\pm}^2, M_{H^0}^2) - F(M_{A^0}^2, M_{H^0}^2)] \\ &+ \cos^2(\beta-\alpha)[F(M_{H^\pm}^2, M_{h^0}^2) - F(M_{A^0}^2, M_{h^0}^2) + F(M_W^2, M_{H^0}^2) - F(M_W^2, M_{h^0}^2) \\ &- F(M_Z^2, M_{H^0}^2) + F(M_Z^2, M_{h^0}^2) + 4M_Z^2\overline{B}_0(M_Z^2, M_{H^0}^2, M_{h^0}^2) - 4M_W^2\overline{B}_0(M_W^2, M_{H^0}^2, M_{h^0}^2)]\} \end{aligned} \tag{3.20}$$

$$\begin{aligned} U = &-S + \frac{1}{\pi M_Z^2}\{\mathcal{B}_{22}(M_W^2, M_{A^0}^2, M_{H^\pm}^2) - 2\mathcal{B}_{22}(M_W^2, M_{H^\pm}^2, M_{H^\pm}^2) \\ &+ \sin^2(\beta-\alpha)\mathcal{B}_{22}(M_W^2, M_{H^0}^2, M_{H^\pm}^2) \\ &+ \cos^2(\beta-\alpha)[\mathcal{B}_{22}(M_W^2, M_{h^0}^2, M_{H^\pm}^2) + \mathcal{B}_{22}(M_W^2, M_W^2, M_{H^0}^2) - \mathcal{B}_{22}(M_W^2, M_W^2, M_{h^0}^2) \\ &- M_W^2\mathcal{B}_0(M_W^2, M_W^2, M_{H^0}^2) + M_W^2\mathcal{B}_0(M_W^2, M_W^2, M_{h^0}^2)]\} \end{aligned} \tag{3.21}$$

[4]Further details on the exact computation of the S, T, U parameters may be found in the Appendix (cf. Sec. B).

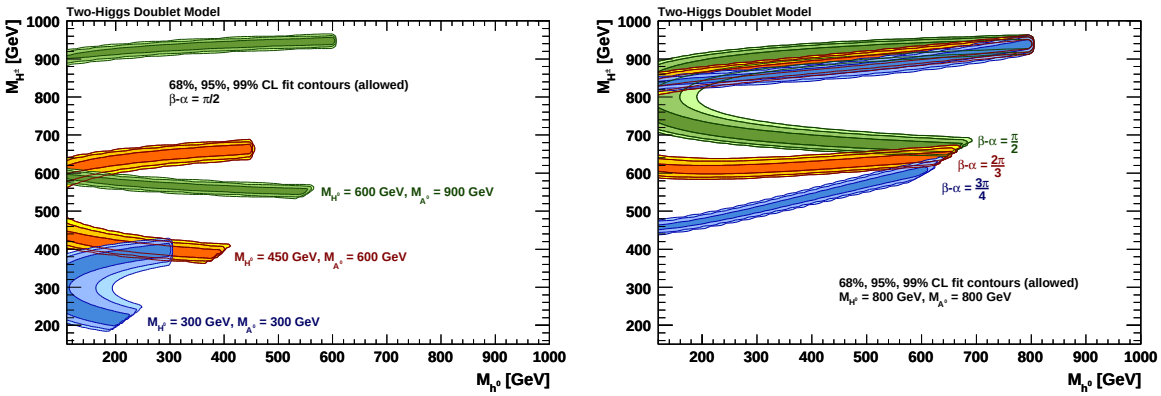

(a) (b)

Figure 3.5.: Constraints in the 2HDM. The 68 %, 95 %, and 99 % CL allowed fit contours as derived from the fit (a) in the (M_{h^0},$M_{H^\pm}$)-plane for $M_{H^0} = 300, 450, 600\,\text{GeV}$ and for $M_{A^0} = 300, 600, 900\,\text{GeV}$, respectively, and (b) in the (M_{h^0},$M_{H^\pm}$)-plane for $M_{H^0} = 800\,\text{GeV}$, $M_{A^0} = 800\,\text{GeV}$, and $\beta - \alpha = \frac{\pi}{2}, \frac{2\pi}{3}, \frac{3\pi}{4}$, respectively.

Figure 3.4 shows the 68 %, 95 %, and 99 % CL allowed contours in the (S,T)-plane (letting U vary freely) as derived in the electroweak fit (orange ellipses) together with the SM and 2HDM predictions (gray and green areas, respectively). For the 2HDM prediction, M_{h^0} was left free to vary within 114 GeV and 1000 GeV while the masses of the other Higgs bosons were restricted to vary between M_{h^0} and 1000 GeV. $\beta - \alpha$ is allowed to vary between -π and π. S adopts relatively small and mainly positive values, whereas the contribution to T can take large positive and negative values.

There is a large overlap between the experimental fit and the 2HDM prediction, so that a variety of model configurations exhibits compatibility with the electroweak precision data. A few of these configurations are shown for fixed values of $M_{H^0} = 600\,\text{GeV}$, $M_{A^0} = 900\,\text{GeV}$, and $\beta - \alpha = \frac{\pi}{2}$. The open symbols depict the predictions for three different masses of the lightest Higgs ($M_{h^0} = 120, 250, 500\,\text{GeV}$) and a fixed charged Higgs mass of 580 GeV. The arrows indicate the 2HDM-induced shifts in S and T with respect to the SM prediction for the same M_{h^0} values. Variations of the charged Higgs mass (full symbols) induce strong effects on T. By choosing adequate values ($M_{H^\pm} = 590, 570, 550\,\text{GeV}$) compatibility with the electroweak data can be achieved even for large M_{h^0}.

Further 2HDM parameter configurations that are allowed by the electroweak data are shown in Fig. 3.5. For fixed M_{H^0}, M_{A^0}, and $\beta - \alpha$, only two small bands of $M_{H^\pm}$ are allowed, namely masses very similar to either M_{H^0} or M_{A^0}, whereas M_{h^0} cannot be constrained other than being the lightest Higgs boson. Towards closer M_{H^0} and M_{A^0} degeneracy the allowed bands for $M_{H^\pm}$ become broader. The widths of the bands also depend on the error of m_t and other relevant electroweak observables. Varying $\beta - \alpha$ (cf. Fig. 3.5(b)) alters the preference of the charged Higgs to adopt similar values as M_{H^0} and M_{A^0} slightly, preserving small bands of allowed masses for $M_{H^\pm}$ but yielding an overall wider range of masses.

Figure 3.6(a) shows the (M_{H^0}, M_{A^0})-plane for fixed $M_{h^0} = 120\,\text{GeV}$ and $\beta - \alpha = \pi/2$ with varying $M_{H^\pm}$. Here, again, one notices that, for either M_{H^0} or M_{A^0}, similar values compared

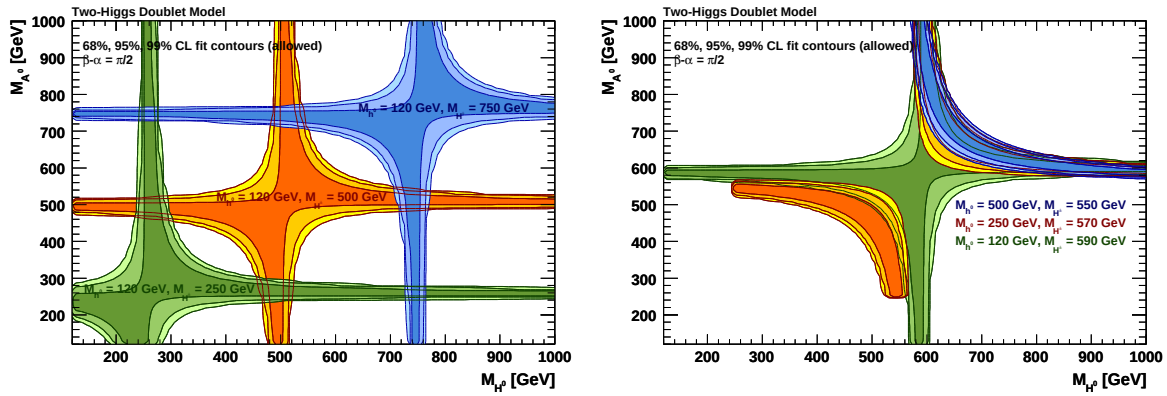

(a) (b)

Figure 3.6.: Constraints in the 2HDM. The 68 %, 95 %, and 99 % CL allowed fit contours as derived from the fit (a) in the (M_{H^0},M_{A^0})-plane for $M_{h^0} = 120\,\text{GeV}$ and $M_{H^0} = 250, 500, 750\,\text{GeV}$, and (b) in the ($M_{H^0}$,$M_{A^0}$)-plane for $M_{h^0} = 120, 250, 500\,\text{GeV}$ and for $M_{H^\pm} = 590, 570, 550\,\text{GeV}$, respectively.

to $M_{H^\pm}$ are preferred, while the other mass is hardly constrained. This almost independent behavior of M_{H^0} and M_{A^0} changes slightly for heavier M_{h^0} values, as illustrated in Fig. 3.6(b). The larger M_{h^0}, the less freedom M_{H^0} and M_{A^0} have to adopt any value, whilst the other mass is fixed to a similar value of $M_{H^\pm}$. In these plots, the same values for M_{h^0} and $M_{H^\pm}$ have been chosen as in Fig. 3.4. The allowed fit contours clearly overlap for the above selected values of $M_{H^0} = 600\,\text{GeV}$ and $M_{A^0} = 900\,\text{GeV}$, indicating the compatibility of all three model configurations with the electroweak precision data.

A previous analysis of the Type-II 2HDM extension [15] was restricted to the CP conserving 2HDM scalar potential, and only included observables sensitive to corrections from the exchange of a charged Higgs boson. The most constraining of these observables involve rare radiative or leptonic decays of B and K mesons, where the charged current mediated by the W is replaced by a charged Higgs. The combination of the constraints obtained, excludes the high-tanβ, low-$M_{H^\pm}$ region spared by the $B \to \tau\nu$ constraint, and leads to a 95 % CL charged-Higgs exclusion below 240 GeV, irrespective of the value of tanβ. This limit increases towards larger tanβ, e.g. $M_{H^\pm} < 780\,\text{GeV}$ are excluded for $\tan\beta = 70$ at 95 % CL. A similar analysis, which also includes neutral B^0 meson mixing, has been reported in Ref. [98]. There, a tanβ independent 95 % CL lower limit of 316 GeV was achieved.

Direct searches for the charged Higgs within the Type-II 2HDM have been performed by the LEP collaborations. The main limitations were irreducible background from diboson production and the kinematic limitation on the production cross section [99–102]. The combined limit determined by the LEP Higgs Working Group is $M_{H^\pm} > 78.6\,\text{GeV}$ [103].

Although the oblique parameter fits do not allow the determination of any of the free 2HDM parameters independently of the other parameters, the electroweak precision constraints will become relevant in case of a discovery or the setting of significant 2HDM Higgs boson exclusion limits at the LHC.

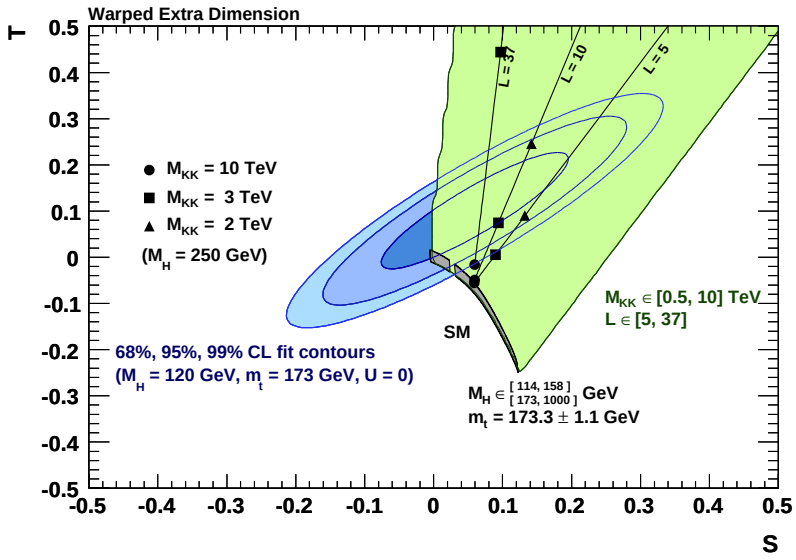

Figure 3.7.: Results for models with warped extra dimensions: Comparison of the S, T, U-fit results with the predictions from the Randall-Sundrum model. The symbols illustrate the predictions for different example settings of the parameters M_{KK} and L. The light green area illustrates the predicted region when varying the free parameters in the ranges indicated in the figure.

3.3.3. Warped Extra Dimensions

A very interesting possibility to solve the hierarchy problem is the introduction of a warped extra dimension as described in Sec. 2.5.1. This analysis presented here follows the studies of Ref. [104] where similar results have been obtained. The leading contributions to the S and T parameters for a model with a brane-localized Higgs sector and bulk gauge and matter fields are found to be [104–106]

$$S = \frac{2\pi v^2}{M_{\mathrm{KK}}^2}\left(1 - \frac{1}{L}\right) , \tag{3.22}$$

$$T = \frac{\pi v^2}{2\cos^2\theta_W M_{\mathrm{KK}}^2}\left(L - \frac{1}{2L}\right) , \tag{3.23}$$

whereas U vanishes. These contributions are coming from gauge KK interaction, top KK loops and the light fermions. Allowing the SM fermions to propagate into the bulk reduces the amount of the oblique corrections and shifts them to small, positive values. If only the SM gauge bosons propagate into the bulk S and T adopt very large and negative values [107].

The predicted S and T regions for $0.5\,\mathrm{TeV} \leq M_{\mathrm{KK}} \leq 10\,\mathrm{TeV}$ and $5 \leq L \leq 37$ are shown by the shaded (green) region in Fig. 3.7. There is a large overlap with the electroweak data (ellipses). The figure also illustrates the decoupling of the RS model for large M_{KK}.

Specific constraints from the electroweak fit on the RS model parameters in correlation with the Higgs mass are shown in Fig. 3.8. Large Higgs masses can be accommodated for comparatively low M_{KK} values counteracting on the strong constraint from T giving rise to lighter KK

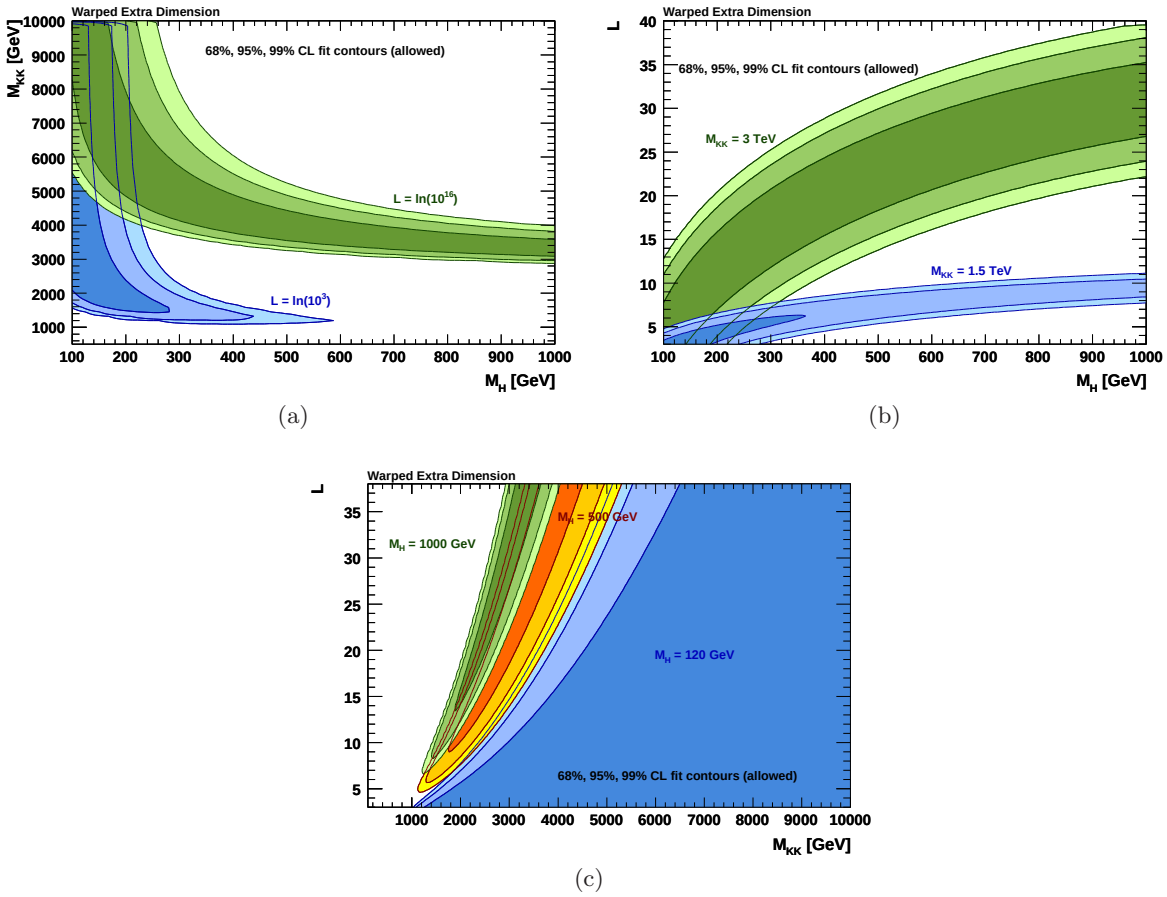

Figure 3.8.: The 68 %, 95 %, and 99 % CL allowed fit contours as derived from the fit (a) in the (M_H, M_{KK})-plane for $L = \ln 10^{16}, \ln 10^3$, (b) in the ($M_H, L$)-plane for $M_{\mathrm{KK}} = 3$, 1.5 TeV and (c) in the (M_{KK}, L)-plane for $M_H = 120, 500, 1000$ GeV.

excitations. A large Higgs mass is in agreement with the Higgs field being localized on the TeV brane. Assuming new physics to stabilize the hierarchy problem at a UV scale of approximately 10^3 TeV (corresponding to $L \approx 9$) would relax the M_{KK} lower bound, cf. Fig. 3.8. In addition, it illustrates how on the other hand small M_{KK} lead to more severe constraints on L than large values of M_{KK}. Vice versa, one finds that small M_{KK} values lead to an increased constraint on L. Addressing the full hierarchy problem ($L \approx 39$), a small contribution to the T parameter constrains M_{KK} to large values and therefore requires the lightest KK modes to be heavy. Albeit this constraint would be alleviated if the Higgs boson is heavy.

Due to their couplings SM particle-antiparticle pairs, KK gravitons can be investigated via a variety of processes, including virtual graviton exchange as well as direct graviton production through gluon-gluon fusion or quark-antiquark annihilation. There have been various experimental searches for high-mass graviton resonances decaying to, e.g. photon or light lepton pairs within the original RS model at the LHC and Tevatron [108–114]. In these analyses, the invariant mass of two-particle final states is used to set limits on the RS-graviton production cross section and lowest-level graviton mass scale. The ATLAS Collaboration has found the

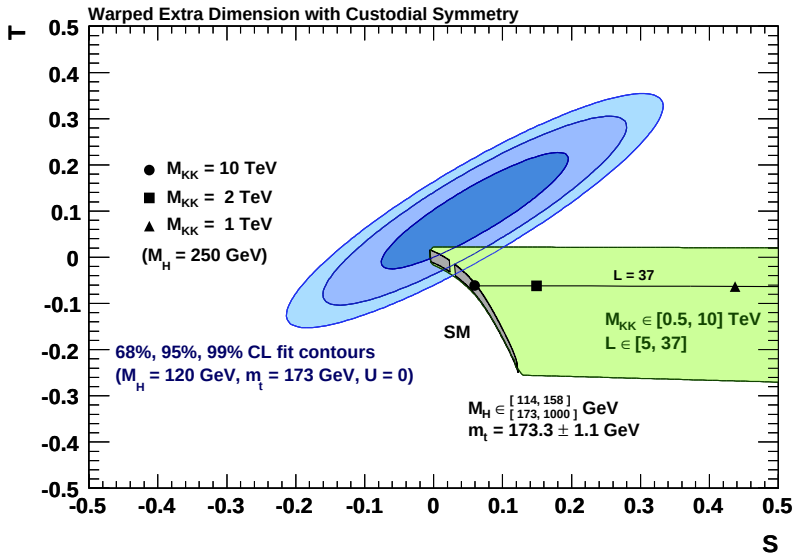

Figure 3.9.: Results for models with warped extra dimensions: Comparison of the S, T, U-fit results with the predictions from the Randall-Sundrum model with custodial symmetry. The symbols illustrate the predictions for different example settings of the parameters M_{KK} and L. The light green area illustrates the predicted region when varying the free parameters in the ranges indicated in the figure.

most stringent 95 % CL lower limits on the RS graviton masses through dilepton events, i.e. $M_G > 2.16(0.91)\,\mathrm{TeV}$ for $\sqrt{8\pi}k/M_{\mathrm{Pl}} = 0.1(0.01)$ [114].

3.3.4. Warped Extra Dimensions with Custodial Symmetry

The main motivation for the introduction of custodial symmetry as described in Sec. 2.5.2 is to relax the constraint from the T parameter on M_{KK}. The contribution to the S and T parameter are coming from gauge KK interactions, top KK loops, and the light fermions again. Compared to the warped extra dimension model mentioned above, adding custodial isospin symmetry leaves the S parameter unchanged with respect to Eq. (3.22), while the T parameter for large warp factors is suppressed rather than enhanced by the custodial and left-right parity symmetries [115] giving rise to very small T values [61, 104]

$$S = \frac{2\pi v^2}{M_{\mathrm{KK}}^2}\left(1 - \frac{1}{L}\right), \tag{3.24}$$

$$T = -\frac{\pi v^2}{4\cos^2\theta_W M_{\mathrm{KK}}^2}\frac{1}{L}. \tag{3.25}$$

The U parameter vanishes. Figure 3.9 illustrates the corresponding allowed region by this model for the same parameter ranges as Fig. 3.7. Only a small overlap with the ellipses resulting from the electroweak fit can be observed. Whereas the dependence of S on M_{KK} is clearly visible the sensitivity to L has been severely reduced and is therefore not specifically shown. The negative T oblique correction inherent in the custodial model adds to that of the SM so that only small values of M_H are allowed.

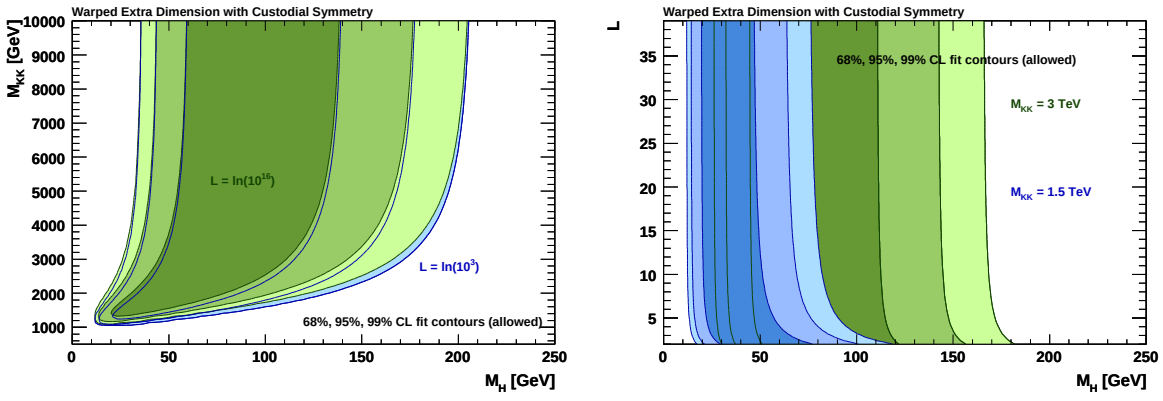

(a) (b)

Figure 3.10.: The 68 %, 95 %, and 99 % CL allowed fit contours as derived from the fit (a) in the (M_H, M_{KK})-plane for $L = \ln 10^{16}, \ln 10^{3}$, (b) in the ($M_H, L$)-plane for $M_{\mathrm{KK}} = 3, 1.5\,\mathrm{TeV}$.

Fig. 3.8 shows the dependence of the two model parameters on the Higgs mass. Even though a light Higgs cannot counteract the new physics contributions the model parameters are less constrained leading to a reduced lower bound on M_{KK}. However, very small M_{KK} lead to excluded Higgs masses. In addition, the strong correlation between M_{KK} and L is removed so that the Higgs mass and M_{KK} are practically independent of L. Therefore, there is no need to introduce a cut-off at a specific scale.

As an alternative to custodial symmetry, it was proposed to reduce the contribution to the T parameter by also allowing the Higgs to propagate into the bulk. This leads to a preferably heavy Higgs, not constrained to the UV brane anymore, which can lower the bound on M_{KK} by several TeV and therefore shift the lightest KK modes in the accessible range of the LHC [116].

4. The ATLAS Detector at the LHC

The proton-proton collision data analyzed in the following analysis was recorded with the ATLAS detector at the Large Hadron Collider (LHC) in 2011. Its main characteristics and the four major experiments are presented. The ATLAS detector and its components are described in further detail. In addition, the measurement of the luminosity is briefly explained.

4.1. The Large Hadron Collider

The LHC [117, 118] is a hadron collider located at the site of CERN at the Franco-Swiss border. It was built inside the former LEP tunnel with a circumference of 27 km and is designed to provide proton-proton collisions at a center-of-mass-energy of up to $\sqrt{s} = 14\,\text{TeV}$ at a frequency of 40 MHz. The design luminosity is $\mathscr{L} = 10^{34}\,\text{cm}^{-2}\text{s}^{-1}$. This setup will be available after a shutdown foreseen for 2013. In 2009, the LHC was operated at $\sqrt{s} = 900\,\text{GeV}$. In 2010 and 2011, the center-of-mass energy was $\sqrt{s} = 7\,\text{TeV}$ and has been further increased to $\sqrt{s} = 8\,\text{TeV}$ since the beginning of 2012. In addition, the LHC provides heavy-ion collisions for several weeks usually towards the end of the year. They are not taken into account in this work.

Inside the accelerator, two beam pipes host the proton bunches in an ultrahigh vacuum. The superconducting magnets operate at a temperature of 1.7 K. 1232 dipole magnets of 15 m length each provide a field of 8.3 T keeping the bunches on their circular tracks. The beam is focused by 392 quadrupole magnets of length between 5 m and 7 m. Before the injection into the LHC, the protons are pre-accelerated by various accelerators including the Proton Synchrotron (PS) and the Super Proton Synchrotron (SPS). The energy of the protons leaving the PS and the SPS is 25 GeV and 450 GeV, respectively. The acceleration to the collision energy is carried out by superconductive radio frequency cavities in the LHC itself. The entire accelerator complex of the LHC is illustrated in Fig. 4.1. Additionally, the four main experiments at the LHC are shown: ATLAS, CMS, LHCb, and ALICE. ATLAS and CMS are multipurpose detectors focusing on precision measurements of the SM and the search for the Higgs Boson. Also, searches for signatures pointing towards physics beyond the SM are a vital part of their physics programs. LHCb is the only asymmetric detector investigating CP-violation in hadrons containing b quarks. ALICE is especially designed for ion-ion-collisions. One research field is the investigation of the quark-gluon-plasma.

One of the major challenges at the LHC is the very high event rate and the amount of interactions per bunch crossing (cf. Sec. 5.2.3). The event rate $\frac{\mathrm{d}N}{\mathrm{d}t}$ is calculated by multiplying the total cross section with the instantaneous luminosity defined as

$$\mathscr{L} = f n_B \frac{n_1 n_2}{4\pi\sigma_x\sigma_y}\,, \tag{4.1}$$

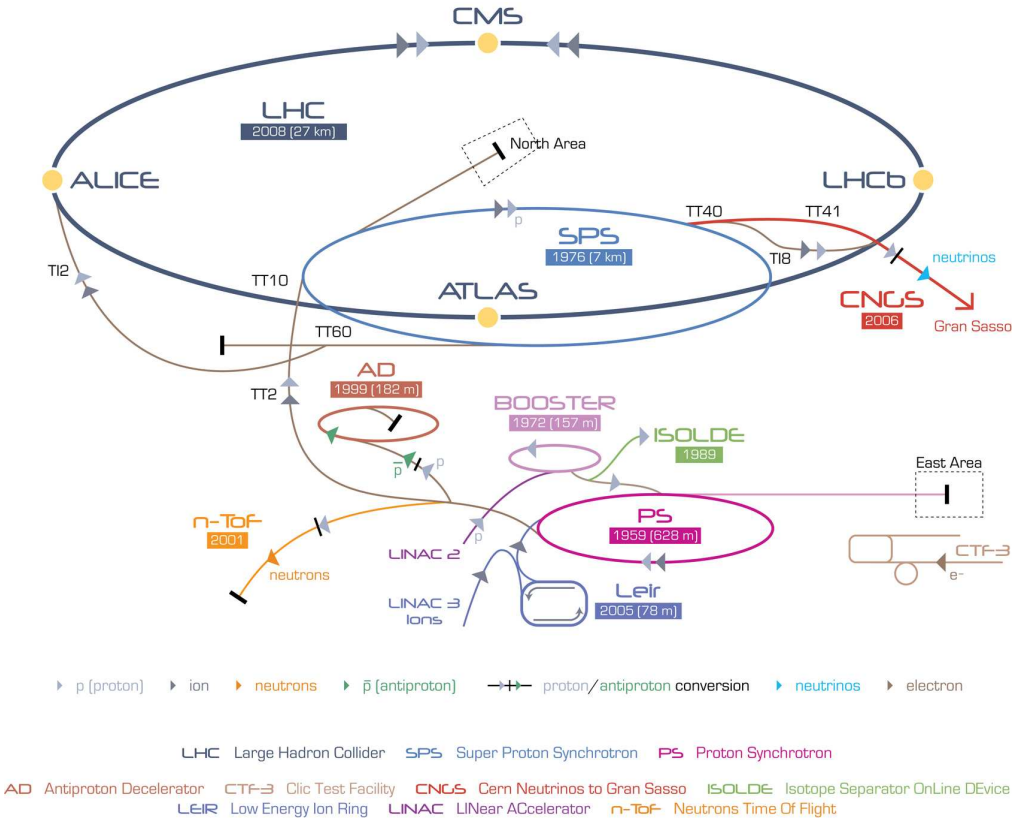

Figure 4.1.: The LHC accelerator complex [119].

where f is the LHC revolution frequency, while n_1, n_2 denote the number of the protons in the n_B collision bunch pairs. The width of the bunches perpendicular to the beam axis is given by σ_x and σ_y. The measurement of the luminosity is briefly explained in Sec. 4.2.7. By increasing the number of bunches and the number of protons per bunch and by reducing the width of the bunches, the instantaneous luminosity reached a maximum of $\mathscr{L} = 6.8 \cdot 10^{33}\,\mathrm{cm}^{-2}\mathrm{s}^{-1}$ in 2012 and the LHC has delivered a total integrated luminosity of approximately $\int \mathscr{L}\mathrm{d}t = 6.1\,\mathrm{fb}^{-1}$ (status as of June 16$^{\mathrm{th}}$, 2012). The aim for the total delivered luminosity in 2012 is $15\,\mathrm{fb}^{-1}$. The total delivered luminosity was $5.6\,\mathrm{fb}^{-1}$ ($48.1\,\mathrm{pb}^{-1}$) in 2011 (2010). A comparison of the cumulative luminosity in those three years is shown in Fig. 4.2. The total proton-proton cross section at the LHC at $\sqrt{s} = 7\,\mathrm{TeV}$ ($\sqrt{s} = 14\,\mathrm{TeV}$) is 91.6 mb (99.4 mb) [11, 120].

4.2. ATLAS Detector

The ATLAS detector is the largest of the four main detectors installed at the LHC with a forward-backward symmetric cylindrical geometry. A detailed description may be found in [122]. Here, only a short summary focusing on the detector components most relevant for the following analysis is given. ATLAS was designed to measure the particle momentum and energy at high precision while offering a nearly 4π solid angle coverage. Figure 4.3 shows a complete overview of the ATLAS detector displaying the main components. The innermost

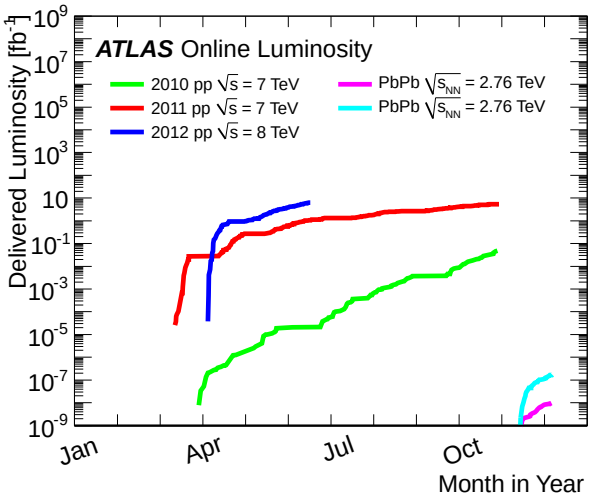

Figure 4.2.: Cumulative luminosity versus day delivered to ATLAS during stable beams and for p-p and Pb-Pb collisions [121]. This is shown for 2010 (green for p-p, magenta for Pb-Pb), 2011 (red for p-p, turquoise for Pb-Pb) and 2012 (blue) running. The online luminosity is shown.

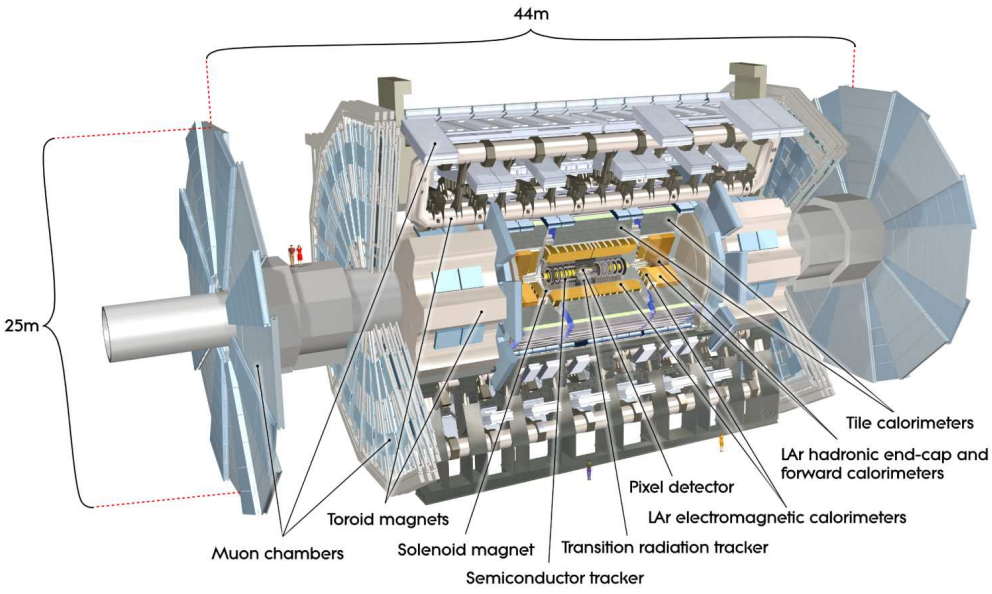

Figure 4.3.: Overview of the ATLAS detector showing the inner detector components, the electromagnetic and hadronic calorimeter, the muon and the magnet system [122].

Detector component	Required resolution	η coverage	
		Measurement	Trigger
Tracking	$\sigma_{p_T}/p_T = 0.05\% p_T \oplus 1\%$	± 2.5	
EM calorimetry	$\sigma_E/E = {}^{10\%}/\sqrt{E} \oplus 0.7\%$	± 3.2	± 2.5
Had. calorimetry			
barrel and end-cap	$\sigma_E/E = {}^{50\%}/\sqrt{E} \oplus 3\%$	± 3.2	± 3.2
forward	$\sigma_E/E = {}^{100\%}/\sqrt{E} \oplus 10\%$	$3.1 < \lvert\eta\rvert < 4.9$	$3.1 < \lvert\eta\rvert < 4.9$
Muon Spectrometer	$\sigma_{p_T}/p_T = 10\%$ at $p_T = 1\,\mathrm{TeV}$	± 2.7	± 2.4

Table 4.1.: General performance goals of the ATLAS detector [122].

part is the tracking system consisting of a pixel and silicon micro-strip tracker (SCT) and the transition radiation tracker (TRT). It is enclosed by a thin superconducting solenoid providing a magnetic field of 2 T. The electromagnetic and hadronic calorimeters are surrounded by the muon system. The performance goals concerning energy and momentum resolution are listed in Table 4.1 for the individual components.

4.2.1. Coordinate System and Kinematic Variables

ATLAS uses a right-handed coordinate system with its origin coinciding with the nominal interaction point (IP) in the center of the detector and the z-axis along the direction of the anti-clockwise beam. The x-axis points from the IP to the center of the LHC ring and the y-axis points upward. Cylindrical coordinates (R, ϕ) are used in the transverse plane, ϕ being the azimuthal angle around the beam pipe with $\tan\phi = {}^{y}/_{x}$. The pseudorapidity which is invariant under Lorentz transformation is defined in terms of the polar angle θ, measured from the beam axis in the R-z-plane, as

$$\eta = -\ln\tan\left(\frac{\theta}{2}\right). \tag{4.2}$$

The coverage in η for each detector component is also listed in Tab. 4.1. The distance between two objects is indicated in the η-ϕ plane as

$$\Delta R = \sqrt{(\Delta\eta)^2 + (\Delta\phi)^2}. \tag{4.3}$$

The transverse momentum $p_{\mathrm{T}} = \sqrt{p_x^2 + p_y^2}$ and the (missing) transverse energy E_{T} ($E_{\mathrm{T}}^{\mathrm{miss}}$) are defined in the plane perpendicular to the beam axis. In the relativistic limit, the transverse momentum and the transverse energy are identical. $E_{\mathrm{T}}^{\mathrm{miss}}$ is the magnitude of the negative vector sum of the momenta of all particles present in an event. Its determination is described in detail in Sec. 6.6. Many searches, including the one presented in the following, rely on $E_{\mathrm{T}}^{\mathrm{miss}}$ as the transverse momentum in an event is conserved but the LSP leaves the detector undetected, resulting in $E_{\mathrm{T}}^{\mathrm{miss}}$.

4.2.2. Magnet System

The magnet system of the ATLAS detector consists of four superconductive magnets. The main purpose is to measure the particle momentum and charge in the tracking system and in

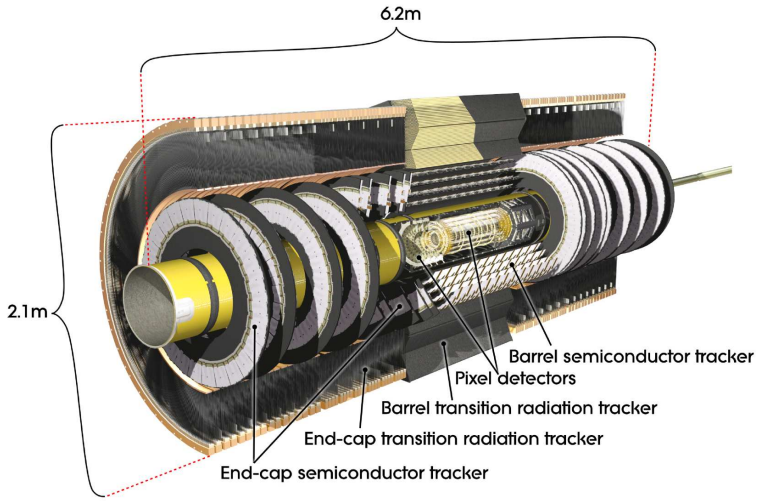

Figure 4.4.: The inner detector consisting of the pixel and silicon micro-strip trackers and the transition radiation tracker [122].

the muon spectrometer, respectively. A central solenoid provides a field of 2 T while barrel (end cap) toroids deliver a field of 0.5 T (1 T). The total energy stored in the magnet system is 1.6 GJ [122]. The solenoid field is aligned with the beam to bend the particle tracks in the plane perpendicular to the beam. The thickness of the magnet corresponds to 0.66 radiation lengths with an inner (outer) radius of 2.46 m (2.56 m). It was designed to keep the amount of material as low as possible to minimize the interference of the material with the energy measurement in the calorimeters [123]. The barrel as well as the end cap toroids, which are air-core magnets, consist of eight coils each installed symmetrically and radially around the beam pipe where the coils of the end cap are rotated with respect to the barrel coils to optimize the homogeneity of the field within the muon spectrometer.

4.2.3. Inner Detector

The inner detector is designed to provide tracking information to precisely measure the momentum of charged particles. It is determined by measuring the bending radius of the track in the R-ϕ-plane caused by the Lorentz force due to the magnetic field. In addition, the position of the primary vertex and possible secondary vertices can be accurately determined. The precise determination of the primary vertex is essential for the suppression of pile-up events. Secondary vertices arise if particles with a finite lifetime such as B mesons decay inside the beam pipe. The combination of the tracking information and the energy measurement of the calorimeter allows for the identification of particles. A schematic illustration of the inner detector is given in Fig. 4.4. It is 7 m long with a diameter of 2 m covering a region of $|\eta| < 2.5$. The general design of the detector components is an arrangement of concentric cylinders around the beam axis in the barrel region and disks perpendicular to the beam in the end-cap region.

Pixel Detector

The main task for the pixel and silicon detectors is to allow a very good track-finding and pattern recognition by providing three and four position measurements, respectively. The pixel detector measures the impact parameter and enables the discrimination of short-lived particles such as hadrons containing b-quarks and τ leptons, the latter being essential for the following analysis. In addition, some SUSY scenarios assume a NLSP which does not decay promptly. The measurement of the decay vertex allows the determination of the lifetime.

Since the pixel detector is closest to the IP, it is exposed to the highest track density and radiation level. Therefore, it is due to be replaced after only three years of operation. It consists of three cylindrical layers where the innermost one is the b-layer, 5.05 cm from the beam pipe, and three discs in the end cap. The barrel hosts 1500 modules with 60 000 pixel elements each. The end cap consists of 1000 disc modules. The minimum size of the identical pixel sensors is $50 \times 400\,\mu\text{m}^2$ providing a resolution of $10\,\mu$m in the $R-\phi$ plane and $115\,\mu$m in R (z) for the barrel region (in the discs) [124]. Each layer has a thickness of approximately 1 % radiation length. The number of readout channels amounts to 80.4 million which is about 90 % of the total number of readout channels of the ATLAS detector.

Silicon Micro-strip Detector

The components of the silicon micro-strip detector (SCT) are eight strip layers in the barrel region where two layers are combined in a pair glued back-to-back at a stereo angle of 40 mrad providing four position measurements. The use of two layers at an angle improves the spatial resolution significantly. In the end cap region, nine silicon disks use strip layers combined to pairs with a stereo angle of 40 mrad as well. Each sensor is 6 cm long and the strip pitch is $80\,\mu$m. The SCT consists of 4088 modules. The accuracy of the position measurement is estimated to be $17\,\mu$m in the $R-\phi$ plane and $580\,\mu$m in R as well as z. The number of read-out channels for the SCT is 6.2 million [125].

Transition Radiation Tracker

The TRT is a drift chamber system of roughly 300 000 straw tubes, 52 544 in the barrel and 245 760 in the end cap, containing a gas mixture of 70% Xe, 27% CO_2, and 3% O_2. The diameter of the straw tubes is 4 mm, where their length varies between 37 cm (end cap) and 144 cm (barrel) [126, 127]. They are equipped with a $31\,\mu$m diameter gold-cased tungsten wire as an anode and aluminum cased coats as a cathode operated at a voltage of 1530 V.

The basic principle of the TRT is ionization which occurs every time a charged particle traverses the gas mixture producing transition radiation in addition. Ultra-relativistic particles such as electrons emit more photons than hadrons leading to a higher signal in the detector. Therefore, the TRT is equipped with two thresholds optimized for the discrimination of hadrons and electrons. The drift time in each tube is measured providing the distance of the track from the read-out wire. The TRT provides up to 36 (22) position measurements in the barrel (end cap) with an overall resolution of $130\,\mu$m in the R-ϕ-plane with a coverage of $|\eta| < 2.0$.

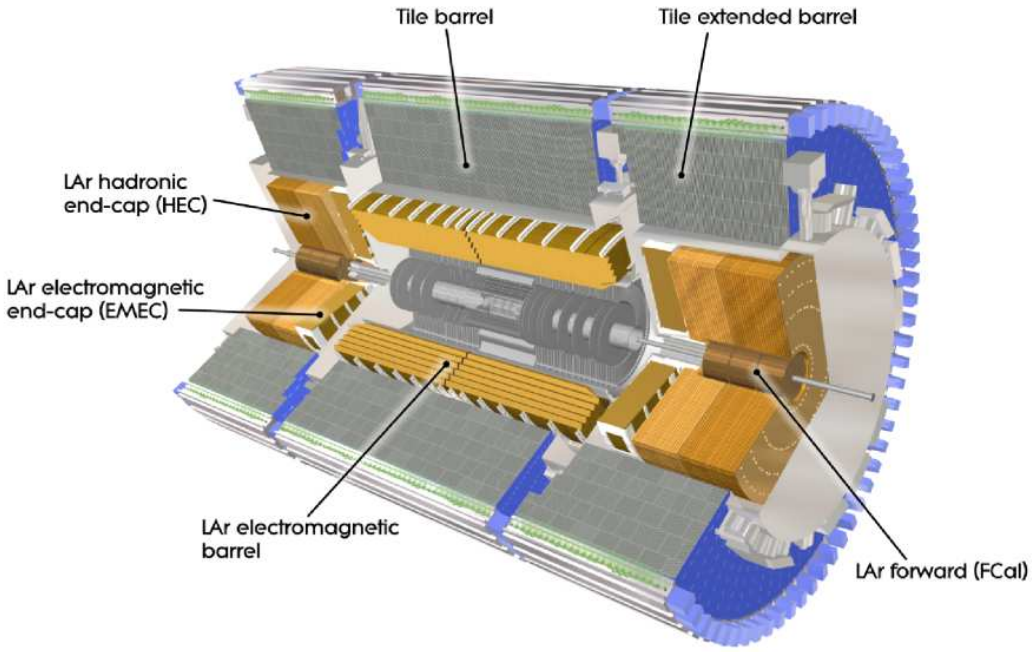

Figure 4.5.: The calorimeter system includes an electromagnetic calorimeter, hadronic calorimeters in the barrel and end cap region, and a forward calorimeter [122].

4.2.4. Calorimetry

The central purpose of the calorimeter system is the measurement of the particle energy. The calorimetry of the ATLAS detector [128] relies on sampling technology where layers of active material alternate with layers of passive absorber material. Particles interact with the absorber material causing the production of secondary particles creating a particle shower and depositing the energy inside the calorimeters. The active material detects a fraction of the energy which is proportional to the initial energy of the primary particle. Electrons and photons interact with the electromagnetic field of the nuclei of the material emitting bremsstrahlung or creating electron-positron pairs. Hadrons interact strongly with the nuclei. Particles that only interact weakly escape the detector and their energy cannot be determined.

The calorimeter system is composed of three parts: the fine-granularity lead/liquid-argon (LAr) electromagnetic calorimeter ($|\eta| < 3.2$), the hadronic iron/scintillating-tile calorimeter in the barrel ($|\eta| < 1.7$, LAr up to $|\eta| < 1.5$), and the LAr forward calorimeters ($|\eta| < 4.9$). As the granularity of the electromagnetic calorimeter allows a position measurement in addition to the energy measurement, the energy clusters in the calorimeter can be matched to tracks. Additionally, the shower shape can be determined which is essential for accurate particle distinction. A schematic overview of the components is presented in Fig. 4.5.

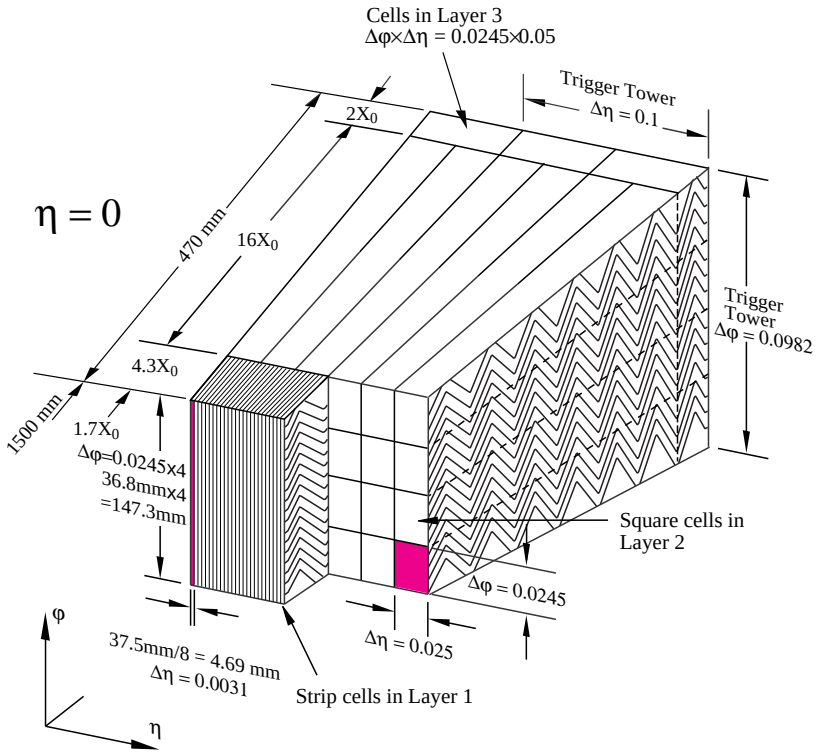

Figure 4.6.: Schematic view of the electromagnetic calorimeter [122].

Electromagnetic Calorimeter

The electromagnetic calorimeter (EM) is a lead LAr detector [129]. The layers of lead serve as the absorber material initiating the particle showers while LAr serves as the active material measuring the energy. It has an accordion shaped structure as shown in Fig. 4.6 offering complete ϕ uniformity. The barrel calorimeter consists of two identical half-barrels covering the region $|\eta| < 1.475$ with a 4 mm small gap at $\eta = 0$. The two end caps, each consist of an outer and an inner wheel covering $1.375 < |\eta| < 2.5$ and $2.5 < |\eta| < 3.2$, respectively. To correct the energy loss of electrons and photons due to the material in the tracking system, the cryostats, and the solenoid, a presampler ($\eta < 1.8$) is prepended to the electromagnetic calorimeter consisting of one active layer of LAr.

The barrel and the outer wheel of the calorimeter are segmented into three radial layers with increasing granularity and a combined thickness of 22 and 24 radiation lengths. The first layer is equipped with very fine strip cells in η at an interval of 4.7 mm. It precisely measures the η position of electrons and photons. It allows the distinction of two photons from a neutral pion decay which is of interest when reconstructing hadronically decaying τ leptons. The second part is the longest (16 radiation lengths) and is divided into cubic cells with a base area of $\Delta\eta \times \Delta\phi = 0.025 \times 0.025$ absorbing most of the energy. Due to the finer granularity, the ϕ position of the particle can be determined. The purpose of the third layer is to detect potential energy leakage from the electromagnetic to the hadronic calorimeter. The inner end cap wheels only consist of two radial layers.

For the energy measurement of electrons, the cells are combined in clusters in squares of 3×3,

starting with the cell in the second layer with the highest energy. For the other layers, all cells intersecting the geometrical projection of this square window are included. The energies of each associated cell are added up individually in each layer, E_0 for the presampler and $E_{1,2,3}$ for the three radial layers. The total energy of the electron is then given by [122]

$$E = \text{offset} + w_0 E_0 + w_{01}\sqrt{E_0 E_1} + \lambda(E_1 + E_2 + E_3) + w_3 E_3\,, \tag{4.4}$$

where offset, w_0, w_{01}, w_3, and λ are correction factors depending on the electron energy and η. Due to the transition region between the barrel and the end caps, the energy measurement is unreliable between $1.37 < |\eta| < 1.52$. The resolution studied in test beam measurements and simulations can be parametrized [130]

$$\frac{\sigma(E)}{E} = \frac{a}{\sqrt{E[\text{GeV}]}} \oplus b\,, \tag{4.5}$$

where $a = 10\,\%\sqrt{\text{GeV}}$ represents a stochastic term and $b = 0.17\,\%$ is a constant term accounting for local irregularities in the calorimeter response. Between 15 GeV and 180 GeV, the energy response is linear within $\pm 0.1\,\%$.

Hadronic Calorimeter

The hadronic calorimeter measures the energy of jets and is used together with the electromagnetic calorimeter for the determination of $E_{\text{T}}^{\text{miss}}$. It is composed of three parts. The first one, the tile calorimeter consists of a segmented barrel part, $|\eta| < 1.0$ and $0.8 < |\eta| < 1.7$, reaching from an inner radius of 2.28 m to 4.25 m. It relies on the sampling technique as well, where plastic scintillator plates, the *tiles*, are enclosed in a steel absorber. The two sides of the scintillator tiles are read out separately by wavelength shifting fibers and photomultiplier tubes. Like the electromagnetic calorimeter, the tile calorimeter consists of three layers with a granularity of $\Delta\eta \times \Delta\phi = 0.1 \times 0.1$ for the first two layers and $\Delta\eta \times \Delta\phi = 0.2 \times 0.1$ for the third layer.

In both end caps, two wheels form the LAr hadronic end-cap calorimeter (HEC) covering $1.5 < |\eta| < 3.2$ where each wheel consists of 32 identical modules. It overlaps slightly with the tile calorimeter as well as the forward calorimeter. The copper absorber is arranged in parallel plates and interleaved by LAr layers serving as the active material. The third part of the hadronic calorimeter is in the forward region and described below.

Forward Calorimeters

The forward calorimeters ($3.1 < |\eta| < 4.9$) consist of three cylindrical modules [131]. The active material is again LAr while the first module is instrumented with copper as absorber while tungsten serves as the passive material of the other two modules. The first module (FCal1) is used for electromagnetic measurements and is optimized in terms of resolution and heat removal. The other two modules (FCal2,3) measure the energy of hadron showers providing containment limiting the lateral spread of the showers. The absorber material is arranged as a solid rod inside longitudinal tubes where the individual cells of FCal1 (FCal2,3) have a size of $\Delta\eta \times \Delta\phi = 0.1 \times 0.1$ ($\Delta\eta \times \Delta\phi = 0.2 \times 0.2$).

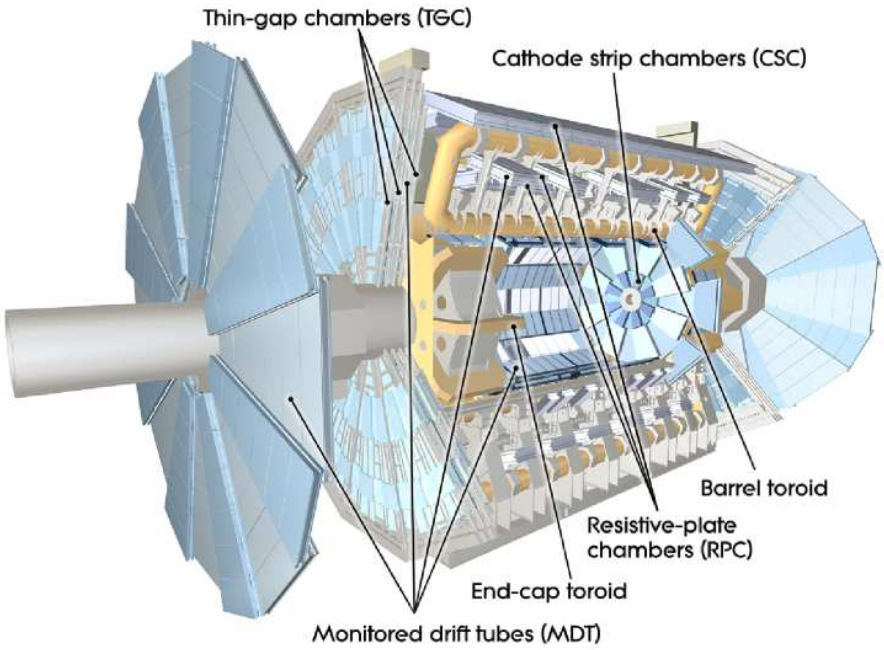

Figure 4.7.: The muon spectrometer containing different chamber types and air-core toroids [122].

4.2.5. Muon Spectrometer

As muons are minimal ionizing particles, they deposit hardly any energy in either of the calorimeters or the tracking system. Hence, a dedicated subdetector is needed for further particle identification and for the measurement of their momentum. The muon spectrometer of ATLAS includes monitored drift tubes (MDT) and cathode strip chambers (CSC). It is complemented by the muon trigger system consisting of thin-gap chambers (TGC) and resistive plate chambers (RPC). An overview of all components of the muon spectrometer is shown in Fig. 4.7.

The purpose of the MDTs and CSCs is to precisely measure the muon tracks. They are arranged either in three layers cylindrical in the barrel around the beam axis or in disks perpendicular to the beam in the end cap. In the barrel, one set of chambers is located inside the toroid. The cathodes of the MDTs are aluminum tubes with a diameter of 30 mm while gold-plated tungsten-rhenium wires with a diameter of 50 μm serve as the anodes. The tubes are filled with 93% Ar and 7% CO_2. Muons ionize the gas when traversing the spectrometer and the drift time is measured. The spatial resolution of a single tube is 80 μm. By combining the measurement of several tubes this value decreases to 35 μm. Most of the barrel range ($|\eta| < 2.7$) is covered by MDTs. CSCs are used for the innermost layer in the end caps. Here, a higher particle flux is expected. Therefore, their granularity and spatial and time resolution exceeds that of the MDTs. The CSCs are multiwire proportional chambers with cathodes segmented into strips. The gas mixture consists of 30% Ar, 50% CO_2, and 20% CF_4. An optical alignment system monitors the exact position of the MDTs and CSCs to ensure the desired accuracy of the track position measurements.

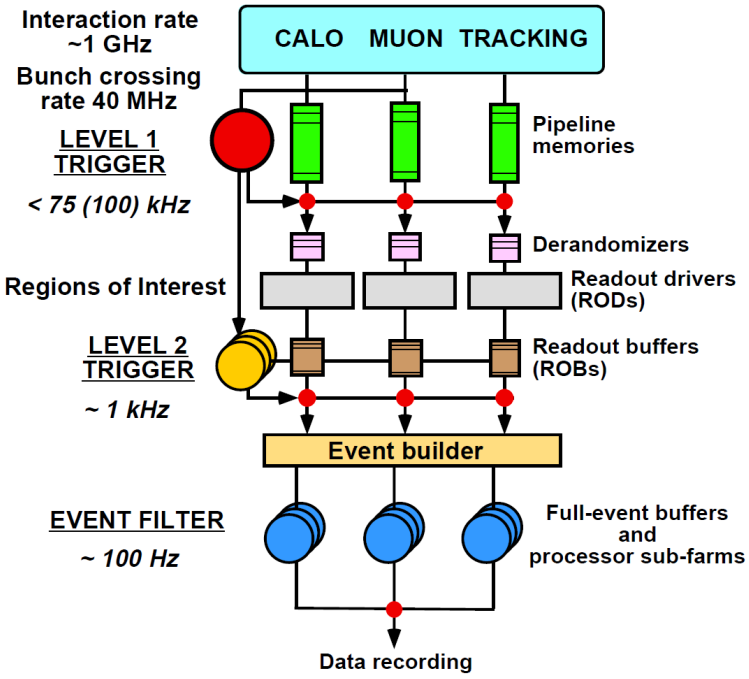

Figure 4.8.: ATLAS trigger system including the First-Level Trigger and the High Level Trigger, consisting of the Level-2 Trigger and the Event Filter [132].

The TGCs and the RPCs are part of the First Level Trigger (cf. Sec. 4.2.6). They identify the bunch crossings allocating the muons to the corresponding event. This is important since the time-of-flight inside the detector due to its size is larger than the inverse bunch crossing rate. In addition, the muon coordinates in direction orthogonal to that of the precision tracking chambers are measured. The TGCs function similarly to the CSCs but have smaller distances between anodes and cathodes and hold a different gas mixture of CO_2 and n-C_5H_{12}. The RPCs are gaseous detectors with parallel plates serving as anodes. The TGCs are installed in the end cap ($|\eta| < 1.05$) and the RPCs in the barrel region ($1.05 < |\eta| < 2.4$). The time resolution of the TGCs and RPCs is 4 ns and 1.5 ns, respectively.

4.2.6. Trigger System

Due to the very high instantaneous luminosity and bunch crossing rates of up to 40 MHz at the LHC, it is impossible to process, record, and store every single event. Hence, a trigger system [133] is needed to reduce the amount of data and select the events of interest for performance studies, SM measurements, and BSM searches. Mainly soft QCD events, *minimum bias events*, are rejected. The ATLAS trigger system is a three level trigger composed of the first trigger level (L1) [132], the second trigger level (L2), and the Event Filter (EF). The former is purely hardware based while the latter two form the High-Level Trigger (HLT) [134] which is software based and runs on large computer farms. Figure 4.8 shows the different trigger levels and the rate reduction performed by each of the three levels. Only events passing the trigger requirement of one level are passed to the next. The rate at which events are stored is approximately 100 Hz - 200 Hz.

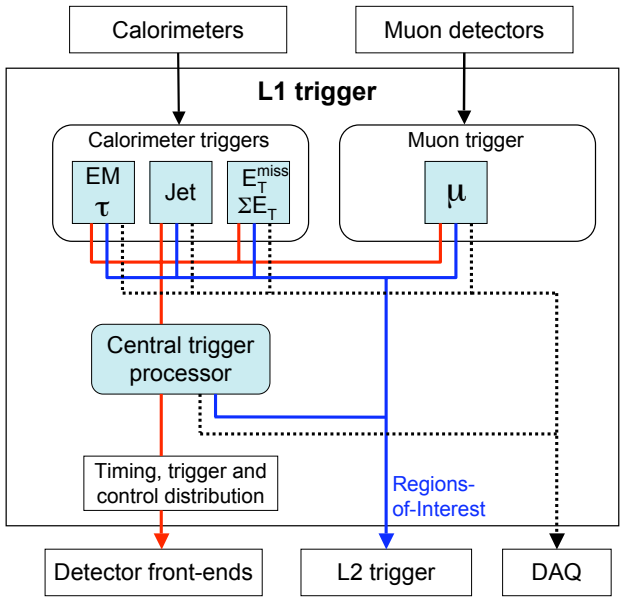

Figure 4.9.: Block diagram of the L1 trigger [122]. The overall L1 accept decision is made by the central trigger processor, taking input from calorimeter and muon trigger results. The paths to the detector front-ends, L2 trigger, and data acquisition system are shown from left to right in red, blue, and black, respectively.

The Level 1 Trigger System

A dedicated hardware system passes the information from the subdetectors and their electronics to the L1 trigger. The rejection or acceptance of events is based on coarse information from the calorimeters and the muon system. The calorimeter trigger focuses on particles such as electrons, photons, hadronically decaying τ leptons, and jets and on events containing a large amount of $E_{\mathrm{T}}^{\mathrm{miss}}$. The muon trigger focuses on high p_{T} muons. Various kinematic thresholds are predefined for the different objects and are considered in the process. Depending on the thresholds certain triggers may be *prescaled* to limit the event rate from low-threshold triggers. Searches for new physics usually rely on the lowest unprescaled trigger available. During the latency of the L1 trigger (2.5 μs) the full event signals are stored in front-end pipelines. Figure 4.9 shows an overview of the L1 trigger. Once an event is accepted, the L1 initiates the read-out of the event by the detector front-ends. L1 identifies *Regions-of-Interest* (RoIs). The geometrical and kinematic informations on location and properties of the RoIs are transmitted to the next trigger level. In addition, all required trigger informations are passed to the ATLAS data acquisition system (DAQ). In total, the event rate is reduced to a maximum of 75 kHz.

High Level Trigger System

The HLT decisions are derived step by step refining the decision of the previous trigger by taking into account more information from different subdetectors and surveying additional selection criteria, e.g. the tracking information is now included. This procedure yields early

rejection of events that do not meet specific demands. The L2 trigger only processes the information of the subdetectors around the RoIs given by L1. The time latency of L2 is about 40 ms reducing the event rate to 3.5 kHz while using the detector data inside the RoIs at full granularity and precision. If the decision is positive the entire event information is collected by the event builder passing the information to the EF which runs the standard ATLAS reconstruction algorithm software. The decision of the EF can take up to a few seconds as the entire detector information is used. It is based on offline analysis procedures reducing the event rate to 200 Hz.

Rejected events are not further processed while accepted events are send to the DAQ system. The combination of three trigger items at the three different levels to select specific events is called a *trigger chain*. Their definition is unambiguous going from EF to L1. Depending on the objects the trigger decision is based on, the data is written to one or more of the four different data streams available: *Egamma*, *Muon*, *JetTauEtmiss*, and *MinBias*. The following analysis uses data from the JetTauEtmiss stream and relies on an EF combined jet and $E_{\mathrm{T}}^{\mathrm{miss}}$ trigger seeded by a lower threshold L1 single jet trigger (cf. Sect. 8.2.1).

4.2.7. Luminosity Determination

The general method for determining the calibration of the luminosity in ATLAS are dedicated *van der Meer* (vdM) scans [135]. The luminosity of a collider can be written as described in Eq. (4.1) which is equivalent to

$$\mathscr{L} = \frac{\mu n_B f}{\sigma_{\mathrm{inel}}} = \frac{\mu_{\mathrm{vis}} n_B f}{\sigma_{\mathrm{vis}}}\,, \tag{4.6}$$

where $\sigma_{\mathrm{vis}} = \epsilon\sigma_{\mathrm{inel}}$ is the total inelastic cross section multiplied by the efficiency of the detector and the algorithm used to determine the luminosity and μ ($\mu_{\mathrm{vis}} = \epsilon\mu$) is the average (observed) number of inelastic interactions per bunch crossing. The absolute luminosity is determined through machine parameters while μ_{vis} is determined experimentally. The calibration of σ_{vis} is done via the aforementioned vdM scans.

In a vdM scan, the beams are separated in iterative steps of a known distance to directly measure σ_x and σ_y, the width of the two beams (cf. Eq. (4.1)). By measuring n_1 and n_2 the peak luminosity can be determined for fully overlapping beams. The visible cross section is then given by comparing this peak luminosity to the peak interaction rate $\mu_{\mathrm{vis}}^{\mathrm{MAX}}$ observed by a given detector and event counting algorithm

$$\sigma_{\mathrm{vis}} = \mu_{\mathrm{vis}}^{\mathrm{MAX}} \frac{2\pi\sigma_x\sigma_y}{n_1 n_2}\,. \tag{4.7}$$

A bunch crossing is counted as an event when fulfilling certain criteria, e.g. if the sum of all hits on both the forward and backward arm of the detector is at least one (inclusive counting) or if there is at least one hit on each side (coincidence counting). These event counts are then converted into μ_{vis}, which is then combined with σ_x and σ_y from the vdM scan to determine σ_{vis}.

The two main detectors with which these event counts are determined are LUCID and BCM (Beam Conditions Monitor) [135]. LUCID was the preferred detector in the beginning of

LHC running while now the luminosity is determined with the BCM. LUCID is a Cerenkov detector consisting of 16 aluminum tubes filled with C_4F_{10}. These tubes surround the beam pipe ($5.6 < |\eta| < 6.0$) on each side of the detector at a distance of 17 m from the IP. The ends of each tube is equipped with photomultipliers. They report a hit once a Cerenkov photon created by a traversing charged particle exceeds a predefined threshold. The BCM consists of four small diamond sensors. They are arranged in a cross pattern around the beam pipe at each side of the IP. The horizontal and vertical sensor pair is read out separately providing two measurements. Using the vdM scans the overall uncertainty of the luminosity measurement in 2011 has been found to be 3.7 % [135].

5. ATLAS Data Taking and Simulated Event Samples

This chapter documents the data and simulated event samples used for the LHC data analysis. It describes the main features of the LHC data taking periods in 2011 and the characteristics of the various simulated signal and background samples. Additionally, the pile-up reweighting procedure applied to simulated events is explained.

5.1. LHC Data of 2011

In 2010 and 2011, the LHC has been providing pp collision data at a center-of-mass energy of $\sqrt{s} = 7\,\text{TeV}$. The delivered data correspond to $48.1\,\text{pb}^{-1}$ and $5.61\,\text{fb}^{-1}$, respectively. The luminosity is determined through van der Meer scans and by counting event rates (cf. Sec. 4.2.7). The cumulative luminosity for the 2011 data taking period is shown in Fig. 5.1 along with the peak luminosity achieved per fill. Its maximum value was $3.65 \cdot 10^{33}\,\text{cm}^{-2}\text{s}^{-1}$. The analysis described in the following (cf. Ch. 8 and 9) uses the data collected from March 13^{th} to August 26^{th}, 2011, corresponding to data taking periods B, D–K. The data periods and their corresponding integrated luminosities are summarized in Table 5.1. Data taking periods A and

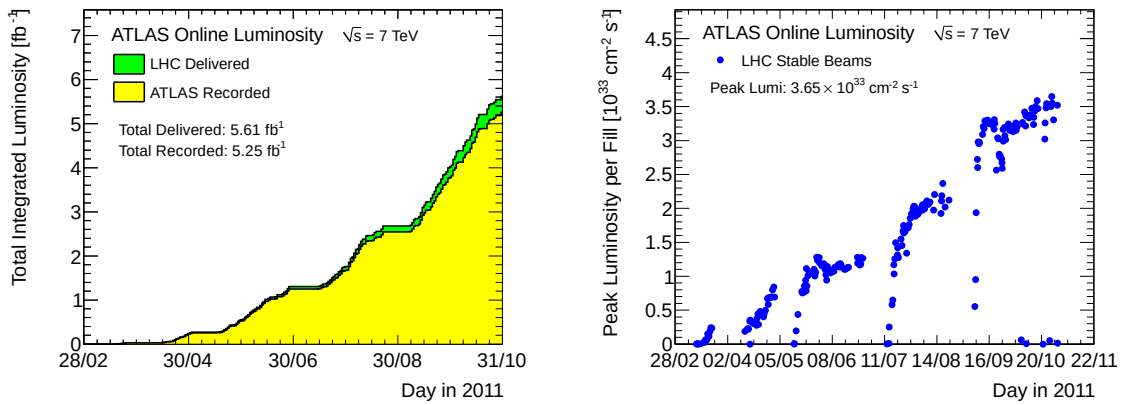

(a) (b)

Figure 5.1.: (a) Cumulative luminosity versus day delivered to (green) and recorded by ATLAS (yellow) during stable beams [121]. The delivered luminosity accounts for the luminosity delivered from the start of stable beams until the LHC requests ATLAS to turn the sensitive detector off to allow a beam dump or beam studies. (b) The maximum instantaneous luminosity versus day delivered to ATLAS during stable beam conditions [121].

Period	Run numbers	Runs	$\int \mathscr{L} dt$ before GRL [pb^{-1}]	$\int \mathscr{L} dt$ after GRL [pb^{-1}]
B	177986–178109	7	17	11
D	179710–180481	23	179	154
E	180614–180776	5	50	43
F	182013–182519	16	152	123
G	182726–183462	28	561	464
H	183544–184169	13	279	240
I	185353–186493	27	400	305
J	186516–186755	9	233	212
K	186873–187815	19	651	500
All		147	2522	2053

Table 5.1.: Data taking periods used in the analysis with their corresponding integrated luminosities.

Sample ID	Name	Generator	LO [pb]	NLO [pb]
137940	GMSB4030 ($\Lambda = 40, \tan\beta = 30$)	Herwig++	0.41	0.45
137921–	GMSB grid	Herwig++	15.8	21.7
–137975	GMSB grid	Herwig++	0.006	0.005

Table 5.2.: GMSB samples used with corresponding sample IDs, event generator, LO and NLO cross sections [3]. LO cross sections are taken from the generator, while NLO cross sections are calculated using `PROSPINO` [136].

C are not used in this analysis because period A was taken with the magnets of the ATLAS detector turned off hence without any possibility to measure the momenta of charged particles while period C was taken at a different center of mass energy of $\sqrt{s} = 2.76\,\text{TeV}$. The employed trigger is a combined jet and $E_{\text{T}}^{\text{miss}}$ trigger, called *EF_j75_a4tc_EFFS_xe45_loose_noMu*. For further details on the trigger and its performance see Sec. 8.2.1.

5.2. Simulated Event Samples

To estimate the background expectation and to optimize the signal selection, this analysis relies on simulated event samples using MC techniques. The simulations are used to extrapolate backgrounds from control regions (CRs) to the signal region (SR) and to evaluate the selection efficiencies for the SUSY models considered.

5.2.1. Signal Samples

Table 5.2 describes the SUSY signal MC samples used in this study. For the minimal GMSB model considered in this analysis, the SUSY mass spectra are calculated using `ISAJET` 7.80 [137]. The MC signal samples are produced using `HERWIG++` 2.4.2 [138] with `MRST2007 LO`* PDFs. The leading-order (LO) cross sections of the different GMSB samples as listed in Tab. 5.2 are

taken from the generator and are for illustration only. The next-to-leading order (NLO) cross sections, depending on the production process, are calculated using PROSPINO 2.1 [136,139–143] with the CTEQ6.6m PDF [144]. The signal events are weighted process-by-process to these NLO cross sections over the GMSB parameter space. The overall NLO cross section per grid point is independent of tanβ but decreases by four orders of magnitude from low to high Λ values (cf. Fig. 8.1).

In the minimal GMSB model, the mass spectrum and therefore the event kinematics are mainly influenced by Λ and $\tan\beta$ (cf. Sect. 2.3.3). The other model parameters are fixed to the following values: $M_{\text{mess}} = 250\,\text{TeV}$, $N_5 = 3$, $\text{sgn}\,\mu = +$, and $C_{\text{grav}} = 1$. GMSB4030, defined by $\Lambda = 40\,\text{TeV}$ and $\tan\beta = 30$ (cf. Sec. 2.3.3), is a typical GMSB point, taken as a benchmark and used in the optimization procedure of the event selection. For the GMSB grid, Λ has been varied between 10 TeV and 80 TeV, in steps of 5 TeV up to 50 TeV and in steps of 10 TeV beyond that, while tanβ adopts values between 2 and 50. Events were generated for 81 grid points in total. Additional intermediate grid points have been generated with sample IDs 142558-142577, 143061-143055 and 152938-152940 to improve the limit determination in the low Λ and low tanβ region where different NLSP regions merge.

5.2.2. Background Samples

MC samples from the official mc10b production of the ATLAS Collaboration are used in this study. Where possible, they are scaled from LO cross sections as calculated by most of the MC generators to next-to-next-to-leading-order (NNLO) cross sections using the values from [145]. In case these NNLO values are not available, the NLO cross sections are considered [145].

Samples of W and Z/γ^* production with accompanying jets are simulated with ALPGEN [146], using CTEQ6L1 PDFs [147]. Top quark pair production, single top production, and diboson pair production are simulated with MC@NLO [148–150] and the NLO PDF set CTEQ6.6 [151]. Fragmentation and hadronization are performed with HERWIG [152], using JIMMY [153] for the underlying event simulation and the ATLAS MC10 parameter tune [154]. TAUOLA [155, 156] and PHOTOS [157] are used to model the decays of τ leptons and the radiation of photons, respectively. The production of multi-jet events is simulated with PYTHIA 6.4.25 [158] using the AMBT1 tune [159] and MRST2007 LO* [160] PDFs. All samples are processed through the GEANT4-based [161, 162] simulation of the ATLAS detector [163].

Tables C.2-C.7 in the Appendix list the SM background samples used in this analysis. The dominant background processes are expected to be $t\bar{t}$ (cf. Tab. C.2) and W + jets production (cf. Tab. C.3). They have NNLO cross sections of 165 pb and 31.4 nb, respectively. The decay of the W in all three charged leptons accompanied by zero to five extra partons in the event is considered while for $t\bar{t}$ fully hadronic and semileptonic decays are taken into account. In addition, single top production (cf. Tab. C.2) in the t-channel and the s-channel with a combined cross section of 37.4 pb is considered.

QCD dijet production (cf. Tab. C.5) contributes with a cross section of approximately 11 mb. In this analysis, the QCD, W + jets, and top background level is determined using a data-driven method making the background estimation less dependent on the MC modeling of the precise cross section.

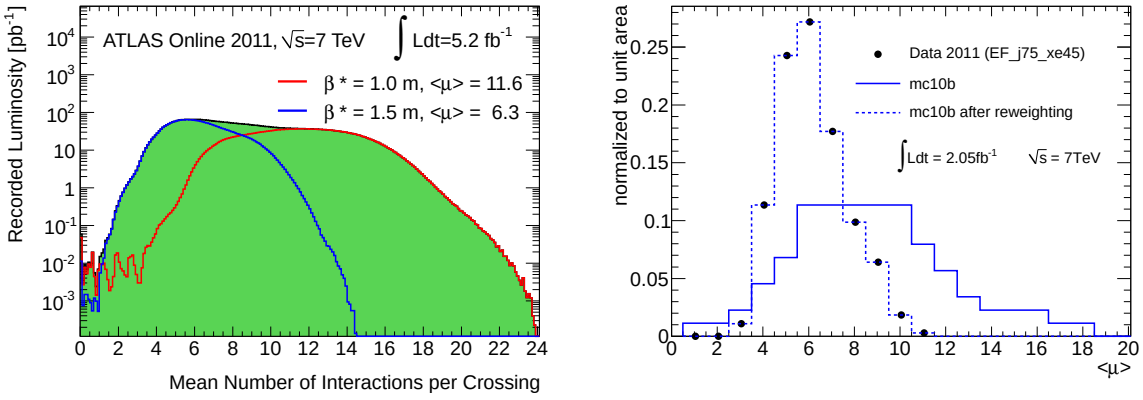

(a) (b)

Figure 5.2.: (a) The luminosity-weighted distribution of the mean number of interactions per bunch crossing for data taken before (blue) and after (red) the September technical stop [121]. (b) The distribution of the mean number of interactions per bunch crossing averaged per luminosity block and bunch crossing ID for data, unweighted MC and the pile-up reweighted MC [164].

Other background processes include $Z+$jets (cf. Tab. C.4), decaying into the various types of leptons accompanied by zero to five extra partons in the event, with a NNLO cross section of 4.22 nb [145], and various diboson production processes (cf. Tab. C.6) including fully and semi leptonic decay channels with a combined NLO cross section of 9.9 pb. Drell-Yan production (cf. Tab. C.7) is also included but found to be negligible.

5.2.3. Pile-up Simulation

Due to the very high instantaneous luminosity, several interactions take place for every bunch crossing. This is known as pile-up. Figure 5.2(a) shows the luminosity-weighted mean number of interactions per bunch crossing $\langle\mu\rangle$ before (blue) and after (red) the short break for technical studies of the accelerator (technical stop) in September. During the data taking period until the end of August up to 14 interactions took place per bunch crossing. This number increased to 24 after β^* was reduced from 1.5 m to 1.0 m.

In general, the mean number of interactions per crossing μ corresponds to the mean of the Poisson distribution on the number of interactions per crossing. It is calculated from the instantaneous luminosity $\mathscr{L}$ as

$$\mu = \frac{\mathscr{L}\sigma_{\text{inel}}}{n_{\text{bunch}} f} \tag{5.1}$$

where σ_{inel} is the inelastic cross section taken to be 71.5 mb, n_{bunch} is the number of colliding bunches, and f is the LHC revolution frequency [165]. The integrated luminosities and the average of the luminosity-weighted mean number of interactions per bunch crossing are given in the figure. The entries at $\langle\mu\rangle \sim 0$ arise from pilot bunches that were present during many of the early LHC fills. The luminosity in these bunches is > 100 times smaller than in the main bunches resulting in values $\mu < 0.1$ [121].

As Fig. 5.2(a) illustrates the pile-up conditions change with time and the setup of the LHC. The variation of the number of pp interactions per bunch crossing as a function of the instantaneous luminosity is taken into account by modeling the simulated number of overlaid minimum bias events according to the observed distribution of the number of pile-up interactions in data, with an average of $\langle\mu\rangle \sim 6$ interactions. Figure 5.2(b) shows the mean number of interactions per bunch crossing for data and the generated MC after the application of the appropriate trigger chosen for this analysis. As they are not identical the MC needs to be reweighted. This is done using the official `PileupReweighting` tool of the ATLAS Collaboration [166]. Events in the MC samples are assigned a varying event weight to reproduce the pile-up conditions measured in data. The pile up conditions for the data set studied are obtained together with the GRL from the official ATLAS data preparation group. Figure 5.2(b) also shows the reweighted MC which is in perfect agreement with the data. By applying the pile-up reweighting 46.4 % of the MC statistics is lost.

6. Reconstruction Algorithms and Object Definition

The various reconstruction algorithms for leptons, jets, and $E_{\mathrm{T}}^{\mathrm{miss}}$ combine the electronic signals of the different detector components and interpret them as the various physics objects with quantities such as momentum, charge, and direction. Since this reconstruction procedure is not unambiguous an identification step follows to suppress background wrongly reconstructed as the corresponding object. The definitions of the physics objects on which the analysis is based on is common to all recent SUSY analyses performed within ATLAS. Only the reconstruction of τ leptons is unique in this work and will be described in more detail. Whenever possible the object selection implemented in the official SUSYTools package [167] has been used.

6.1. Jet Reconstruction

Jets are reconstructed using the anti-k$_t$ jet clustering algorithm [168] with four-momentum recombination and distance parameter $R = 0.4$ in the $y - \phi$ space. This jet algorithm is infrared and collinear safe, meaning collinear splitting or soft emission does not influence the general reconstruction of the jets. It reconstructs the three-dimensional shower topology for particles within the calorimeter, via the input of topological clusters[1]. The distance between particles d_{ij} and between one of them and the beam line d_{iB} are defined as

$$d_{ij} = \min\left(k_{ti}^{2p}, k_{tj}^{2p}\right) \frac{\Delta_{ij}^2}{R^2} \tag{6.1}$$

$$d_{iB} = k_{ti}^{2p}\,, \tag{6.2}$$

where $\Delta_{ij}^2 = (y_i - y_j)^2 + (\phi_i + \phi_j)^2$, and k_{ti}, y_i, and ϕ_i are the transverse momentum, the rapidity, and the azimuth of the particle, respectively. By introducing the radius parameter R, d_{ij} is scaled with respect to d_{iB} in such a way that any pair of final jets a and b are at least separated by $\Delta_{ab}^2 = R^2$ while p governs the relative power of the energy versus the geometrical (Δ_{ij}^2) scales. For the anti-k$_t$ algorithm, $p = -1$. Setting $p = 0$ ($p = 1$) corresponds to the inclusive Cambridge/Aachen algorithm [169, 170] (k$_t$ algorithm [171]).

The clustering procedure now identifies the smallest distance and combines the particles i and j by adding the four momenta if $d_{ij} < d_{iB}$. Otherwise if $d_{iB} < d_{ij}$, i is called a jet and is removed from the list of particles. All distances are recalculated and the procedure is repeated

[1] The seeds for topological clusters are cells with an energy deposition of $|E_i| > 4\sigma_{\mathrm{noise}}$, where σ_{noise} is the Gaussian width of the EM cell energy distribution. They are then built by adding all neighboring cells with $|E_i| > 2\sigma_{\mathrm{noise}}$. As a last step, all cells next to the cluster are absorbed as well. The use of topological clusters helps to suppress noise and ensures that only cells above a certain energy threshold are taken into account.

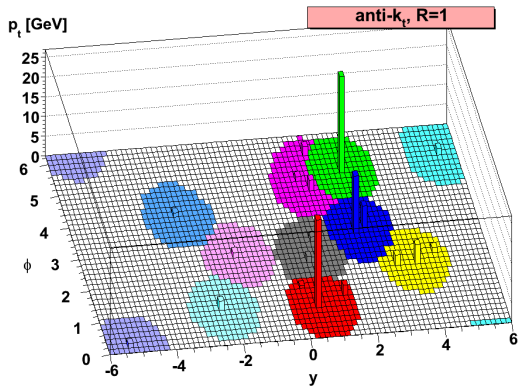

Figure 6.1.: A sample parton-level event illustrating the shape of the jets reconstructed with the anti-k$_t$ algorithm [168].

until no particles are left. Using the anti-k$_t$ algorithm leads to hard jets being circular with radius R while softer jets might have more complex structures [168], as illustrated in Fig. 6.1. If an event contains only a few hard particles but many soft particles the distance d_{ij} between one of the hard particles and one of the soft ones will be driven by k_t of the hard particle and their separation while the d_{ij} of two soft particles will be much larger due to the lower momentum. If around a hard particle ($d_{ij} > 2R$) no other hard particle is found it absorbs all soft particles and a circular jet is reconstructed. For small distances $d_{ij} < R$ between two hard particles, also one jet is reconstructed centered around the harder of the two particles. For medium distances $R < d_{ij} < 2R$, the two hard particles do not cluster and two jets are built.

For this analysis, jets with reconstructed $|\eta| < 2.5$ and $p_{\mathrm{T}} > 20\,\mathrm{GeV}$ are selected. Further subsequent jet requirements are introduced during the event selection (cf. Secs. 8.2 and 8.3), e.g. involving higher p_{T} thresholds for the two leading jets.

6.2. Reconstruction and Identification of τ Leptons

With a mean lifetime of $\tau_\tau = 2.9 \cdot 10^{-13}\,\mathrm{s}$ (path length $87\,\mu\mathrm{m}$) [5], τ leptons decay within the beam pipe, either leptonically $\tau \to \ell\nu_\ell\nu_\tau$ ($\ell = e, \mu$) with a branching fraction of 35.3 % or hadronically, primarily into pions $\tau \to \pi\nu_\tau$, with a branching fraction of 64.7 %. The presence of one or two neutrinos in the final state of the τ decay prevents the complete reconstruction of the τ momentum. The hadronic decay modes are classified as so-called *one-prong* or *three-prong* decays indicating the number of charged decay products in the τ decays. The reconstruction of hadronically decaying τ leptons is discussed in the following.

A common property of τ final states is the low multiplicity of charged tracks. In addition, energy from charged or neutral hadrons is deposited in the calorimeter in a narrow cone around the initial τ direction leading to shower shapes different from those of jets or electrons. The main source for misidentified τ candidates are jets with low energy and a low track multiplicity, especially since their production cross section is several orders of magnitude higher than that for weak interaction processes involving τ leptons.

Seeds for the reconstruction of τ candidates [172] are calorimeter jets found with the anti-k_t algorithm with distance parameter $R = 0.4$ and a calibrated (Local Hadron Calibration, LC [173]) transverse energy of $E_{\mathrm{T}} > 10\,\mathrm{GeV}$. While the LC calibration is used during the jet seed finding, additional η- and p_{T}-dependent energy calibration factors are applied to further adjust the energy scale appropriate for true hadronically decaying τs. These calibration factors are derived from MC and are prepared by the Tau Working Group [174].

The measurements of η and ϕ are taken from the sum of the four-vectors of the clusters associated to the seed jet. The clusters are assumed to be massless. Tracks that are within $\Delta R > 0.2$ from the τ candidate and fulfill the following criteria are allocated to the τ:

- $p_{\mathrm{T}} > 1\,\mathrm{GeV}$
- # pixel hits ≥ 2
- # pixel hits + # SCT hits ≥ 7
- $|d_0| < 1.0\,\mathrm{mm}$
- $|z_0 \sin\theta| < 1.5\,\mathrm{mm}$,

where $d_0(z_0)$ is the shortest distance of the track to the primary vertex in the transverse (longitudinal) plane.

After the reconstruction step many QCD jets are still considered τ candidates. An identification step is introduced to minimize this background. There are three different alternatives: a cut-based method, a projective likelihood, and a boosted decision tree classifier (BDT) [172, 175]. All methods rely on kinematic identification variables that are calculated using tracking and calorimeter information. In this analysis, the identification via the BDT jet score has been chosen. It is based on eight (eleven) discriminating variables for 1-prong (multi-prong) candidates [172]. The variables for the 1-prong and multi-prong candidates include:

Core energy fraction (f_{core}): the ratio of E_{T} measured of a τ candidate within $\Delta R = 0.1$ to that measured within $\Delta R = 0.4$

$$f_{\mathrm{core}} = \frac{\sum_{i\in\{all\}}^{\Delta R_i<0.1} E_{\mathrm{T},i}}{\sum_{j\in\{all\}}^{\Delta R_j<0.4} E_{\mathrm{T},j}}\,, \tag{6.3}$$

where $i(j)$ runs over all calorimeter cells associated to the τ candidate within $\Delta R < 0.1(0.4)$.

Leading track momentum fraction (f_{track}): the ratio of the p_{T} of the leading reconstructed track to the p_{T} of the τ candidate

$$f_{\mathrm{track}} = \frac{p_{\mathrm{T},1}^{\mathrm{track}}}{p_{\mathrm{T}}^{\tau}}\,. \tag{6.4}$$

Track radius (R_{track}): the p_{T}-weighted width of the track system associated to the cluster

$$R_{\mathrm{track}} = \frac{\sum_{i}^{\Delta R_i<0.4} p_{\mathrm{T},i}\Delta R_i}{\sum_{i}^{\Delta R_i<0.4} p_{\mathrm{T},i}}\,, \tag{6.5}$$

where i runs over all tracks of the τ candidate. If the number of tracks within the τ candidate is one, then R_{track} simplifies to ΔR between the track and the τ.

Cluster mass ($m_{\text{eff,clusters}}$): the invariant mass of the clusters associated to the seed jet. To minimize the pileup sensitivity only the clusters carrying the dominant fraction of the seed's energy are considered.

Number of isolation tracks ($N^{\text{iso}}_{\text{tracks}}$): the number of tracks within an isolation annulus around the τ candidate between $\Delta R = 0.2$ and $\Delta R = 0.4$.

Calorimetric radius R_{cal}: the shower width in the calorimeters weighted by the E_{T} of each calorimeter part

$$R_{\text{Cal}} = \frac{\sum_i^{\Delta R_i<0.4} E_{\text{T},i} \Delta R_i}{\sum_i^{\Delta R_i<0.4} E_{\text{T},i}}\,, \tag{6.6}$$

where i runs over all cells in the calorimeters.

First three leading clusters energy ratio ($f_{\text{lead3clusters}}$): the fraction of energy carried in the leading three reconstructed calorimeter clusters compared to the total energy of all clusters associated to the τ.

Leading track IP significance ($S_{\text{lead track}}$): the impact parameter significance of the leading track of the τ

$$S_{\text{lead track}} = \frac{d_0}{\delta d_0}\,, \tag{6.7}$$

where δd_0 is the uncertainty of d_0.

For multi-prong candidates the following variables are also considered:

Maximum ΔR (ΔR_{max}): the maximum distance between one of the reconstructed tracks and the τ candidate axis.

Track mass (m_{tracks}): the invariant mass of the tracks including the core and the isolation tracks.

Transverse flight path significance ($S_{\text{T}}^{\text{flight}}$): the decay length significance of the secondary vertex for multi-prong τ candidates in the transverse plane

$$S_{\text{T}}^{\text{flight}} = \frac{L_{\text{T}}^{\text{flight}}}{\delta L_{\text{T}}^{\text{flight}}}\,, \tag{6.8}$$

where $L_{\text{T}}^{\text{flight}}$ is the reconstructed decay length with an uncertainty of $\delta L_{\text{T}}^{\text{flight}}$. For the fit of the secondary vertex, only the core tracks are taken into account.

Distributions for a selection of these variables are shown in Fig. 6.2. They are shown for reconstructed τ candidates matched to true hadronically decaying τ leptons in $Z \to \tau\tau$ and $W \to \tau\nu$ events (signal) and for QCD jets reconstructed as τ candidates (background). The more distinct the difference is between two distributions, the higher is the separation power of the corresponding variable. The BDT is trained separately for 1-prong and 3-prong τ candidates. The distribution of the BDT score variable is shown in Fig. 6.3, again for 2011 dijet data considered background and $Z \to \tau\tau$ and $W \to \tau\nu_\tau$ MC signal samples.

The signal and background efficiencies are defined as

$$\epsilon_{\text{sig}}^{n-prong} = \frac{\#\text{ identified } \tau \text{ candidates with } n \text{ reconstructed tracks}}{\#\text{ true decays with } n \text{ prongs}} \tag{6.9}$$

$$\epsilon_{\text{bkg}}^{n-prong} = \frac{\#\text{ identified } \tau \text{ candidates with } n \text{ reconstructed tracks}}{\#\text{ reconstructed } \tau \text{ candidates with } n \text{ tracks}} \tag{6.10}$$

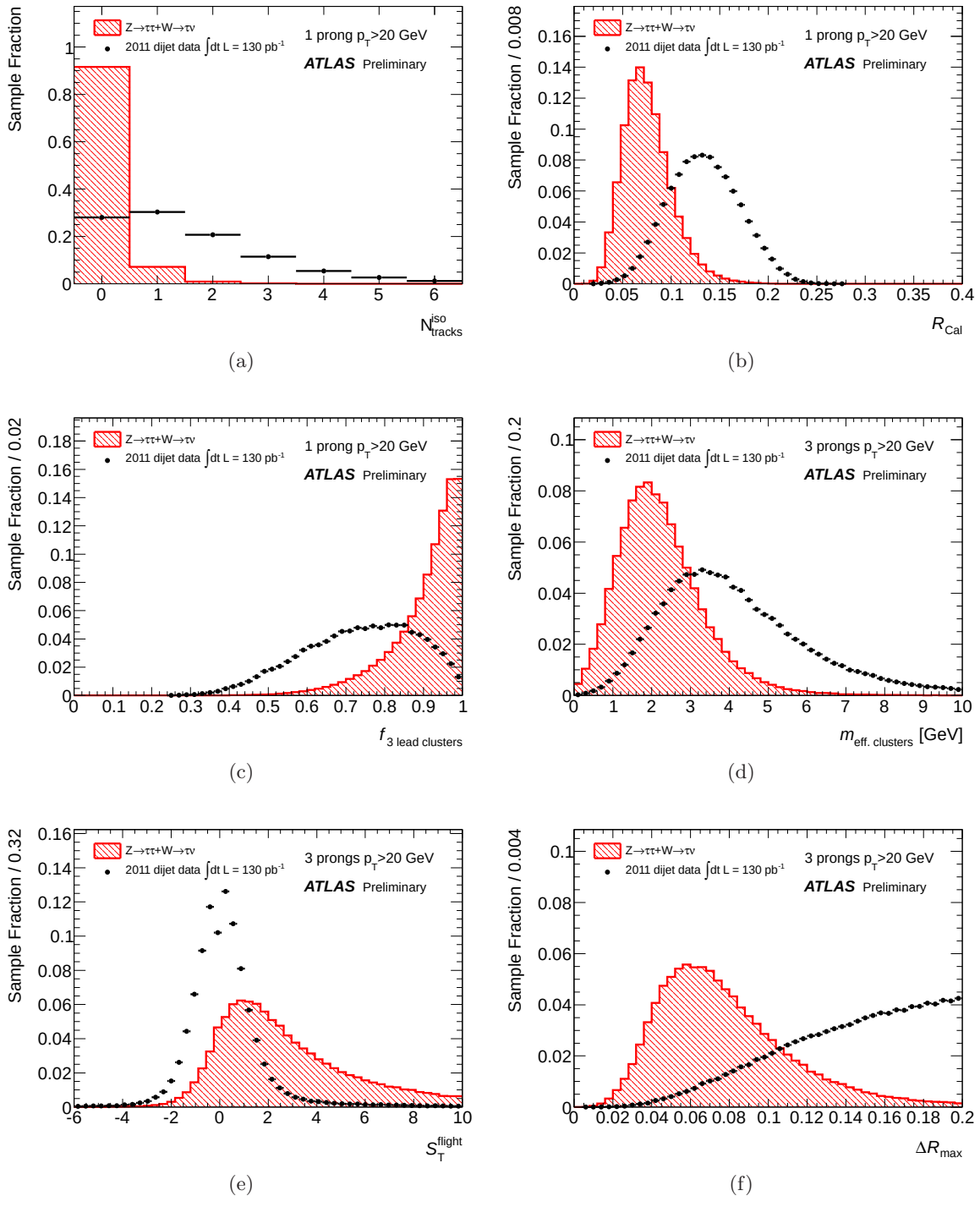

Figure 6.2.: Distributions of a selection of jet discriminating variables for MC simulated $Z \rightarrow \tau\tau$ and $W \rightarrow \tau\nu$ signal samples and a dijet background sample selected from 2011 data [172]. The distributions are normalized to unity. The distributions of (e) the transverse flight path significance and (f) the maximum ΔR are used for multi-prong τ candidates only.

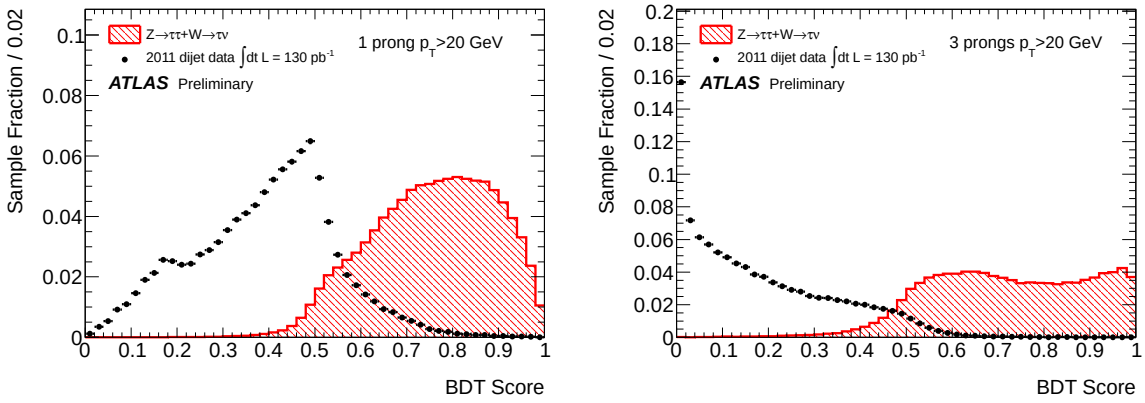

(a) (b)

Figure 6.3.: Jet BDT score for (a) 1-prong and (b) 3-prong τ candidates [172].

Three working points *loose*, *medium*, and *tight* have been defined for each of the three discriminants yielding a flat signal efficiency of 60 %, 50 %, and 30 %, respectively. The corresponding background efficiencies are 10 %, 3 %, and 0.5 % [172]. A comparison of the signal efficiency versus the inverse background efficiency using the medium selection can be seen in Fig. 6.4 for the three discriminants. The multivariate methods clearly outperform the cut-based identification. Especially, in the low p_{T}^{τ} range, the performance of the BDT is noticeably better than for the likelihood making it the optimal choice for the following analysis. Detailed studies and comparisons of the three working points in the context of this analysis have been carried out identifying the loose working as the best option (cf. Sec. 8.4).

Since also electrons can be misreconstructed as 1-prong τ candidates, additional further discriminants towards electrons have been developed: a cut-based method and a BDT. Even though in general, the BDT outperforms the cut-based method, the latter has been chosen for this analysis since it has been found to make no significant difference in this special case. The most distinguishing attributes between an electron and a τ lepton are that a τ lepton does not emit transition radiation and the shower of a τ tends to be longer and wider. Therefore, the cut-based discriminant is based on two shower shape and two track variables: the TRT high-threshold fraction (f_{HT}), the maximum strip E_{T} ($E_{\mathrm{T,max}}^{\mathrm{strip}}$), the hadronic ($f_{\mathrm{Had}}^{\mathrm{track}}$), and the electromagnetic track fraction ($f_{\mathrm{EM}}^{\mathrm{track}}$). Again, three working points have been defined yielding an efficiency of 95 %, 85 %, and 75 %, respectively [172]. The loose cut set has been chosen to match the jet discriminant.

Identified τ leptons are selected if they satisfy $|\eta| < 2.5$ and $p_{\mathrm{T}} > 20\,\mathrm{GeV}$. They are required to either have one or three reconstructed tracks whereas the sum of the track charges needs to be $|q| = 1$.

6.3. Electron Reconstruction and Identification

Electron candidates are only used for event veto in this analysis. The reconstruction of electrons [176, 177] in the central region ($|\eta| < 2.47$) is done via the association of a reconstructed

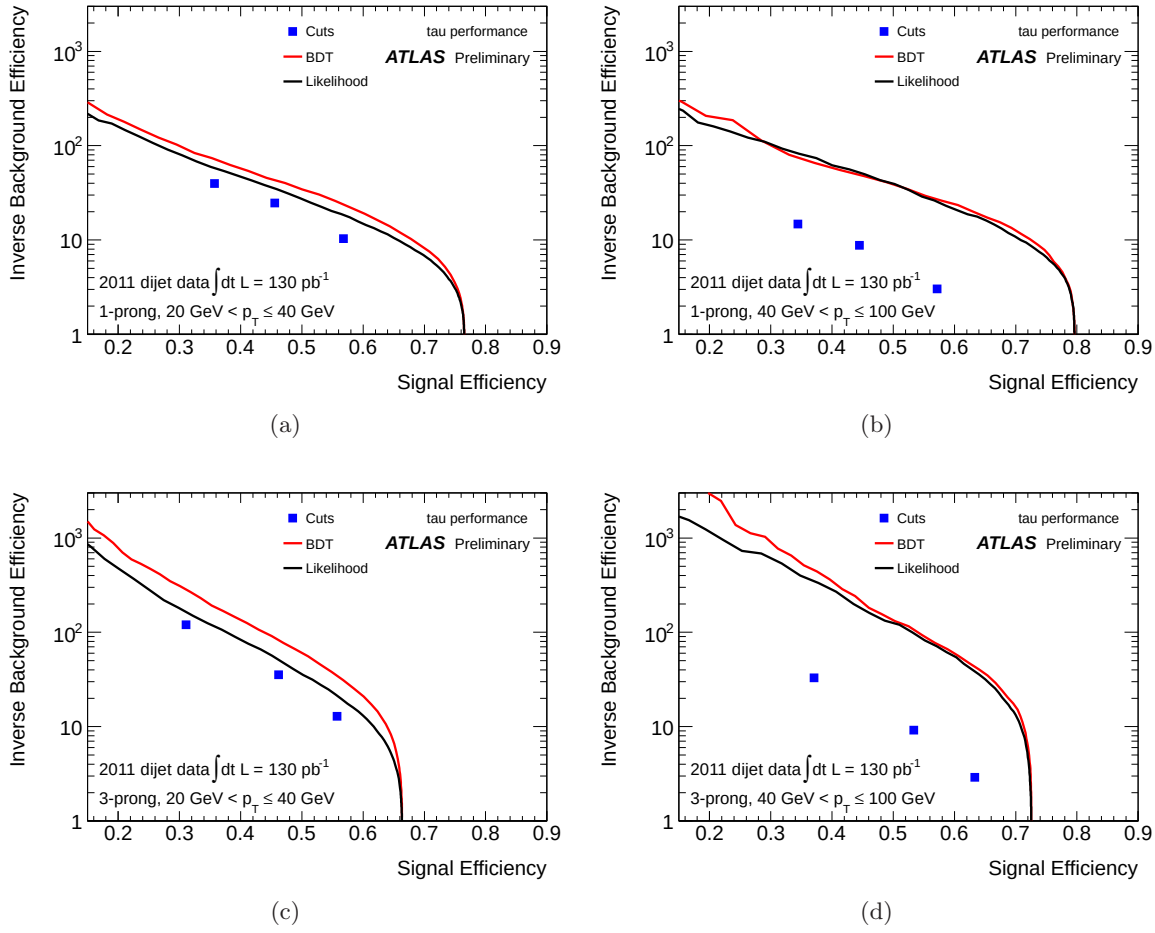

Figure 6.4.: Inverse background efficiency as a function of the signal efficiency for 1-prong (top) and 3-prong (bottom) candidates, in the low (left) and the high (bottom) p_{T} range, for all three jet discriminants [172].

track in the inner detector to an energy deposit (cluster) in the EM calorimeter. A sliding window algorithm builds EM clusters from seed clusters of longitudinal towers with a total $E_{\mathrm{T}} > 2.5\,\mathrm{GeV}$. The window size corresponds to the granularity of the middle layer of the EM calorimeter. The reconstructed tracks are extrapolated from their last hit to this calorimeter layer and matched to the seed clusters, where the track impact point and the cluster position need to be within $\Delta|\eta| < 0.05$. If several tracks are matched to the same cluster, tracks without silicon hits are rejected and the closest track to the seed cluster is chosen.

The energy of the cluster is defined as the measured energy deposit in the cluster itself plus the estimated external energy deposit outside the cluster (lateral leakage) and in front of and beyond (longitudinal leakage) the EM calorimeter. The energy of the reconstructed electron is identical to the cluster energy whereas its momentum is determined by using cluster and track information. Electrons are required to satisfy $p_{\mathrm{T}} > 20\,\mathrm{GeV}$. The direction of the associated track is also taken as the direction of the reconstructed electron. In case of very few hits, the direction of the cluster is used instead.

A cut-based identification with three different working points *loose*, *medium*, and *tight* is defined by combining calorimeter and tracking information. The main goal is the suppression of non-isolated electrons, secondary electrons, e.g. from photon conversions, and jets reconstructed as electrons. The loose selection is based on shower shape and hadronic leakage variables while the medium selection additionally takes EM calorimeter strip layer, track quality, and track-cluster matching variables into account. For the following analysis, electrons passing the medium identification are selected. Electron candidates falling in the region of the dead front end boards in the LAr calorimeter (cf. Sec. 8.2.2) are rejected as well as forward electrons ($2.5 < |\eta| < 4.9$).

6.4. Muon Reconstruction and Identification

Muon candidates as well are only used for event veto in this analysis. Two reconstruction algorithms for muons [178] exist within ATLAS: MuId and Staco [179, 180]. In the following, only the latter will be considered. The reconstruction can either rely on the muon spectrometer only (*stand alone* μ) or on the muon spectrometer and additionally the inner detector (*combined* μ, *segment tagged* μ). Since events containing muons will be rejected during the event selection a high purity of the reconstruction is preferred over a high efficiency. Therefore, stand alone muons are not considered.

For combined muons, the track is reconstructed independently by the inner detector and the muon spectrometer and afterwards both are matched provided that the momenta measured for both tracks are compatible. This matching reduces the number of wrongly reconstructed muons. Jets with high momentum might punch through the calorimeter system into the muon spectrometer where they create a high hit multiplicity. For segment tagged muons, a good track reconstructed in the inner detector is extrapolated and associated to a track segment found in the muon spectrometer. This method allows the recovery of muons with insufficient hits in the muon spectrometer. The p_{T} is determined by combining the information of the track p_{T} from the inner detector as well as the muon spectrometer including the energy deposited in the calorimeter.

Reconstructed muons need to pass at least the loose identification criteria which are defined by: at least two hits in the pixel detector where one of them is in the b-layer and at least six hits in the SCT. For muons in the central region $|\eta| < 1.9$, at least six hits in the TRT are required, where dead modules traversed by the extrapolated muon track are counted as hits. Muons are selected if they satisfy $|\eta| < 2.4$ and $p_{\mathrm{T}} > 20\,\mathrm{GeV}$. To reject muons from cosmic rays, the tracks are required to have a longitudinal impact parameter of $|z_0| < 1\,\mathrm{mm}$ and a transverse impact parameter of $|d_0| < 0.2\,\mathrm{mm}$ [181].

6.5. Overlap Removal

It often occurs that the same objects are reconstructed and identified by several of the algorithms. Therefore, to avoid double counting a preference to one of the objects needs to be defined. No events are lost in the process. If a jet is overlapping[2] with an electron it is

[2] Overlapping refers to the ΔR-cone between the two objects being smaller than 0.2.

discarded. Due to the higher efficiency and purity of the electron and muon reconstruction algorithms, these are kept while an overlapping[3], reconstructed τ candidate is discarded. Since the decay products of a τ are hadronic they are always also reconstructed as jets. Therefore, the overlapping jet is discarded. Finally, any remaining electron or muon that is within $\Delta R < 0.4$ of a jet is rejected.

6.6. Determination of Missing Transverse Momentum

In hadron collisions, momentum conservation is expected in the plane transverse to the beam axis. Therefore, the imbalance of momentum in this plane, missing transverse momentum $E_{\mathrm{T}}^{\mathrm{miss}}$ [182], is a useful quantity. It is determined from the negative vector sum of the momenta of all particles present in an event. Many searches for new physics, including the one presented in the following, rely on $E_{\mathrm{T}}^{\mathrm{miss}}$ since its presence might indicate the existence of undiscovered weakly interacting, e.g. SUSY, particles. A precise knowledge of $E_{\mathrm{T}}^{\mathrm{miss}}$ also improves the determination of the top quark mass in $t\bar{t}$ events and supports the search for the Higgs boson in $H \to WW$ or $H \to \tau\tau$ decays.

The magnitude of $E_{\mathrm{T}}^{\mathrm{miss}}$ and its azimuth are calculated as [182]

$$E_{\mathrm{T}}^{\mathrm{miss}} = \sqrt{(E_x^{\mathrm{miss}})^2 + (E_y^{\mathrm{miss}})^2}\,, \tag{6.11}$$

$$\phi^{\mathrm{miss}} = \arctan(E_y^{\mathrm{miss}}, E_x^{\mathrm{miss}})\,, \tag{6.12}$$

where the two components combine contributions from energy deposits in the calorimeters and from muons

$$E_{x(y)}^{\mathrm{miss}} = E_{x(y)}^{\mathrm{miss,calo}} + E_{x(y)}^{\mathrm{miss},\mu}\,. \tag{6.13}$$

The calculation of the calorimeter terms is based on calorimeter cells associated to an identified physics object. All other cells are combined in a term called $E_{x(y)}^{\mathrm{miss,CellOut}}$ and contribute to $E_{\mathrm{T}}^{\mathrm{miss}}$ as well

$$\begin{aligned} E_{x(y)}^{\mathrm{miss,calo}} = {} & E_{x(y)}^{\mathrm{miss},e} + E_{x(y)}^{\mathrm{miss},\gamma} + E_{x(y)}^{\mathrm{miss},\tau} + E_{x(y)}^{\mathrm{miss,jets}}\,, \\ & + E_{x(y)}^{\mathrm{miss,softjets}} + E_{x(y)}^{\mathrm{miss,CellOut}} + E_{x(y)}^{\mathrm{miss,calo},\mu}\,, \end{aligned} \tag{6.14}$$

where

- $E_{x(y)}^{\mathrm{miss},e}$, $E_{x(y)}^{\mathrm{miss},\gamma}$, $E_{x(y)}^{\mathrm{miss},\tau}$ are reconstructed from cluster cells associated to electrons, photons, and hadronically decaying τs,
- $E_{x(y)}^{\mathrm{miss,jets}}$ is reconstructed from cluster cells associated to jets with $p_{\mathrm{T}} > 20\,\mathrm{GeV}$,
- $E_{x(y)}^{\mathrm{miss,softjets}}$ is reconstructed from cluster cells associated to jets with $7\,\mathrm{GeV} < p_{\mathrm{T}} < 20\,\mathrm{GeV}$,
- $E_{x(y)}^{\mathrm{miss,CellOut}}$ is reconstructed from cells in topological clusters not included in any of the reconstructed objects, and

[3] Overlapping refers to the ΔR-cone between the two objects being smaller than 0.4.

- $E_{x(y)}^{\text{miss,calo},\mu}$ is the contribution from the energy deposit of non-isolated muons in the calorimeter.

The energy deposition from isolated muons is not accounted for to avoid double-counting of the muon energy. Each of the above terms is the negative sum of the calibrated cell energies according to the corresponding object

$$E_x^{\text{miss,term}} = -\sum_{i=0}^{N_{\text{cell}}^{\text{term}}} E_i \sin\theta_i \cos\phi_i \tag{6.15}$$

$$E_y^{\text{miss,term}} = -\sum_{i=0}^{N_{\text{cell}}^{\text{term}}} E_i \sin\theta_i \sin\phi_i \,, \tag{6.16}$$

where E_i, θ_i, and ϕ_i are the energy, the polar angle, and the azimuth of the individual physics objects, respectively. The muon term is determined by summing over the track momenta within $|\eta| < 2.7$ of all combined and segment tagged muons

$$E_{x(y)}^{\text{miss},\mu} = -\sum_{\mu\text{s}} p_{x(y)}^{\mu} \,. \tag{6.17}$$

Crucial for an accurate determination of $E_{\text{T}}^{\text{miss}}$ is the optimization of the detector coverage, the detector resolution, and the correct treatment of dead regions and noise. All these different contributions are potential sources of misinterpreted $E_{\text{T}}^{\text{miss}}$. The coverage of the ATLAS calorimeter extends to large pseudorapidities to detect high energy particles flying in the forward direction. During the event selection cuts are applied to reject events containing misreconstructed $E_{\text{T}}^{\text{miss}}$ from cosmic-rays and beam-halo muons. The resolution of $E_{\text{T}}^{\text{miss}}$ is found to be $\sigma = k \cdot \sqrt{\sum E_{\text{T}}}$ with $k \approx 0.5\,\text{GeV}^{1/2}$ [182].

7. Study of the ATLAS discovery potential with $\sqrt{s} = 10\,\mathrm{TeV}$ using simulated events

In this following study, the ATLAS discovery potential in the GMSB parameter space with τ final states is determined for a center-of-mass energy of $\sqrt{s}$=10 TeV using a cut-based analysis applied to simulated event samples corresponding to $200\,\mathrm{pb}^{-1}$. In 2008, this scenario was expected as a possible running option in the early phase of the LHC. The results presented here have been obtained during the early period of the work on this thesis and have been made public by the ATLAS collaboration in [46]. The main results are presented here.

The event selection is optimized for the characteristic GMSB6 benchmark scenario featuring a large amount of $E_{\mathrm{T}}^{\mathrm{miss}}$, highly energetic jets, and a large number of τ leptons (cf. Sec. 2.3.3) using simulated signal and background samples. It is then also applied to various other GMSB scenarios in a scan of the GMSB parameter space. The corresponding simulated event samples were simulated using a fast simulation approach [183, 184] after a careful comparison of the fast and full simulation results. In addition, the prospects for the measurement of endpoints in the invariant mass spectra of two τ leptons in the final state is studied for the above-mentioned GMSB benchmark scenario. It is based on $8\,\mathrm{fb}^{-1}$ of simulated events to illustrate the technique for the determination of kinematic end-points. The presentation of this MC study closely follows [46].

7.1. Event Generation and Simulation

For the simulation of the GMSB signal, the SUSY mass spectrum and the branching ratios of the SUSY particles were calculated using ISAJET 7.74 [137]. The events were generated by HERWIG/JIMMY [152, 153, 185] including the hard scattering, the decays of SUSY particles, parton showers, hadronization, and the simulation of the underlying event. For the simulation of the response of the ATLAS detector a full GEANT4 [161, 162] simulation was used for the example scenario, GMSB6, while for the scan in the GMSB parameter space a fast simulation approach was adopted.

Given the LO cross section of supersymmetric particles (mainly pairs of squarks and gluinos) of $\sigma_{\mathrm{GMSB6}} = 1.2\,\mathrm{pb}$ [152], the number of available fully simulated signal events for the GMSB6 scenario (9 500) corresponds to an integrated luminosity of $7.9\,\mathrm{fb}^{-1}$. For the estimation of the discovery potential, all numbers and figures are normalized to an integrated luminosity of $\mathscr{L} = 200\,\mathrm{pb}^{-1}$, whereas for the determination of the invariant mass end-point all numbers and figures are normalized to an integrated luminosity of $\mathscr{L} = 8\,\mathrm{fb}^{-1}$.

For the simulation of the SM background, the processes listed in Tab. 7.1 are used. The data sets include dijet and γ-jet events generated by PYTHIA 6.4 [158], W+jets and Z+jets production generated by ALPGEN [146], and diboson, $t\bar{t}$ and single t events generated by

Generator	Process	Cross section [pb]
MC@NLO	$t\bar{t}$	400
	single t	48
	diboson	9.2
ALPGEN	Z+jets	$4.4 \cdot 10^3$
	W+jets	$4.8 \cdot 10^4$
Pythia	dijet	$1.3 \cdot 10^{10}$
	γ-jet	$2.2 \cdot 10^5$

Table 7.1.: Different SM background processes considered and their cross sections.

MC@NLO [148–150]. Higher order corrections are included in the form of k-factors where available: for the ALPGEN samples NLO corrections are applied, for the $t\bar{t}$ MC@NLO sample approximate NNLO corrections. GEANT4 was used for the simulation of the full detector response for all SM background processes.

For the study of the discovery potential in the GMSB parameter space a large number of events was needed. Due to limited CPU resources, a fast simulation of the ATLAS detector response [183, 184] was used. A thorough comparison of the fast and full simulation results of the critical variables used in this study was performed for the GMSB6 example scenario. Example distributions are shown in the Appendix (cf. Fig. C.6) for the full and fast simulation. The observed agreement of the distributions of all variables crucial for the event selection in the full and fast simulation gives confidence that the number of selected events obtained from the fast simulation reliably reproduces the results of the full simulation. Hence, the fast simulation was used in the scanning procedure of the GMSB parameter space.

Event samples were simulated with 10 000 events each in 380 parameter points in the Λ-tanβ-plane for $M_{\text{mess}} = 250\,\text{TeV}$, $N_5 = 3$, $\text{sgn}\,\mu = +$ and $C_{\text{grav}} = 1$, including the GMSB6 benchmark scenario. The locations of the samples in the plane was chosen carefully to allow the investigation of the details of the phenomenology of the parameter space.

7.2. Event Selection and Discovery Potential

In regions of the GMSB parameter space where the NLSP is the $\widetilde{\tau}_1$, long cascade decays of the initial squarks and gluinos lead to many highly energetic jets, many τ leptons, and a significant amount of $E_{\text{T}}^{\text{miss}}$. For this reason the following preselection is used to separate the GMSB6 signal from the SM background:

1. Events must pass the trigger selection which is optimized to select events containing at least one jet with $p_{\text{T}} > 70\,\text{GeV}$ and $E_{\text{T}}^{\text{miss}} > 30\,\text{GeV}$. This standard SUSY trigger selection was expected to be part of the ATLAS trigger menu foreseen for early data taking [186]. The trigger efficiency for GMSB6 signal events is 80.6%. For events passing the preselection cuts, the trigger efficiency is 96.9%.

2. Two or more jets[1] ($N_{\text{jet}} \geq 2$) within $|\eta| < 2.5$ have to be found, with $p_{\text{T}}^{\text{jet1}} > 100\,\text{GeV}$ and $p_{\text{T}}^{\text{jet2}} > 50\,\text{GeV}$. Jet candidates also reconstructed as τ candidates are excluded.[2]
3. At least one hadronically decaying τ lepton ($N_\tau \geq 1$) with $|\eta| < 2.5$ and $p_T > 15\,\text{GeV}$ has to be found with $p_T > 20\,\text{GeV}$ for the leading τ. For the reconstruction of the hadronically decaying τ leptons the standard ATLAS algorithm [186] was used. To distinguish hadronic τ decays from QCD background processes as well as from electrons and muons a number of variables offering good discrimination power was used in a combined likelihood function.[3] τ candidates also reconstructed as electron candidates[4] are excluded[3].
4. The missing transverse energy[5] of the events must exceed 60 GeV: $E_{\text{T}}^{\text{miss}} > 60\,\text{GeV}$.
5. For the removal of events with mismeasured $E_{\text{T}}^{\text{miss}}$ from mismeasured jets, the azimuthal angle between the leading jet and direction of $E_{\text{T}}^{\text{miss}}$ needs to exceed 0.2: $|\Delta\phi(E_{\text{T}}^{\text{miss}}, \text{leading jet})| > 0.2\,.$

Table 7.2 shows the total number of events from the various physics processes before and after this preselection. It can be seen that the signal-to-background ratio is greatly increased by the preselection retaining more than 40 % of the GMSB signal events. For illustration Fig. 7.1(a) displays the total event numbers after each step of the preselection. The strong decrease of the background contribution is clearly visible, while the loss in signal efficiency is moderate. The strongest impact on the SM background can be observed for the trigger requirement and the requirement of at least one τ lepton. In Fig. 7.1(b) and Fig. 7.1(c) the distributions of $E_{\text{T}}^{\text{miss}}$ and N_τ after the preselection are shown for the various physics processes under study. For large values of $E_{\text{T}}^{\text{miss}}$ and N_τ the GMSB6 signal dominates the SM background mainly consisting of $t\bar{t}$ and W events.

For further suppression of the residual SM background a two-dimensional optimization of the signal significance as a function of the cut values of $E_{\text{T}}^{\text{miss}}$ and N_τ is performed for the GMSB6 scenario. A simplified measure for the signal significance S as a function of the cut values for the two variables is shown in Fig. 7.2 using the definition

$$S = N_S/\sqrt{N_B}\,, \tag{7.1}$$

where N_S (N_B) is the number of signal (background) events. The maximum significance can be achieved for

- $E_{\text{T}}^{\text{miss}}$ >280 GeV
- N_τ ≥2.

[1] Jets are reconstructed from calorimeter towers using a cone algorithm with cone size of 0.4.
[2] Two candidates are assumed to be the same if $|\Delta R| < 0.1$ with $(\Delta R)^2 = (\Delta\eta)^2 + (\Delta\phi)^2$.
[3] The combined likelihood is optimized for the selection of τ leptons from $Z \to \tau\tau$ decays where the dominant background consists of misidentified QCD dijet events. Compared to a cut-based τ identification designed for first data, larger data sets are required for the study of the performance of the τ identification using the likelihood method as it relies on a detailed detector understanding. A cut-based identification would result in a slightly lower background rejection. A detailed study of the performance of the algorithm can be found in [186].
[4] Electron candidates are reconstructed and identified with the ATLAS standard *medium* purity requirements [186]. In particular, these *medium* cuts include E_{T} dependent isolation criteria. In addition, the electron candidate must fulfill: $p_T > 10\,\text{GeV}$ and $|\eta| < 2.5$.
[5] The value of $E_{\text{T}}^{\text{miss}}$ is computed from calorimeter cells.

Process	Initial	Preselection	Final selection
GMSB6	240.0 ± 2.5	102.1 ± 1.6	20.4 ± 0.7
$t\bar{t}$, single t	$(8.96 \pm 0.01) \cdot 10^4$	1301 ± 11	1.1 ± 0.3
diboson	$(1.84 \pm 0.08) \cdot 10^3$	3.7 ± 0.4	-
Z+jets	$(8.836 \pm 0.008) \cdot 10^5$	182.1 ± 4.3	0.2 ± 0.1
W+jets	$(9.692 \pm 0.005) \cdot 10^6$	2058 ± 45	1.1 ± 1.1
dijet	$(2.537 \pm 0.004) \cdot 10^{12}$	$(3.5 \pm 1.7) \cdot 10^3$	-
γ-jet	$(4.40 \pm 0.01) \cdot 10^7$	20.1 ± 6.1	-

Table 7.2.: Total numbers of selected events for the signal and various SM background processes at different stages of the event selection for $\mathscr{L} = 200\,\text{pb}^{-1}$ and $\sqrt{s} = 10\,\text{TeV}$. The uncertainties given correspond to statistical uncertainties from the limited MC statistics. Some background processes give contributions significantly below one event after the final selection due to the selection cuts on the jet p_T and E_T^miss and are therefore negligible.

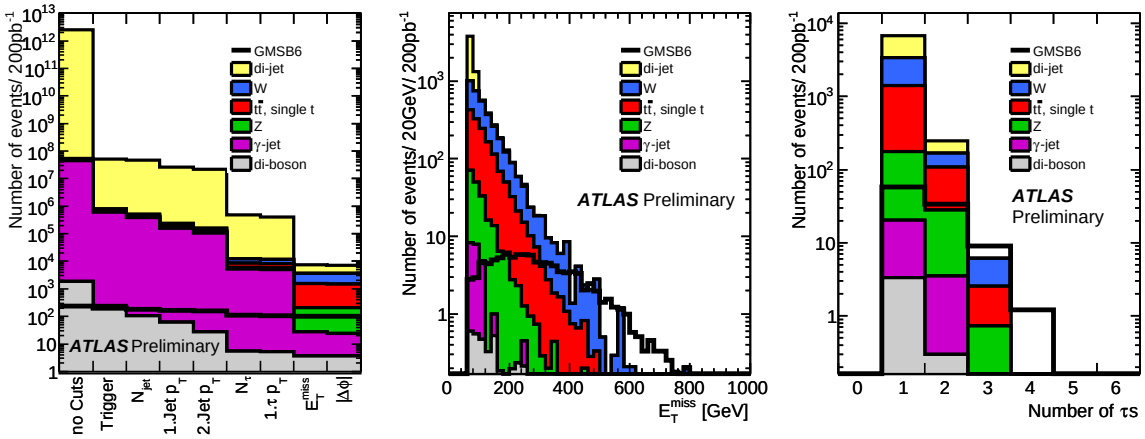

(a) (b) (c)

Figure 7.1.: (a) Total number of events after each step of the preselection and event distributions after the preselection for the GMSB signal and the various SM backgrounds: (b) E_T^miss and (c) number of τ leptons with $p_\text{T} > 15\,\text{GeV}$ ($p_\text{T} > 20\,\text{GeV}$ for the leading τ).

With these two additional cuts 20.4 ± 0.7 signal events are expected for the GMSB6 scenario while the total number of expected background events is 2.5 ± 1.5 for $\mathscr{L} = 200\,\text{pb}^{-1}$. The reason for the large rejection of dijet events is that only a small fraction of such events have a sufficiently hard scatter ($p_\text{T}^\text{jet1} > 100\,\text{GeV}$) to pass the preselection cuts. This fraction is even smaller after the hard requirement on E_T^miss as used for the final selection. In Fig. 7.3(a) and Fig. 7.3(b) the distributions of E_T^miss and N_τ after the final selection excluding the cut on the displayed distributions are shown for the various physics processes under study.

The simple definition of Eq. (7.1) neglects the influence of systematic uncertainties on the background expectation (N_B). In a real data analysis, the background contribution and its uncertainty are usually estimated using data-driven methods. In [186] the corresponding relative uncertainty, including e. g. the uncertainties from the electromagnetic and hadronic

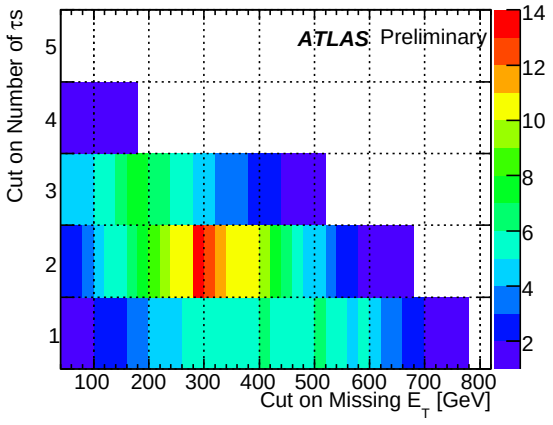

Figure 7.2.: Signal significance ($S = N_S/\sqrt{N_B}$) as a function of the cut values of $E_{\mathrm{T}}^{\mathrm{miss}}$ and N_τ. The maximum significance is obtained for $E_{\mathrm{T}}^{\mathrm{miss}}$ >280 GeV and $N_\tau \geq 2$.

energy scale, is conservatively estimated for electron and muon final states from Z, W, and $t\bar{t}$ background processes to be 20 % for a centre-of-mass energy of 14 TeV[6]. For a smaller energy, as studied here ($\sqrt{s}$=10 TeV), higher uncertainties can be expected in particular for smaller data sets, as many estimates for different uncertainty sources are limited by the size of the control sample used. Taking this effect into account, an uncertainty of 50 % for smaller datasets ($\mathscr{L} = 200\,\mathrm{pb}^{-1}$) is assigned [187]. This relative uncertainty decreases linearly with $\mathscr{L}$ and reaches a minimum of 20 % for $\mathscr{L} = 1\,\mathrm{fb}^{-1}$. In addition, the statistical uncertainty resulting from the limited MC statistics for some MC processes enters as systematic uncertainty.

Following [188] these systematic uncertainties can be included in a more appropriate calculation of the significance Z_n using:

$$Z_n = \sqrt{2}\,\mathrm{erf}^{-1}(1-2p)\,, \tag{7.2}$$

where erf^{-1} is the inverse error function and p is the probability that the background fluctuates to the number of measured events $N_D = N_S + N_B$, given by

$$p = A\int_0^\infty db\, G(b; N_B; \delta N_B) \sum_{i=N_D}^{\infty} \frac{e^{-b} b^i}{i!}\,, \tag{7.3}$$

where $G(b; N_B; \delta N_B)$ is a Gaussian distribution and A is the normalization factor given by

$$A^{-1} = \int_0^\infty db\, G(b; N_B; \delta N_B) \sum_{i=0}^{\infty} \frac{e^{-b} b^i}{i!}\,. \tag{7.4}$$

In general, this approach provides a more conservative estimate of the signal significance than using Eq. (7.1), e. g. for the GMSB6 scenario a reduced signal significance of $Z_n = 5.7$ is obtained compared to $S = 13$. The two-dimensional optimization procedure using the significance definition of Eq. (7.2) yields the same optimal selection cuts for $E_{\mathrm{T}}^{\mathrm{miss}}$ and N_τ as before using Eq. (7.1).

[6]The uncertainties on the background for τ final states, resulting for example from the performance of the τ reconstruction, in real data might be larger.

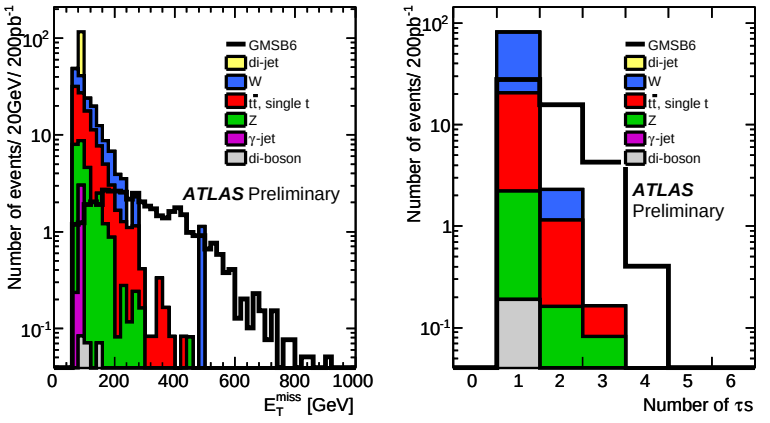

(a) (b)

Figure 7.3.: Kinematic event distributions after the final selection for the GMSB signal and the various SM backgrounds: (a) $E_{\text{T}}^{\text{miss}}$ after the $N_\tau \geq 2$ cut, (b) N_τ with $p_{\text{T}} > 15\,\text{GeV}$ ($p_{\text{T}} > 20\,\text{GeV}$ for the leading τ) after the $E_{\text{T}}^{\text{miss}} > 280\,\text{GeV}$ cut.

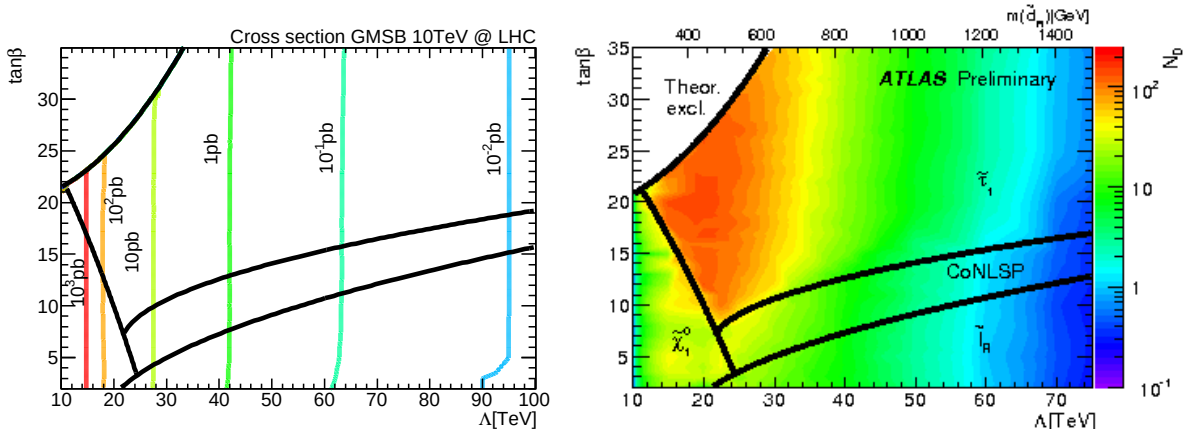

(a) (b)

Figure 7.4.: (a) Total SUSY cross section in pb and (b) expected number of selected signal events for $\mathscr{L} = 200\,\text{pb}^{-1}$ at $\sqrt{s} = 10\,\text{TeV}$ in the Λ-tanβ-plane for $M_{\text{mess}} = 250\,\text{TeV}$, $N_5 = 3$, $\text{sgn}\,\mu = +$ and $C_{\text{grav}} = 1$.

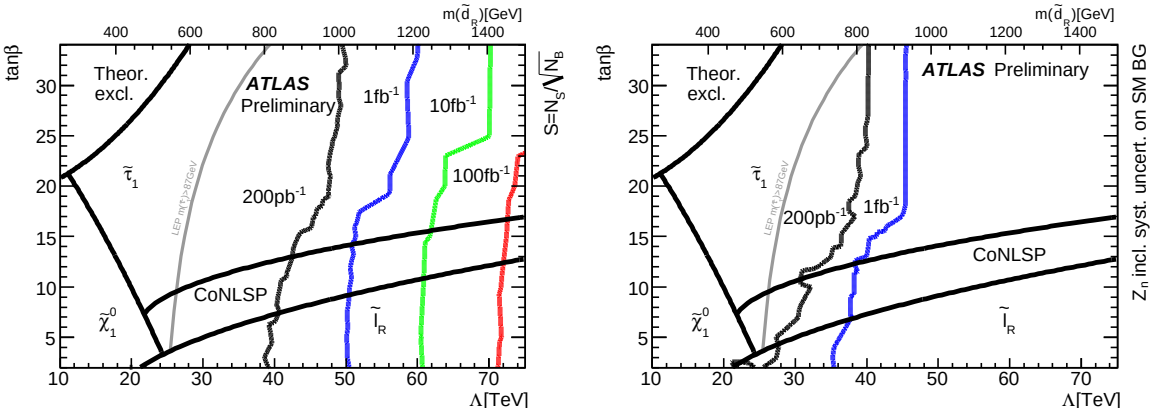

(a) (b)

Figure 7.5.: Integrated luminosity needed for a signal significance of $S = 5$ or $Z_n = 5$, respectively, in the Λ-tanβ-plane for $M_{\text{mess}} = 250\,\text{TeV}$, $N_5 = 3$, $\text{sgn}\,\mu = +$ and $C_{\text{grav}} = 1$ using (a) the simple calculation of the significance following (7.1) which neglects the uncertainty on the SM background and (b) using (7.2) which properly includes this uncertainty.

The discovery potential is studied in the Λ-tanβ-plane for $M_{\text{mess}} = 250\,\text{TeV}$, $N_5 = 3$, $\text{sgn}\,\mu = +$ and $C_{\text{grav}} = 1$. Figure 7.4(a) shows the total SUSY production cross section in the studied plane. While only a small dependence of the cross section on tanβ can be observed, it strongly depends on Λ due to the increase of the masses of the SUSY particles with increasing Λ, e.g. in the range $10\,\text{TeV} < \Lambda < 50\,\text{TeV}$ the cross section decreases by four orders of magnitude. This is reflected in the values of the total number of selected signal events displayed in Fig. 7.4(b) for $200\,\text{pb}^{-1}$. In addition to the decrease of the production cross section with Λ, the nature of the NLSP has a strong influence on the number of selected events. While the regions with a $\widetilde{\tau}_1$ NLSP feature a large fraction of selected events, selection losses can be observed in regions where the NLSP is given by $\widetilde{\ell}_R$, $\widetilde{\chi}_1^0$ or in the CoNLSP region due to the dominant final states with electrons, muons or photons for which the selection is not optimized.

The number of selected signal events in the Λ-tanβ-plane for $200\,\text{pb}^{-1}$ (cf. Fig. 7.4(b)) and the expected number of background events can be translated into a signal significance as a function of the integrated luminosity $\mathscr{L}$ using the definitions in Eq. (7.1) or Eq. (7.2) and an appropriate scaling with $\mathscr{L}$. The corresponding results are shown in Fig. 7.5(a) using Eq. (7.1) for the calculation of the signal significance which neglects the systematic uncertainties of the background. As expected, the values of $\mathscr{L}$ needed for $S = 5$ are small in regions with a $\widetilde{\tau}_1$ NLSP and small/medium values of Λ. With a luminosity of only $\mathscr{L} = 200\,\text{pb}^{-1}$, as was expected to be available after one year of data taking, $S = 5$ can be reached in the parameter space region up to $\Lambda \sim 45\,\text{TeV}$. Due to the strong reduction of the cross section the signal significance strongly decreases with increasing Λ leading to $S = 5$ regions up to $\Lambda \sim 60\,\text{TeV}$ ($\Lambda \sim 70\,\text{TeV}$) for $\mathscr{L} = 1\,\text{fb}^{-1}$ ($\mathscr{L} = 10\,\text{fb}^{-1}$).

The inclusion of the background uncertainty in the calculation of the signal significance following Eq. (7.2) leads to more conservative results as displayed in Fig. 7.5(b). With this definition, the parameter region for a $5\,\sigma$ discovery with $\mathscr{L} = 200\,\text{pb}^{-1}$ ($1\,\text{fb}^{-1}$) is reduced to the region up to $\Lambda \sim 40\,\text{TeV}$ ($45\,\text{TeV}$). With the assumptions on the background uncertainty

of 20 % for data samples of $1\,\text{fb}^{-1}$ or higher the discovery reach cannot be improved. However, the contributions to the background uncertainty, which are limited by the size of the used control samples, will gain directly from a larger data sample and therefore decrease. Further, an improved understanding of the backgrounds and their uncertainties is expected from dedicated studies by the time larger data sets of real τ leptons expected from SM processes are available.

7.3. Study of the Invariant Ditau Mass Distribution

After a possible SUSY discovery the investigation of the underlying SUSY model is an important step in which the determination of the masses of SUSY particles is vital. In the presence of two undetected LSPs only differences of SUSY masses can be determined at the LHC, e.g. from kinematic end-points in invariant mass distributions. The end-point of the reconstructed ditau invariant mass was used to determine the underlying masses in an mSUGRA scenario in which the lightest neutralino ($\widetilde{\tau}_1$) is the LSP (NLSP) yielding the decay chain $\widetilde{\chi}_2^0 \to \widetilde{\tau}_1\tau \to \widetilde{\chi}_1^0\tau\tau$. In the following, the application of the techniques developed in the aforementioned scenario to the GMSB6 model was studied. Slightly different kinematics (due to the massless gravitino) and additional background from other SUSY decays ($\widetilde{\ell}_R$, $\widetilde{\chi}_2^0$) are expected.

For the study of the kinematic end-point of the invariant mass of two τ leptons, larger data sets ($8\,\text{fb}^{-1}$) are considered and the final selection criteria of Sec. 7.2 are loosened to allow for a sufficient event statistics which is needed for the following measurement and the estimation technique for the SM contribution. The selection includes the standard preselection cuts and in addition the following requirements

$$N_\tau \geq 2 \qquad \text{and} \qquad \left(\frac{E_\text{T}^\text{miss}}{300\,\text{GeV}}\right)^2 + \left(\frac{p_\text{T}^\text{jet1}}{600\,\text{GeV}}\right)^2 > 1. \tag{7.5}$$

The number of events is shown in the (E_T^miss-p_T^jet1)-plane for the signal in Fig. 7.6(a) and for the background in Fig. 7.6(b). They illustrate an efficient background suppression while keeping a good signal fraction. With this relaxed final selection, $29.2 \pm 0.9\,(1169 \pm 5)$ signal events are expected for the GMSB6 scenario while the total number of expected background events is $6.1 \pm 2.3\ (244 \pm 14)$ for $\mathscr{L} = 200\,\text{pb}^{-1}\ (8\,\text{fb}^{-1})$.

For selected signal events, the distribution of the ditau invariant mass $m_{\tau\tau}$ at generator level is shown in Fig. 7.7(a). As expected from Eqs. (2.17)-(2.19) the distribution consists of three contributions: decays of the two lightest neutralinos and decays of either right-handed selectrons or smuons. The contributions from neutralino decays feature the typical triangular shape including the edge at the theoretically expected end-points (120.1 GeV, 253.3 GeV). The distribution from slepton decays has, however, no sharp triangular end-point due to the additional lepton arising in the decay which is not included in the mass calculation.

The corresponding $m_{\tau\tau}$ distributions at reconstruction level, calculated from the visible decay products of the τ pair, are shown in Fig. 7.7(b) assuming the correct combination of the final state τ leptons using MC information. Due to the unmeasured neutrinos in the τ decays the characteristic kinematic end-point of the $\widetilde{\chi}_1^0$ decays is lost and the direct extraction of the end-point is impeded. In addition, it can be seen that only a small fraction of the τ leptons

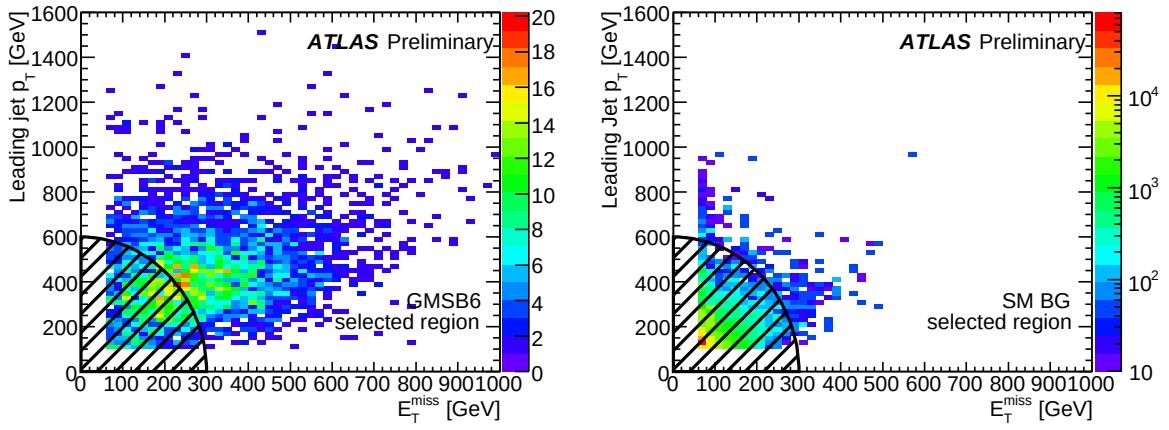

(a) (b)

Figure 7.6.: Distribution of events in the plane of $E_{\mathrm{T}}^{\mathrm{miss}}$ and p_{T} of the leading jet for (a) the signal and (b) the SM background for $8\,\mathrm{fb}^{-1}$. The elliptical cut is indicated by the hashed region. All events outside this region are selected.

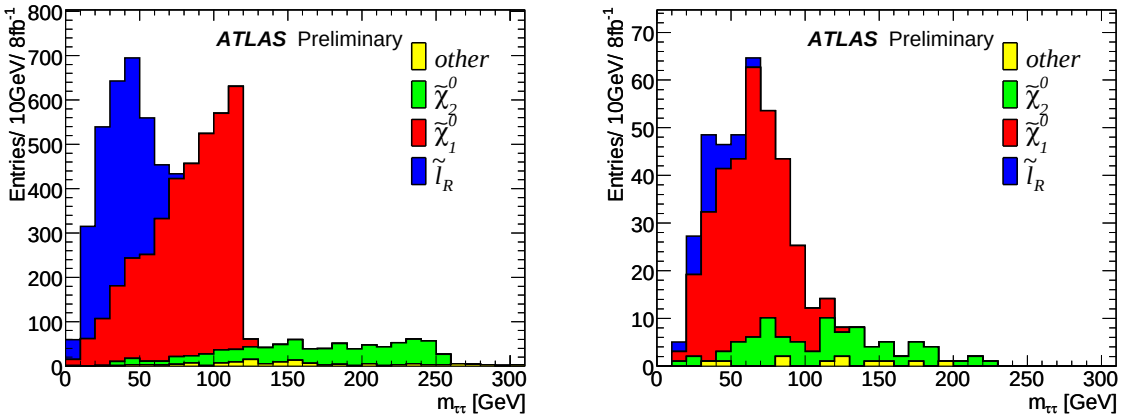

(a) (b)

Figure 7.7.: Invariant mass distribution of two τ candidates originating from different decay processes for the GMSB6 signal: (a) generator level, (b) reconstruction level for selected events.

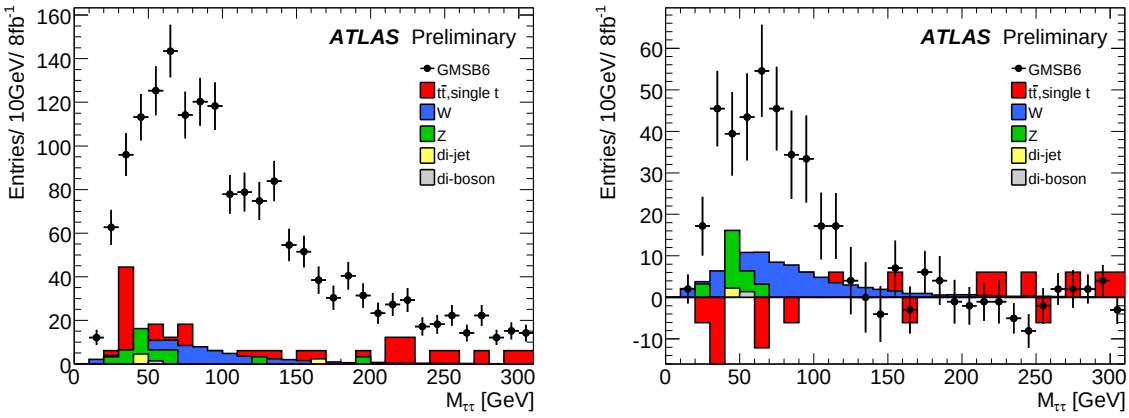

(a) (b)

Figure 7.8.: Invariant mass distribution of (a) any two τ candidates for the GMSB6 signal and the SM background after the selection and (b) the same-sign distribution (SS) subtracted from the opposite-sign distribution (OS) for $\mathscr{L} = 8\,\text{fb}^{-1}$.

from $\widetilde{\ell}_R$ decays are reconstructed. The reason is the additional lepton in the slepton decay. It is often located inside the τ reconstruction cone due to the small mass difference between $\widetilde{\tau}_1$ and the slepton (cf. Fig. 2.7). The additional lepton inside the cone leads to differences in the distributions of the individual variables used for the construction of the likelihood and consequently to a smaller acceptance. In addition, τ leptons from slepton decays yield smaller values of p_T leading to a further reduction of the reconstruction efficiency due to the $p_\text{T}^\tau > 15\,\text{GeV}$ ($p_\text{T}^{\tau 1} > 20\,\text{GeV}$)requirement.

In the real experiment, the correct combination and origin of the final state τ candidates is unknown and all possible combinations must be considered. The resulting invariant mass distribution is shown in Fig. 7.8(a) for the GMSB6 signal and the various SM background processes. It can be seen that the overall contribution from SM background is small. Here, different combinations of true and misidentified τ leptons are possible, although the main contribution comes from the combination of one true and one misidentified τ lepton, from W boson or $t\bar{t}$ production. Besides the contribution from misidentified τ leptons, the GMSB signal contains up to four τ leptons, leading to a large number of wrong combinations. The contribution of ditau pairs from wrong combinations can be corrected by a subtraction of the $m_{\tau\tau}$ distribution of two τ leptons with the same measured charge from the distribution with opposite charge (OS-SS), assuming that wrong ditau combinations contribute equally to the OS and SS distributions. The corresponding distributions are shown in Fig. 7.8(b) for the GMSB6 signal and the SM background processes.

Applying the procedure proposed for the clean SU3 scenario [186] the combined OS-SS distribution can be fitted using an appropriate function[7] to extract the inflection point of the distribution $M_{\tau\tau}^\text{IP}$ which can be directly translated into the kinematic end-point $m_{\tau\tau}^\text{max}$ using a linear calibration curve in [186]. The calibration curve was determined from fast

[7]The used function was optimized for the clean SU3 scenario and does not reflect the additional contribution ($\widetilde{\ell}_R$, $\widetilde{\chi}_2^0$) present in GMSB scenarios.

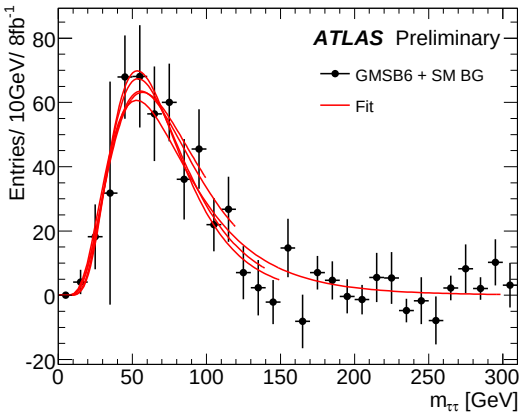

Figure 7.9.: Example fits of the invariant mass (OS-SS) distribution using different fit ranges.

simulation results of 14 similar scenarios with varying $\widetilde{\tau}_1$ and neutralino masses as $M_{\tau\tau}^{\mathrm{IP}} = (0.47 \pm 0.02) m_{\tau\tau}^{\mathrm{max}} + (15 \pm 2)\,\mathrm{GeV}$. The covariance between the slope and the intercept of the calibration function was determined to be -0.034 GeV.

Using this method for the GMSB6 scenario, an inflection point of $M_{\tau\tau}^{\mathrm{IP}} = (78.4 \pm 2.0)\,\mathrm{GeV}$ is obtained resulting in a kinematic end-point of $m_{\tau\tau}^{\mathrm{max}} = (135.0 \pm 4.3)$ GeV, where the error given specifies the uncertainty from the fit only. The determination of the kinematic end-point as detailed above is subject to several sources of systematic uncertainty:

- **Uncertainty from varying fit ranges:** The fits to the $m_{\tau\tau}$ spectrum are repeated using various fit ranges as detailed in Fig. 7.9: $\sigma^{\mathrm{fit\,range}} = ^{+10}_{-4}$ GeV.
- **Uncertainty from the initial calibration curve:** The calibration curve for the translation of the deflection point into an end-point measurement has an uncertainty. Taking into account the uncertainty and the correlations results in an additional systematic uncertainty of $\sigma^{\mathrm{calib}} = \pm 2.7\,\mathrm{GeV}$.
- **Uncertainty from τ polarization:** Parity violation in weak interactions in conjunction with momentum and angular momentum conservation leads to a correlation between the visible τ energy and the polarization of the τ. Hence, the ditau invariant mass distribution has a dependence on the τ polarization. Within the GMSB model the τ polarization is known for the different SUSY particles decaying into a τ. Nevertheless, the relative composition of different decays can change. A systematic uncertainty of $\sigma^{\mathrm{pol}} = \pm 7.0\,\mathrm{GeV}$ is assigned due to variations in the τ polarization [186].
- **Uncertainty from SM background contributions:** The OS-SS ditau invariant mass distribution is used to remove wrong ditau combinations from our sample. With this technique most of the SM background is removed. As can be seen in Fig. 7.8(b) the SM background is not zero on average and hence some residual dependence from the SM background on the measured kinematic end-point is expected. As mentioned above, the uncertainty on the background estimation is assumed to be around 20 %. For an estimation of the related uncertainty on the final result the background is multiplied by factors of 1.2 and 0.8 and the deviations of $m_{\tau\tau}^{\mathrm{max}}$ from the central result were determined.

In order to account for possible differences in the shape or normalization between OS and SS distributions, the background is varied separately for OS and SS: $\sigma^{\text{SM BG}} = ^{+1.9}_{-2.3}$ GeV.

Adding these systematic uncertainties and the statistical uncertainty resulting from the fit in quadrature, $m_{\tau\tau}{}^{\text{max}} = \left(135^{+13}_{-10}\right)$ GeV is obtained. A slight overestimation ($1.5\,\sigma$) of the reconstructed end-point compared to the expected value of 120 GeV can be observed. This overestimation is a result of the additional SUSY background contribution from $\widetilde{\chi}_2^0$ and $\widetilde{\ell}_R$ decays which are not taken into account in the fit function. Due to the small statistics available and the unknown underlying true distribution of each contribution a simultaneous fit of all contributions was found to be very challenging for $\mathscr{L} = 8\,\text{fb}^{-1}$. In a real measurement, other decay chains might be used to additionally constrain these contributions from other SUSY processes. Since the $\widetilde{\chi}_2^0$ background is mainly located at high values of $m_{\tau\tau}$ a slight bias of the method is expected. On the other hand the $\widetilde{\ell}_R$ background is located at low values of $m_{\tau\tau}$ which could partly compensate the effect from the $\widetilde{\chi}_2^0$ decays.

The impact of the additional SUSY background strongly depends on the unknown SUSY model realized in nature. For a more detailed study of this effect the $m_{\tau\tau}$ fit is repeated for the GMSB6 example scenario on truth-matched[8] τ candidates excluding or doubling those from the $\widetilde{\chi}_2^0$ or $\widetilde{\ell}_R$ decays. A shift of the final result of ± 13 GeV can be observed. This range gives an indication of the additional systematic uncertainty resulting from additional SUSY background which must be taken into account. In addition, samples of fast simulations at various points in the GMSB parameter space are studied and in general a much smaller bias towards larger values is found (always within $1\,\sigma$).

Including the contribution from SUSY background as an additional systematic uncertainty results in:

$$m_{\tau\tau}^{\text{max}} = \left(\,135 \pm 4\,(\text{stat.})\,^{+13}_{-9}\,(\text{sys.}) \pm 13\,(\text{SUSY model})\,\right)\ \text{GeV}\,. \tag{7.6}$$

The results obtained in this chapter demonstrate that a measurement of the end-point of the invariant ditau mass spectrum might be possible in the GMSB6 example scenario with a small bias from additional SUSY background. The determined value could be used to constrain the space of the underlying parameters of the GMSB model, maybe in combination with other experimental results in a global fit of the GMSB model.

[8] A reconstructed τ candidate is called truth-matched if a τ lepton at generator level is found in a cone of $\Delta R < 0.1$ around the candidate.

8. Search for New Physics with Large Transverse Momentum, Jets, and at least Two τ Leptons

In the following, a search for new physics with large $E_{\mathrm{T}}^{\mathrm{miss}}$, jets, and at least two τ leptons using $2.05\,\mathrm{fb}^{-1}$ of LHC pp collision data at a center-of-mass energy of 7 TeV recorded with the ATLAS detector is presented. After briefly revisiting the event phenomenology, the resulting event selection is presented based on the objects previously defined in Ch. 6. Semi data-driven methods are used to predict the expectation of the most important SM backgrounds in the signal region. Before presenting the results and their interpretation within GMSB models in Ch. 9, the contributing systematic uncertainties are discussed.

The results have been published by the ATLAS Collaboration in [2] and [189]. The presentation of the analysis leading to these results partially follows the more detailed description in [3].

8.1. Event Phenomenology

The general event phenomenology of GMSB events using pp collisions is described in Sec. 2.3.3 and is very similar to the one for a center-of-mass of 10 TeV (cf. Ch. 7). Since the GMSB parameter settings are the same, only the cross section and the kinematics change due to the lower center-of-mass energy but the branching ratios are identical leading to the same final states. However, those are less boosted.

For the GMSB4030 benchmark point (cf. Sec. 2.3.3), the NLO cross section at $\sqrt{s} = 7\,\mathrm{TeV}$ is 0.45 pb, approximately three times smaller than the LO cross section for $\sqrt{s} = 10\,\mathrm{TeV}$. For the Λ-tanβ-plane, the NLO cross section is shown in Fig. 8.1. The general behavior is again a steep decrease with Λ due to the increasing sparticle masses (cf. also Fig. 7.4(a)). The event selection has been optimized for the respective parameter region where events contain many τ candidates in addition to high-energy jets and large $E_{\mathrm{T}}^{\mathrm{miss}}$.

Figure 8.2(a) shows the average number of generated hadronically decaying τ leptons per event. In the stau region, often more than three τ leptons are expected per event. About half of these are reconstructed and identified as loose τ candidates, as can be seen from Fig. 8.2(b). This loss is caused by, e.g. the minimum $p_{\mathrm{T}}^{\tau} > 20\,\mathrm{GeV}$ requirement often exceeding that of the τ candidates.

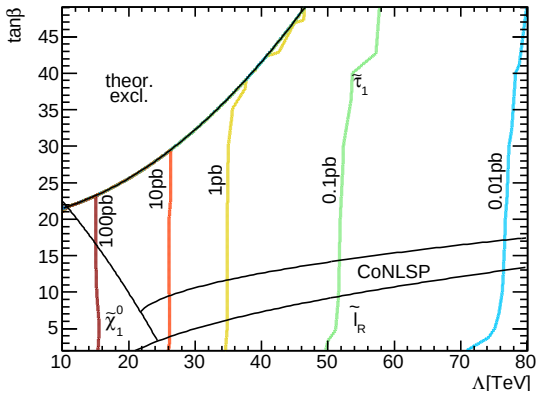

Figure 8.1.: Total GMSB NLO cross section in pb at $\sqrt{s} = 7\,\text{TeV}$ in the Λ-tanβ-plane for $M_{\text{mess}} = 250\,\text{TeV}$, $N_5 = 3$, $\text{sgn}\,\mu = +$, and $C_{\text{grav}} = 1$.

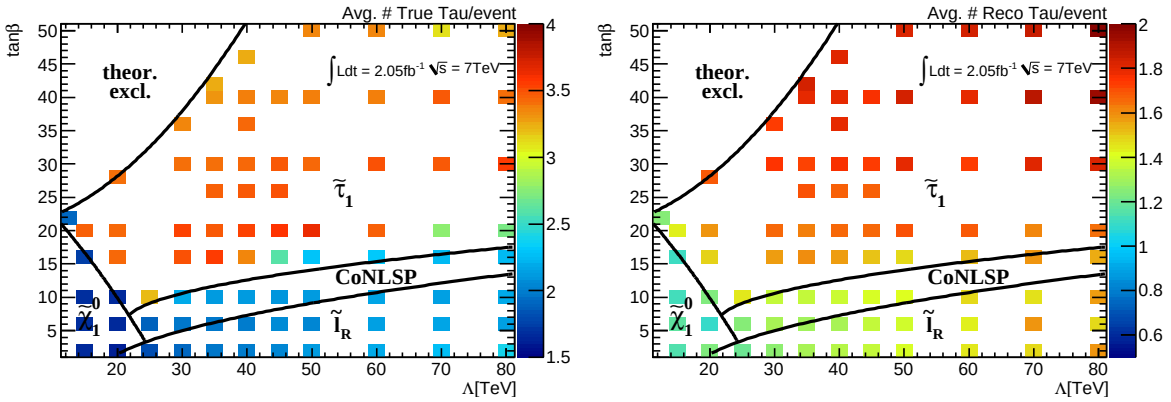

(a) (b)

Figure 8.2.: (a) Average number of generated hadronically decaying τ candidates and (b) average number of reconstructed loose τ candidates per event in the Λ-tanβ-plane for $M_{\text{mess}} = 250\,\text{TeV}$, $N_5 = 3$, $\text{sgn}\,\mu = +$, and $C_{\text{grav}} = 1$.

8.2. Preselection

A dedicated event selection is crucial for the impact of a search for supersymmetric events. The selection cuts have been chosen carefully to allow for a maximal background suppression as well as a reasonable signal selection efficiency. In the following, the event selection is presented. It is similar to the one employed in the analysis requiring the presence of at least one τ candidate [190].

8.2.1. Trigger

This analysis relies on a trigger that is based on one high-p_{T} jet and a significant amount of $E_{\text{T}}^{\text{miss}}$. For data period B, the trigger used is *EF_j75_a4_EFFS_xe45_loose_noMu*. Starting with period D, the corresponding trigger is *EF_j75_a4tc_EFFS_xe45_loose_noMu*. In the former

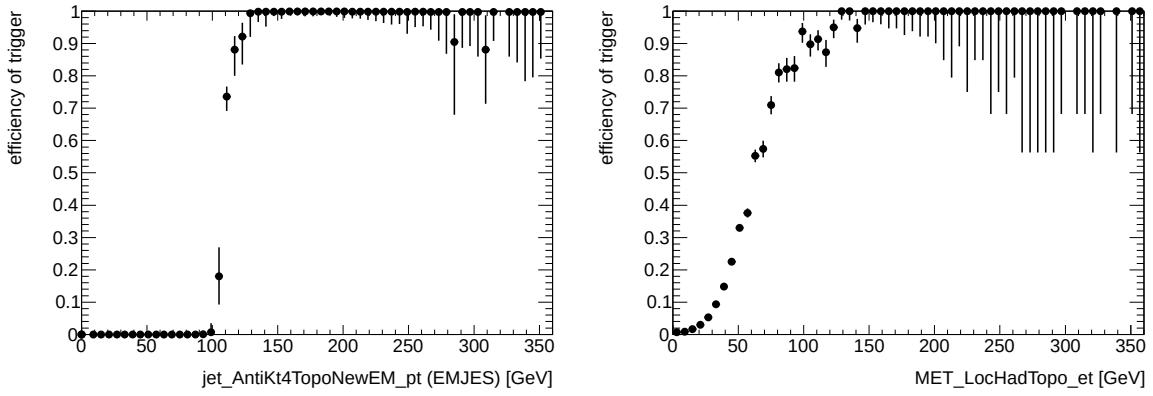

(a) (b)

Figure 8.3.: *EF_j75_a4tc_EFFS_xe45_loose_noMu* trigger efficiencies using data from period D [195]: (a) projection on the jet p_{T} axis after requiring $E_{\mathrm{T}}^{\mathrm{miss}} > 130\,\mathrm{GeV}$ and (b) on the $E_{\mathrm{T}}^{\mathrm{miss}}$ axis after requiring $p_{\mathrm{T}}^{\mathrm{jet1}} > 130\,\mathrm{GeV}$.

case, the trigger decision concerning the jet was based on trigger towers, while in the latter the jet is built from topological clusters (cf. Sec. 6.1) instead. This change introduced a higher robustness against pile-up. These triggers were the lowest-threshold unprescaled trigger available of this type.

The trigger behavior is not well reproduced in simulated events. Therefore, a kinematic selection according to the trigger objects is applied instead, i.e. tighter cuts on $E_{\mathrm{T}}^{\mathrm{miss}}$ and on $p_{\mathrm{T}}^{\mathrm{jet1}}$ with respect to the trigger threshold are set to achieve a trigger efficiency of almost unity. Only in real collision data, the triggers were used for the event selection. This procedure has been executed in all other SUSY analyses in ATLAS using these triggers, namely the analyses relying on different jet multiplicities and $E_{\mathrm{T}}^{\mathrm{miss}}$ and no leptons [191, 192] and on b-jets [193, 194].

The trigger performance has been studied in detail in [195]. The efficiency has been determined using a bootstrap method on a sample triggered by looser single jet triggers, *EF_j75_a4_EFFS* and *EF_j75_a4tc_EFFS*, respectively. Corrections for the correlation between the two triggers and the efficiency of the looser trigger have been taken into account. It has been found that applying cuts of $p_{\mathrm{T}}^{\mathrm{jet1}} > 130\,\mathrm{GeV}$ and $E_{\mathrm{T}}^{\mathrm{miss}} > 130\,\mathrm{GeV}$ leads to a trigger efficiency of almost 100 %. The trigger efficiencies as a projection in the plateau region of the other offline cut variable are shown in Fig. 8.3 justifying the respective offline cut.

This trigger was originally designed for a search of SUSY with jets and $E_{\mathrm{T}}^{\mathrm{miss}}$. It has been chosen mainly for simplicity reasons and due to a lack of sufficient understanding of the τ triggers in the early 2011 data taking period. Since the studied events contain τ leptons in addition, alternative triggers for the data taking period following the technical stop in August 2011 have been studied that might offer a better performance.

Trigger	Kinematic selection
EF_j75_xe45_loose_noMu	$p_{\mathrm{T}}^{\mathrm{jet1}}$ >130 GeV, $E_{\mathrm{T}}^{\mathrm{miss}}$ >130 GeV
EF_j80_xe60_loose_noMu	$p_{\mathrm{T}}^{\mathrm{jet1}}$ >135 GeV, $E_{\mathrm{T}}^{\mathrm{miss}}$ >140 GeV
EF_j75_j45_xe55_loose_noMu	$p_{\mathrm{T}}^{\mathrm{jet1}}$ >130 GeV, $p_{\mathrm{T}}^{\mathrm{jet2}}$ >100 GeV $E_{\mathrm{T}}^{\mathrm{miss}}$ >135 GeV
EF_xe70_loose_noMu	$E_{\mathrm{T}}^{\mathrm{miss}}$ >150 GeV
EF_xe70_tight	$E_{\mathrm{T}}^{\mathrm{miss}}$ >180 GeV
EF_2tau16_loose_xe55_loose_noMu	$p_{\mathrm{T}}^{\tau 1}$ >30 GeV, $E_{\mathrm{T}}^{\mathrm{miss}}$ >135 GeV
EF_tau29T_medium1_tau20T_medium1	$p_{\mathrm{T}}^{\tau 1}$ >40 GeV, $p_{\mathrm{T}}^{\tau 2}$ >35 GeV
EF_tau29T_medium_xe35_noMu_3L1J10	$p_{\mathrm{T}}^{\tau 1}$ >40 GeV, $E_{\mathrm{T}}^{\mathrm{miss}}$ >100 GeV, N_{jet} ≥2
EF_tau29T_medium_xe75_noMu	$p_{\mathrm{T}}^{\tau 1}$ >40 GeV, $E_{\mathrm{T}}^{\mathrm{miss}}$ >150 GeV

Table 8.1.: Tested trigger items for the trigger menu used for the data taking period that started in September 2011.

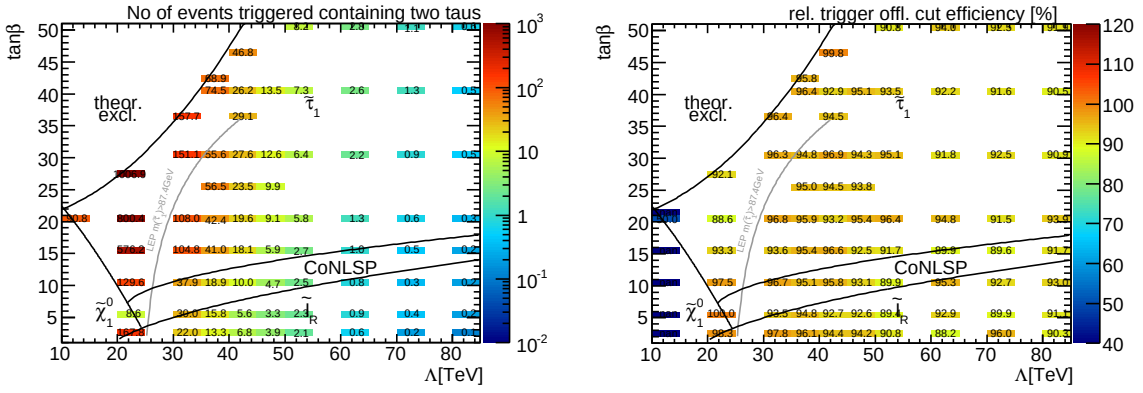

(a) (b)

Figure 8.4.: (a) Number of events that are selected via the current trigger offline cuts of the current trigger *EF_j75_xe45_loose_noMu* containing two reconstructed τ candidates and (b) relative trigger efficiency of the new *EF_j80_xe60_loose_noMu* trigger with respect to the current one.

Potential Future Triggers

To estimate the relative selection efficiency of different triggers in comparison to the trigger used here, the corresponding kinematic selection cuts have been tested. Table 8.1 lists all the triggers considered including their corresponding kinematic selection. These are the lowest-threshold, unprescaled jet and $E_{\mathrm{T}}^{\mathrm{miss}}$ triggers, single $E_{\mathrm{T}}^{\mathrm{miss}}$ triggers, ditau triggers, and τ and $E_{\mathrm{T}}^{\mathrm{miss}}$ triggers being available for the entire 2011 data taking period. Since the trigger performance of these triggers has not been estimated yet, the kinematic selection has been assessed either from the current lower threshold triggers or from the corresponding single τ trigger efficiencies shown in Fig. C.1.

Figure 8.4(a) shows the number of events that are selected by the employed trigger via the respective trigger offline cuts in the Λ-tanβ-plane and also contain two τ candidates. This

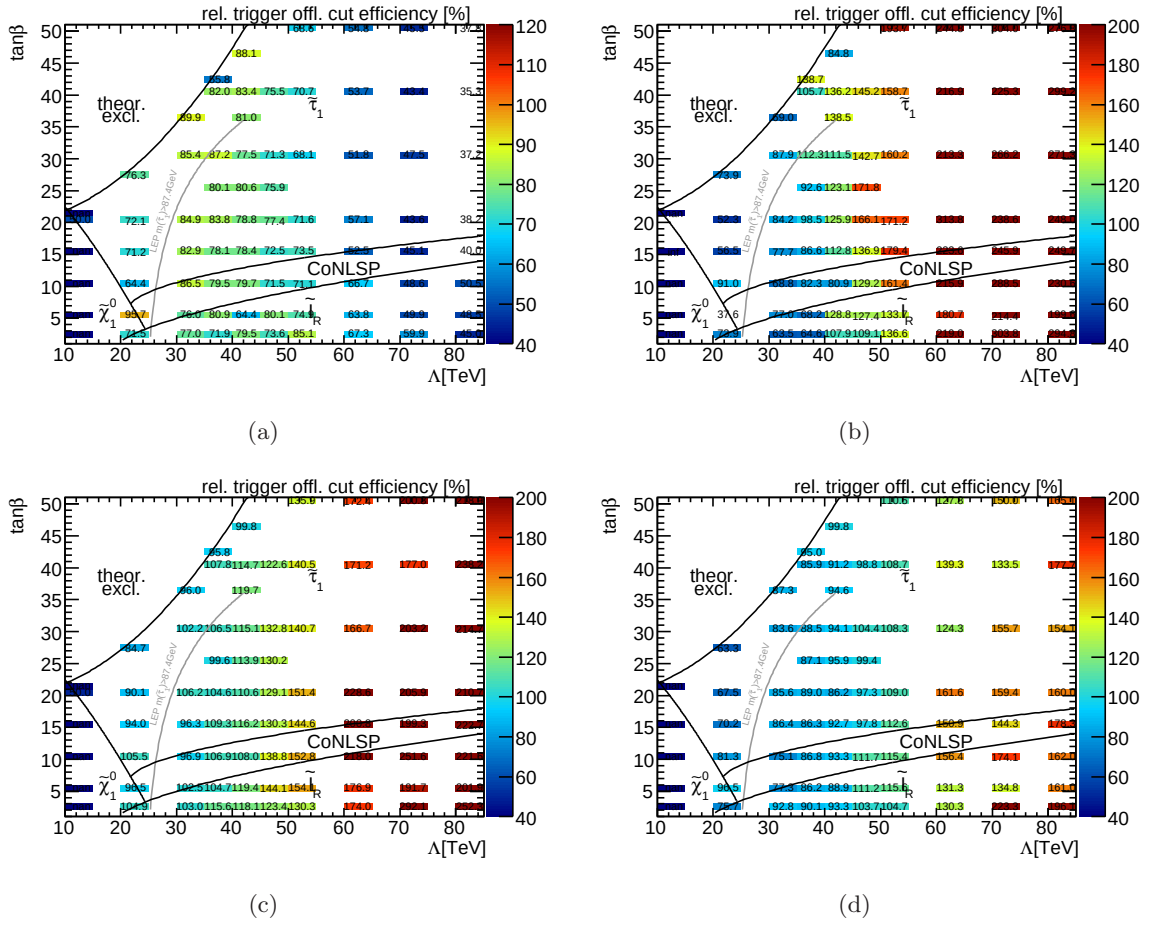

Figure 8.5.: Relative trigger efficiency tested via their corresponding offline cuts with respect to the efficiency of the current trigger *EF_j75_xe45_loose_noMu* containing two reconstructed τ candidates for (a) the new 2jet+$E_{\mathrm{T}}^{\mathrm{miss}}$ trigger (*EF_j75_j45_xe55_loose_noMu*), (b) the two τ trigger (*EF_tau29T_medium1_tau20T_medium1*) (c) a high $E_{\mathrm{T}}^{\mathrm{miss}}$ trigger (*EF_xe70_loose_noMu*), and (d) the corresponding tight high $E_{\mathrm{T}}^{\mathrm{miss}}$ trigger (*EF_xe70_tight*).

additional selection cut of two τ candidates was chosen to allow for a more unambiguous comparison with the τ triggers. The drop in the number of events due to the decreasing cross section with increasing Λ is clearly visible. Figure 8.4(b) shows the efficiency for the new lowest unprescaled jet and $E_{\mathrm{T}}^{\mathrm{miss}}$ trigger. As expected, the efficiency drops homogeneously and a rather flat efficiency across the plane between 90 % and 100 % can be observed.

Instead of increasing the leading jet energy and the $E_{\mathrm{T}}^{\mathrm{miss}}$ threshold a second jet can be added to the current trigger requirements. The corresponding efficiency can be seen in Fig. 8.5(a) offering a much worse performance than simply increasing the two thresholds. Especially in the higher Λ region, a decrease to 50% can be noted. On the other hand, a ditau trigger might be a valid alternative. As can be seen in Fig. 8.5(b), in the higher Λ regions the efficiency far exceeds that from the current trigger for events containing two reconstructed τ candidates. However, here no minimal leading jet p_{T} or $E_{\mathrm{T}}^{\mathrm{miss}}$ has been required. These cuts will have to be chosen according to the specific analysis and will lower the overall efficiency. The same

behavior can be observed for the single $E_{\mathrm{T}}^{\mathrm{miss}}$ trigger offering a superior performance with the respect to the current trigger, as shown in Figs. 8.5(c) and 8.5(d). Here again, the requirement of two reconstructed τ candidate has been applied.

A dedicated and more detailed trigger study will be needed for the analysis of the full 2011 data set to fully exploit the potential of the available triggers. Detailed numbers on the trigger selection efficiencies for the different triggers can be found in the Appendix in Tab. C.8.

8.2.2. Event Cleaning

GRL

To ensure a sufficient quality of the final, analyzed data sample, a good-runs-list (GRL) selection is applied. This list contains all runs and their corresponding luminosity blocks (LB) that are considered of ample good conditions. A run usually coincides with one fill of the LHC. One LB is 60 s or 120 s long in which the luminosity conditions are considered to be stable. To determine if a LB fulfills the conditions to be defined as good quality, the status of each detector subsystem is checked, i.e. the GRL criteria require that all ATLAS subdetectors are operating at optimal voltages and that the solenoid and toroid are at full field strength. The detectors and magnet system reached an efficiency of approximately 99 % during stable beams. The main reasons for inefficiencies in the LAr calorimeter came from high-voltage trips and occasional noise bursts.

The GRL criteria depend on the requirement of the various physics analysis and the objects needed to perform it. Since searches for new physics are often complex and rely on the combination of many physics objects and $E_{\mathrm{T}}^{\mathrm{miss}}$, all subdetectors need to be working perfectly to ensure that the distributions of all reconstructed objects do not deviate significantly from expectations. In particular, the following analysis relies on τ leptons, jets, and $E_{\mathrm{T}}^{\mathrm{miss}}$. The GRL criteria are common to all other $E_{\mathrm{T}}^{\mathrm{miss}}$-based analyses in the SUSY group [196]. After their application, the amount of data is reduced by approximately 18 % and the total integrated luminosity available for analysis is $2.05\,\mathrm{fb}^{-1}$, with an uncertainty on the luminosity estimated to be 3.7% [197]. There is no equivalent to GRL criteria for simulated events.

Primary Vertex

The hard-interaction primary vertex is defined as the vertex with the highest scalar sum of the transverse momenta of the individual tracks. The presence of at least one reconstructed primary vertex is required in each event having at least five associated tracks. Mainly non-collision background is rejected by this requirement.

Temporarily dead front-end boards

During several weeks of the early data taking period of 2011, some modules in the electromagnetic calorimeter were dysfunctional due to a broken fuse on the controller board. This led to energy deposited in the range of $-0.1 < \eta < 1.5$ and $-0.9 < \phi < -0.5$ not being measured. Depending on the analysis, different treatment strategies have been developed. For

	Looser	Loose
		Looser or
HEC Spikes	$f_{\mathrm{HEC}} > 0.5$ & $\lvert Q_{\mathrm{HEC}}\rvert > 0.5$ & mean $Q_{\mathrm{LAr}} > 0.8$ or $\lvert\text{neg. } E\rvert > 60\,\mathrm{GeV}$	$f_{\mathrm{HEC}} > 0.5$ & $\lvert Q_{\mathrm{HEC}}\rvert > 0.5$
EM coherent noise	$f_{\mathrm{EM}} > 0.95$ & $\lvert Q_{\mathrm{LAr}}\rvert > 0.8$ & mean $Q_{\mathrm{LAr}} > 0.8$ & $\lvert\eta\rvert < 2.8$	$f_{\mathrm{EM}} > 0.95$ & $\lvert Q_{\mathrm{LAr}}\rvert > 0.8$ & $\lvert\eta\rvert < 2.8$
Non-collision bkg & cosmics	$f_{\mathrm{EM}} < 0.05$ & $f_{\mathrm{charge}} < 0.05$ & $\lvert\eta\rvert < 2$ or $f_{\mathrm{EM}} < 0.05$ & $\lvert\eta\rvert \geq 2$ or $F_{\mathrm{max}} > 0.99$ & $\lvert\eta\rvert < 2$	$\lvert t\rvert > 25\,\mathrm{ns}$

Table 8.2.: Loose and very loose criteria for the rejection of events containing badly reconstructed jets [198].

this analysis, the "simple" veto has been used [167, 198]. Any event in which the direction of at least one of the two selected, leading jets points into the critical region is rejected, where the critical region includes the temporary dead front-end boards and the nearby dead tile module. The transverse momentum of jets pointing towards the dead front-end boards is calculated as follows

$$p_{\mathrm{T}}^{\mathrm{corr}} \equiv p_{\mathrm{T}} \frac{1 - B_{ch,corr,jet}}{1 - B_{ch,corr,cell}}, \tag{8.1}$$

where $B_{ch,corr,jet}$ is the fraction of the jet energy coming from a jet level correction using jet shape from MC computed for all dead cells after the jet reconstruction and $B_{ch,corr,cell}$ is the fraction of the jet energy coming from a cell level correction using neighboring cells assuming the same energy density used for the dead tile module and applied at the cell level before jet and $E_{\mathrm{T}}^{\mathrm{miss}}$ reconstruction. This correction accounts for the expected energy mismeasurement in the dead front-end boards region and induces the discarding of events where a significant energy mismeasurement is to be expected. The corrected transverse momentum of jets pointing towards the dead front-end boards needs to exceed at least 30 GeV to cause the event to be rejected.

In addition, a veto on reconstructed τ candidates pointing towards the LAr hole region is applied removing them from the event. The size of the critical region is slightly increased in both η and ϕ by 0.05 in each direction to account for the fact that the calorimeter-seeded τ candidate position may be outwardly biased for candidates near the edge of the veto region. Since this veto is applied before the overlap removal, the corresponding reconstructed jet remains in the event and the event might still be rejected in case the corrected transverse momentum of the jet exceeds the threshold of 30 GeV.

Jet cleaning

Detector noise and calorimeter malfunction might cause the reconstruction of jets not originating from genuine physics processes. These jets are considered disruptive to the event structure and any event containing such a jet (according to the *loose* criterion) is discarded. The detailed criteria according to which such a jet is defined are listed in Tab. 8.2. f_{EM} is the fraction

of jet energy reconstructed in the electromagnetic calorimeter; f_{HEC} is the fraction of energy in the hadronic end cap (HEC); Q_{LAr} and Q_{HEC} are jet-quality variables based on LAr and HEC pulse shapes, whereas the normalization of $|Q| = 0(1)$ has been chosen to correspond to high (low) quality jets; $|\mathrm{neg.}\, E|$ is the sum of the negative cell energies within a jet; t denotes the measured jet time and F_{max} is the maximum energy fraction in one calorimeter layer; and f_{charge} is the ratio of the sum of the track p_{T} associated to the jet to the E_{T} measured in the calorimeter. These criteria are also implemented in the SUSYTools package [167] while further details can be found in [198]. About 2 % of data compared to the previous selection step are rejected by this veto.

8.3. Optimization of the Event Selection

Following the preselection including the trigger offline cuts and the event cleaning described in the previous section, the main objective of the event selection is to maximize the signal to background ratio by mainly rejecting events containing misidentified τ candidates and mismeasured $E_{\mathrm{T}}^{\mathrm{miss}}$. Since the analysis has been carried out as a blind analysis[1], the optimization of the event selection has been done with simulated events only.

The left column of Fig. 8.6 shows the number of jets and the two leading jet p_{T} distributions after the preselection. As can be seen the GMSB signal tends to have a higher jet multiplicity featuring higher energetic jets. Therefore, a second jet with a $p_{\mathrm{T}} > 30\,\mathrm{GeV}$ is required. These cuts are indicated in Fig. 8.6 via a black line. The right column of Fig. 8.6 shows the number of reconstructed loose τ candidates and the two leading τ p_{T} distributions after the preselection. In addition, a light lepton veto, i.e. electrons and muons, is introduced to allow for an easy combination of this channel with others. Two τ candidates with $p_{\mathrm{T}}^{\tau} > 20\,\mathrm{GeV}$ are required rejecting almost all QCD and diboson as well as the complete Drell-Yan background.

Another effective way to reject QCD dijet background is to require a minimum distance between the leading jets of the event and $E_{\mathrm{T}}^{\mathrm{miss}}$. In QCD events, $E_{\mathrm{T}}^{\mathrm{miss}}$ and the leading jets are often aligned suggesting that the p_{T} of the jet was mismeasured, artificially creating $E_{\mathrm{T}}^{\mathrm{miss}}$. Hence, the $\Delta\phi$ between the two leading jets and $E_{\mathrm{T}}^{\mathrm{miss}}$ is required to exceed 0.4 radians. This is illustrated in Fig. 8.7.

The final selection cuts, illustrated in Fig. 8.8, further maximize the signal to background ratio by exploiting the GMSB feature of high energetic jets and τ leptons as well as high $E_{\mathrm{T}}^{\mathrm{miss}}$. These are combined in the effective mass

$$m_{\mathrm{eff}} = E_{\mathrm{T}}^{\mathrm{miss}} + p_{\mathrm{T}}^{\mathrm{jet1}} + p_{\mathrm{T}}^{\mathrm{jet2}} + \sum_{all\,\tau} p_{\mathrm{T}}^{\tau}, \tag{8.2}$$

and the transverse mass of a τ_i candidate

$$m_{\mathrm{Ti}} = \sqrt{2 p_{\mathrm{T}}^{\tau_i} E_{\mathrm{T}}^{\mathrm{miss}} (1 - \cos(\Delta\phi(\tau_i, p_{\mathrm{T}}^{\mathrm{miss}})))}. \tag{8.3}$$

[1] In this case, blind analysis is referring to the procedure of determining the event selection on simulated events only and estimating the SM background expectation from the control regions before the number of real collision data events in the signal region is determined to ensure an event selection unbiased by the real collision data distributions.

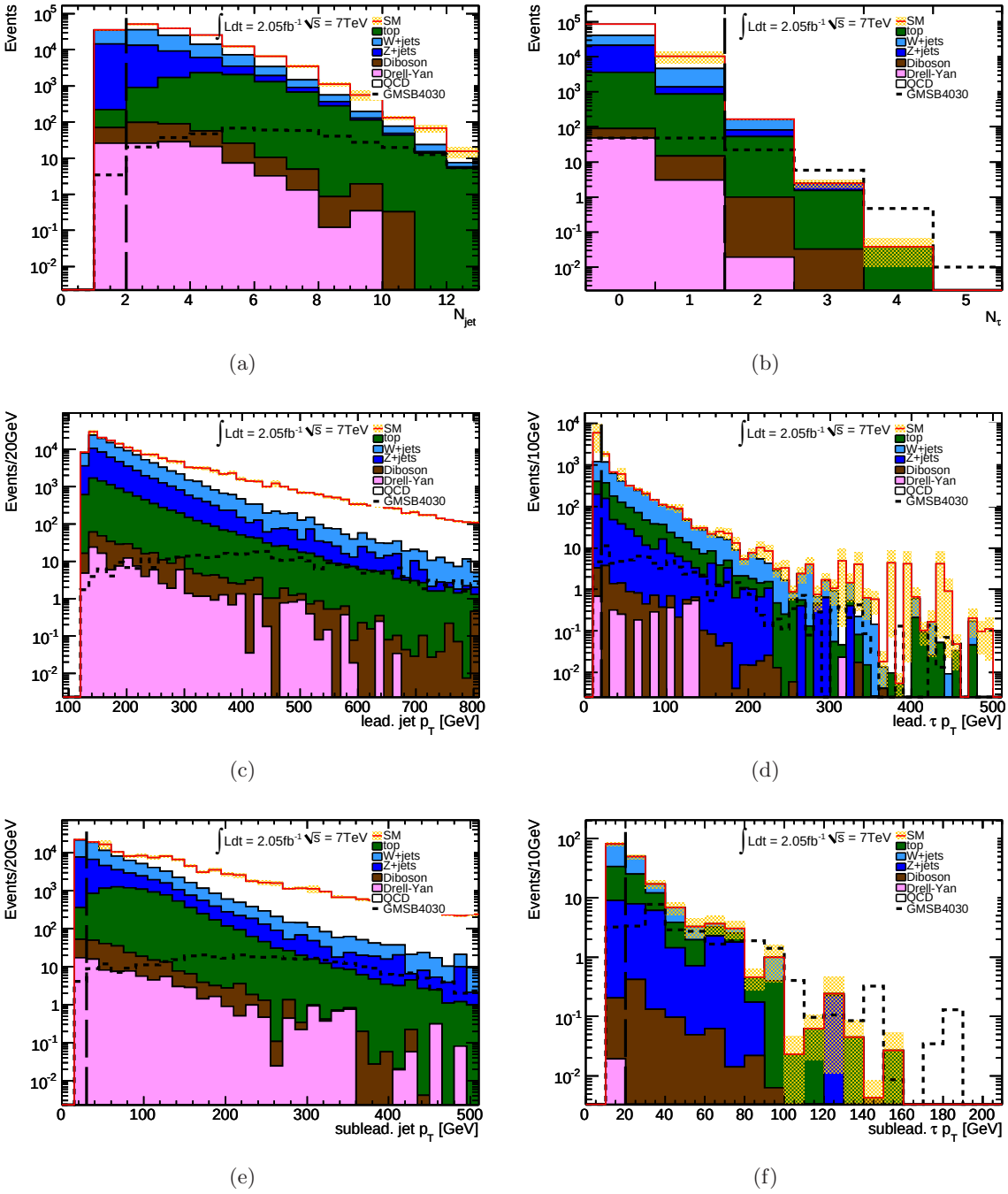

(a) (b)

(c) (d)

(e) (f)

Figure 8.6.: (a) Number of jets after the trigger offline requirement, (b) number of reconstructed τ candidates after the light lepton veto, and p_{T} of (c) the leading jet, (d) the leading τ, (e) the subleading jet, and (f) the subleading τ. The dashed black lines indicate the cut values on the respective variable. The yellow band shows the statistical error of the SM background MC distribution.

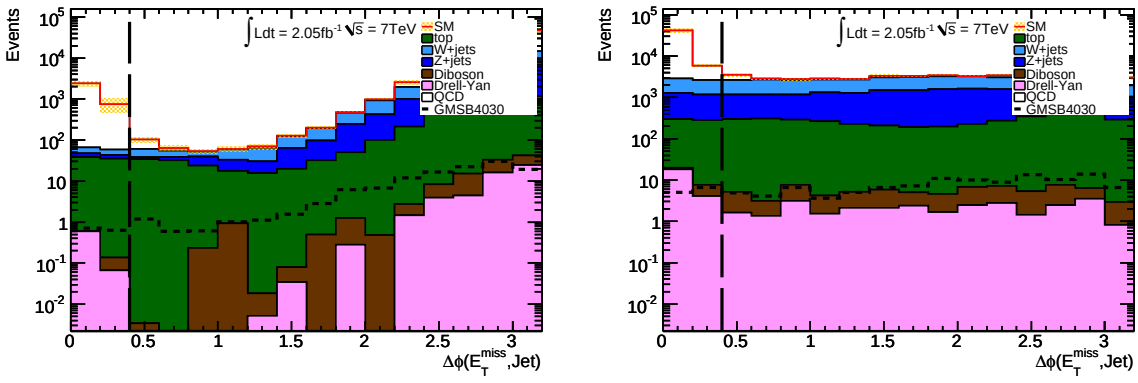

(a) (b)

Figure 8.7.: $\Delta\phi$ between $E_{\mathrm{T}}^{\mathrm{miss}}$ and the two leading jets. The cut on this variable, indicated by the black line, mainly reduces QCD background. The yellow band shows the statistical error of the SM background MC distribution.

The signal region is defined by $m_{\mathrm{eff}} > 700\,\mathrm{GeV}$ and $m_{\mathrm{T1}} + m_{\mathrm{T2}} > 80\,\mathrm{GeV}$. The exact value for the m_{eff} cut has been determined via a scan of the Asimov significance z_{A} [199], taking into account the number of signal (background) events N_S (N_{BG}), for various GMSB benchmark points

$$z_{\mathrm{A}} \equiv \sqrt{2\left[(N_S + N_{BG})\log\left(1 + \frac{N_S}{N_{BG}}\right) - N_S\right]}, \tag{8.4}$$

aiming for a reasonably high signal efficiency across the grid, especially in the area where the limit is expected (also cf. Fig. 8.13(d)). The transverse mass describes the alignment of $E_{\mathrm{T}}^{\mathrm{miss}}$ and the direction of the τ. In SM events with real τ decays, such as $Z \to \tau\tau$, the $E_{\mathrm{T}}^{\mathrm{miss}}$ is

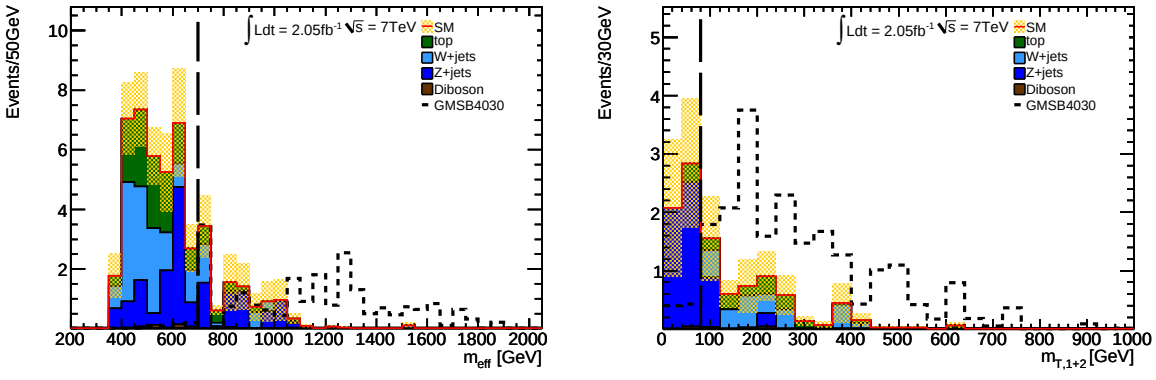

(a) (b)

Figure 8.8.: (a) m_{eff} distribution after requiring two τ candidates per event and the $\Delta\phi$ requirement. (b) $m_{\mathrm{T1}} + m_{\mathrm{T2}}$ distribution after $m_{\mathrm{eff}} > 700\,\mathrm{GeV}$. The two cuts indicated by the black line define the final selection cuts. The yellow band shows the statistical error of the SM background MC distribution.

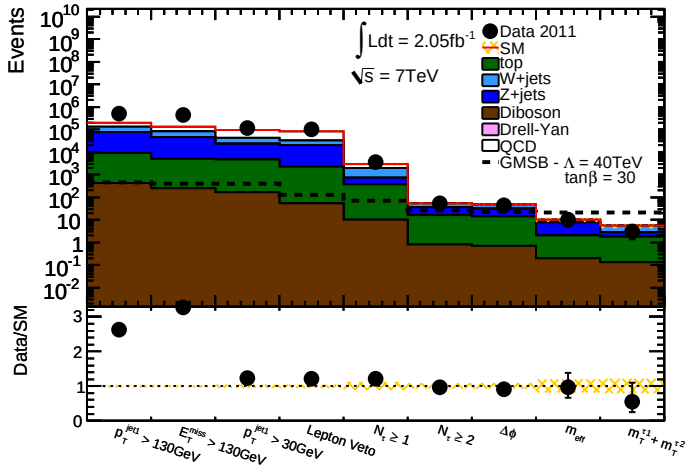

Figure 8.9.: Cutflow for the event selection in the ditau channel. The top and W+jets background has been scaled according to the scaling factor obtained in Sec. 8.6.

aligned to the τ decay products since the neutrinos are causing the $E_{\mathrm{T}}^{\mathrm{miss}}$. However, in SUSY events the $E_{\mathrm{T}}^{\mathrm{miss}}$ is caused by different particles, generating much higher values of m_{T}^{τ} as can be seen in Fig. 8.8(b).

The number of events for each individual background process and the GMSB benchmark point after each individual cut step are summarized in Tab. 8.3. For the final selection, the expectation for the GMSB4030 benchmark point and the sum of the SM backgrounds are 20.8 ± 3.4 and 5.4 ± 1.1 events, respectively. The cutflow is shown in Fig. 8.9. Since no trigger requirement has been applied to simulated events, the first two cuts included are the kinematic selection cuts according to the trigger. It can be seen that requiring a second jet with $p_{\mathrm{T}}^{\mathrm{jet2}} > 30\,\mathrm{GeV}$ reduces the disagreement between data and MC greatly. The scaling factors obtained from data driven techniques describes in Sec. 8.6 have been applied explaining why the agreement is best after the requirement of two τ candidates.

Figure 8.10 shows comparison of the kinematic distributions of jets and τ candidates as well as the $E_{\mathrm{T}}^{\mathrm{miss}}$ distribution after the light lepton veto and before the τ requirements are applied for real collision data and simulated events. All distributions show a good agreement between data and the simulated events within the statistical uncertainties. Further comparisons of data and MC in the signal region and the resulting conclusions are detailed in Ch. 9. These figures have been obtained after the determination of the scaling factors (cf. Sec. 8.6) and the official unblinding of the analysis.

As a cross check, it has been tested if the event selection introduces a preference for a certain number of vertices. Figure 8.11(a) shows the number of vertices after the trigger offline cuts while requiring one τ candidates. No specific scaling has been applied which explains the slight overestimation of the data by MC. Nonetheless, the distribution is very compatible with the pile-up conditions (cf. Sec. 5.2.3) and does not show a precedence for a certain number of vertices per event. Similar findings have been made for several other stages of the event selection also shown in Fig. 8.11. All distributions are found to be in good agreement showing no particular bias.

	GMSB4030	QCD	top	W	Z	DY	DiBoson	$\sum$ SM
Preselection	692 ± 13	$(4.47 \pm 0.0039) \cdot 10^9$	390000 ± 310	$(6.21 \pm 0.0025) \cdot 10^7$	$(8.24 \pm 0.0032) \cdot 10^6$	$(1.82 \pm 0.0017) \cdot 10^7$	19394 ± 55	$(4.56 \pm 0.0039) \cdot 10^9$
$E_{\mathrm{T}}^{\mathrm{miss}} > 130\,\mathrm{GeV}$	461 ± 11	60000 ± 5900	17820 ± 33	116000 ± 690	65430 ± 490	181 ± 10	437.1 ± 8.4	260000 ± 6000
$p_{\mathrm{T}}^{\mathrm{jet1}} > 130\,\mathrm{GeV}$	406.6 ± 9.5	53500 ± 4300	9229 ± 25	71830 ± 560	40020 ± 380	117.3 ± 8.4	241.3 ± 6.6	175000 ± 4300
$p_{\mathrm{T}}^{\mathrm{jet2}} > 30\,\mathrm{GeV}$	399.0 ± 9.4	51700 ± 4300	8776 ± 24	38130 ± 240	18550 ± 260	70.2 ± 5.1	162.9 ± 5.8	117000 ± 4300
LeptonVeto	123.6 ± 6.4	49900 ± 4200	4416 ± 18	23340 ± 200	18050 ± 260	51.7 ± 4.4	53.5 ± 3.7	95800 ± 4300
$N_\tau \geq 1$	71.6 ± 5.7	470 ± 160	695.2 ± 6.3	2525 ± 51	353 ± 25	2.41 ± 0.81	10.0 ± 1.0	4060 ± 170
$N_\tau \geq 2$	25.0 ± 3.5	0.03 ± 0.01	14.83 ± 0.60	17.7 ± 2.2	19.9 ± 3.4	0.00 ± 0.00	0.81 ± 0.14	53.3 ± 4.0
$\Delta\phi(E_{\mathrm{T}}^{\mathrm{miss}}, jet1, 2) > 0.4$	22.2 ± 3.4	0.00 ± 0.00	13.40 ± 0.58	16.5 ± 2.1	16.4 ± 3.0	0.00 ± 0.00	0.68 ± 0.13	47.0 ± 3.7
$m_{\mathrm{eff}} > 700\,\mathrm{GeV}$	21.7 ± 3.4	0.00 ± 0.00	1.90 ± 0.23	2.55 ± 0.81	5.6 ± 1.8	0.00 ± 0.00	0.19 ± 0.06	10.3 ± 2.0
$m_{\mathrm{T1}} + m_{\mathrm{T2}} > 80\,\mathrm{GeV}$	20.83 ± 3.37	0.00 ± 0.00	1.59 ± 0.37	2.55 ± 1.02	1.08 ± 0.70	0.00 ± 0.00	0.14 ± 0.05	5.35 ± 1.29

Table 8.3.: Number of selected events for the signal and SM backgrounds. The MC numbers have been scaled to the integrated luminosity of the data analysed ($2.05\,\mathrm{fb}^{-1}$). The additional scale factor of $f_{\mathrm{Wtop}} = 0.50 \pm 0.12$ have been applied to the W and top background from the ditau requirement onward as detailed in Sect. 8.6.1. Only statistical uncertainties are given.

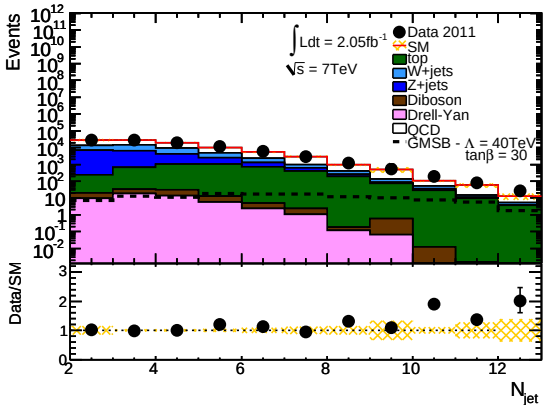

(a)

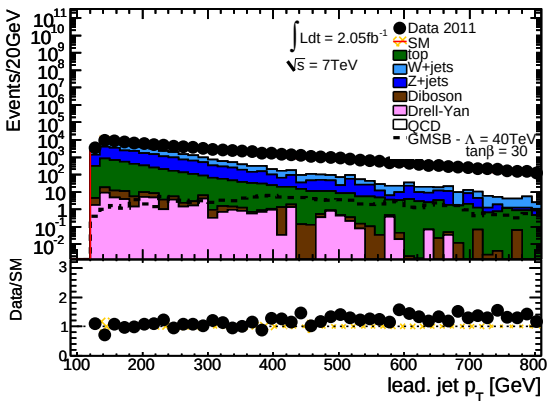

(b)

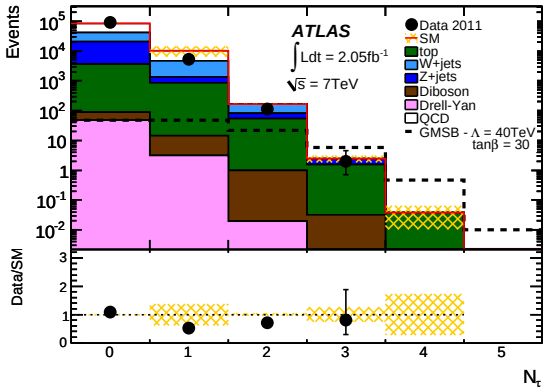

(c)

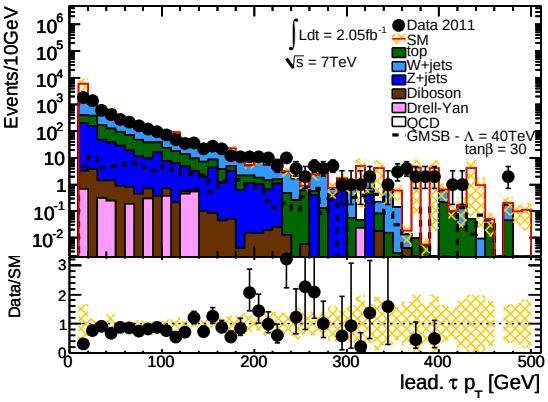

(d)

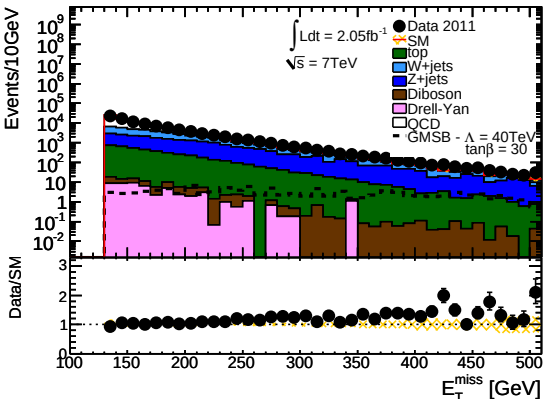

(e)

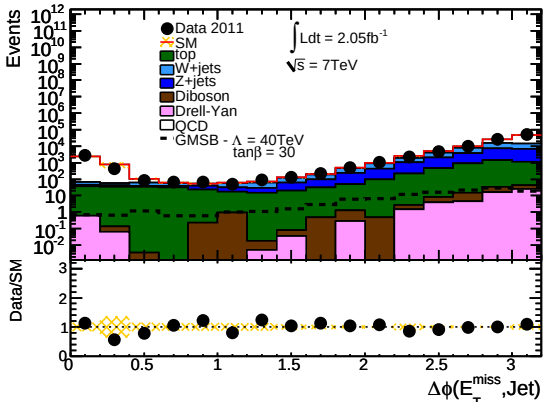

(f)

Figure 8.10.: Some of the kinematic variables after the application of the light lepton veto: (a) number of jets, (b) p_{T} of leading jet, (c) number of reconstructed τ candidates, (d) p_{T} of leading τ, (e) $E_{\mathrm{T}}^{\mathrm{miss}}$, and (f) $\Delta\phi$ between $E_{\mathrm{T}}^{\mathrm{miss}}$ and the leading jet. The yellow band shows the statistical error of the SM background MC distribution.

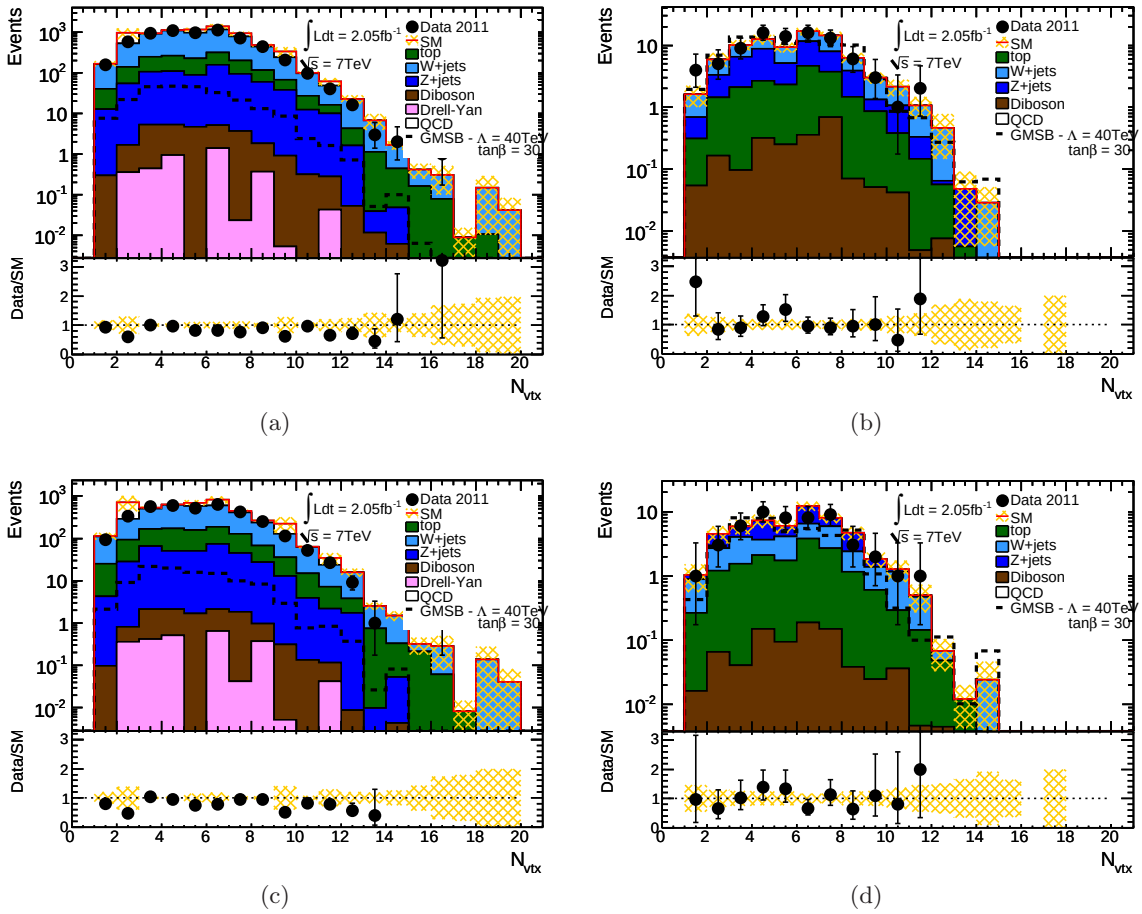

Figure 8.11.: Number of vertices after the trigger offline cuts while simultaneously requiring (a) one τ or (b) two τ candidates and at the (c) one-τ stage, and the (d) ditau stage in the event selection.

8.4. τ Identification and τ Truth-matching

The choice of the τ identification has been evaluated and the number of generated and misidentified τ candidates has been studied to test if the event selection is indeed optimal. As described in Sec. 6.2, there are three different working points *loose*, *medium*, and *tight* representing different reconstruction efficiencies (60 %, 40 %, 30 %) and background rejections(10 %, 3 %, 0.5 %).

Figure 8.12 (left column) shows the number of τ leptons per event at generator level and the number of truth-matched τ candidates[2] (right column) in the signal region when requiring two loose, medium, or tight reconstructed τ candidates. The majority of the GMSB events contain at least three generated, hadronically decaying τ leptons while most of the SM background is dominated by events that only contain one generated τ lepton, which implies one

[2] A reconstructed τ candidate is called truth-matched if a generated, hadronically decaying τ is found within $\Delta R < 0.2$ around it.

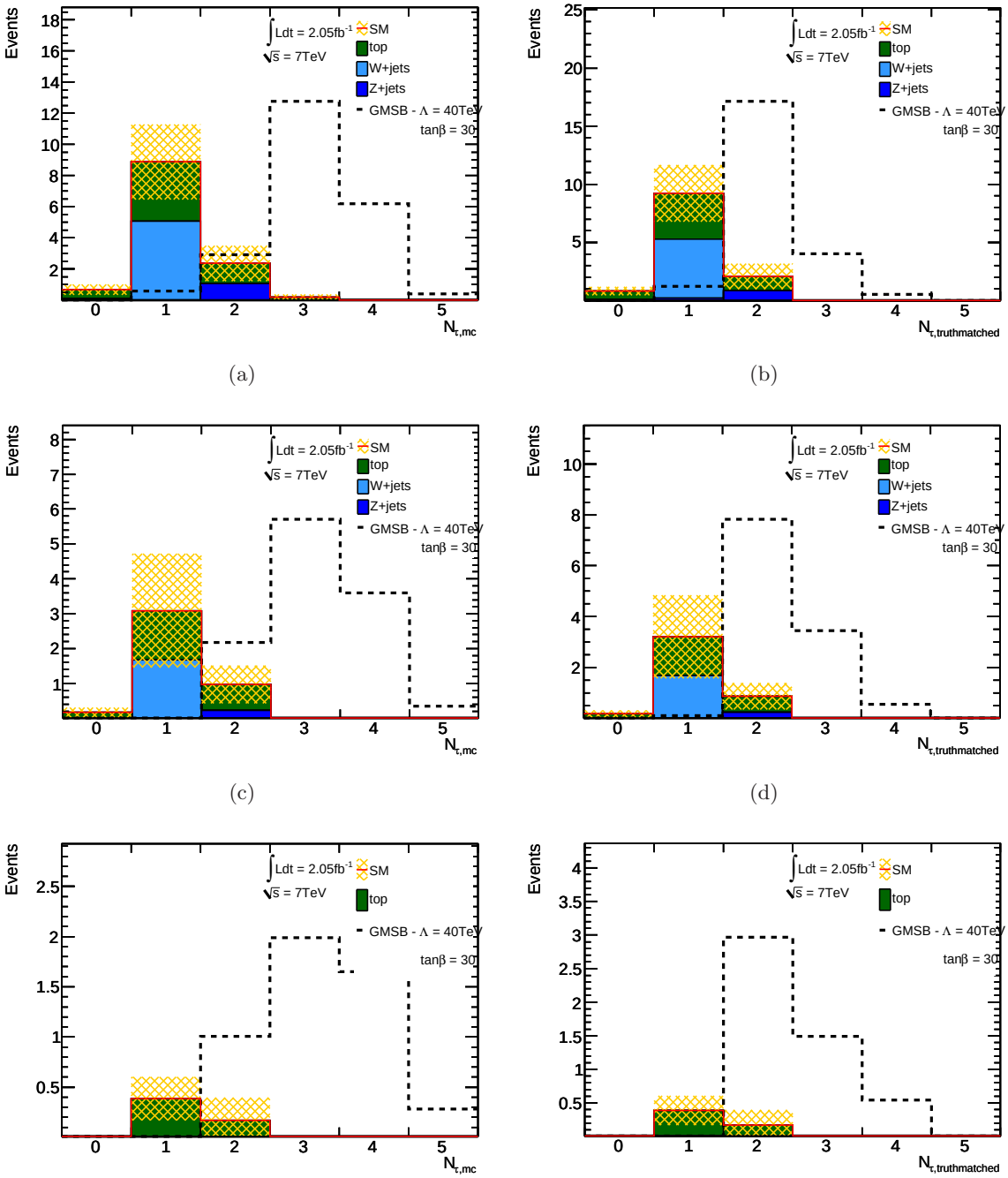

Figure 8.12.: Number of generated, hadronically decaying τ leptons (left) and truth-matched (right) τ candidates per event for the three τ identification working points *loose* (top), *medium* (middle), and *tight* (bottom).

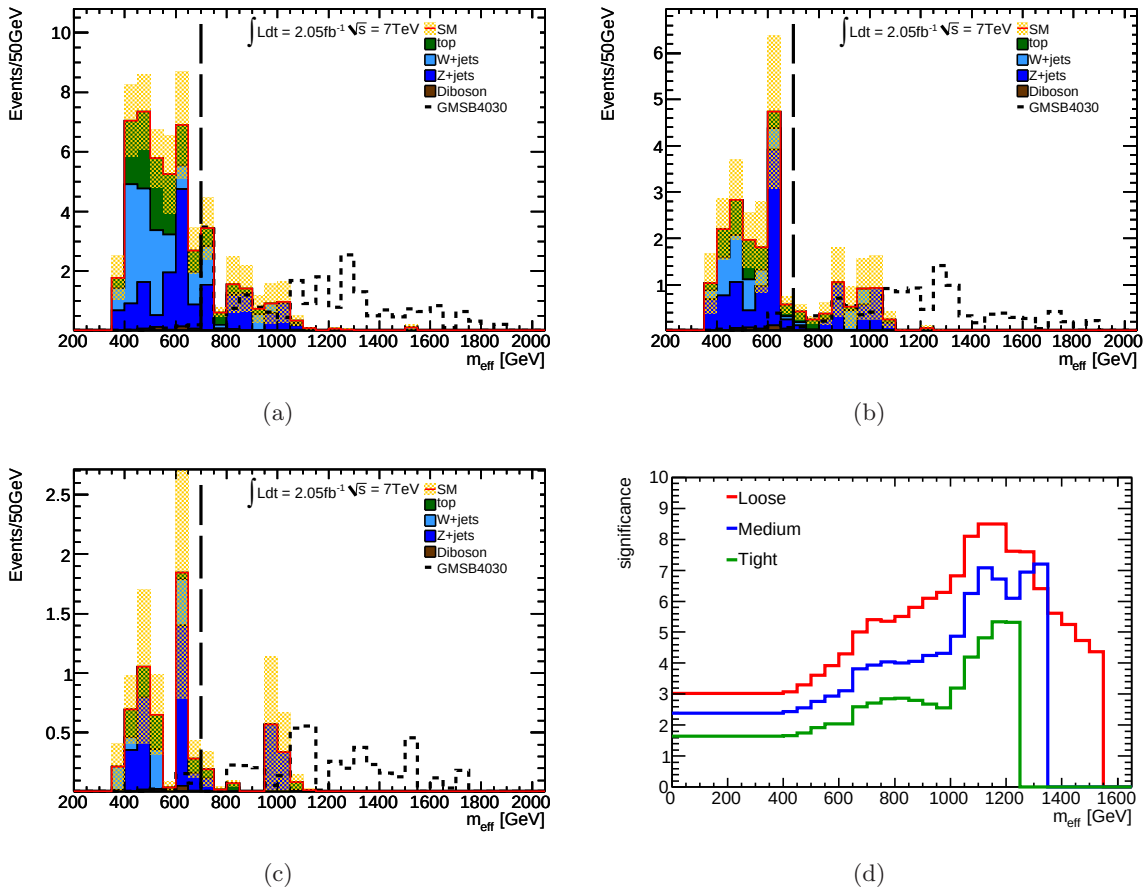

Figure 8.13.: m_{eff} distribution for (a) loose, (b) medium, and (c) tight τ identification and (d) a comparison of the Asimov significance scan.

wrongly reconstructed τ candidate per event. This general behavior can be observed in all three τ identification scenarios. No significant improvement is visible when tightening the τ identification while the available statistics drops significantly.

For the SM background, the number of generated and truth-matched τ candidates is almost identical. For GMSB, one τ lepton per event is lost during the reconstruction. This is due to the overall lower τ momentum in GMSB. In addition, the busier environment of SUSY events in general compared to SM events, i.e. the events contain more physics objects, lowers the overall reconstruction efficiency. Here again, no improvement in terms of the amount of wrongly reconstructed τ can be observed when tightening the τ identification requirements. Instead, when choosing the loose selection the GMSB events are already dominated by at least two truth-matched τ per event.

The m_{eff} distribution for the three τ identification scenarios is shown in Fig. 8.13 along with a scan of the Asimov significance. The most prominent feature of these distributions is the drop in statistics. The comparison of the significances shows that as expected a higher cut on m_{eff} will yield a higher significance, whereas beyond a cut value of 1000 GeV the distribution is clearly dominated by the absence of SM background. It also shows a clear preference for

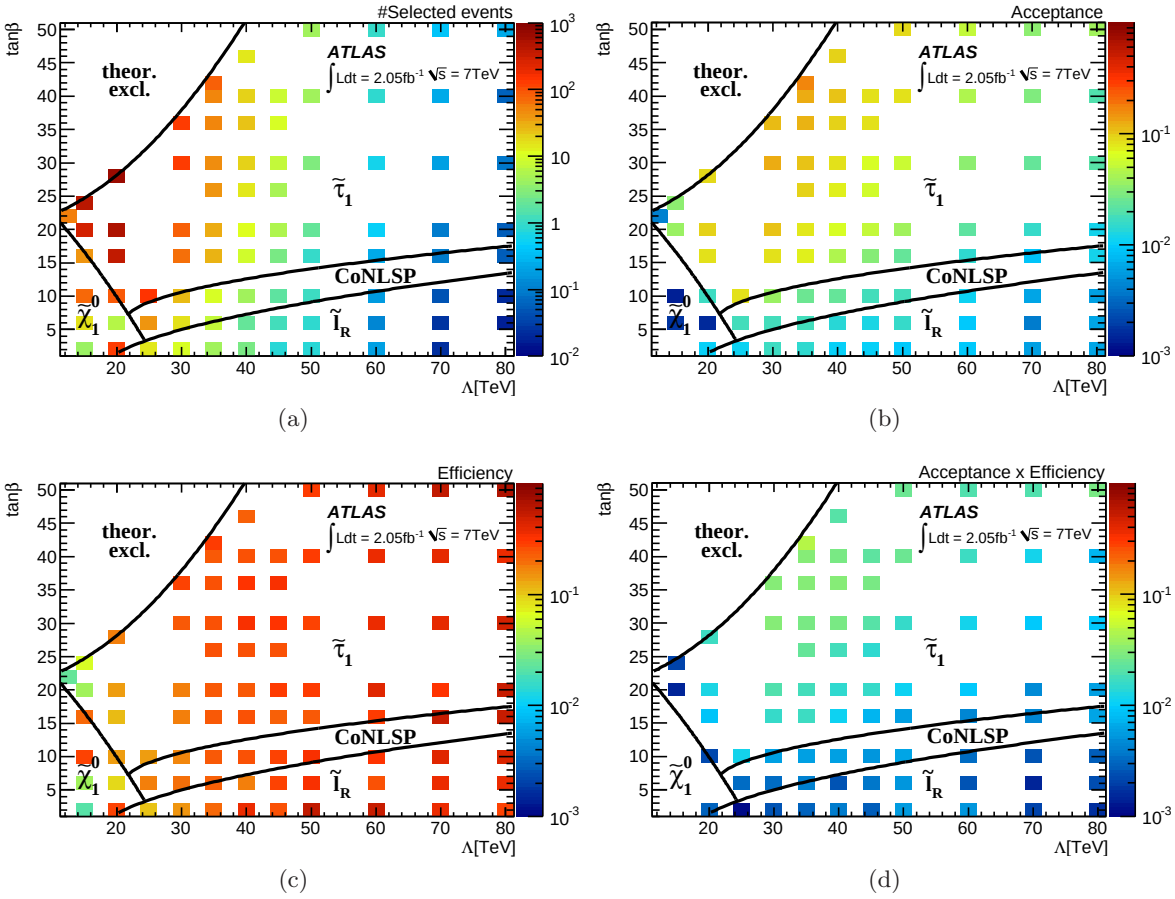

Figure 8.14.: (a) Number of selected events in the Λ-tanβ-plane, (b) acceptance of the signal selection at generator level, (c) efficiency at reconstruction level, and (d) the product of the two variables.

the loose identification in terms of statistics and the actual significance value.

8.5. Signal Efficiency

Figure 8.14(a) shows the number of expected events in the Λ-tanβ-plane for the described event selection. The dominant feature is again the decrease in the number of events with increasing Λ. The overall number of selected events drops by four orders of magnitude as does the cross section (cf. Fig. 8.1). The number of selected events is driven by the acceptance and the efficiency of the event selection.

The acceptance (Fig. 8.14(b)) is defined by the ratio of the number of events that fulfill the event selection criteria at generator level to the total number of events. It clearly features the different NLSP regions which are also indicated and is highest ($\approx 12\,\%$) for high tanβ and lower Λ. The efficiency (Fig. 8.14(c)) on the other hand, defined as the ratio of the number of

events that are selected to the number of accepted events, is almost flat over the intermediate Λ range and increases slightly for higher values. It takes values between 20 % and 40 %.

Taking the product of the acceptance and efficiency (Fig. 8.14(d)) leads to an overall selection efficiency of 1 % to 5 % in the $\widetilde{\tau}_1$ NLSP region where the pattern of the acceptance is clearly visible. This value is rather low compared to other analyses searching for events containing light leptons (up to 20 %) [200] or photons (up to 30 %) [201]. However, considering the lower reconstruction efficiency of hadronically decaying τ leptons makes this value acceptable for this kind of search.

8.6. Background Estimation

In this section, semi data-driven estimates for the number of top, W+jets, and QCD background events in the signal region are presented. Due to the very small number of real τ candidates present in QCD events, the observed background yield is dominated by jets misidentified as τ candidates. As shown in Fig. 8.12 the same is true for one of the two selected τ candidates in most of the selected top and W+jets events. These misidentified τ candidates are not well modeled in MC.

The general procedure for estimating the number of events for a given type of background starts with the definition of a control region that is disjoint from the signal region, to derive a scaling factor in that region, and to apply it to the number of MC events in the signal region. Nonetheless, the shape is taken from MC and only the overall scaling is derived from data.

The other backgrounds are assumed to be either well modeled in the simulation (Z+jets) because they are dominated by events containing a negligible amount of misidentified τ candidates or have an insignificant contribution to the signal region (diboson, Drell-Yan).

8.6.1. W and top Background

As can be seen from Tab. 8.3, W+jets and top events are the dominant background remaining in the signal region. The top contribution consists mostly of $t\bar{t}$ and very few single top events. The W+jets contribution consists exclusively of events featuring the decay $W \to \tau\nu_\tau$. It has been attempted to separate these two main backgrounds by exploiting the presence of b-jets in top events and their general absence in W+jets events. In addition, the composition of the events concerning their generated and misidentified τ content has been studied.

The W+top enhanced control region is defined by inverting the cut on m_{eff} in the event selection. Table 8.4 lists the event numbers for the different SM backgrounds. The QCD and Drell-Yan contribution have been found to be negligible in this control region. The number of events for the Z+jets and diboson contributions is measurable but their amount is small compared to the number of W and top events. Figure 8.15(a) shows the m_{eff} distribution in the control region before the scaling has been applied.

It can be deduced from Fig. 8.15 as well as from the number of events listed in Tab. 8.4 that the number of simulated events strongly overestimates the number of real collision data events and a scaling factor well below unity needs to be applied. This is due to the mismodeling of

Channel	Number of events
Data	25 ± 5
W+jets	24.88 ± 3.65
top	21.19 ± 1.01
Z+jets	1.59 ± 0.85
diboson	0.27 ± 0.08

Table 8.4.: Number of data and simulated events per background channel observed in the W+top control region. The simulated event numbers are not scaled.

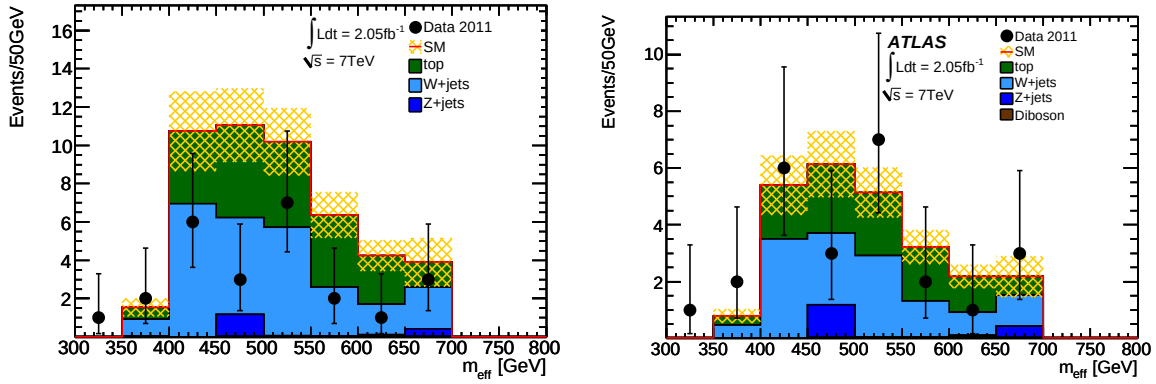

(a) (b)

Figure 8.15.: m_{eff} distribution in the W+top control region, (a) unscaled and (b) with the computed scaling factor applied.

misidentified τ candidates in the simulation compared to real collision data. Similar findings have been reported by the recent $H \to \tau\tau$ [202] and $Z \to \tau\tau$ [172] analyses.

The scaling factor is computed by subtracting the number of expected MC events of non-W and non-top background from the data in the control region. The resulting number is divided by the MC expectation for the W+top background:

$$f_{W\text{top}} = \frac{N_{\text{CR}}^{\text{data}} - N_{\text{CR}}^{\text{non}W\text{top}}}{N_{\text{CR}}^{\text{top}} + N_{\text{CR}}^{W}}, \tag{8.5}$$

where $f_{W\text{top}}$ denotes the derived scaling factor, $N_{\text{CR}}^{\text{data}}$ the number of data events, $N_{\text{CR}}^{\text{top}}$ (N_{CR}^{W}) the number of top (W+jets) events and $N_{\text{CR}}^{\text{non}W\text{top}}$ the number of non-W and non-top events in the combined W+top control region.

The predicted number of W and top events in the signal region $N_{\text{SR}}^{\text{W top}}$ is subject to statistical uncertainties comprising uncertainties from limited number of events in MC and data. The MC uncertainties are driven by the event statistics but take all event weights into account (e.g. pile-up reweighting, luminosity). For real collision data, Poisson errors are assumed. All these errors are properly propagated to the calculation of the uncertainty of the scaling factor

$\sigma_{f_{\mathrm{Wtop}}}$, whereas the resulting uncertainty is taken as the statistical uncertainty on the scaling factor. Accordingly, the scaling factor was determined to be $f_{\mathrm{Wtop}} = 0.50 \pm 0.12$.

Figure 8.15(b) shows the m_{eff} distribution in the control region after the determined scaling has been applied. An improvement concerning the data and MC agreement can clearly be seen and within the statistical uncertainties (yellow band) a reasonably good description is achieved. Nonetheless, some deviations are visible when comparing the shape of the MC to the one of the data. To further investigate these deviations Fig. 8.16 shows all the distributions of the variables included in the m_{eff} calculation. The best agreement can be observed for $p_{\mathrm{T}}^{\mathrm{jet2}}$ and $p_{\mathrm{T}}^{\tau 1}$. However, $p_{\mathrm{T}}^{\mathrm{jet1}}$, $p_{\mathrm{T}}^{\tau 2}$, and $E_{\mathrm{T}}^{\mathrm{miss}}$ show large statistical fluctuations which transfer into the m_{eff} distribution.

To separate the W+jets and the top contribution, the number of b-jets per event is considered. Since the branching ratio for $t \to Wb$ is almost unity while the considered W+jets events rarely contain any b-jets, the combined control region is split into a W control region where $N_{b-\mathrm{jets}} = 0$ and a top enhanced control region where the number of b-jets is $N_{b-\mathrm{jets}} \geq 1$. Requiring $N_{b-\mathrm{jets}} \geq 1$ generates a very clean top sample as shown in Fig. 8.17(a). Due to the very small statistics in both the combined as well as these separated control regions no attempt has been made to derive separate scaling factors for subregions dominated by truth-matched or misidentified τ candidates. Since Fig. 8.18 shows that the composition of truth-matched and misidentified τ candidates is similar in the signal and control region this approach is justified (see more detailed discussion below).

Figure 8.17(b) shows the m_{eff} distribution in the very clean top control region. The scaling factor is determined similarly as it has been for the combined control region (cf. Eq. (8.5)) by subtracting the non-top MC contributions $N_{\mathrm{CRtop}}^{\mathrm{non-top}}$ from the data $N_{\mathrm{CRtop}}^{\mathrm{data}}$ followed by a normalization to the top MC contribution $N_{\mathrm{CRtop}}^{\mathrm{top}}$

$$f_{\mathrm{top}} = \frac{N_{\mathrm{CRtop}}^{\mathrm{data}} - N_{\mathrm{CRtop}}^{\mathrm{non-top}}}{N_{\mathrm{CRtop}}^{\mathrm{top}}}. \tag{8.6}$$

The resulting scaling factor is $f_{\mathrm{top}} = 0.69 \pm 0.22$. It has been applied in Fig. 8.17(c). It is larger than f_{Wtop} as some of the top events contain two real τ leptons reducing the degree of mismodeling. The agreement between data and simulated events is reasonable within the large statistical errors. For the complementary W control region the same procedure is applied. However, it can be seen in the unscaled (scaled) m_{eff} distribution in Fig. 8.17(d) (8.17(e)) that the purity is not as high as in the top control region. Therefore, the corresponding scale factor is taken into account

$$f_{\mathrm{W}} = \frac{N_{\mathrm{CRW}}^{\mathrm{data}} - f_{\mathrm{top}} \cdot N_{\mathrm{CRW}}^{\mathrm{top}} - N_{\mathrm{CRW}}^{\mathrm{nonWtop}}}{N_{\mathrm{CRW}}^{\mathrm{W}}}. \tag{8.7}$$

Table 8.5 summarizes the number of events in the individual control regions and the obtained scaling factors including their relative statistical uncertainty. For the data, the non-top and non-W contributions have been subtracted and the MC only includes the corresponding top and W contributions. The scaling factors for the individual control regions are independent since their derived from disjoint regions. It can be seen that they are compatible with the central value of the combined scaling within approximately 1σ, whereas the relative statistical uncertainty is significantly larger. In addition, no great improvement can be observed in the agreement between data and MC in the individual m_{eff} contributions (cf. Figs. 8.17(b)

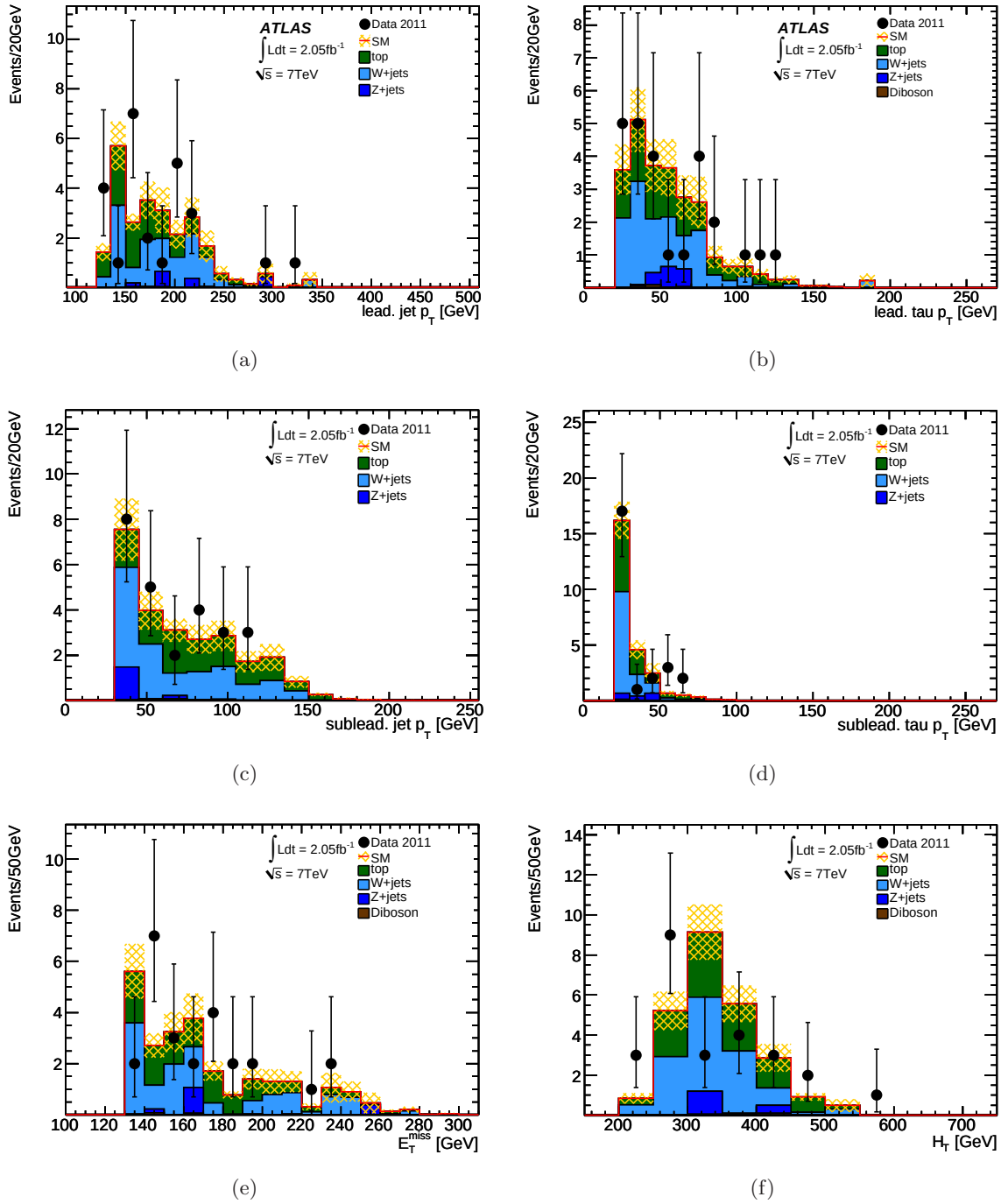

Figure 8.16.: Distributions of the kinematic variables used to compute the m_{eff} in the W+top control region (CR). The computed scaling factor is applied to all distributions.

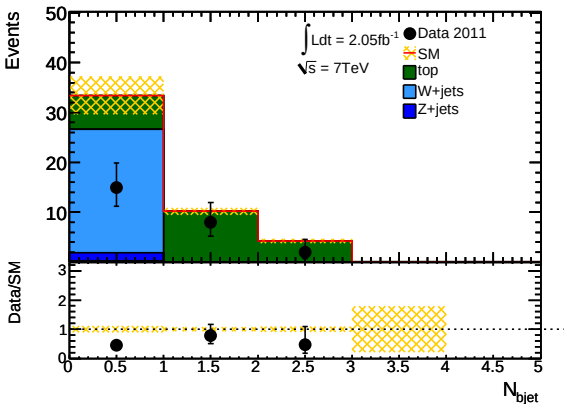

(a) $N_{b-\text{jets}}$ in W+top CR unscaled

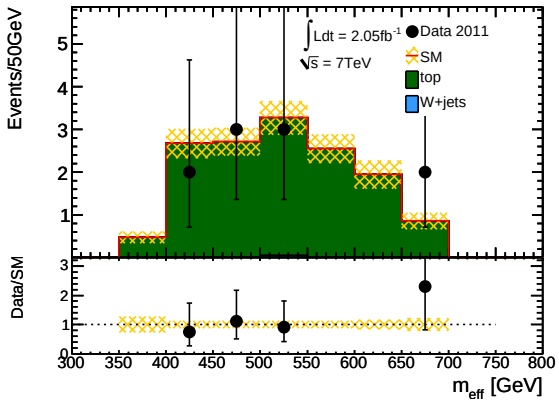

(b) m_{eff} in top CR unscaled

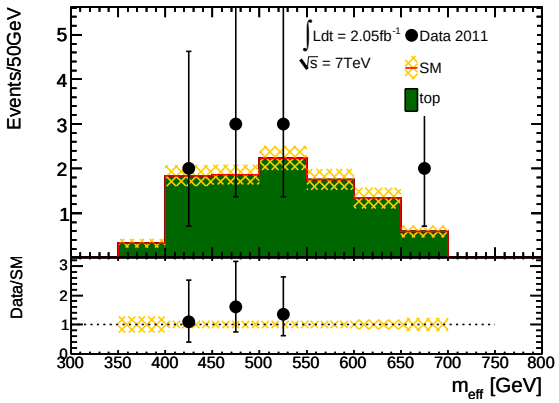

(c) m_{eff} in top CR scaled

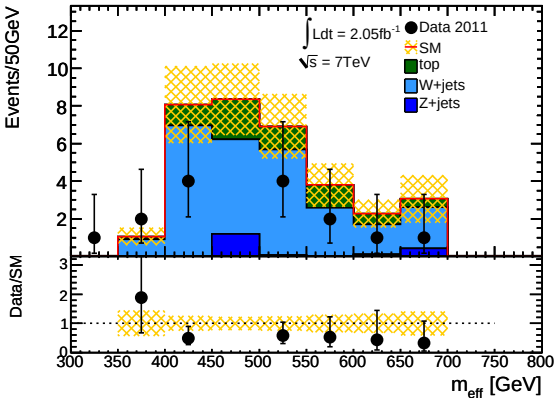

(d) m_{eff} in W CR unscaled

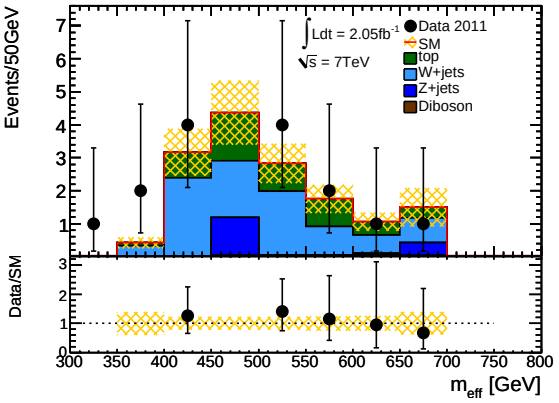

(e) m_{eff} in W CR scaled

Figure 8.17.: (a) Number of b-jets and (b)-(d) the m_{eff} distribution in the separate W and top control regions with the respective scale factors applied.

	Corrected Data	Corresponding MC	Scaling factor	Rel. stat. uncertainty
W+top control region	23±5	46.1±3.8	0.50±0.12	24%
top control region	10±3	14.46±0.81	0.69±0.22	32%
W control region	8 ±3	24.83±3.65	0.32±0.16	50%

Table 8.5.: Number of observed and expected events and scaling factors derived from for the combined and the two separate control regions. The number quoted for "Corrected Data" is the number of observed data events minus the number of MC events from background channels not under study in the respective control region.

	Background prediction	Statistical uncertainty	Rel. stat. uncertainty
Without scaling	9.46	1.81	19.1%
Common scaling	5.35	1.29	24.1%
Separate scaling	5.14	2.18	42.5%

Table 8.6.: Number of events expected for the signal region with and without scaling.

and 8.17(d)) compared to the combined region (cf. Fig. 8.15(b)). For this reason, the combined scaling is used for the background prediction in the signal region.

Table 8.6 lists the number of events that can be expected in the signal region with and without the appropriate scaling factors applied. The amount of expected events is greatly reduced when applying the scaling factors correcting for the overestimation of the misidentified τ content in MC. When choosing the combined scaling the number of expected MC events in the signal region amounts to 5.35 ± 1.29 events which corresponds to a relative statistical error of 24.1 %.

Truth-matched and Misidentified τ Candidates

In Sec. 8.4, the number of true and truth-matched τ candidates per event has been studied. It was found that in the signal region most of the signal events contain two or more truth-matched τ candidates whereas most background events contain one truth-matched and one misidentified τ. It is essential that for the background events the ratio of truth-matched and misidentified τ candidates is almost identical in the signal and the control region. If these ratios differ, the application of the scale factor, as determined above, in the signal region is not justified and a separate treatment of events dominated by truth-matched τ candidates and dominated by misidentified τ candidates is necessary.

Figure 8.18 shows the fraction of generated τ candidates, of truth-matched τ candidates, and of selected τ candidates as a comparison. It is notable that approximately 75 % of the events in the control region as well as in the signal region contain one truth-matched τ candidate and that the shape of the two distributions is very similar. When comparing the distributions, the

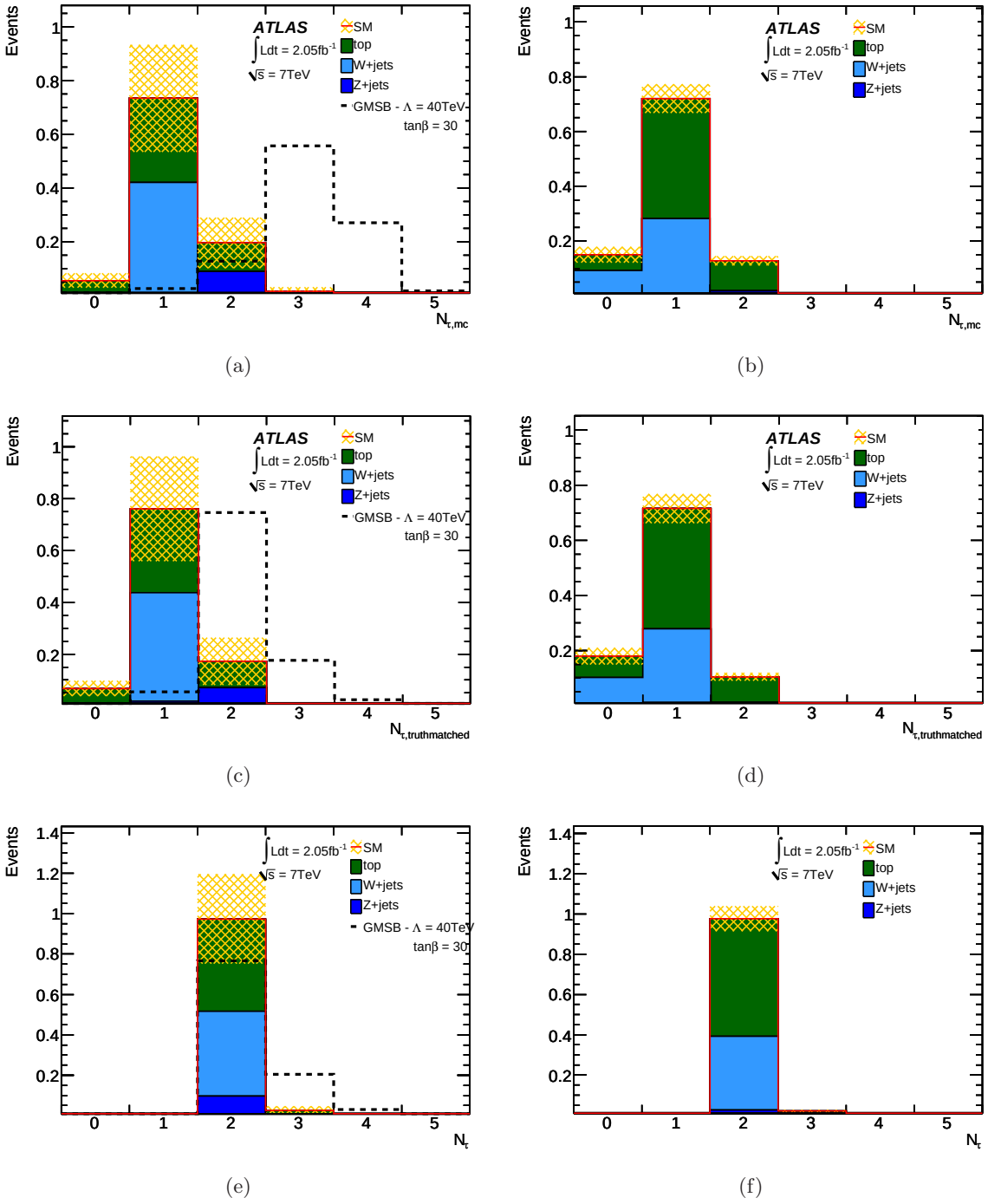

Figure 8.18.: (a) Ratio of generated τ candidates in the signal and (b) the W+top control region. (c) Ratio of truth-matched τ candidates in the signal and (d) the W+top control region. As comparison, (e) the ratio of selected loose τ candidates in the signal and (f) the W+top control region is shown.

Leading τ candidate	Remaining τ candidates	Scaling factor	BG prediction	Rel. stat. uncertainty	GMSB4030
loose	loose	0.50 ± 0.12	5.35 ± 1.29	24 %	21 ± 3
medium	loose	0.51 ± 0.14	4.83 ± 1.31	27 %	20 ± 3
tight	loose	0.63 ± 0.19	3.06 ± 1.02	33 %	10 ± 1
medium	medium	0.48 ± 0.23	1.65 ± 0.76	46 %	10 ± 1
tight	tight	0.61 ± 0.51	0.23 ± 0.23	100 %	4 ± 1

Table 8.7.: Influence of the various τ identifications on the scaling factors obtained from the control region [3].

$Z \rightarrow \tau\tau$ contribution in the signal region may be neglected, since it is not subject to scaling. The fraction of events containing two truth-matched τ for the top background is also the same in both regions ($\approx 10\,\%$). The only noticeable difference concerns events containing no correctly reconstructed τ. In that case, the percentage of events in the control region is slightly larger than in the signal region. While for top events, this deviation is rather small a lack of W+jets in this bin in the signal region can be observed. However, this deviation is relatively small and is not expected to alter the background prediction in a significant manner.

Influence of the τ Identification

Since the choice of the τ identification proved to be crucial for the event selection also the scaling factors have been tested concerning their robustness against the various working points. Five scenarios have been considered. They are listed in Tab. 8.7 along with the according scaling factor, the resulting background prediction for the signal region including its relative statistical uncertainty as well as the number of expected GMSB events. Even though a tighter τ identification increases the scaling factor due to the relatively higher rejection of misidentified τ candidates all scale factors are compatible within one standard deviation. In addition, a tighter selection naturally reduces the statistics and leads to a significant increase of the relative statistical uncertainty for the background prediction in the signal region confirming the choice of the τ candidates identified as loose.

Signal Events in the Control Region

If a high number of signal events was present in data in the control region, a large distortion of the calculation of the scaling factors could be expected. They would be too large and might prevent a discovery in the signal region since the background would consequently be overestimated. Therefore the amount of GMSB events has been checked in the control region. Figure 8.19 shows the ratio of signal events to background events in the Λ-tanβ-plane. The typical pattern of a steep decrease towards higher Λ values induced by the cross section is again apparent. In the region where the limit is expected ($40\,\text{TeV} \leq \Lambda \leq 50\,\text{TeV}$) this ratio adopts values of approximately 1-2 % and is therefore negligible for the calculation of the scaling factors or the limit determination. The rather high ratio for low Λ can be neglected since those model points have been excluded by previous experiments [203–206].

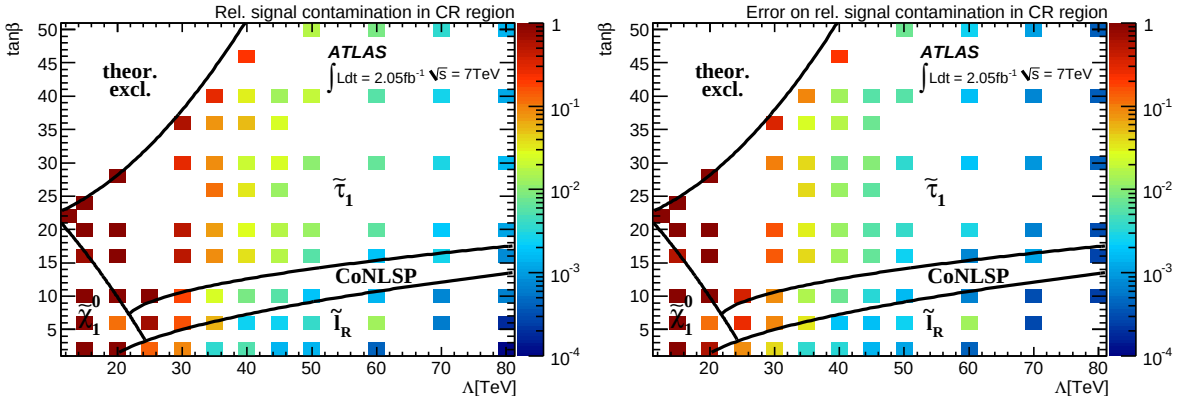

(a) (b)

Figure 8.19.: (a) Ratio of the number of signal events to the number of background events in the combined W+top CR and (b) the statistical error on this ratio.

Control region	Nominal selection	$p_{\mathrm{T}}^{\mathrm{jet2}} > 50\,\mathrm{GeV}$
W+top	0.50±0.12	0.55±0.14
top	0.69±0.22	0.76±0.26
W	0.34±0.16	0.27±0.22

Table 8.8.: Scaling factors with their respective statistical uncertainty obtained for the different control regions when requiring a higher $p_{\mathrm{T}}^{\mathrm{jet2}}$.

Influence of Different Kinematic Cuts

The analysis had originally been performed with a p_{T} cut of 15 GeV for the reconstructed τ candidates. This resulted in a higher number of misidentified τ candidates. Nonetheless, it did not change the overall performance of the analysis or the result in a significant manner. Also the scaling factors were compatible with the ones presented in Sec 8.6.1 and 8.6.2. However, selecting a high number of misidentified τ candidates is not desirable and the threshold was therefore set to $p_{\mathrm{T}}^{\tau} > 20\,\mathrm{GeV}$, as suggested by the ATLAS Collaboration.

In addition, the influence of a higher $p_{\mathrm{T}}^{\mathrm{jet2}}$ threshold on the scaling factors has been tested. Table 8.8 lists the scaling factors for the individual control regions in comparison to the ones if $p_{\mathrm{T}}^{\mathrm{jet2}} > 50\,\mathrm{GeV}$ is used. For the combined and the top control region the scaling factor increases due to fewer events containing misidentified τ candidates being selected. However, for the W control region the scaling factor becomes even smaller with a much higher relative statistical uncertainty. Figure 8.20 compares the two different combined control regions where the different scaling factors have been applied. The data events in the lower m_{eff} region are rejected and the agreement between data and MC slightly improves but only while losing a noticeable amount of events. Consequently, due to the lack of clear improvement the event selection has not been changed.

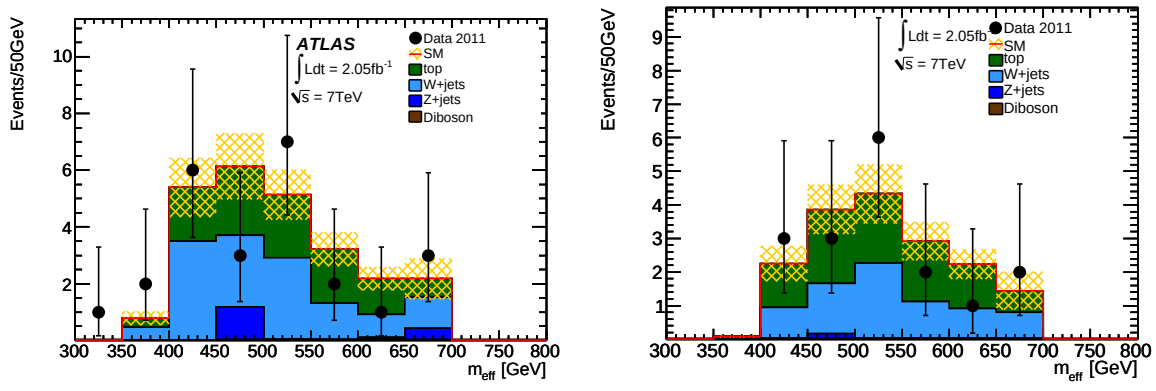

(a) (b)

Figure 8.20.: m_{eff} distribution in the W+top control region with the obtained scaling factors applied for (a) the nominal selection and (b) one kinematically restricted sub-region with $p_{\text{T}}^{\text{jet2}} > 50\,\text{GeV}$.

8.6.2. QCD Background

Since the accurate determination of the production cross section for multi-jet events is very difficult and it is subject to a large uncertainty, a dedicated estimate of the QCD dijet background has been performed to determine the overall normalization similar to the W+jets and top background discussed in Sec. 8.6.1. Another difficulty is that most of the $E_{\text{T}}^{\text{miss}}$ originates from instrumental effects often resulting in mismeasured $p_{\text{T}}^{\text{jet}}$.

The QCD enhanced control region is defined by the $\Delta\phi$-cuts and the cut on m_{eff}. The latter mainly reduces the signal contamination in the control region to a minimum. In addition, the ratio of $E_{\text{T}}^{\text{miss}}$ over m_{eff} is required to be lower than 0.4 since the number of QCD events decreases greatly for higher values. Figure 8.21 shows each of the kinematic variables used for the definition of the control region, where the cuts on the other variables are applied. The dominance of the QCD background in the selected region indicated by the black line is clearly visible.

To determine the amount of QCD events in the signal region, the QCD control region is divided into three separate *sidebands* depending on the number of reconstructed τ candidates. The unweighted $E_{\text{T}}^{\text{miss}}/m_{\text{eff}}$ distributions for the individual sidebands are shown in the left column of Fig. 8.22. The 0-τ sideband is used to determine the overall normalization. The QCD cross section correction factor w_0 is obtained by comparing the number of events in data and MC similar to Eq. (8.5)

$$w_0 = \frac{N_{\text{data}}^{0\tau} - N_{\text{non-QCD}}^{0\tau}}{N_{\text{QCD}}^{0\tau}}\,, \tag{8.8}$$

where $N_{\text{data}}^{0\tau}$ denotes the number of data events in the 0-τ sideband, $N_{\text{QCD}}^{0\tau}$ the number of QCD events selected in MC and $N_{\text{non-QCD}}^{0\tau}$ the sum of all non QCD events. Since the 0-τ sideband is not free of W and top contributions, scaling factors have been computed as discussed

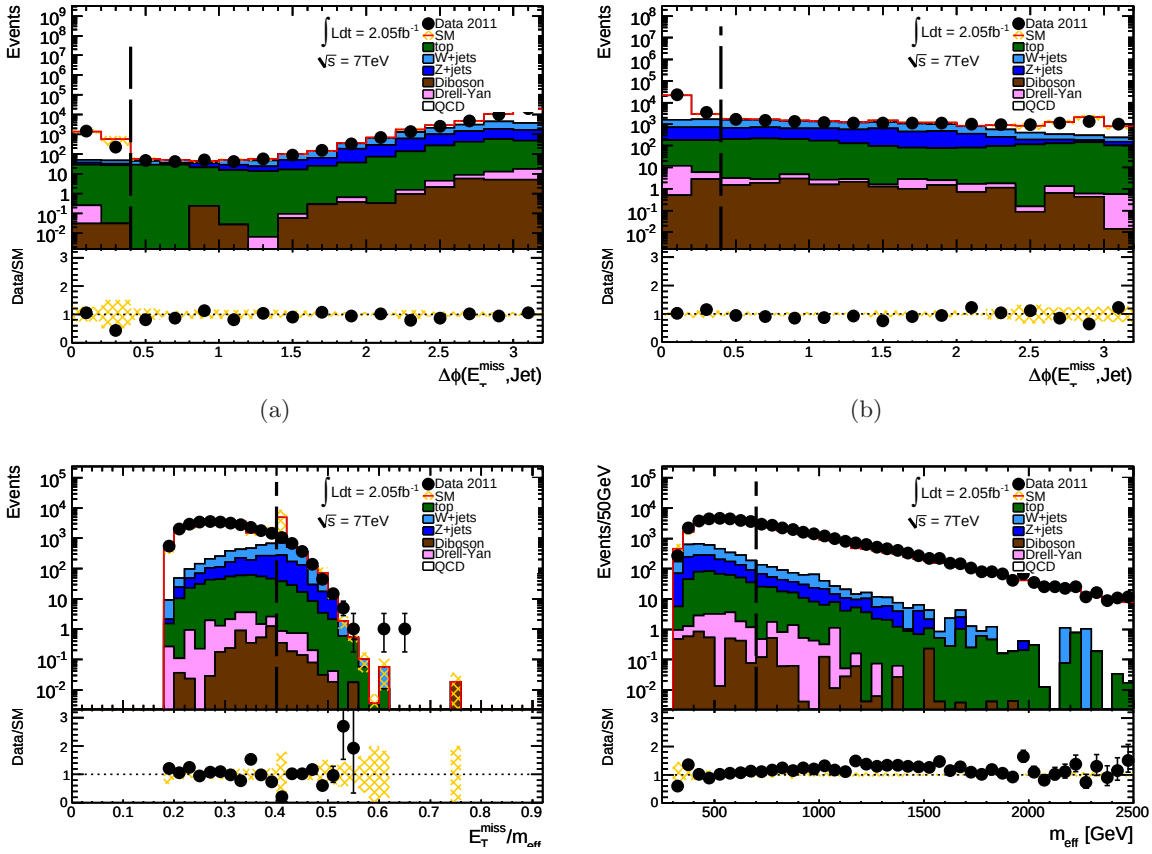

Figure 8.21.: Distributions of kinematic variables used for the definition of the QCD control region. The selected QCD control region is on the left of the black lines.

above but requiring no τ candidate. When applying the scaling factor for top and W+jets $f^{0\tau}_{W\text{top}} = 1.142 \pm 0.014$, the overall normalization is found to be $w_0 = 1.027 \pm 0.065$.

The 1-τ sideband is now used to determine the misidentification rate based on the assumption that the amount of generated τ candidates is very small and that all reconstructed τ candidates are misidentified jets. The scaling factor and the misidentification rate for the 1-τ sideband are again obtained by comparing the number of events in data and MC

$$f = \frac{w_1}{w_0} = \frac{N^{1\tau}_{\text{data}} - N^{1\tau}_{\text{non-QCD}}}{w_0 \cdot N^{1\tau}_{\text{QCD}}}, \tag{8.9}$$

where a scaling factor for top and W+jets of $f^{1\tau}_{W\text{top}} = 0.820 \pm 0.024$ has been applied. The scaling for the QCD contribution and the correction factor are found to be $w_1 = 0.46 \pm 0.24$ and $f = 0.52 \pm 0.28$, respectively. The relatively large errors are caused by the limited statistics due to the 1-τ requirement. Nonetheless, the values are very comparable to the results of other analyses, namely $H \to \tau\tau$ [202] and $Z \to \tau\tau$ [172].

Once two reconstructed τ candidates are required, no QCD event is selected in MC. Therefore,

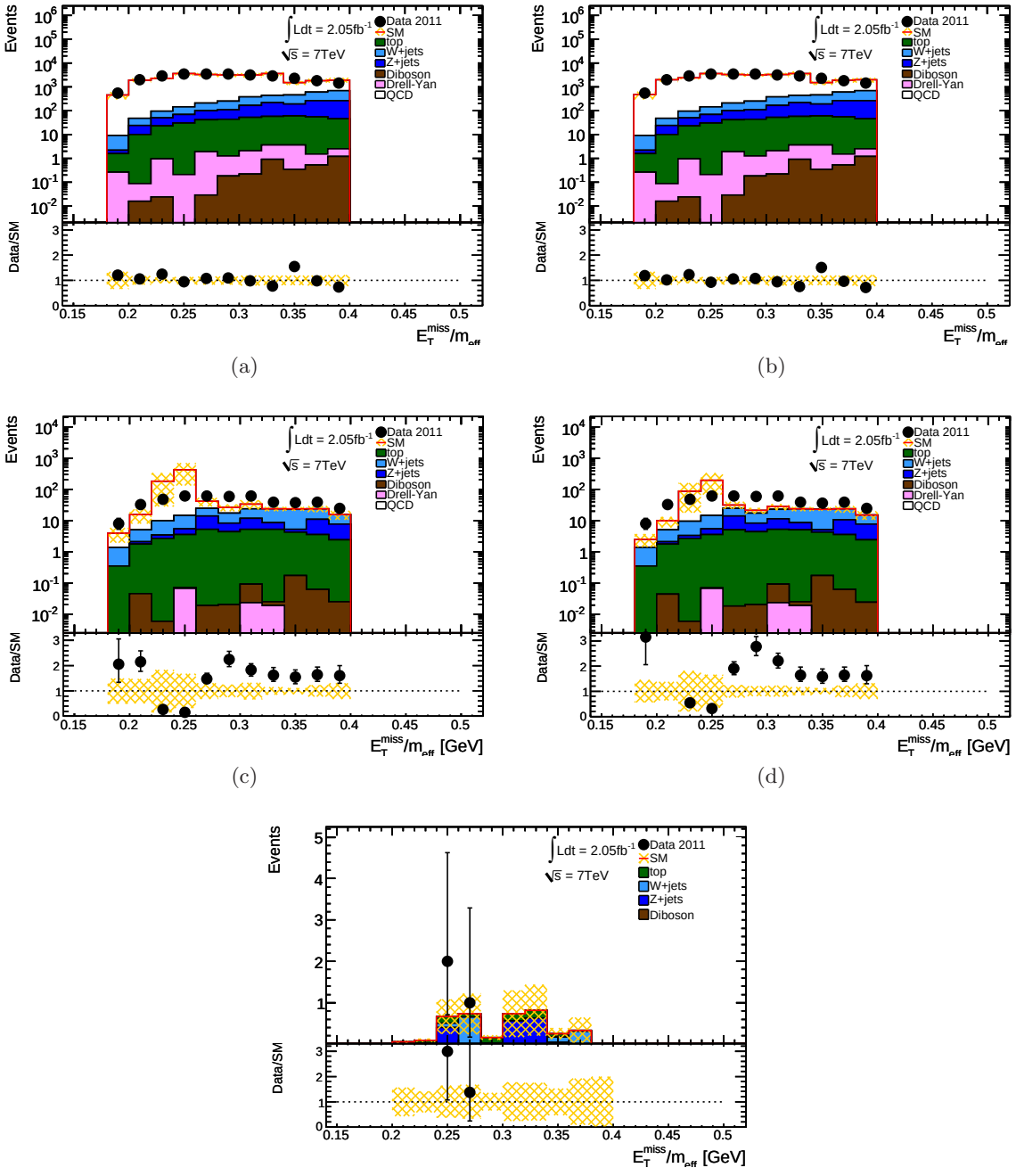

Figure 8.22.: $E_{\mathrm{T}}^{\mathrm{miss}}/m_{\mathrm{eff}}$ distributions in the three QCD sidebands (0-τ, 1-τ, 2-τ). The left column shows the unweighted distributions while the right column shows the distributions weighted according to their determined scaling factors.

	0τ	1τ	2τ
N_{QCD}	23570±1490	624±324	0±0
$N_{\mathrm{non-QCD}}$	3314±90	182±12	3.8±1.1
N_{data}	27533	472	3
w	1.027±0.065	0.46±0.24	0.21± 0.22

Table 8.9.: Scaling factors for the determination of the QCD background taking into account the scale factors that have been determined for W and top in the appropriate region.

the scaling in the 2-τ sideband can only be determined indirectly by

$$w_2 = w_0 \cdot f^2 \tag{8.10}$$

and is found to be $w_2 = 0.21 \pm 0.22$. Since the scaling factors for the 1-τ and 2-τ sidebands depend on that of the 0-τ, which itself depends on the τ identification and thus is sensitive to the misidentification rate, a bias is introduced. The misidentification rate was found to be 6 % for $Z \to \tau\tau$ events [172]. Assuming a conservative upper limit on the misidentification rate of 10 % due to the different event structure of QCD events leads to a bias in the signal region of approximately 15 % in this analysis.

The $E_{\mathrm{T}}^{\mathrm{miss}}/m_{\mathrm{eff}}$ distributions for the individual sidebands weighted accordingly to the determined scaling factors are shown in the right column of Fig. 8.22. The number of events used to determine the scaling factors are summarized in Tab. 8.9. While a reasonable agreement between data and MC can be observed in the 0-τ sideband, the MC statistics are considerably reduced in the 1-τ sideband introducing large statistical errors yielding a noticeable disagreement in the shape of the distribution. The 2-τ sideband does not contain any QCD dijet events.

Replacement of τ candidates with τ jets

An attempt to improve the agreement of the shape is the replacement of the reconstructed τ candidates with so-called τ-jets, low track-multiplicity jets kinematically resembling τ candidates to create an enriched sample. τ-jets are required to satisfy $p_{\mathrm{T}} > 20\,\mathrm{GeV}$ and $|\eta| < 2.5$, where the number of associated tracks is seven or less. A similar technique has been used in the analysis requiring at least one τ candidate [190]. The τ-jet enriched $E_{\mathrm{T}}^{\mathrm{miss}}/m_{\mathrm{eff}}$ distribution in the 1-τ sideband before and after applying the scale factor w_1 can be seen in Fig. 8.23. A great improvement of the shape agreement can be observed validating the use of τ-jets. Nonetheless, the overall normalization is taken from the original QCD MC samples. However, no QCD event has been found in the signal as well as the control region when requiring at least two reconstructed τ candidates. Therefore, the determined scaling w_2 is not applicable and the QCD contribution in the signal region is considered to be negligible.

The number of tracks that are associated to the τ-jets has been chosen to be seven at maximum. It has been checked if the shape agreement changes significantly if the number of associated tracks is varied, e.g. between three and fifteen. It has been found that the effect of various number of associated tracks is negligible except for a slight increase or decrease of statistics.

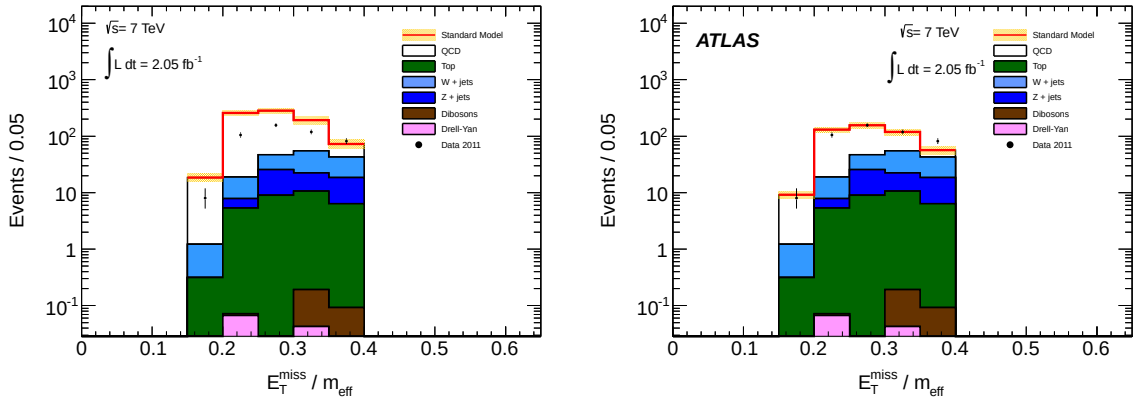

(a) (b)

Figure 8.23.: $E_{\mathrm{T}}^{\mathrm{miss}}/m_{\mathrm{eff}}$ distribution in the 1-τ sideband when including τ-jets (a) without and (b) with the scaling on QCD applied [3].

	0 medium τ	1 medium τ	2 medium τ	0 tight τ	1 tight τ	2 tight τ
N_{QCD}	23980±1520	217±156	0±0	24040±1520	157±154	0±0
$N_{\mathrm{non-QCD}}$	3404±90	114.8±9.7	1.33±0.73	3473±90	62.6±6.7	1.11±0.73
N_{data}	27524	226	0	27524	100	0
w	1.017±0.064	0.51±0.37	0.26±0.37	1.016±0.064	0.28±0.23	0.08±0.13

Table 8.10.: Scaling factors for the determination of the QCD background taking into account the scale factors that have been determined for W and top in the appropriate region.

Influence of the τ identification

The estimation of the number of QCD events has also been tested for the three different τ identification methods. Figure 8.24 shows the $E_{\mathrm{T}}^{\mathrm{miss}}/m_{\mathrm{eff}}$ distribution in the 0-τ and 1-τ sideband for medium and tight τ candidates. The number of events in the individual sidebands according to the τ identification as well as the determined scaling factors are listed in Tab. 8.10. Here, the different scaling factors are correlated because the tight (medium) sidebands are a subset of the medium (loose) sidebands leading to an overestimation of the errors on w_{medium} and w_{tight}.

It is notable that the overall normalization (w_0) is robust against the different identification methods. This is not the case for the 1-τ sideband. While $w_{1,\mathrm{medium}}$ is still compatible with $w_{1,\mathrm{loose}}$, with a greatly increased statistical error, it is not in good agreement $w_{1,\mathrm{tight}}$. Also the data and MC agreement has not significantly improved (cf. Fig. 8.24). The tighter the τ identification criteria the more events are suppressed, especially those containing misidentified τ candidates impeding a reasonable calculation of the misidentification rate. Therefore, it can be concluded again that the loose τ identification is a reasonable choice for this analysis.

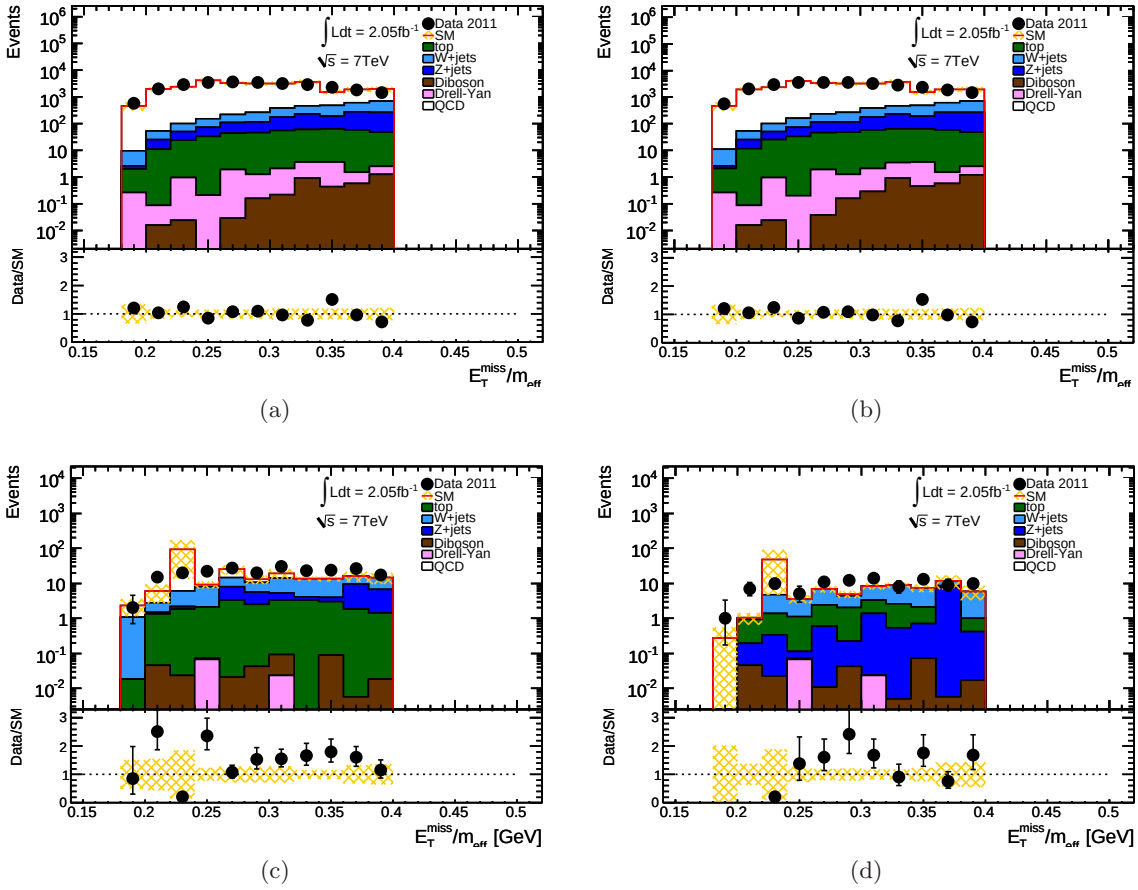

Figure 8.24.: $E_{\mathrm{T}}^{\mathrm{miss}}/m_{\mathrm{eff}}$ distribution in the 0-τ sideband for (a) medium and (b) tight τ candidates and for the 1-τ sideband for (c) medium and (d) tight τ candidates.

8.7. Systematic Uncertainties

Many of the quantities used in this analysis are subject to systematic uncertainties. The most relevant include uncertainties on

- the jet and τ energy scale
- the jet and τ energy resolution
- the τ reconstruction efficiency
- the τ misidentification rate
- $E_{\mathrm{T}}^{\mathrm{miss}}$
- the signal and background MC predictions and cross-sections
- the impact of pile-up and
- the luminosity.

8.7.1. Experimental Systematic Uncertainties

In the following, a detailed description is given for the various contributions and their treatment to obtain a quantitative estimate of the individual systematic uncertainties following closely the description in [3].

Jet Energy Scale

The relationship between a calorimeter signal and the corresponding jet energy is not known precisely. This uncertainty on the jet energy scale (JES) is determined by the jet and $E_{\mathrm{T}}^{\mathrm{miss}}$ Performance Group in MC studies [207] where nominal results are compared to samples with varied hadronic shower and physics models and alternative detector configurations. In addition, a data versus MC comparison of the jet response as a function of η is performed [207]. The results are implemented in the `JESUncertaintyProvider` tool [208], which is employed in the presented analysis to rescale the energies of all jets in a correlated way. Additional corrections are taken into account for close-by jets as described in [209]. Those are implemented in the `MultijetJESUncertaintyProvider` [210] used for jets in the region $|\eta| < 2.9$ where a sufficiently good double jet resolution is provided. Both providers are part of the `JetUncertainties` package. The latest tag 00-03-04-02 available for this analysis has been adapted to the 2011 pileup conditions.

Variations applied to the jet energies are propagated to $E_{\mathrm{T}}^{\mathrm{miss}}$:

$$E_{x,y}^{\mathrm{miss,var}} = E_{x,y}^{\mathrm{miss}} + \sum_{\mathrm{jets}} p_{x,y} - \sum_{\mathrm{jets}} p_{x,y}^{\mathrm{var}}, \tag{8.11}$$

where $E_{x,y}^{\mathrm{miss,var}}$ ($E_{x,y}^{\mathrm{miss}}$) denotes the varied (nominal) missing momentum and $p_{x,y}^{\mathrm{var}}$ ($p_{x,y}$) the jet momentum with (without) the variations applied. The variations are applied in two different ways, either added to the corresponding quantity or subtracted from it. Hence, the event selection is repeated twice using the recalculated jet energies and $E_{\mathrm{T}}^{\mathrm{miss}}$ resulting in a modified SM background prediction for the signal region.

The JES uncertainty in the central calorimeter region ($|\eta| < 0.8$) is lower than 2.5% for high p_{T} jets with $60\,\mathrm{GeV} < p_{\mathrm{T}}^{\mathrm{jet}} < 800\,\mathrm{GeV}$, and less than 4.6% for the full p_{T}-range $p_{\mathrm{T}}^{\mathrm{jet}} > 20\,\mathrm{GeV}$. In the end-cap ($0.8 < |\eta| < 2.8$) and forward ($2.8 < |\eta| < 4.5$) regions, the uncertainty for jets with $p_{\mathrm{T}}^{\mathrm{jet}} > 50\,\mathrm{GeV}$ is below 4% and 6%, respectively. It is largest for low p_{T} jets in the range $20\,\mathrm{GeV} < p_{\mathrm{T}}^{\mathrm{jet}} < 30\,\mathrm{GeV}$ and in the most forward region ($3.2 < |\eta| < 4.5$) where it amounts to 14 % [207].

These variations are applied before the overlap removal between jets and reconstructed τ candidates is applied (cf. Sec. 6.5). Hence, they are not only applied to jets themselves but also to jets later identified as τ candidates. This procedure is appropriate because in the definition of $E_{\mathrm{T}}^{\mathrm{miss}}$ τ candidates are simply treated as jets.

Jet and τ Energy Resolution

The jet energy resolution (JER) is simulated with finite precision by the `GEANT4` detector simulation. The agreement between the jet energy resolution in data and MC has been studied using the spread of the p_{T} imbalance in dijet events [211] with different in-situ techniques [212]. Deviations have been found to be in the order of 10%. A `JetEnergyResolutionProvider` [213] has been developed providing p_{T} and η dependent resolutions and uncertainties. All jet momenta are varied uncorrelated and randomly with a Gaussian of mean 1 and a standard deviation computed from the values provided by the tool.

The modified jet energies are again propagated to the $E_{\mathrm{T}}^{\mathrm{miss}}$ calculation following Eq. 8.11. The corrections are again deployed before the performing of the jet and τ overlap removal. Consequently, these uncertainties are applied to all jets and implicitly all τ candidates as well as $E_{\mathrm{T}}^{\mathrm{miss}}$ as for JES.

Since the reconstruction of hadronically decaying τ leptons is affected by this uncertainty as well, all τ momenta are varied by applying the same procedure as for the jets. Nonetheless, without propagating the corrections to the $E_{\mathrm{T}}^{\mathrm{miss}}$ calculation since this has been done by varying the underlying jet candidate already. Following this procedure, all hadronic objects are treated with the JER uncertainty while avoiding double counting for the $E_{\mathrm{T}}^{\mathrm{miss}}$ computation.

τ Energy Scale

Systematic uncertainties for the τ energy scale are studied in detail by the Tau Working Group. The method used to calculate the τ energy scale uncertainty is based on MC studies and follows the procedure in [175]. Uncertainties are evaluated by comparing the reconstructed p_{T}^{τ} of τ candidates passing the loose identification in the nominal MC simulation and in simulations with alternative configurations. Samples of $Z \to \tau\tau$, $W \to \tau\nu_{\tau}$, and $Z \to \tau\tau$ processes are used. Uncertainties are calculated in the barrel, end-cap and transition regions, for 1-prong and multi-prong candidates. In each region, the uncertainties are evaluated in six different p_{T}^{τ} bins ranging from 15 to 110 GeV.

The systematic uncertainty on the τ energy scale is evaluated from seven distinct sources: the MC event generator and underlying event model; the hadronic shower model; the amount of detector material; the electromagnetic energy scale; the topological clustering noise thresholds; pileup; and non-closure. The non-closure accounts for deviations of the reconstructed τ kinematics from the generated kinematics.

These sources can be quantified by various parameters which are varied and their effect on the τ energy scale is estimated. The largest uncertainties have been found to originate from the hadronic shower model and the non-closure. The uncertainty for the hadronic shower model has a maximum of 4 % and 6 % for 1-prong and multi-prong candidates in the central η region, respectively. It has a maximum of 5 % for low p_{T} multi-prong candidates. The resulting systematic uncertainty is p_{T}^{τ}, η^{τ}, and $n_{\mathrm{prong}}^{\tau}$ dependent ranging from 3.5% up to 9.5%. Further detailed studies and results are documented in [172] and [175].

τ Identification Efficiency

The systematic uncertainties on the τ identification efficiency have also been studied in detail by the Tau Working Group. Generally, these uncertainties depend on the τ identification algorithm, the kinematics of the τ sample, and the number of tracks associated to the reconstructed τ candidate. Two studies, using $Z \to \tau\tau$ and $W \to \tau\nu_\tau$ events, respectively, have been performed using tag and probe methods. They have been documented in [172].

Since the dominant backgrounds comprise mainly W+jets events the study based on events including a generated $W \to \tau\nu_\tau$ decay has been chosen as a basis to determine the uncertainties on the τ identification efficiency. For the efficiency uncertainty, the estimated combined statistical and systematic errors have been taken into account resulting in a relative uncertainty on the τ identification of 4.3% while for the misidentification probability of jets as τ candidates only a statistical uncertainty of 9.4% has been determined which is taken as the misidentification uncertainty [172]. The resulting systematic effects for this analysis are evaluated by increasing or decreasing the τ efficiency by the measured uncertainties. For the estimation of the efficiency uncertainty of only truth-matched τ candidates are considered.

For the determination of the systematic effect concerning the τ misidentification rate the expected SM background events in the signal region are scaled up or down by the measured uncertainty. Thereby, the reconstructed τ candidates are required to *not* be truth-matched.

Missing Transverse Momentum

The $E_{\mathrm{T}}^{\mathrm{miss}}$ is foremost affected by various uncertainties on the energy measurement of physics objects in the ATLAS detector. Hence, variations of the jet and lepton energies are propagated to the $E_{\mathrm{T}}^{\mathrm{miss}}$ calculation as described in the respective sections resulting in a variation of $E_{\mathrm{T}}^{\mathrm{miss}}$ itself. These contributions are the main uncertainty of the $E_{\mathrm{T}}^{\mathrm{miss}}$ measurement.

Pile-up

There are two different approaches available how to reweight the MC to the actual pile-up conditions. For the nominal analysis, the mean number of interactions per bunch crossing is averaged over a LB. This mean is used as input for the reweighting. Alternatively, the mean number of interactions for each bunch-crossing can be determined individually resulting in a slightly different $\langle\mu\rangle$ distribution to be used for the reweighting procedure. The analysis has been repeated with this latter, alternative pile-up distribution. The relative deviations from the nominal analysis have been taken as the systematic uncertainty related to pile-up.

Luminosity

The uncertainty of the total integrated luminosity used for the analysis depends on the total uncertainty of the luminosity measurement in ATLAS studied by the Luminosity Working Group. For the 2011 data this uncertainty is determined to be 3.7 % [197]. Since the QCD, W+jets, and top backgrounds are determined from data, this uncertainty only affects the remaining Z+jets, Drell-Yan, and diboson background. The overall uncertainty assigned in the signal region due to the luminosity is thereby reduced to 0.8 %.

8.7.2. Theory Uncertainties on the Signal Cross Section Predictions

For most of the different SUSY production processes, the central value of the NLO cross section is calculated by PROSPINO [136, 139–143] with the CTEQ6.6m PDF [151] (cf. Sec. 5.2.1). The three contributing uncertainties are the uncertainties on the PDF, on the strong coupling constant, and on the factorization and renormalization scale. The impact from the scale and the PDF uncertainty dominate ($\approx 10\,\%$), while the one from the strong coupling constant is the smallest ($\approx 1\,\%$). The combined theory uncertainty is not subject to large fluctuations across the GMSB signal grid (cf. Fig. 9.6(c)) and amounts to roughly 15 %.

PDF

The uncertainties on the PDF are represented by 22 sets of eigenvectors used in the PDF global fit. The 44 error PDF sets [214] included in the CTEQ6.6m are the 90% CL upper and lower bound variation of the PDF with respect to each eigenvector. The uncertainty can be evaluated by the Hessian method [215] taking the envelope of the deviations from the central value with these uncertainties. It is defined as the maximum positive and negative errors on the observable X_i

$$\Delta X_+ = \frac{1}{1.645}\sqrt{\sum_{i=1}^{22}\left(max[(X_i^+ - X_0),(X_i^- - X_0),0]\right)^2},$$
$$\Delta X_- = \frac{1}{1.645}\sqrt{\sum_{i=1}^{22}\left(max[(X_0 - X_i^+),(X_0 - X_i^-),0]\right)^2}, \tag{8.12}$$

where X_i^+, X_i^-, X_0 are the upper, lower, and nominal values of the eigenvector X_i, respectively. The factor 1.645 is used to convert the 90% CL uncertainty into a 68% CL uncertainty (1σ). The total symmetrized PDF uncertainty is obtained by averaging ΔX_+ and ΔX_-.

Strong Coupling Constant

The theoretical uncertainties of the strong coupling constant α_s are represented by two extreme CTEQ6.6AS variations, i.e. AS-2 and AS+2. The actual uncertainty is estimated as one half of the difference between the resulting cross sections using both PDFs

$$\Delta\sigma(\alpha_s) = \frac{1}{2}\frac{1}{1.645}\left|\sigma[AS-2] - \sigma[AS+2]\right|, \tag{8.13}$$

where σ is the NLO cross section using the specified PDF. Again, the factor 1.645 is used to convert the 90% CL uncertainty into a 68% CL uncertainty (1σ).

Scale

The nominal scale is given by $Q = m_{\tilde{p}}$ where $\tilde{p}$ is the produced sparticle. The scale uncertainty is evaluated by changing the factorization and renormalization scales by a factor of 2 or 1/2 in the PROSPINO calculations. The uncertainties are estimated simply by comparing PROSPINO NLO cross section values obtained with or without scale variations.

Combination

Using the CTEQ6.6AS method guarantees a correct and independent treatment of the α_s and PDF uncertainty. Nonetheless, some correlation between the α_s and PDF parameters may exist. Hence, for the combination of the PDF and α_s uncertainties, the recommendations of Ref. [216] have been followed. The scale uncertainty is then added in quadrature.

8.7.3. Theory Uncertainties on the Transfer Factor

The theoretical uncertainty on the MC-based corrected extrapolation of the W and top backgrounds from the control region into the signal region is estimated using alternative MC samples obtained by varying the renormalization and factorization scales, the functional form of the factorization scale, and the matching threshold in the parton shower process [217]. Extensive studies on this have been carried out in the context of the search for SUSY with single light leptons described in detail in [218]. Therefore, the same methods have been applied here [219]. Minor adjustments were necessary.

The original selection did not consider τ leptons which are therefore not present in the additionally generated MC samples. Instead of requiring two generated τ leptons, one muon and one jet are selected, replacing one generated, leptonically decaying τ and one misidentified τ. Despite the detector effects for muons being different than for τ candidates these differences were not quantified and are missing from this study. Due to the nature of the study, it was not feasible to easily repeat it. The effect on the uncertainty is assumed to be tolerable.

To further emphasize the domination of events containing one generated τ and one misidentified τ only semileptonic $t\bar{t}$ events have been considered. The different scale variations are treated as uncorrelated and have been combined taking the largest deviations possible. The W and top backgrounds are combined treating them fully correlated since the same scaling is applied to both backgrounds.

8.7.4. Systematic Uncertainties for the SM Background

In the following, a quantitative estimation for all the systematic uncertainties mentioned above is given for each of the individual background contributions. The general procedure is applying the individual systematic uncertainties to the affected objects, i.e. for JES, or the event, i.e. pile-up, determining the deviation in the number of selected events in the signal region compared to the selection in the nominal MC sample. This deviation is then taken as contribution to the overall systematic uncertainty.

All the systematic uncertainties presented here for the SM background affect the signal events in exactly the same manner. They are vitally important for the limit setting procedure and are shown in the following chapter (cf. Sec. 9.2).

	diboson		Z+jets		W+jets, top	
Systematic variation	No. of events	Rel. deviation	No. of events	Rel. deviation	No. of events	Rel. deviation
Nominal	0.135		1.08		4.09	
JES	0.147	8.5%	1.51	39.3%	5.59	13.2%
JER	0.136	0.1%	1.08	0.0%	3.13	-24.0%
TES	0.145	6.7%	1.28	18.0%	5.64	6.3%
TauID	0.145	7.1%	1.17	7.9%	4.13	0.2%
TauFake	0.140	3.6%	1.10	1.9%	4.04	-1.9%
Scaling	0.135	0.0%	1.08	0.0%	5.32	30.0%
Pileup	0.146	7.6%	1.09	1.3%	4.11	-0.1%
Luminosity	0.140	3.7%	1.12	3.7%	4.09	0.0%
Theory	0.135	0.0%	1.08	0.0%	4.93	20.6%
Total		19.1%		58.0%		47.8%

Table 8.11.: Effect of the systematic variations studied for all separate background channels after the full event selection [3].

W+jets and top background

The dominant backgrounds W and top are affected by the individual systematic uncertainties themselves and by simultaneously induced changes of the scaling factor. To account for both effects, the transfer factor as well as the background prediction have been recalculated using a data set in which all properties were varied by the respective systematic uncertainty for each individual subsample. The various predictions and their relative deviation are listed in Tab. 8.11. The greatest contributions are the JES, JER, and theory uncertainties.

For these backgrounds, an additional uncertainty "Scaling" has been introduced. It takes into account that the central value of the scaling and transfer factor depends on the definition of the control region and is sensitive to the slightly different composition of generated and misidentified τ candidates in the control region compared to the signal region. This introduces another uncertainty of approximately 30 % accounting for the largest uncertainty.

Uncertainties arising due to the limited data and MC statistics in the signal and control region have been computed separately and propagated to the statistical uncertainties of the predicted event number.

Z+jets background

Due to the very limited statistics present for Z+jets, the different systematics have been calculated after various steps of the cutflow to minimize the effect of statistical fluctuations induced by very few events with varying event weights. The cut on m_{eff} is mostly sensitive to variations of the jet kinematics. Therefore, the systematics on the τ contributions are calculated while omitting this requirement. Likewise, it was attempted to estimate the uncertainties for the jet

contributions while not requiring $m_{\mathrm{T1}} + m_{\mathrm{T2}} > 80\,\mathrm{GeV}$. However, this has been found to be not feasible since m_{T} depends both on the τ kinematics as well as $E_{\mathrm{T}}^{\mathrm{miss}}$. As a result the systematics for JES and JER are dominated by single events passing or failing the selection. The remaining variations are not affected as strongly by statistical fluctuations and are estimated after applying the final selection.

The Z+jets background is dominated by events containing two generated τ leptons and recoil jets resulting in TES and JES having the strongest impact on the resulting uncertainties (cf. Tab. 8.11).

Diboson background

The number of diboson events relies on the prediction of MC only. Hence, the treatment of the systematic uncertainties can be done without any necessary alterations and the general procedure has been applied to calculate all uncertainties mentioned above. No unexpected behavior can be found and the results are listed in Tab. 8.11.

Drell-Yan and QCD background

The signal region contains no events originating from Drell-Yan production. It has been checked that this prediction remains constant under the systematic variations. It has been found that neither of the effects studied affects the expected number of background events.

Since the SM background prediction is negligible for QCD, the same test has been performed. The same results as for the Drell-Yan background have been found except for the JES variations where 0.001 background events are predicted. Nonetheless, both channels are not considered further due to their insignificant contribution compared to the other backgrounds.

Combination

The individual systematic uncertainties combined for all channels can be found in Tab. 8.12. The dominant contributions are on the one hand the jet kinematics and on the other hand the scaling due to W and top being the dominant background, and the theoretical uncertainty. To obtain a total systematic error on the prediction of SM background events in the signal region, these individual uncertainties need to be combined taking into account possible existing correlations. This concerns JES and TES because both systematics are subject to calorimetric mismeasurements and biased calibrations. They show notable asymmetries depending on if the variations are added or subtracted. Therefore, those two contributions have been added fully correlated to account for this asymmetry and avoid an underestimation of the error

$$\sigma_{\mathrm{JES/TES}} = \frac{|\sigma_{\mathrm{JESup}}| + |\sigma_{\mathrm{TESdown}}|}{2} + \frac{|\sigma_{\mathrm{TESup}}| + |\sigma_{\mathrm{JESdown}}|}{2}. \tag{8.14}$$

All other contributions are uncorrelated and added in quadrature

$$\sigma_{\mathrm{Syst}}^{\mathrm{Tot}} = \sqrt{\sigma_{\mathrm{JES/TES}}^2 + \sigma_{\mathrm{JER}}^2 + \sigma_{\mathrm{TauID}}^2 + \sigma_{\mathrm{TauFake}}^2 + \sigma_{\mathrm{Scaling}}^2 + \sigma_{\mathrm{Pileup}}^2 + \sigma_{\mathrm{Lumi}}^2}, \tag{8.15}$$

Systematic variation	No. of events	Rel. deviation
Nominal	5.31	
JES	6.24	17.6%
JER	4.34	-18.1%
TES	5.65	6.6%
TauID	5.44	2.5%
TauFake	5.28	-0.5%
Scaling	6.53	23.1%
Pileup	5.35	0.9%
Luminosity	5.35	0.8%
Theory	6.15	15.9%
Total		41.4%

Table 8.12.: Effect of the systematic variations studied for all backgrounds combined after the full event selection [3].

where the individual uncertainties correspond to those listed in Tab. 8.12. The overall systematic uncertainty is 41.4 %, resulting in a SM background and GMSB benchmark point prediction for the signal region of $5.3 \pm 1.3(\text{stat}) \pm 2.2(\text{sys})$ and $20.8 \pm 3.4(\text{stat}) \pm 3.6(\text{sys}) \pm 3.3(\text{theo})$, respectively.

9. Results of the Search for New Physics with Large Transverse Momentum, Jets, and at least Two τ Leptons

In the following, a detailed comparison between real collision data and simulated events at different stages of the event selection is presented verifying the correct estimation of the SM background and the general understanding of the data, especially the τ kinematics. No excess above the SM expectation has been found in data and model-independent exclusion limits are set on the number of events from new physics and on the visible cross section. The results are also interpreted within the minimal GMSB model. Upper limits on the GMSB model parameters as well as the production and visible cross section are presented. They represent the most stringent limits to date.

9.1. Kinematic Distributions in the Signal Region

The number of expected events for the SM background in the signal region is $5.3 \pm 1.3(\text{stat}) \pm 2.2(\text{sys})$ which is in very good agreement with the three events observed in real collision data. Table 9.1 lists the number of events expected after each selection step for the sum of all SM background and the data. For comparison, it also shows the number of events expected for the

	$\sum$ SM	Data	GMSB4030
Preselection	$(4.56 \pm 0.0039) \cdot 10^9$	$2.6 \cdot 10^7$	696 ± 13
$E_{\text{T}}^{\text{miss}} > 130\,\text{GeV}$	260000 ± 6000	509069	462 ± 12
$p_{\text{T}}^{\text{jet1}} > 130\,\text{GeV}$	175000 ± 4300	440351	407.4 ± 9.5
$p_{\text{T}}^{\text{jet2}} > 30\,\text{GeV}$	117000 ± 4300	116655	400.0 ± 9.5
Lepton Veto	95800 ± 4300	99078	123.6 ± 6.4
$N_\tau \geq 1$	4060 ± 170	3647	71.6 ± 5.7
$N_\tau \geq 2$	53.3 ± 6.7	52	25.1 ± 3.5
$\Delta\phi(E_{\text{T}}^{\text{miss}}, \text{jet1/2}) > 0.4$	47.0 ± 6.2	43	22.2 ± 3.4
$m_{\text{eff}} > 700\,\text{GeV}$	10.3 ± 2.1	10	21.7 ± 3.4
$m_{\text{T1}} + m_{\text{T2}} > 80\,\text{GeV}$	$5.3 \pm 1.3(\text{stat}) \pm 2.2(\text{sys})$	3	$20.8 \pm 3.4(\text{stat}) \pm 3.6(\text{sys}) \pm 3.3(\text{theo})$

Table 9.1.: Comparison between the number of expected events for the sum of the different SM processes, $2.05\,\text{fb}^{-1}$ of the 2011 data, and the GMSB benchmark point. For the W and top background the scaling factor has been applied. The systematic uncertainties are given only for the final selection after applying all cuts.

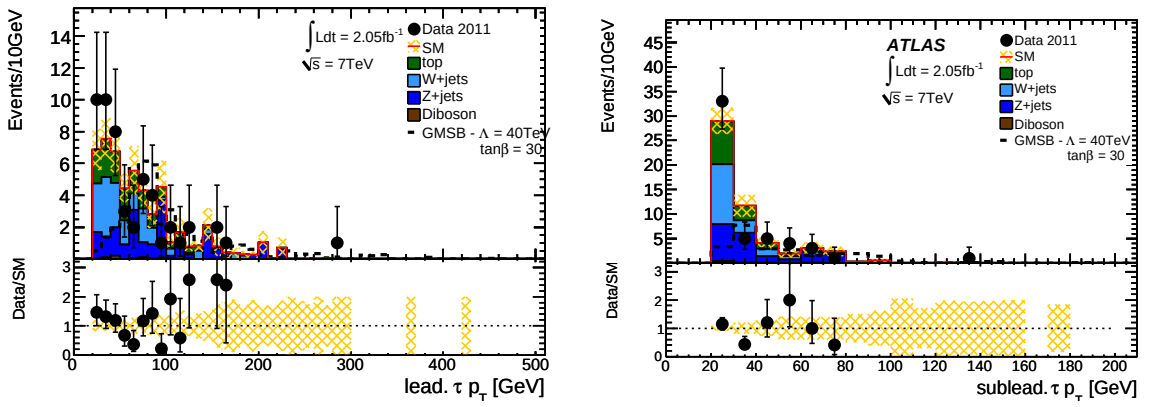

(a) (b)

Figure 9.1.: (a) $p_{\mathrm{T}}^{\tau 1}$ and (b) $p_{\mathrm{T}}^{\tau 2}$ after requiring at least two τ. Here and in the following, the W and top scaling factor has been applied.

chosen GMSB4030 benchmark point. A good agreement between data and MC can be seen at most of the cut steps, especially after the requirement of two τ candidates. The leading and subleading p_{T}^{τ} after requiring at least two reconstructed τ candidates per event and applying the scaling factors are shown in Fig. 9.1. Clearly, the distributions are dominated by large statistical fluctuations impeding a reasonable comparison of the shapes.

Further kinematic distributions after the ditau requirement are shown in Figs. 9.2 and C.2 in the Appendix. The H_{T}, $E_{\mathrm{T}}^{\mathrm{miss}}$, and consequently the m_{eff} distributions are also subject to large statistical uncertainties. Nonetheless, the agreement between data and MC is within the statistical uncertainties. The invariant mass distribution of the two leading τ candidates (cf. Fig. 9.2(d)) shows an excellent agreement between data and MC concerning its shape demonstrating that the scaling factor can indeed be transferred from the control to the signal region. Additionally, it confirms the assumption that Z+jets events are indeed well modeled in MC and do not need to be estimated separately from data in contrast to W+jets and $t\bar{t}$ events.

The m_{eff} distribution is again shown in Fig. 9.3(a) after events containing jets aligned with $E_{\mathrm{T}}^{\mathrm{miss}}$ have been rejected. Fig. 9.3(b) shows the $m_{\mathrm{T1}} + m_{\mathrm{T2}}$ distribution before the corresponding cut is applied. As mentioned above, three data events are selected. For one of them, Fig. 9.4 shows the event display. The upper left part shows the x-y-plane of the detector where two jets (objects pointing towards the top and left) and two τ candidates (right and bottom) are visible. They are nicely separated and not aligned to $E_{\mathrm{T}}^{\mathrm{miss}}$ (red line). The gray lines illustrate the reconstructed tracks in the inner detector, while the green and red bars illustrate the energy deposition in the electromagnetic and hadronic calorimeter, respectively. The smaller plot on the right shows the momentum of the four objects and $E_{\mathrm{T}}^{\mathrm{miss}}$ in the ϕ-η-plane. They were found to be $p_{\mathrm{T}}^{\mathrm{jet1}} = 214\,\mathrm{GeV}$, $p_{\mathrm{T}}^{\mathrm{jet2}} = 177\,\mathrm{GeV}$, $p_{\mathrm{T}}^{\tau 1} = 66\,\mathrm{GeV}$, $p_{\mathrm{T}}^{\tau 2} = 48\,\mathrm{GeV}$, and $E_{\mathrm{T}}^{\mathrm{miss}} = 202\,\mathrm{GeV}$. The bottom part shows the event in the y-z-plane.

Kinematic distributions in the signal region can be found in Figs. 9.5 and C.3 in the Appendix. Naturally, the low number of selected events prevents a reasonable comparison between the shapes of the distributions from data and simulated events. Nonetheless, they illustrate that

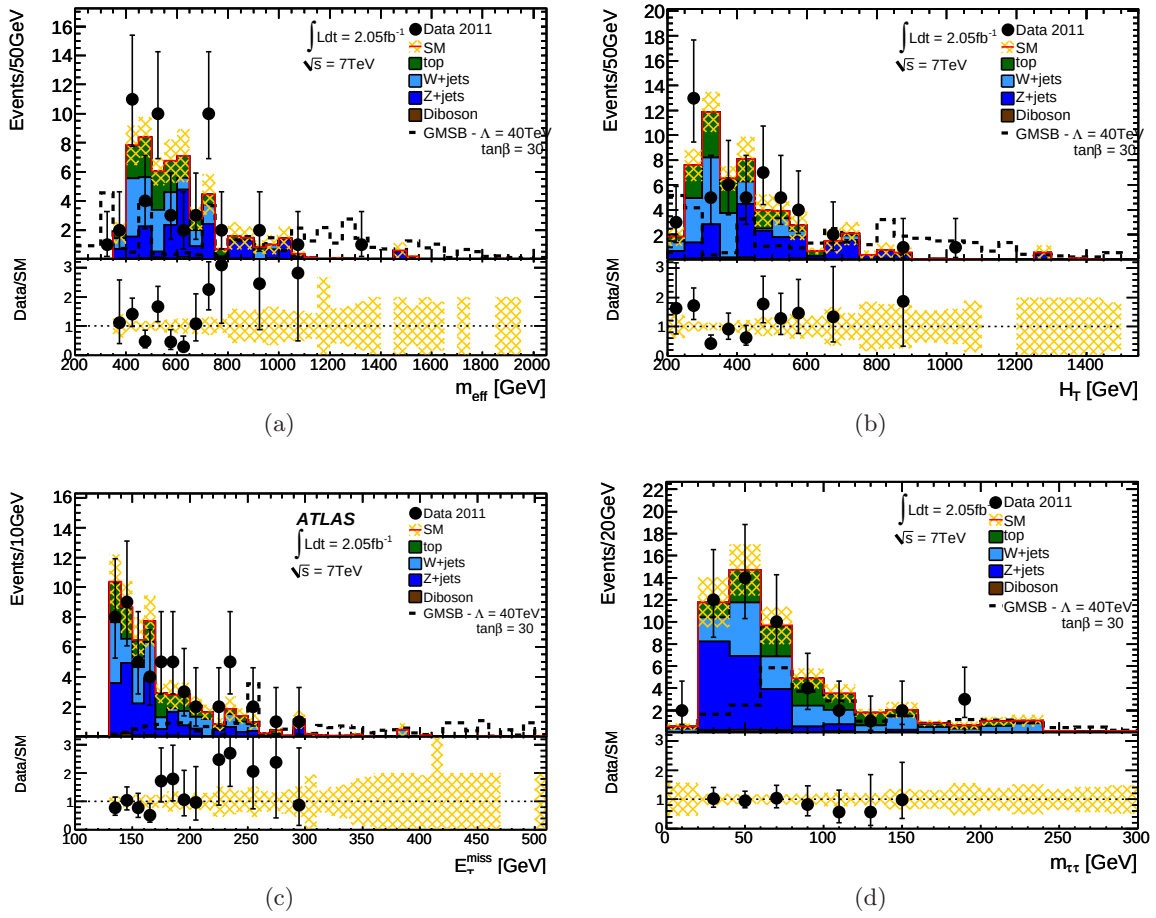

(a) (b) (c) (d)

Figure 9.2.: (a) m_{eff}, (b) H_{T}, (c) $E_{\text{T}}^{\text{miss}}$, and (d) $m_{\tau\tau}$ after the ditau requirement in the event selection.

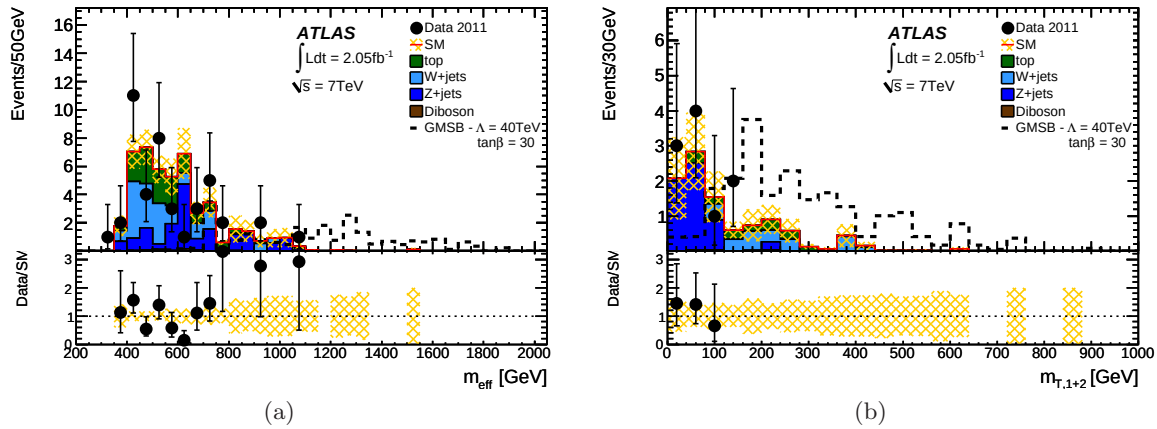

(a) (b)

Figure 9.3.: (a) m_{eff} after applying the $\Delta\phi$ cuts and (b) the sum of the transverse mass of the two leading τ candidates after applying $m_{\text{eff}} > 700\,\text{GeV}$.

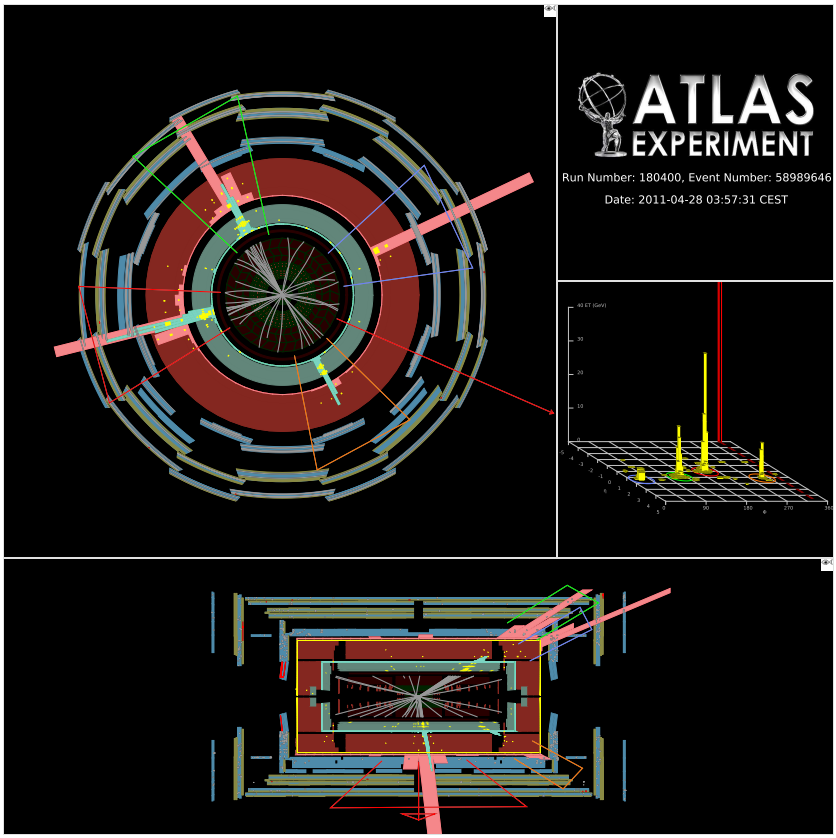

Figure 9.4.: Event display for one of the three candidate data events selected in the signal region (run 180400, event 58989646). The two jets (top and left object in x-y-plane) and the two τ candidates (bottom and right) are easily visible and nicely separated. The red line indicates $E_{\mathrm{T}}^{\mathrm{miss}}$ [220].

no unexpected behavior occurs in any of the distributions. In most cases, the SM background tends to adopt low values in contrast to the GMSB benchmark adopting higher values. In general, the data points can also be found in the kinematically lower regions illustrating that no hints of GMSB events can be seen. No signs for new physics with two τ candidates and large $E_{\mathrm{T}}^{\mathrm{miss}}$ is observed and therefore, limits on the minimal GMSB model parameters are set. Details on the limit setting procedure can be found in the Appendix (cf. Sec. A).

9.2. Exclusion Limits

If a SUSY scenario is excluded or not, depends on the number of observed data events ($N_{\mathrm{data}} = 3$) and the expected number of background ($N_{\mathrm{bkg}} = 5.3 \pm 1.3(\mathrm{stat}) \pm 2.2(\mathrm{sys})$) and signal events ($N_{\mathrm{GMSB4030}} = 20.8 \pm 3.4(\mathrm{stat}) \pm 3.6(\mathrm{sys}) \pm 3.3(\mathrm{theo})$). For the GMSB Λ-tanβ-plane studied in this thesis, the number of expected signal events along with the acceptance and selection efficiency is shown in Fig. 8.14. Depending on the exact model parameter setting the exact number varies between 400 and 0.01 events in the chosen parameter range for low and high Λ values, respectively. In addition, the uncertainties on the number of events of the signal

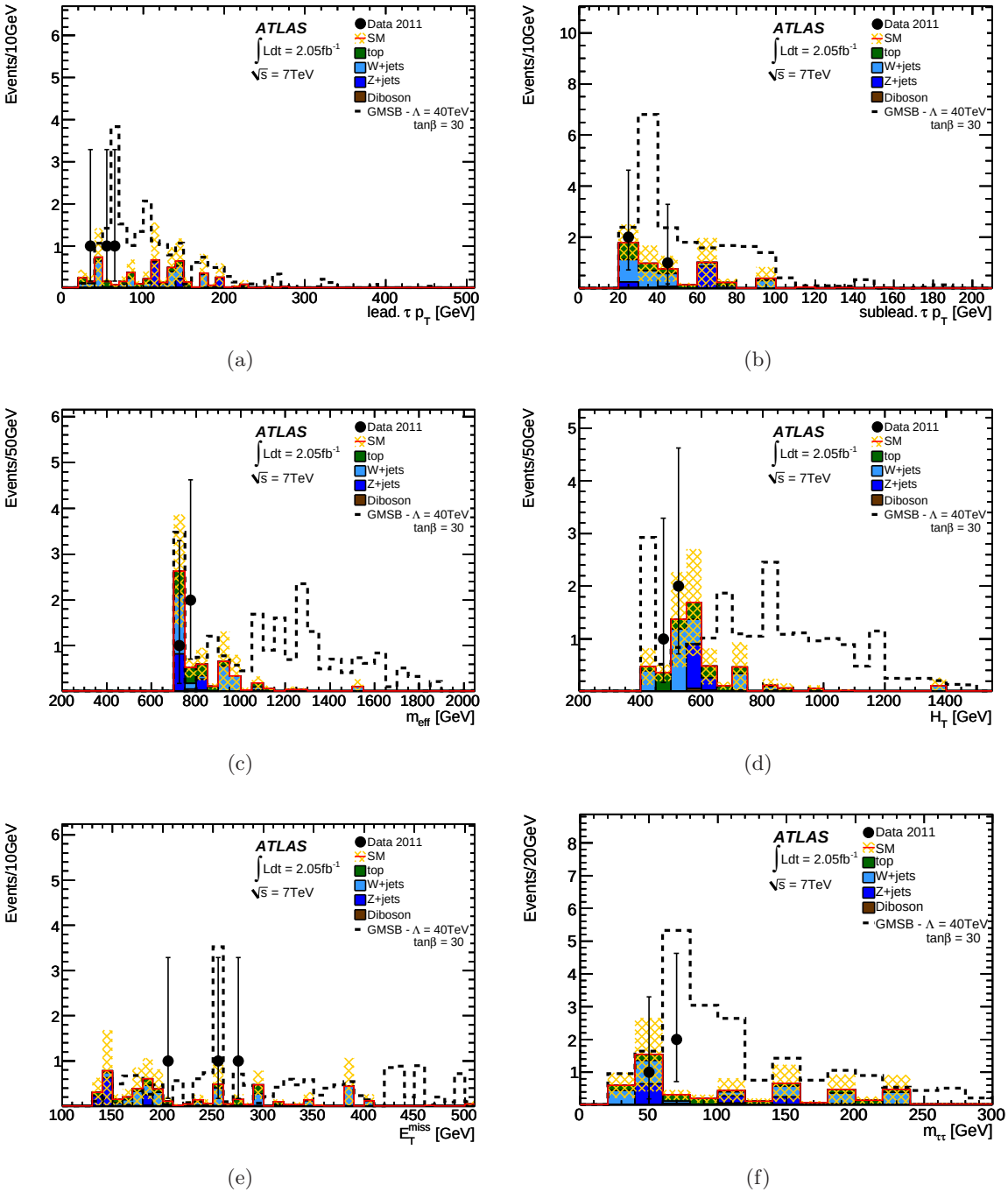

Figure 9.5.: (a) $p_{\mathrm{T}}^{\tau 1}$, (b) $p_{\mathrm{T}}^{\tau 2}$, (c) m_{eff}, (d) H_{T}, (e) $E_{\mathrm{T}}^{\mathrm{miss}}$, and (f) $m_{\tau\tau}$ in the signal region. The error bands comprise both statistical and systematic uncertainties.

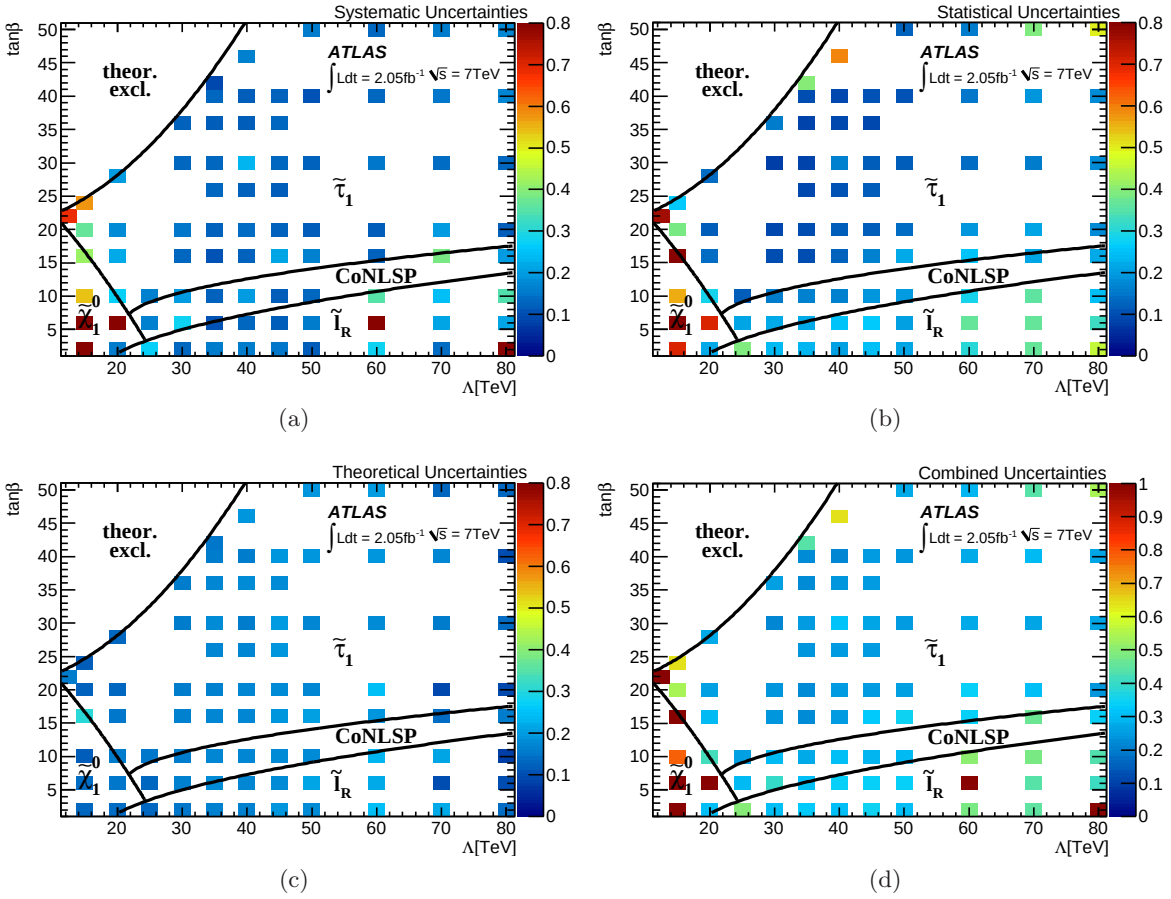

Figure 9.6.: (a) Relative uncertainty on the number of events from the systematic uncertainties, (b) from the limited MC statistics of the generated signal samples, and (c) from theory uncertainties over the GMSB parameter space. (d) Relative combined uncertainties taking into account all other uncertainties.

scenarios play a pivotal role in the limit setting procedure. Since the production process, the NLSP and thus the event kinematics vary across the GMSB parameter space a variation of the uncertainties is expected as well.

The systematic uncertainties considered for the GMSB grid are identical to the ones considered for the SM background discussed in detail in Sec. 8.7. The jet and τ energy scale uncertainty are treated as correlated as demonstrated in Eq. (8.14). The remaining uncertainties are treated as uncorrelated. In case of asymmetric uncertainties, the larger uncertainty value was chosen. The total relative systematic uncertainty on the number of signal events across the grid is shown in Fig. 9.6(a). In the $\tilde{\tau}_1$ NLSP region the distribution is rather flat and adopts values between 8 % and 20 %. Higher values can be observed mainly in the non-$\tilde{\tau}$ NLSP regions where the sensitivity of this analysis is low.

The uncertainties from the limited MC statistics of the used sample can be as low as 9 % in the intermediate Λ range for which the analysis is optimized because the exclusion limit is expected in that region. It is shown in Fig. 9.6(b). The variations across the grid are similar to

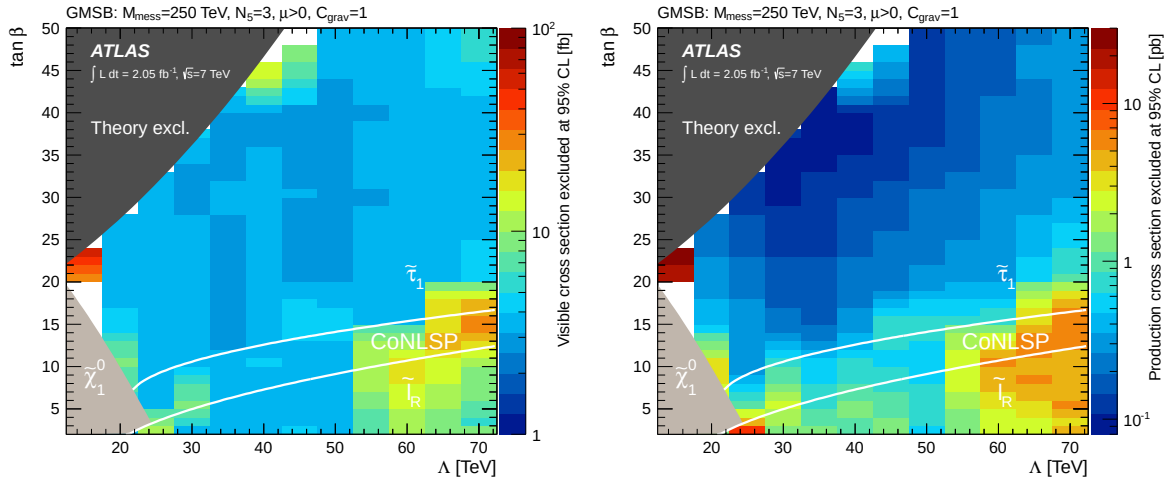

(a) (b)

Figure 9.7.: Observed 95 % CL upper limits on (a) the visible and (b) the production cross section for the minimal GMSB model parameters Λ and $\tan\beta$ for $\widetilde{\tau}_1$ and $\tilde{\ell}$ NLSP [220]. The light gray area indicates the region where the NLSP is the neutralino, which is not considered here. The white lines indicate the different NLSP regions determining the phenomenology. Further model parameters are $M_{\text{mess}} = 250\,\text{TeV}$, $N_5 = 3$, $\text{sgn}\,\mu = +$, and $C_{\text{grav}} = 1$.

the systematic uncertainties and adopt their highest values in the non-$\widetilde{\tau}$ NLSP region.

Figure 9.6(c) shows the combined theory uncertainties (cf. Sec. 8.7.2) from the PDF, α_s, and scale uncertainties. The theoretical uncertainties are flat across the grid and have a negligible effect on the exclusion limit. It has been determined with and without including the theoretical uncertainties and no visible difference on the 95 % CL level contour in the GMSB parameter space has been found (cf. Fig. C.4 in the Appendix). Although the theory uncertainties are large ($\approx 15\,\%$), they are not dominating the overall combined uncertainty.

The combined overall uncertainties for each grid point show the same features as the systematic and statistical uncertainties, a rather flat behavior in the $\widetilde{\tau}$ NLSP region accompanied by higher values in the other NLSP regions. The combined uncertainties vary mostly between 20 % and 30 %. They are shown in Fig. 9.6(d).

Using the number of observed and expected background events, the p-value of the background only hypothesis can be determined for every grid point, i.e. for any number of expected signal events. This can be converted into a 95 % CL limit on the number of events in the signal region from new physics. The observed (expected) limit[1] is found to be 5.9 (7.0) events.

The *visible* cross section σ_{vis} is defined by the product of the cross section, the branching fraction, the detector acceptance, and the event selection efficiency. From the limit on the number of signal events immediately a limit on the visible cross section can be derived by dividing it by the integrated luminosity. The observed (expected) 95 % CL upper limit is

[1]The expected limit is the limit that would be set if the data events were identical to the expected number of background events.

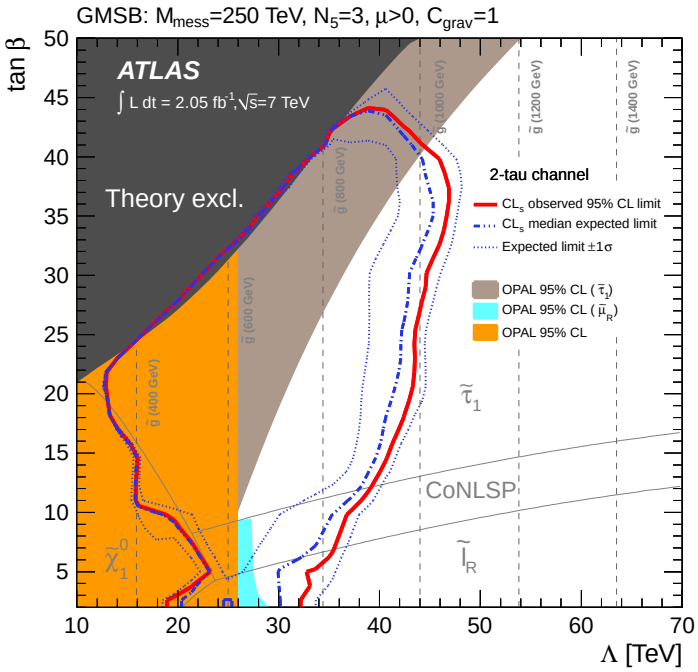

Figure 9.8.: Expected and observed 95 % CL limits on the minimal GMSB model parameters in the Λ-tanβ-plane for $M_{\text{mess}} = 250\,\text{TeV}$, $N_5 = 3$, $\text{sgn}\,\mu = +$, and $C_{\text{grav}} = 1$. It is in excellent agreement with the limits shown in [2].

found to be 2.9 fb (3.4 fb). These limits are model-independent and do not depend on the GMSB model parameters.

Since the limit on the number of events from new physics depends on the systematic uncertainties and the uncertainty from the limited MC signal sample size, a limit on the visible cross section can be determined for each individual signal grid point. The observed 95 % CL upper limits are shown in Fig. 9.7(a) adopting values of $\sigma_{\text{vis}} < (3 - 25)\,\text{fb}$. The shape is dominated by the structure of the uncertainties that are reflected in the different NLSP regions. From the limit on the visible cross section also a limit on the production cross section σ_{prod} can be determined by correcting for the branching ratio, the acceptance, and the selection efficiency. Figure 9.7(b) shows the observed 95 % CL upper limit on the production cross section across the GMSB grid. Here, the dominant contributing factor is the acceptance leading to the best limit ($\sigma_{\text{prod}} < 0.1\,\text{pb}$) in the intermediate Λ and high $\tan\beta$ range.

From the limit on the number of events also the limit on the minimal GMSB parameters can be derived. Figure 9.8 shows the observed (expected) exclusion limit across the GMSB grid. The observed limit exceeds the expected due to the number of observed events being smaller than the number of expected events from SM background. For $10 < \tan\beta < 40$, the region $\Lambda < 40 - 50$ TeV is excluded, while, for higher and lower values of $\tan\beta$, the limit decreases to slightly lower values. For lower $\tan\beta$ values, this is due to the NLSP changing from $\widetilde{\tau}_1$ to $\widetilde{\ell}_{\text{R}}$. Since this change is smooth the exclusion also expands into this region but is less stringent. The best limit is obtained for $\Lambda = 47\,\text{TeV}$ and $\tan\beta = 37$. In general, $\Lambda < 32\,\text{TeV}$ is excluded independent of $\tan\beta$.

Process	Nominal	No lepton veto
Data	3	3
SM	$5.3 \pm 1.3(\text{stat}) \pm 2.2(\text{sys})$	$5.7 \pm 1.3 \pm 2.4$
GMSB4030	$20.8 \pm 3.4(\text{stat}) \pm 3.6(\text{sys}) \pm 3.3(\text{theo})$	$46.6 \pm 9.0 \pm 13.9$

Table 9.2.: Number of observed and expected background and signal events in the signal region for the nominal selection and omitting the light lepton veto [221].

This exclusion goes beyond previous LEP searches also shown in Fig. 9.8, except in the very high tanβ region. The LEP searches for $\widetilde{\tau}$ NLSP scenarios focused on neutralino ($e^+e^- \to \widetilde{\chi}_1^0\widetilde{\chi}_1^0 \to \widetilde{\tau}_1\tau\widetilde{\tau}_1\tau$), chargino ($e^+e^- \to \widetilde{\chi}^\pm\widetilde{\chi}^\mp \to \widetilde{\tau}_1^+\nu_\tau\widetilde{\tau}_1^-\nu_\tau$), and direct $\widetilde{\tau}_1$ production ($e^+e^- \to \widetilde{\tau}_1^+\widetilde{\tau}_1^-$) leading to either two or four τ leptons in the final state. Various NLSP lifetimes were considered. Approximately $600\,\text{pb}^{-1}$ of collision data at a center-of-mass energy of 189-209 GeV was analyzed. The light brown area shows the limit on the $\widetilde{\tau}_1$ mass of $m_{\widetilde{\tau}_1} > 87\,\text{GeV}$ while the orange region shows the previous exclusion limit of $\Lambda < 26\,\text{TeV}$ [204].

The limits presented here have been converted into a limit on the gluino mass as gluino production is the main production process. Values below $m_{\widetilde{g}} < 990\,\text{GeV}$ are excluded at 95 % CL for $\tan\beta > 20$ with $M_{\text{mess}} = 250\,\text{TeV}$, $N_5 = 3$, $\text{sgn}\,\mu = +$, and $C_{\text{grav}} = 1$.

9.3. Further development of the Nominal Analysis

In order to allow for an easy combination of this analysis with other channels including τ leptons, the ATLAS collaboration decided to reject events containing light leptons. Due to the very different development of the different analyses, this combination has been postponed to be done on the full 2011 data set. Therefore, this analysis has been repeated omitting the application of this veto. Table 9.2 compares the number of observed and expected background and signal events in the signal region for the nominal selection with the corresponding number of events when vetoing events containing light leptons. It can be seen that the number of observed events does not change at all and the number of expected background events changes only by approximately 5 %. The selection efficiency and the number of signal events however increases by a factor of two having huge implications on the limits of the GMSB parameters.

The very rare occurrence of additional leptons in ditau events for SM processes causes the change in the event selection to be insignificant for the SM background. However, GMSB events containing up to four τ leptons are rather frequent. Taking into account that approximately 34 % of these τ leptons decay leptonically, finding additional leptons in the event is not uncommon.

Figure 9.9 shows the observed and expected limit for this alternative selection and a direct comparison to the limit contours of the nominal selection. It can be seen that the best limit improves by 5 TeV up to $\Lambda = 52\,\text{TeV}$ for $\tan\beta > 38$. The $\tan\beta$ independent exclusion limit improves by 8 TeV to $\Lambda < 40\,\text{TeV}$. Gluino masses below $m_{\widetilde{g}} < 1150\,\text{GeV}$ are excluded at 95 % CL. The shape of the small area at very high tanβ values is dominated by the granularity of the grid points and is excluded as well.

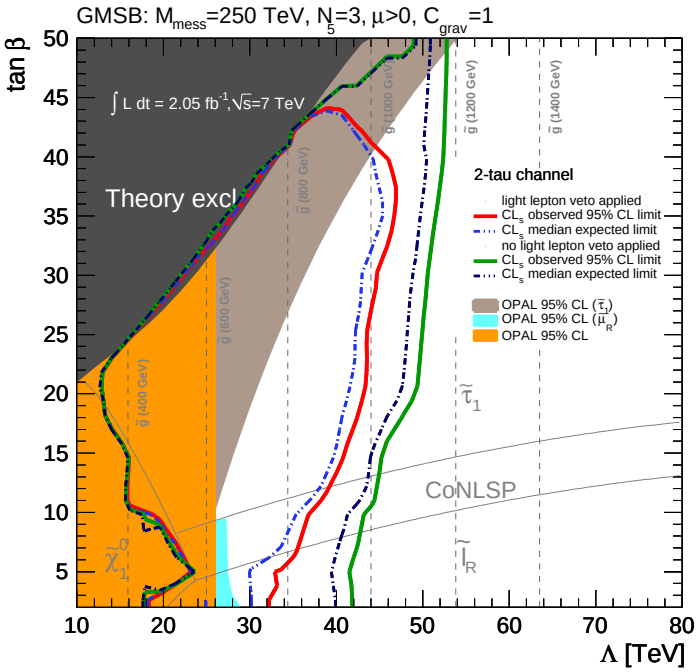

Figure 9.9.: Comparison of the expected and observed 95% CL limits investigating the impact of the light lepton veto on the minimal GMSB model parameters in the Λ-tanβ-plane for $M_{\text{mess}} = 250\,\text{TeV}$, $N_5 = 3$, $\text{sgn}\,\mu = +$, and $C_{\text{grav}} = 1$.

9.4. Comparison to other Analyses

Several other analyses have interpreted their results within GMSB models, e.g. a search for events containing exactly two leptons [222] or at least one τ candidate [190] within ATLAS. Figure 9.10 compares the expected and observed 95 % CL exclusion limits on the GMSB model parameters Λ and $\tan\beta$ for these two searches as well as the ditau search presented here. The one τ search exclusion line features a very similar shape but has a significantly lower reach than the presented search in all regions of the considered parameter space. The one τ search relies on at least one tight reconstructed τ candidate in comparison to at least two loose τ candidates in the ditau search. As has been demonstrated in Sec. 8.4, selecting loose τ candidates offers a higher event yield as well as a higher significance and therefore a stronger limit in the ditau case. When requiring only one τ candidate, a tight selection is necessary for background suppression purposes. Nonetheless, it also lowers the signal event yield and therefore the exclusion range.

The dilepton search relies on the leptonically decaying τ leptons only in the $\widetilde{\tau}$ NLSP region. Therefore, its limit is not competitive with neither the one τ nor the ditau search in that region as the leptons originating from the τ decay are often soft and the branching ratio is only 34 %. The exclusion lines of the τ searches and the dilepton search nicely cross where the CoNLSP region starts. The strength of the dilepton search lies within the $\tilde{\ell}_R$ NLSP region excluding higher values of Λ than the τ searches even though the analyzed data set is only $1\,\text{fb}^{-1}$, only half the size of the other two analyses. Taking into account the same luminosity as the τ searches will improve the limit also in the $\widetilde{\tau}$ NLSP region.

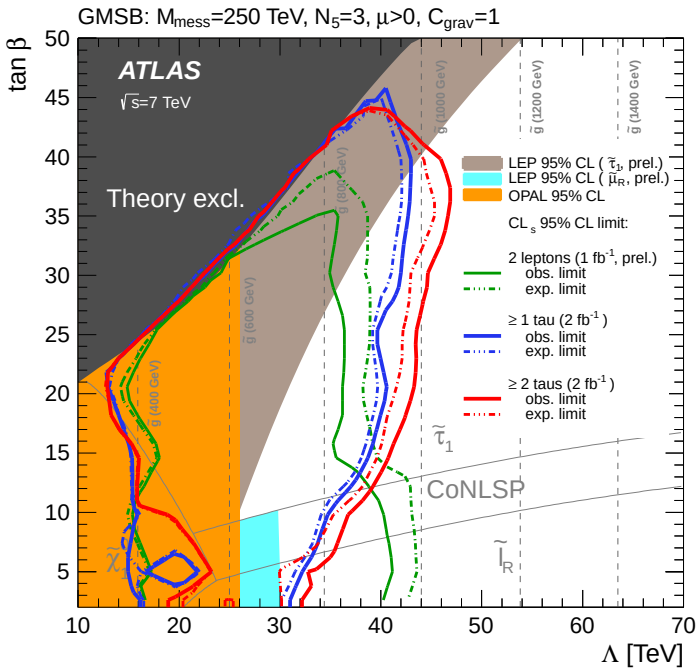

Figure 9.10.: Expected and observed 95% CL exclusion limits on the minimal GMSB model parameters Λ and $\tan\beta$ [220]. Further model parameters are $M_{\text{mess}} = 250\,\text{TeV}$, $N_5 = 3$, $\text{sgn}\,\mu = +$, and $C_{\text{grav}} = 1$. Shown are the limits from this ditau SUSY search, the ATLAS ≥ 1 τ SUSY search and the ATLAS 2 leptons SUSY search (preliminary), together with the limits from LEP (preliminary) and OPAL.

Figure 9.11 shows a wide variety of results of searches for SUSY models with different final states performed by ATLAS. The blue bars indicate the exclusion range of the search concerning one typical mass parameter characteristic for the studied model. The ditau search presented in this thesis has a similar exclusion strength concerning the mass parameter of the respective model and is part of the inclusive searches shown in the very first block of the figure labeled ATLAS-CONF-2012-002. So far, none of these searches have found a significant excess in data. The analysis of the complete 2011 data sample will further increase the exclusion range of the ditau search. A comparison of the reach of the two software versions that are used for the two different data taking periods ($2.05\,\text{fb}^{-1}$, the full 2011 data set) can be found in the appendix (cf. Fig. C.5). It includes an improved τ reconstruction algorithm where the overestimation of the number of misidentified τ candidates is reduced. It offers an increased reconstruction and identification efficiency and the reconstructed τ distributions are more compatible with data. Therefore, the exclusion increases slightly when using the same amount of data and the same selection procedure.

CMS has also studied dilepton events including τ leptons using the 2010 [224] and 2011 data sets [225] and performed a dedicated ditau search for supersymmetric events [226]. Both searches have also found a good agreement between the SM prediction and the observed number of events. These results have not been interpreted within the GMSB model not allowing for a more detailed comparison. In 2010, CMS performed a multi-lepton search [227] investigating models with gauge-mediation with split messengers (GMSM) [228]. These models are very

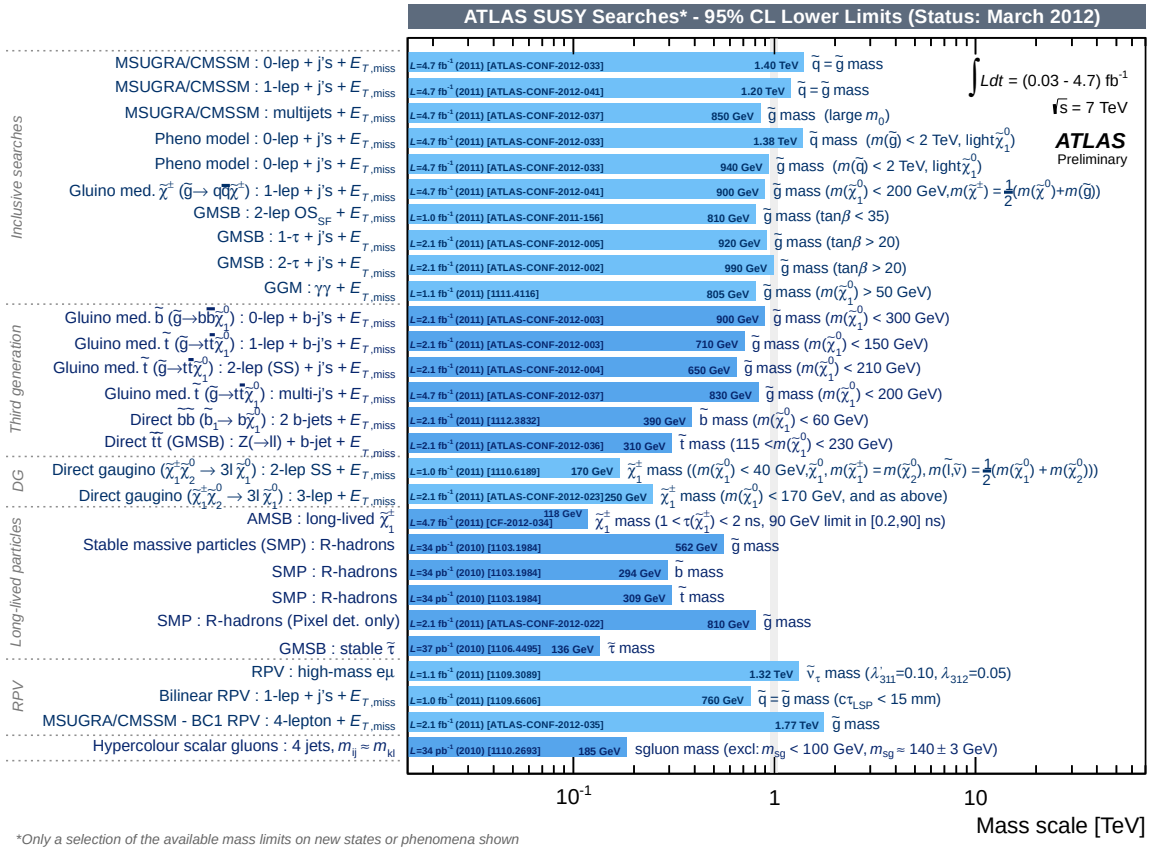

*Only a selection of the available mass limits on new states or phenomena shown

Figure 9.11.: Mass reach of ATLAS searches for various SUSY models [223]. Only a representative selection of the available results is shown.

similar to GMSB with the gravitino as LSP and sleptons as CoNLSP. Squark and gluino masses of up to 830 GeV and 1040 GeV are excluded, respectively. These results are similar to the findings of this search. Within GMSB models, the search presented provides the most extensive and stringent limits to date.

10. Conclusions and Outlook

In this thesis, the results of a search for events containing two or more hadronically decaying τ leptons, large $E_{\mathrm{T}}^{\mathrm{miss}}$, and jets using $2.05\,\mathrm{fb}^{-1}$ of $\sqrt{s} = 7\,\mathrm{TeV}$ pp collision data recorded with the ATLAS detector at the LHC have been presented. In a selection optimized for a SUSY signal, three events are found, consistent with the expected SM background of $5.3 \pm 1.3(\mathrm{stat}) \pm 2.2(\mathrm{sys})$ events. The results are used to set a model-independent 95 % CL upper limit of 5.9 events on the existence of new phenomena, corresponding to an upper limit on the visible cross section of 2.9 fb. Limits on the model parameters are set for a minimal GMSB model. The limit on the SUSY breaking scale Λ of 32 TeV is determined independently of $\tan\beta$. It increases up to 47 TeV for $\tan\beta = 37$. These results have been published by the ATLAS Collaboration [2]. They provide the most stringent tests in a large part of the parameter space considered to date, improving the previous best limits set by the LEP experiments.

Further improvement of the aforementioned results has been achieved by altering the nominal event selection and omitting the veto on events containing light leptons. Applying this selection, three data events are found again while the SM background expectation slightly increases to $5.7 \pm 1.3(\mathrm{stat}) \pm 2.4(\mathrm{sys})$ events, which is compatible with the data. Due to the increase of the selection efficiency of GMSB events by a factor of two, the limits on the breaking scale Λ improve significantly. For any $\tan\beta$, $\Lambda < 40\,\mathrm{TeV}$ is excluded, while the best limit can be set at Λ of 52 TeV for $\tan\beta > 38$. The limit on the gluino mass improves from $m_{\tilde{\mathrm{g}}} < 990\,\mathrm{GeV}$ to $m_{\tilde{\mathrm{g}}} < 1150\,\mathrm{GeV}$.

Since the cross section for GMSB drops by many orders of magnitude over the studied GMSB Λ-tanβ-plane, only a limited improvement of these limits is expected for a future analysis using the full 2011 data set corresponding to an integrated luminosity of $4.7\,\mathrm{fb}^{-1}$. First studies have shown that the limit is expected to be the same as for the event selection tested when omitting the lepton veto. Therefore, the combination of the searches for events containing at least one or at least two τ leptons, and events containing at least one τ lepton and one light lepton will be necessary to further extend these limits. However, improvement can also be expected from data taken at higher center-of-mass energies, i.e. $\sqrt{s} = 8\,\mathrm{TeV}$ in 2012 and $\sqrt{s} = 14\,\mathrm{TeV}$ in 2014 and beyond, since the GMSB cross section increases exponentially, e.g. by one order of magnitude when increasing the center-of-mass energy from 7 TeV to 14 TeV.

Another option considered for the 2012 data analysis is the interpretation of the results within more general gauge mediated scenarios (GGM) [229, 230] rather than within the minimal GMSB model. In GGM scenarios, the electroweak production is enhanced and the branching ratio of the $\widetilde{\chi}_1^0 \to \widetilde{\tau}_1\tau$ decay may be fixed to 100 % by decoupling the remaining sparticles of the spectrum, thus increasing the amount of high p_{T} τ leptons produced.

In a dedicated study using simulated events with $\sqrt{s} = 10\,\mathrm{TeV}$, which was the foreseen center-of-mass energy for the early LHC running period, the expected performance of the ATLAS detector in GMSB models with a $\widetilde{\tau}_1$ NLSP has been studied. It was demonstrated that a

discovery of GMSB models would have been possible in large parts of the parameter space using a cut-based analysis. After a possible discovery, a determination of the end point in the invariant ditau mass spectrum would be possible with data sets of about $10\,\mathrm{fb}^{-1}$, considering the GMSB6 benchmark point.

Furthermore, the results of a determination of the oblique corrections from a fit to electroweak precision data using the STU-formalism have been used to set constraints on the free parameters of the two Higgs doublet model and models with warped extra dimensions. Allowed regions within the parameter space which often allow for a heavier Higgs boson have been determined. In the two Higgs doublet model, the T parameter is unconstrained while S adopts small, positive values. Agreement with the electroweak precision data has been found for various model parameter configurations. In general, similar masses of the additional Higgs bosons are preferred. In warped extra dimension models, larger Higgs boson masses lead to a stronger constraint on the M_{KK} scale. When incorporating custodial symmetry in these models, heavy Higgs bosons cannot be accommodated.

The discovery of the Higgs at 125 GeV would strongly impact the allowed parameter space of these new physics models by increasing the constraints on the model parameter S and the then known amount of weak isospin violation in the electroweak SM. In the two Higgs doublet model, the T parameter would still be unconstrained while the allowed values for S would be significantly decreased. However, a light Higgs would not allow a precise prediction of the other free parameters. In warped extra dimension model, a light Higgs would make a direct discovery at the LHC of any of the KK states very difficult if the model is assumed to solve the hierarchy up to the Planck scale. If the cut-off is at a lower energy, the mass of the KK states would be smaller and the particles could be within the discovery reach of the LHC. On the other hand, warped extra dimension models with custodial symmetry are ruled out unless the Higgs is found in this mass range.

A. Limit Setting Method

Various methods for the determination of exclusion limits are discussed within the literature and among the LHC experiments. ATLAS adopted the CL_s method [231] (a Frequentist approach) which is also used by other collaborations as well (CMS, Tevatron experiments) allowing for an easy comparison of results. The name originates from exclusion limits being given at a certain *confidence level* (CL) indicating the degree of certainty of the exclusion. The CL_s method is derived from the CL_{s+b} method.

To determine the exclusion limits for the presented analysis a test statistic q needs to be defined that allows the distinction between two hypothesis: the data contains only background events b or the data contains signal and background events $s + b$. The corresponding test statistics are $f(q|b)$ and $f(q|s + b)$, respectively, are illustrated in Fig. A.1(a). The p-value for the b $(s+b)$ hypothesis is defined as the probability to find a value q that is equal or less compatible with the b $(s + b)$ hypothesis compared to what has actually been observed q_{obs}. It is derived from the test statistic. In general, a signal model is excluded at a CL

$$CL_{s+b} = 1 - \alpha\,, \tag{A.1}$$

if the corresponding p-value drops below α

$$p_{s+b} < \alpha\,, \tag{A.2}$$

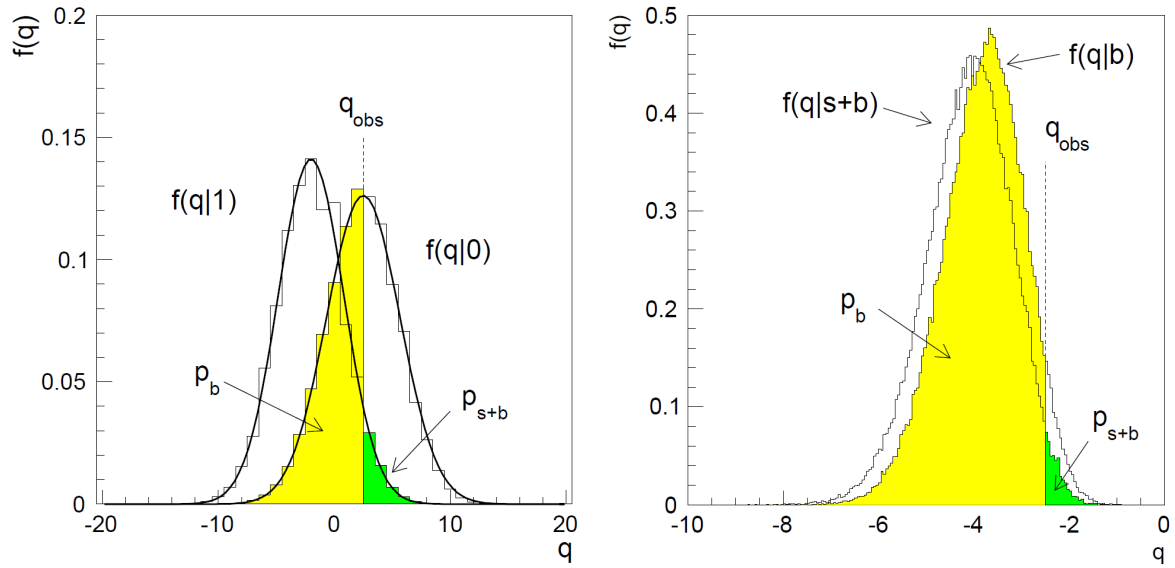

(a) (b)

Figure A.1.: (a) Distribution of the test variable q for the $s + b$ and b hypotheses and (b) in the case of very low sensitivity to the signal model [232].

where, e.g. $\alpha = 0.05$ converts into a 95 % CL.

Unfortunately, the CL_{s+b} procedure suffers from excluding models where the actual sensitivity is very low. This occurs if the number of expected signal events is much smaller than the number of background events. If $s \ll b$ and the observed number of events fluctuates downwards below $s + b$ the signal model might be excluded by mistake.

To avoid such wrong exclusions of models where there is no or only little sensitivity the CL_s method was proposed instead by altering the definition of the p-value

$$p_s = \frac{p_{s+b}}{1 - p_b} < \alpha. \tag{A.3}$$

The p-value is rescaled by $1 - p_b$. The higher the sensitivity the further apart are the two test statistics and $1 - p_b$ is close to one allowing a similar exclusion as if only relying on p_{s+b} itself. The lower the sensitivity the closer are the test statistics for the $s + b$ and the b hypothesis together as can be seen in Fig. A.1. In that case, $1 - p_b$ becomes very small thus increasing the redefined p-value and preventing an exclusion. Since this approach will always generate a p-value slightly larger than p_{s+b} the CL_s approach is considered conservative. The models excluded by CL_s will always be excluded by applying the original criterion stated in Eq. (A.2). However, the limits on the parameter, set with the CL_s method, are slightly weaker than with the CL_{s+b} method.

In ATLAS, a likelihood function is considered for the test statistic. It can be written as the product of a Poisson distribution P_{SR} for the signal region and a probability density function regarding the systematic uncertainties P_{syst} [233]

$$\begin{aligned} L(n_S, \boldsymbol{\theta}^0 | \mu, \boldsymbol{b}, \boldsymbol{\theta}) &= P_{SR} \times P_{syst} \\ &= P(n_S | \lambda_S(\mu, \boldsymbol{b}, \boldsymbol{\theta}) \times P_{syst}(\boldsymbol{\theta}^0, \boldsymbol{\theta})), \end{aligned} \tag{A.4}$$

where n_S is the number of observed events in the signal region. λ_S is a Poisson distribution depending on the background normalization factors $\boldsymbol{b}$, and the nuisance parameters $\boldsymbol{\theta}$ parametrizing the systematic uncertainties whereas $\boldsymbol{\theta}^0$ are the nominal values around which $\boldsymbol{\theta}$ are varied. If the nuisance parameters are uncorrelated P_{syst} is the product of the probability distributions which is usually a Gaussian. μ is the signal normalization factor or signal strength. Hereby, $\mu = 0$ corresponds to a model with no signal contribution (which is equivalent to the background only hypothesis), while for $\mu = 1$ the full number of expected signal events is taken into account (equivalent to the sum of the expected number of signal and background events).

The p-value is derived from a profile log likelihood ratio test

$$\begin{aligned} \Lambda(\mu) \equiv \Lambda(\mu, n_S, \boldsymbol{\theta}^0) &\equiv -2 \ln(Q) \\ &= -2 \ln \left(\frac{L(n_S, \boldsymbol{\theta}^0 | \mu, \hat{\hat{\boldsymbol{b}}}, \hat{\hat{\boldsymbol{\theta}}})}{L(n_S, \boldsymbol{\theta}^0 | \hat{\mu}, \hat{\boldsymbol{b}}, \hat{\boldsymbol{\theta}})} \right), \end{aligned} \tag{A.5}$$

where $\hat{\mu}, \hat{\boldsymbol{b}}, \hat{\boldsymbol{\theta}}$ maximize the likelihood function and $\hat{\hat{\boldsymbol{b}}}, \hat{\hat{\boldsymbol{\theta}}}$ maximize the likelihood function for the specific, fixed value of the signal strength μ and the data $\boldsymbol{n}, \boldsymbol{\theta}^0$. When testing specific models, it is sufficient to consider test for the nominal signal strength $\mu = 1$. Calculating the χ^2

distribution for the log likelihood ratio test given in Eq. (A.5) allows the determination of the one-sided p-value for a given χ^2: $p_{\chi^2}(\Lambda(\hat{\mu}))$. The complete description can be found here [233]. For the explicit calculation the implementation of the SUSY Working group `Combination package` [234] has been used.

B. Formulae of the Two Higgs Doublet Model

The contribution to the oblique parameters for a general two Higgs doublet model have been computed in [95, 96]. In this model, the five physical Higgs bosons (h^0, H^0, A^0, $H^\pm$) have the masses (M_{h^0}, M_{H^0}, M_{A^0}, $M_{H^\pm}$). The following formulas give the one loop corrections to S, T, and U from the two Higgs doublet model and do therefore not include the SM Higgs corrections to S, T, and U.

$$\begin{aligned} S = & \frac{1}{\pi M_Z^2}\{\sin^2(\beta-\alpha)\mathcal{B}_{22}(M_Z^2, M_{H^0}^2, M_{A^0}^2) - \mathcal{B}_{22}(M_Z^2, M_{H^\pm}^2, M_{H^\pm}^2) \\ & + \cos^2(\beta-\alpha)[\mathcal{B}_{22}(M_Z^2, M_{h^0}^2, M_{A^0}^2) + \mathcal{B}_{22}(M_Z^2, M_Z^2, M_{H^0}^2) - \mathcal{B}_{22}(M_Z^2, M_Z^2, M_{h^0}^2) \\ & - M_Z^2\mathcal{B}_0(M_Z^2, M_Z^2, M_{H^0}^2) + M_Z^2\mathcal{B}_0(M_Z^2, M_Z^2, M_{h^0}^2)]\} \end{aligned} \tag{B.1}$$

$$\begin{aligned} T = & \frac{1}{16\pi M_W^2 s_w^2}\{F(M_{H^\pm}^2, M_{A^0}^2) + \sin^2(\beta-\alpha)[F(M_{H^\pm}^2, M_{H^0}^2) - F(M_{A^0}^2, M_{H^0}^2)] \\ & + \cos^2(\beta-\alpha)[F(M_{H^\pm}^2, M_{h^0}^2) - F(M_{A^0}^2, M_{h^0}^2) + F(M_W^2, M_{H^0}^2) - F(M_W^2, M_{h^0}^2) \\ & - F(M_Z^2, M_{H^0}^2) + F(M_Z^2, M_{h^0}^2) + 4M_Z^2\overline{B}_0(M_Z^2, M_{H^0}^2, M_{h^0}^2) - 4M_W^2\overline{B}_0(M_W^2, M_{H^0}^2, M_{h^0}^2)]\} \end{aligned} \tag{B.2}$$

$$\begin{aligned} U = & -S + \frac{1}{\pi M_Z^2}\{\mathcal{B}_{22}(M_W^2, M_{A^0}^2, M_{H^\pm}^2) - 2\mathcal{B}_{22}(M_W^2, M_{H^\pm}^2, M_{H^\pm}^2) \\ & + \sin^2(\beta-\alpha)\mathcal{B}_{22}(M_W^2, M_{H^0}^2, M_{H^\pm}^2) \\ & + \cos^2(\beta-\alpha)[\mathcal{B}_{22}(M_W^2, M_{h^0}^2, M_{H^\pm}^2) + \mathcal{B}_{22}(M_W^2, M_W^2, M_{H^0}^2) - \mathcal{B}_{22}(M_W^2, M_W^2, M_{h^0}^2) \\ & - M_W^2\mathcal{B}_0(M_W^2, M_W^2, M_{H^0}^2) + M_W^2\mathcal{B}_0(M_W^2, M_W^2, M_{h^0}^2)]\} \end{aligned} \tag{B.3}$$

$$\mathcal{B}_0(q^2, m_1^2, m_2^2) = 1 + \frac{1}{2}\left[\frac{x_1+x_2}{x_1-x_2} - (x_1-x_2)\right]\ln\frac{x_1}{x_2} + \frac{1}{2}f(x_1, x_2) \tag{B.4}$$

$$\overset{m_1=m_2}{\Rightarrow} 2 - 2\sqrt{4x_1-1}\arctan\frac{1}{\sqrt{4x_1-1}} \tag{B.5}$$

$$\overline{B}_0(m_1^2, m_2^2, m_3^2) = \frac{m_1^2\ln m_1^2 - m_3^2\ln m_3^2}{m_1^2 - m_3^2} - \frac{m_1^2\ln m_1^2 - m_2^2\ln m_2^2}{m_1^2 - m_2^2} \tag{B.6}$$

$$\begin{aligned}\mathcal{B}_{22}(q^2,m_1^2,m_2^2) = \frac{q^2}{24}\{&2\ln q^2 + \ln(x_1x_2) + [(x_1-x_2)^3 - 3(x_1^2-x_2^2)\\ &+ 3(x_1-x_2)]\ln\frac{x_1}{x_2} - \left[2(x_1-x_2)^2 - 8(x_1+x_2) + \frac{10}{3}\right]\\ &- [(x_1-x_2)^2 - 2(x_1+x_2)+1]f(x_1,x_2) - 6F(x_1,x_2)\} \qquad \text{(B.7)}\end{aligned}$$

$$\overset{m_1=m_2}{\Rightarrow} \frac{q^2}{24}\left[2\ln q^2 + 2\ln x_1 + \left(16x_1 - \frac{10}{3}\right) + (4x_1-1)G(x_1)\right] \qquad \text{(B.8)}$$

$$F(x_1,x_2) = \frac{x_1+x_2}{2} - \frac{x_1x_2}{x_1-x_2}\ln\frac{x_1}{x_2} \qquad \text{(B.9)}$$

$$G(x) = -4\sqrt{4x-1}\arctan\frac{1}{\sqrt{4x-1}} \qquad \text{(B.10)}$$

$$f(x_1,x_2) = \begin{cases} -2\sqrt{\Delta}\left[\arctan\frac{x_1-x_2+1}{\sqrt{\Delta}} - \arctan\frac{x_1-x_2-1}{\sqrt{\Delta}}\right] & \text{if } \Delta > 0\\ 0 & \text{if } \Delta = 0\\ \sqrt{-\Delta}\ln\frac{x_1+x_2-1+\sqrt{-\Delta}}{x_1+x_2-1-\sqrt{-\Delta}} & \text{if } \Delta < 0 \end{cases} \qquad \text{(B.11)}$$

$$\Delta = 2(x_1+x_2) - (x_1-x_2)^2 - 1 \qquad \text{(B.12)}$$

where $x_i \equiv \frac{m_i^2}{q^2}$. The above expressions are taken from [235].

C. LHC Data Analysis

C.1. GMSB6 mass spectrum

The following table shows the masses of the sparticle spectrum for the benchmark point GMSB4030 or GMSB6. It is illustrated in Fig 2.7. The corresponding GMSB parameters are $\Lambda = 40\,\text{TeV}$, $M_{\text{mess}} = 250\,\text{TeV}$, $N_5 = 3$, $\tan\beta = 30$, $\text{sgn}\,\mu = +$ and $C_{\text{grav}} = 1$.

$\widetilde{\text{g}}$	915.3	$\widetilde{\chi}_1^0$	158.0	$\widetilde{\nu}_e$	252.4	h	110.9
$\widetilde{\text{u}}_L$	891.6	$\widetilde{\chi}_2^0$	273.4	$\widetilde{\text{e}}_L$	266.8	H	372.5
$\widetilde{\text{u}}_R$	860.9	$\widetilde{\chi}_3^0$	335.7	$\widetilde{\text{e}}_R$	129.8	A	370.1
$\widetilde{\text{d}}_L$	895.5	$\widetilde{\chi}_4^0$	385.9	$\widetilde{\nu}_\tau$	247.5	$\text{H}^\pm$	381.6
$\widetilde{\text{d}}_R$	859.3	$\widetilde{\chi}_1^\pm$	273.8	$\widetilde{\tau}_1$	102.8		
$\widetilde{\text{b}}_1$	834.8	$\widetilde{\chi}_2^\pm$	384.6	$\widetilde{\tau}_2$	272.1		
$\widetilde{\text{b}}_2$	865.2						
$\widetilde{\text{t}}_1$	788.3						
$\widetilde{\text{t}}_2$	878.5						

Table C.1.: Detailed mass spectrum for the GMSB6 benchmark point. All masses are in GeV. The quasi-massless gravitino (2.4 eV) is not listed.

C.2. Event Samples and Cross Sections

The following tables list all MC samples that have been considered as background for the first $2.05\,\text{fb}^{-1}$ 2011 LHC data analysis searching for new physics events containing at least two τ leptons, jets, and $E_{\text{T}}^{\text{miss}}$. They include $t\bar{t}$ and single top production, W+jets and Z+jets production, as well as diboson, QCD dijet, and Drell-Yan production. The tables include the sample IDs, the generators used, and where available the leading and (N)NLO cross sections obtained by applying k-factors and the number of generated events.

Sample ID	Name	Generator	NLO [pb]	k-factor	NNLO [pb]	No. of events
105200	$t\bar{t}$ semileptonic (T1)	MCAtNLOJimmy	79.99	1.117	89.35	14967040
105204	$t\bar{t}$ full hadronic	MCAtNLOJimmy	64.03	1.175	75.23	1198875
108340	t-channel $t \to e\nu$	MCAtNLOJimmy	7.12			299897
108341	t-channel $t \to \mu\nu$	MCAtNLOJimmy	7.12			299879
108342	t-channel $t \to \tau\nu$	MCAtNLOJimmy	7.10			299879
108343	s-channel $t \to e\nu$	MCAtNLOJimmy	0.47			299831
108344	s-channel $t \to \mu\nu$	MCAtNLOJimmy	0.47			299877
108345	s-channel $t \to \tau\nu$	MCAtNLOJimmy	0.47			299864
108346	single top Wt	MCAtNLOJimmy	14.59			899336

Table C.2.: $t\bar{t}$ and single t MC samples used with their corresponding sample ID, event generator, NLO cross section and number of generated events. In the case of the $t\bar{t}$ MC samples applying the k-factor yields the NNLO cross sections [145].

Sample ID	Name	Generator	LO [pb]	k-factor	NNLO [pb]	No. of events
107680	WenuN0p	AlpgenJimmy	6921.6	1.20	8305.92	3455037
107681	WenuN1p	AlpgenJimmy	1304.3	1.20	1565.16	641361
107682	WenuN2p	AlpgenJimmy	378.3	1.20	453.95	3768265
107683	WenuN3p	AlpgenJimmy	101.4	1.20	121.72	1009641
107684	WenuN4p	AlpgenJimmy	25.9	1.20	31.04	249869
107685	WenuN5p	AlpgenJimmy	7.0	1.20	8.40	69953
107690	WmunuN0p	AlpgenJimmy	6919.6	1.20	8303.52	3466523
107691	WmunuN1p	AlpgenJimmy	1304.2	1.20	1565.04	641867
107692	WmunuN2p	AlpgenJimmy	377.8	1.20	453.39	3768893
107693	WmunuN3p	AlpgenJimmy	101.9	1.20	122.26	1009589
107694	WmunuN4p	AlpgenJimmy	25.8	1.20	30.90	254879
107695	WmunuN5p	AlpgenJimmy	6.9	1.20	8.30	69958
107700	WtaunuN0p	AlpgenJimmy	6918.6	1.20	8302.32	3416438
107701	WtaunuN1p	AlpgenJimmy	1303.2	1.20	1563.84	641809
107702	WtaunuN2p	AlpgenJimmy	378.2	1.20	453.82	3768750
107703	WtaunuN3p	AlpgenJimmy	101.5	1.20	121.81	1009548
107704	WtaunuN4p	AlpgenJimmy	25.6	1.20	30.77	249853
107705	WtaunuN5p	AlpgenJimmy	7.0	1.20	8.45	63692

Table C.3.: W + jets MC samples used with their corresponding sample ID, event generator, LO cross section, and section, k-factor, NNLO cross section [145], and number of generated events.

Sample ID	Name	Generator	LO [pb]	k-factor	NNLO [pb]	No. of events
107650	ZeeN0p	AlpgenJimmy	668.3	1.25	835.40	6612265
107651	ZeeN1p	AlpgenJimmy	134.4	1.25	167.95	1333745
107652	ZeeN2p	AlpgenJimmy	40.54	1.25	50.68	404873
107653	ZeeN3p	AlpgenJimmy	11.16	1.25	13.95	109942
107654	ZeeN4p	AlpgenJimmy	2.88	1.25	3.60	29992
107655	ZeeN5p	AlpgenJimmy	0.83	1.25	1.04	8992
107660	ZmumuN0p	AlpgenJimmy	668.7	1.25	835.85	6619010
107661	ZmumuN1p	AlpgenJimmy	134.1	1.25	167.68	1334723
107662	ZmumuN2p	AlpgenJimmy	40.33	1.25	50.41	403886
107663	ZmumuN3p	AlpgenJimmy	11.19	1.25	13.99	109954
107664	ZmumuN4p	AlpgenJimmy	2.75	1.25	3.44	29978
107665	ZmumuN5p	AlpgenJimmy	0.77	1.25	0.96	9993
107670	ZtautauN0p	AlpgenJimmy	668.4	1.25	835.50	6618801
107671	ZtautauN1p	AlpgenJimmy	134.8	1.25	168.51	1334664
107672	ZtautauN2p	AlpgenJimmy	40.36	1.25	50.45	404853
107673	ZtautauN3p	AlpgenJimmy	11.25	1.25	14.06	109944
107674	ZtautauN4p	AlpgenJimmy	2.79	1.25	3.49	29982
107675	ZtautauN5p	AlpgenJimmy	0.77	1.25	0.96	9993
107710	ZnunuNp0	AlpgenJimmy	26.71	1.282	34.22	60485
107711	ZnunuNp1	AlpgenJimmy	451.4	1.282	578.54	864799
107712	ZnunuNp2	AlpgenJimmy	197.6	1.282	253.29	165454
107713	ZnunuNp3	AlpgenJimmy	59.89	1.282	76.75	128934
107714	ZnunuNp4	AlpgenJimmy	15.61	1.282	20.01	24986
107715	ZnunuNp5	AlpgenJimmy	4.17	1.282	5.34	6994

Table C.4.: Z + jets MC samples used with their corresponding sample ID, event generator, LO cross section, k-factor, NNLO cross section [145], and number of generated events.

Sample ID	Name	Generator	LO [pb]	No. of events
105009	J0	Pythia	9860800000	16388258
105010	J1	Pythia	678180000	7382565
105011	J2	Pythia	40982000	2796084
105012	J3	Pythia	2192900	2796879
105013	J4	Pythia	87701.	2793179
105014	J5	Pythia	2350.1	2790576
105015	J6	Pythia	33.61	2790601
105016	J7	Pythia	0.13744	1395025
105017	J8	Pythia	0.0000062	1353250

Table C.5.: Dijet MC samples used with their corresponding sample ID, event generator, cross section and number of generated events.

Sample ID	Generator	Final state	NLO [fb]	No. of events
105921	McAtNlo_JIMMY	$W^+W^- \to e\nu e\nu$	503.77	199960
105922	McAtNlo_JIMMY	$W^+W^- \to e\nu\mu\nu$	503.77	199960
105923	McAtNlo_JIMMY	$W^+W^- \to e\nu\tau\nu$	503.77	199966
105924	McAtNlo_JIMMY	$W^+W^- \to \mu\nu\mu\nu$	503.77	199956
105925	McAtNlo_JIMMY	$W^+W^- \to \mu\nu e\nu$	503.77	199961
105926	McAtNlo_JIMMY	$W^+W^- \to \mu\nu\tau\nu$	503.77	199960
105927	McAtNlo_JIMMY	$W^+W^- \to \tau\nu\tau\nu$	503.77	199966
105928	McAtNlo_JIMMY	$W^+W^- \to \tau\nu e\nu$	503.77	199958
105929	McAtNlo_JIMMY	$W^+W^- \to \tau\nu\mu\nu$	503.77	199957
105930	McAtNlo_JIMMY	$ZZ \to \ell\ell q\bar{q}$	523.54	24990
105931	McAtNlo_JIMMY	$ZZ \to \ell\ell\ell\ell$	24.68	99982
105932	McAtNlo_JIMMY	$ZZ \to \ell\ell\nu\nu$	150.33	99978
106036	McAtNlo_JIMMY	$ZZ \to 2\ell 2\tau$	24.68	24995
106037	McAtNlo_JIMMY	$ZZ \to 4\tau$	6.17	24991
113192	McAtNlo_JIMMY	$ZZ \to \tau\tau\nu\nu$	75.17	24996
113193	McAtNlo_JIMMY	$ZZ \to \tau\tau q\bar{q}$	261.77	24990
105940	McAtNlo_JIMMY	$W^+Z \to \ell\nu q\bar{q}$	1688.9	24989
105941	McAtNlo_JIMMY	$W^+Z \to \ell\nu\ell\ell$	159.24	24995
105942	McAtNlo_JIMMY	$W^+Z \to q\bar{q}'\ell\ell$	498.36	24992
106024	McAtNlo_JIMMY	$W^+Z \to \tau\nu\ell\ell$	79.62	24994
106025	McAtNlo_JIMMY	$W^+Z \to \ell\nu\tau\tau$	79.62	24992
106026	McAtNlo_JIMMY	$W^+Z \to \tau\nu\tau\tau$	39.81	24990
113190	McAtNlo_JIMMY	$W^+Z \to q\bar{q}'\tau\tau$	249.18	24987
105970	McAtNlo_JIMMY	$W^-Z \to \ell\nu q\bar{q}$	912.64	24993
105971	McAtNlo_JIMMY	$W^-Z \to \ell\nu\ell\ell$	86.05	99972
105972	McAtNlo_JIMMY	$W^-Z \to q\bar{q}'\ell\ell$	269.3	99968
106027	McAtNlo_JIMMY	$W^-Z \to \tau\nu\ell\ell$	43.02	24997
106028	McAtNlo_JIMMY	$W^-Z \to \ell\nu\tau\tau$	43.02	24993
106029	McAtNlo_JIMMY	$W^-Z \to \tau\nu\tau\tau$	21.51	24941
113191	McAtNlo_JIMMY	$W^-Z \to q\bar{q}'\tau\tau$	134.65	24989

Table C.6.: Diboson MC samples used with their corresponding sample ID, event generator, final state, NLO cross section, and number of generated events.

Sample ID	Name	Generator	LO [pb]	k-factor	NNLO [pb]	No. of events
116250	ZeeNp0Mll10to40	AlpgenJimmy	3055.2	1.25	3819.00	999859
116251	ZeeNp1Mll10to40	AlpgenJimmy	84.92	1.25	106.15	299940
116252	ZeeNp2Mll10to40	AlpgenJimmy	41.40	1.25	51.75	499880
116253	ZeeNp3Mll10to40	AlpgenJimmy	8.38	1.25	10.48	149940
116254	ZeeNp4Mll10to40	AlpgenJimmy	1.85	1.25	2.31	39973
116255	ZeeNp5Mll10to40	AlpgenJimmy	0.46	1.25	0.58	9995
116260	ZmumuNp0Mll10to40	AlpgenJimmy	3054.9	1.25	3818.63	979869
116261	ZmumuNp1Mll10to40	AlpgenJimmy	84.87	1.25	106.09	299890
116262	ZmumuNp2Mll10to40	AlpgenJimmy	41.45	1.25	51.81	499864
116263	ZmumuNp3Mll10to40	AlpgenJimmy	8.38	1.25	10.48	149939
116264	ZmumuNp4Mll10to40	AlpgenJimmy	1.85	1.25	2.31	39988
116265	ZmumuNp5Mll10to40	AlpgenJimmy	0.46	1.25	0.58	9996
116270	ZtautauNp0Mll10to40	AlpgenJimmy	3055.1	1.25	3818.88	999865
116271	ZtautauNp1Mll10to40	AlpgenJimmy	84.93	1.25	106.16	299937
116272	ZtautauNp2Mll10to40	AlpgenJimmy	41.47	1.25	51.84	499886
116273	ZtautauNp3Mll10to40	AlpgenJimmy	8.36	1.25	10.45	149941
116274	ZtautauNp4Mll10to40	AlpgenJimmy	1.85	1.25	2.31	39984
116275	ZtautauNp5Mll10to40	AlpgenJimmy	0.46	1.25	0.58	9995

Table C.7.: Drell-Yan MC samples used with their corresponding sample ID, event generator, LO cross section, k-factor, NNLO cross section [145], and number of generated events.

C.3. Trigger Details

Table C.8 contains the trigger efficiencies that have been determined testing different triggers using their corresponding offline cuts for two GMSB benchmark points. They might be applicable for the full 2011 data analysis. These efficiencies have been plotted over the entire GMSB grid in Figs. 8.4 and 8.5.

The first column lists the cut on $E_{\mathrm{T}}^{\mathrm{miss}}$ or the p_{T} of a jet, τ, electron, or muon in GeV. The second column lists any additional cut that was applied to reduce the ambiguity of the offline cuts. In most cases this means requiring additional τ leptons to allow for an easier comparison with τ-triggers. The third column lists the number of events that were selected applying the corresponding cuts. The column labeled "% all" lists the corresponding percentage of events that were selected from all events. The following two columns give the percentage of events selected based on the number of events containing at least one or two reconstructed τ candidates. E.g. the trigger offline cuts applied for this analysis are $E_{\mathrm{T}}^{\mathrm{miss}} > 130\,\mathrm{GeV}$ and $p_{\mathrm{T}}^{\mathrm{jet1}} > 130\,\mathrm{GeV}$. The trigger efficiency obtained by this selection is only 3.4 %. Considering that the event selection requires at least two τ candidates, this number increases to 34.4 %.

The second half of the table contains lists those events that do not fulfill the nominal trigger selection applied in this analysis and therefore indicate the gain in the number of events.

Trigger Cut	Kin. Sel.	GMSB3020	% all	% 2tau 15	GMSB4030	% all	% 2tau 15
		4007.1			848.4		
MET 130 jet 130		1577.4	39.4		290.2	34.2	
MET 130 jet 130	2tau 15	109.6	2.7	35.7	28.8	3.4	34.4
MET 140 jet 135		1514.5	37.8		278.5	32.8	
MET 140 jet 135	2tau 15	106.3	2.7	34.7	27.9	3.3	33.4
	2tau 15	306.5	7.6	100.0	83.6	9.9	100.0
tau 40 tau 35		92.0	2.3	30.0	32.3	3.8	38.6
2tau 30 MET 135		63.2	1.6	20.6	21.4	2.5	25.6
MET 150	2tau 15	116.6	2.9	38.0	33.4	3.9	40.0
MET 180	2tau 15	93.4	2.3	30.5	27.3	3.2	32.7
MET 130 jet 130 jet 100	2tau 15	92.2	2.3	30.1	21.9	2.6	26.2
not MET 130 jet 130							
	2tau 15	196.9	4.9	100.0	54.8	6.5	100.0
tau 40 tau 35		53.2	1.3	27.0	19.0	2.2	34.6
2tau 30 MET 135		10.6	0.3	5.4	4.4	0.5	8.0
MET 150	2tau 15	16.1	0.4	8.2	6.7	0.8	12.2
MET 180	2tau 15	7.9	0.2	4.0	4.0	0.5	7.2

Table C.8.: Numbers for Trigger offline cut testing for a luminosity of $2.05\,\mathrm{fb}^{-1}$, with loose tau selection

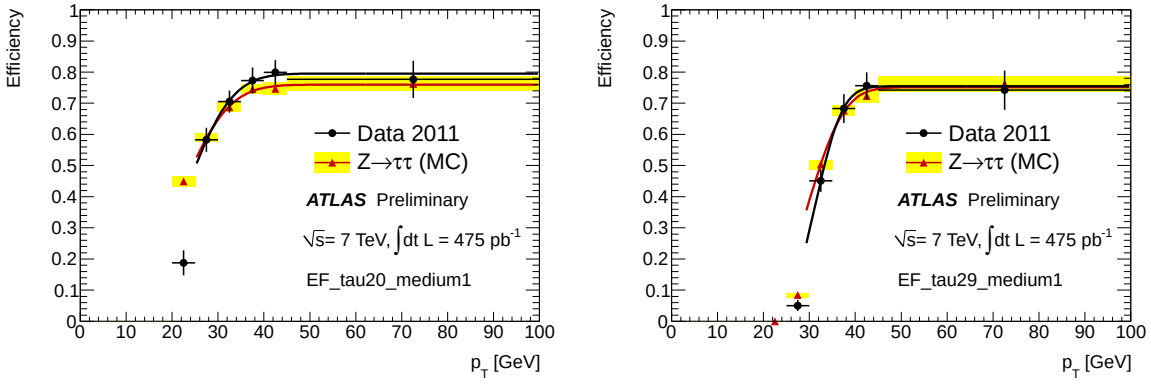

(a) (b)

Figure C.1.: Turn-on curves in data and MC for the single τ triggers (a) *EF_tau20_medium* and (b) *EF_tau29_medium* [236].

Figure C.1 shows the turn-on curve for two different triggers based on a single τ candidate.

C.4. Results

Figure C.2 shows the distributions of several jet variables and the $\Delta\phi$ between the two leading jets and $E_{\mathrm{T}}^{\mathrm{miss}}$ after two τ candidates are required in the event selection. A good MC and data agreement can be observed within the statistical errors.

Figure C.3 shows the same jet distributions after the full event selection. The yellow error bands now also include the systematic uncertainties. However, the low data statistics does not allow for an exhaustive data and MC comparison.

Figure C.4 shows the expected and observed 95% CL limits including and excluding the theoretical uncertainties. No noticeable difference can be observed between them.

Figure C.5 shows the expected and observed 95% CL limits using two different software versions. The newer version employed after the technical stop in September includes an improved τ reconstruction algorithm where the overestimation of the number of misidentified τ candidates is reduced. It is an increased efficiency and the reconstructed τ distributions are more compatible with data.

C.5. MC Studies prior to LHC Data Taking

Figure C.6 shows a detailed comparison between the full (circles) and fast (triangles) simulation of the variables relevant for the event selection described in Ch. 7. No significant discrepancy can be observed in any of the variables.

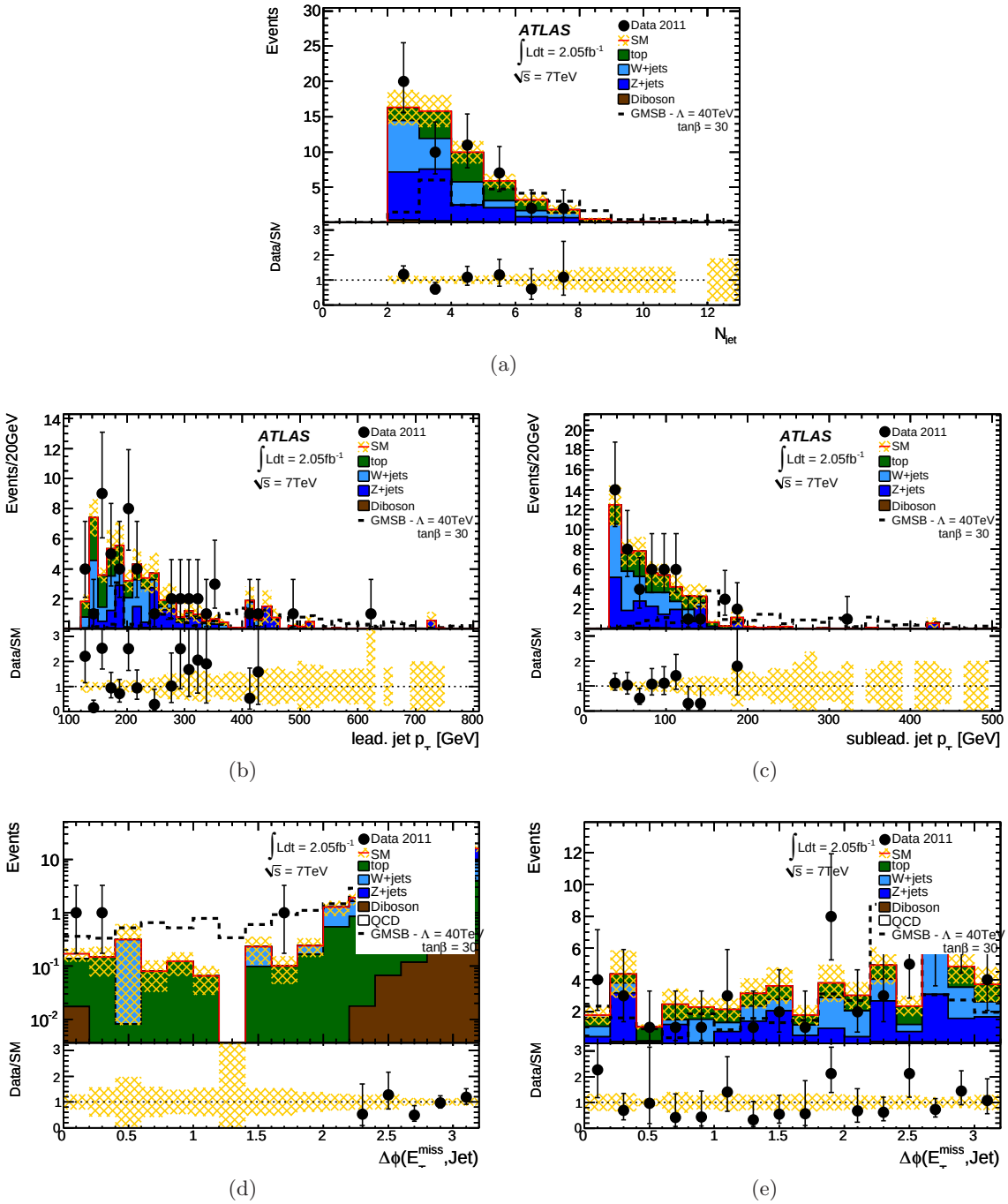

(a)

(b)

(c)

(d)

(e)

Figure C.2.: Distributions for some of the jet kinematic variables after requiring two reconstructed τ candidates. The scaling factor for the W and top background has been applied. The yellow error band denotes the statistical error only.

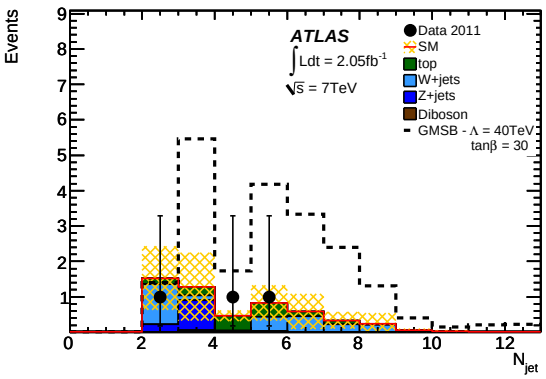

(a)

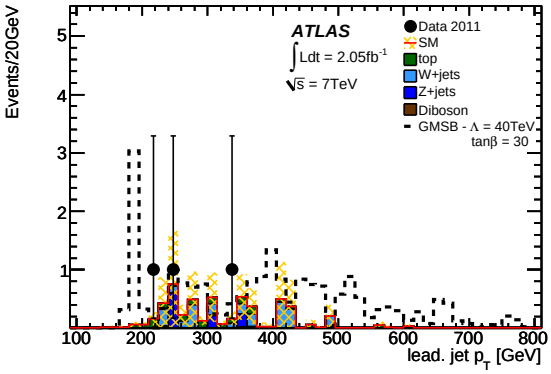

(b)

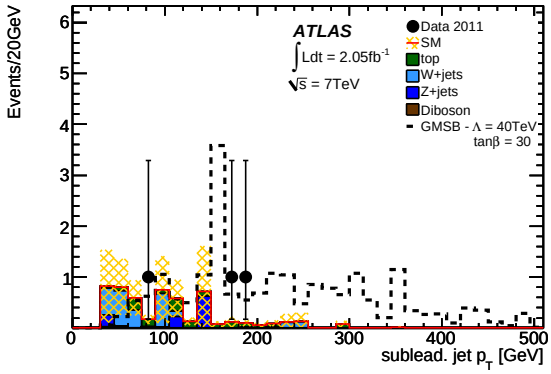

(c)

Figure C.3.: Distributions for some of the jet kinematic variables in the signal region. The errors comprise both statistical and systematic uncertainties.

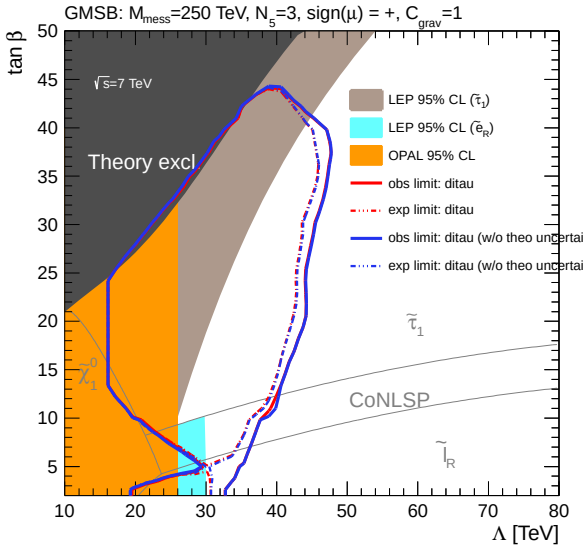

Figure C.4.: Expected and observed 95% CL limits with and without the theoretical errors included on the minimal GMSB model parameters in the Λ-tanβ-plane for $M_{\text{mess}} = 250\,\text{TeV}$, $N_5 = 3$, $\text{sgn}\,\mu = +$, and $C_{\text{grav}} = 1$ [3].

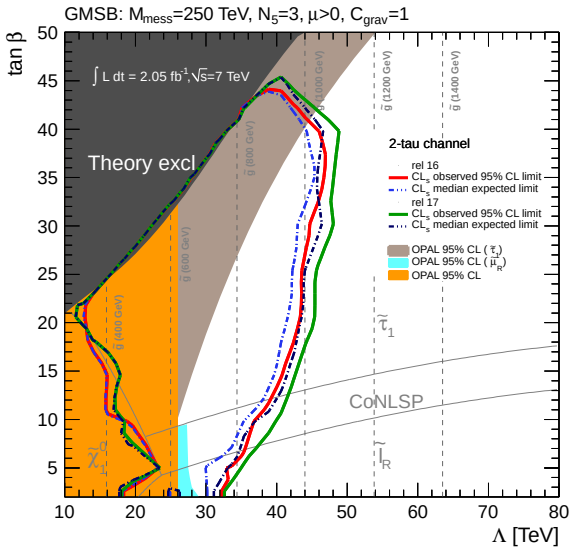

Figure C.5.: Expected and observed 95% CL limits on the minimal GMSB model parameters in the Λ-tanβ-plane for $M_{\text{mess}} = 250\,\text{TeV}$, $N_5 = 3$, $\text{sgn}\,\mu = +$, and $C_{\text{grav}} = 1$. Two different ATLAS software versions have been used for the reconstruction of the events [221].

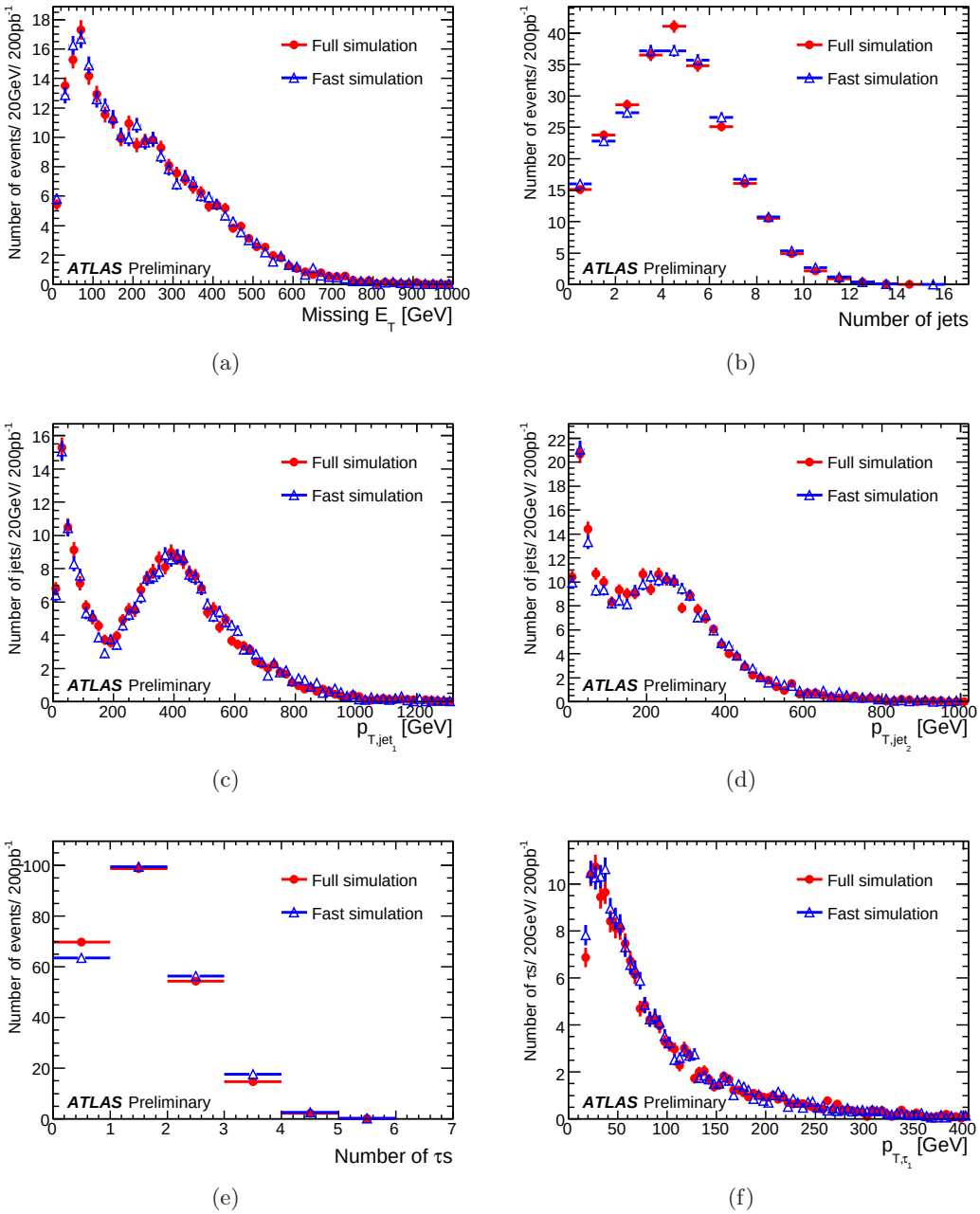

Figure C.6.: Comparison of the full (circles) and fast (triangles) simulation: (a) $E_{\mathrm{T}}^{\mathrm{miss}}$, (b) N_{jet} with p_{T} >20 GeV, (c) $p_{\mathrm{T}}^{\mathrm{jet1}}$, (d) $p_{\mathrm{T}}^{\mathrm{jet2}}$, (e) N_{τ} with $p_{\mathrm{T}} > 15$ GeV, and (f) $p_{\mathrm{T}}^{\tau 1}$.

Bibliography

[1] M. Baak *et al.*, Updated Status of the Global Electroweak Fit and Constraints on New Physics, Eur. Phys. J. **C72**, 2003 (2012), hep-ph/1107.0975.

[2] ATLAS Collaboration, Search for Events with Large Missing Transverse Momentum, Jets, and at least Two Tau Leptons in 7 TeV Proton-Proton Collision Data with the ATLAS Detector, Phys. Lett. **B714**, 180 (2012), hep-ex/1203.6580.

[3] F. Bührer *et al.*, Search for Supersymmetry with Jets, Missing Transverse Momentum, and two or more Taus at $\sqrt{s} = 7\,\text{TeV}$: Support Note for 2011 Analysis, ATL-PHYS-INT-2012-024, Apr, 2012.

[4] S. Glashow, Nucl. Phys. **22** (1961) 579, S. Weinberg, Phys. Rev. Lett. **19** (1967) 1264, A. Salam, in Elementary Particle Theory, ed. N. Svartholm, Stockholm, "Almquist and Wiksell" (1968), 367.

[5] K. Nakamura *et al.* (Particle Data Group), J. Phys. G **37**, 075021 (2010).

[6] Tevatron Electroweak Working Group, Combination of CDF and DO results on the mass of the top quark using up to $5.8\,\text{fb}^{-1}$ of data, (2011), 1107.5255.

[7] H. Fritzsch, M. Gell-Mann, and H. Leutwyler, Phys. Lett. **B47**, 365 (1973).

[8] D. Gross and F. Wilczek, Ultraviolet Behavior of Nonabelian Gauge Theories, Phys. Rev. Lett. **30**, 1343 (1973).

[9] H. Politzer, Reliable Perturbative Results for Strong Interactions?, Phys. Rev. Lett. **30**, 1346 (1973).

[10] H1 and ZEUS Collaboration, H1prelim-11-042, ZEUS-prel-11-010, https://www.desy.de/h1zeus/combined_results/index.php?do=proton_structure_fits2011_herapdf1.5NNLO_figures.

[11] S. Catani *et al.*, QCD, (2000), hep-ph/0005025.

[12] N. Cabibbo, Phys. Rev. Lett. **10**, 531 (1963).

[13] M. Kobayashi and T. Maskawa, Prog. Theor. Phys. **49**, 652 (1973).

[14] P. W. Higgs, Phys. Lett. **12**, 132 (1964).

[15] H. Flaecher *et al.*, Gfitter - Revisiting the Global Electroweak Fit of the Standard Model and Beyond, Eur. Phys. J. **C60**, 543 (2009), Erratum-ibid. **C71** (2011) 1718, hep-ph/0811.0009.

[16] Gfitter Group, M. Baak *et al.*, Updated results at: http://cern.ch/gfitter.

[17] The ALEPH, DELPHI, L3 and OPAL Collaborations, and LEP Working Group for Higgs Boson Searches, R. Barate *et al.*, Search for the standard model Higgs boson at LEP, Phys. Lett. **B565**, 61 (2003), hep-ex/0306033.

[18] TEVNPH (Tevatron New Phenomina and Higgs Working Group), CDF and D0 Collaboration, Combined CDF and D0 Upper Limits on Standard Model Higgs Boson Production with up to $8.6\,\mathrm{fb}^{-1}$ of Data, (2011), 1107.5518.

[19] CMS Collaboration, S. Chatrchyan *et al.*, Combined results of searches for the standard model Higgs boson in pp collisions at $\sqrt{s} = 7\,\mathrm{TeV}$, Phys. Lett. **B710**, 26 (2012), 1202.1488.

[20] CERN Report No. ATLAS-CONF-2012-019, 2012 (unpublished).

[21] WMAP Collaboration, E. Komatsu *et al.*, Seven-Year Wilkinson Microwave Anisotropy Probe (WMAP) Observations: Cosmological Interpretation, Astrophys.J.Suppl. **192**, 18 (2011), 1001.4538.

[22] A. Sakharov, Violation of CP Invariance, c Asymmetry, and Baryon Asymmetry of the Universe, Pisma Zh.Eksp.Teor.Fiz. **5**, 32 (1967).

[23] A. G. Cohen, D. Kaplan, and A. Nelson, Progress in Electroweak Baryogenesis, Ann. Rev. Nucl. Part. Sci. **43**, 27 (1993), hep-ph/9302210.

[24] M. Gavela, P. Hernandez, J. Orloff, O. Pene, and C. Quimbay, Standard Model CP Violation and Baryon Asymmetry. Part 2: Finite Temperature, Nucl. Phys. **B430**, 382 (1994), hep-ph/9406289.

[25] S. Martin, A Supersymmetry Primer, (1997), hep-ph/9709356.

[26] Y. A. Golfand and E. P. Likhtman, Extension of the Algebra of Poincare Group Generators and Violation of p Invariance, JETP Lett. **13**, 323 (1971).

[27] A. Neveu and J. H. Schwarz, Factorizable Dual Model of Pions, Nucl. Phys. **B31**, 86 (1971).

[28] P. Ramond, Dual Theory for Free Fermions, Phys. Rev. **D3**, 2415 (1971).

[29] D. V. Volkov and V. P. Akulov, Is the Neutrino a Goldstone Particle?, Phys. Lett. **B46**, 109 (1973).

[30] J. Wess and B. Zumino, Supergauge Transformations in Four-Dimensions, Nucl. Phys. **B70**, 39 (1974).

[31] P. Fayet, Spontaneously Broken Supersymmetric Theories of Weak, Electromagnetic and Strong Interactions, Phys. Lett. **B69**, 489 (1977).

[32] G. R. Farrar and P. Fayet, Phenomenology of the Production, Decay, and Detection of New Hadronic States Associated with Supersymmetry, Phys. Lett. **B76**, 575 (1978).

[33] R. Barbier *et al.*, R-parity violating supersymmetry, Phys. Rept. **420**, 1 (2005), hep-ph/0406039.

[34] L. Alvarez-Gaume, J. Polchinski, and M. Wise, Minimal Low-energy Supergravity, Nucl. Phys. **B221**, 495 (1983).

[35] L. Ibanez, Locally Supersymmetric SU(5) Grand Unification, Phys. Lett. **B118**, 73 (1982).

[36] J. Ellis, D. Nanopoulos, and K. Tamvakis, Grand Unification in Simple Supergravity, Phys. Lett. **B121**, 123 (1983).

[37] K. Inoue, A. Kakuto, H. Komatsu, and S. Takeshita, Aspects of Grand Unified Models with Softly Broken Supersymmetry, Prog. Theor. Phys. **68**, 927 (1982).

[38] A. Chamseddine, R. Arnowitt, and P. Nath, Locally Supersymmetric Grand Unification, Phys. Rev. Lett. **49**, 970 (1982).

[39] M. Dine and W. Fischler, A Phenomenological Model of Particle Physics Based on Supersymmetry, Phys. Lett. **B110**, 227 (1982).

[40] L. Alvarez-Gaume, M. Claudson, and M. Wise, Low-energy Supersymmetry, Nucl. Phys. **B207**, 96 (1982).

[41] C. R. Nappi and B. A. Ovrut, Supersymmetric Extension of the SU(3) x SU(2) x U(1) Model, Phys. Lett. **B113**, 175 (1982).

[42] M. Dine and A. Nelson, Dynamical Supersymmetry Breaking at Low-energies, Phys. Rev. **D48**, 1277 (1993), `hep-ph/9303230`.

[43] M. Dine, A. Nelson, and Y. Shirman, Low-energy Dynamical Supersymmetry Breaking Simplified, Phys. Rev. **D51**, 1362 (1995), `hep-ph/9408384`.

[44] M. Dine, A. Nelson, Y.Nir, and Y. Shirman, New Tools for Low-energy Dynamical Supersymmetry Breaking, Phys. Rev. **D53**, 2658 (1996), `hep-ph/9507378`.

[45] S. Ambrosanio, B. Mele, S. Petrarca, G. Polesello, and A. Rimoldi, Measuring the SUSY Breaking Scale at the LHC in the Slepton NLSP Scenario of GMSB models, JHEP **0101**, 014 (2001), `hep-ph/0010081`.

[46] ATLAS Collaboration, Expected Performance of the ATLAS Detector in GMSB Models with Tau Final States, ATL-PHYS-PUB-2009-089, Nov, 2009.

[47] I. Hinchliffe and F. E. Paige, Measurements in Gauge Mediated SUSY Breaking Models at LHC, Phys. Rev. **D60**, 095002 (1999), `hep-ph/9812233`.

[48] B. C. Allanach *et al.*, The Snowmass points and slopes: Benchmarks for SUSY searches, Eur. Phys. J. **C25**, 113 (2002), `hep-ph/0202233`.

[49] H. E. Haber, G. L. Kane, and T. Sterling, The Fermion Mass Scale and Possible Effects of Higgs Bosons on Experimental Observables, Nucl. Phys. **B161**, 493 (1979).

[50] S. Davidson and H. E. Haber, Basis-independent methods for the two-Higgs-doublet model, Phys. Rev. **D72**, 035004 (2005), `hep-ph/0504050`.

[51] H. E. Haber and D. O'Neil, Basis-independent methods for the two-Higgs-doublet model. II: The significance of tan(beta), Phys. Rev. **D74**, 015018 (2006), `hep-ph/0602242`.

[52] J. M. Cline and P.-A. Lemieux, Electroweak phase transition in two Higgs doublet models, Phys. Rev. **D55**, 3873 (1997), `hep-ph/9609240`.

[53] J. F. Gunion, H. E. Haber, G. L. Kane, and S. Dawson, The Higgs Hunter's Guide, *The Higgs Hunter's Guide*, Perseus Publishing, Cambridge, MA, 1990, SCIPP-89/13, UCD-89-4, BNL-41644.

[54] J. F. Gunion, H. E. Haber, G. L. Kane, and S. Dawson, Errata for the Higgs Hunter's Guide, (1992), `hep-ph/9302272`.

[55] L. F. Abbott, P. Sikivie, and M. B. Wise, Constraints on Charged Higgs Couplings, Phys. Rev. **D21**, 1393 (1980).

[56] N. Arkani-Hamed, S. Dimopoulos, and G. R. Dvali, The hierarchy problem and new dimensions at a millimeter, Phys. Lett. **B429**, 263 (1998), hep-ph/9803315.

[57] I. Antoniadis, N. Arkani-Hamed, S. Dimopoulos, and G. R. Dvali, New dimensions at a millimeter to a Fermi and superstrings at a TeV, Phys. Lett. **B436**, 257 (1998), hep-ph/9804398.

[58] T. Appelquist, H.-C. Cheng, and B. A. Dobrescu, Bounds on universal extra dimensions, Phys. Rev. **D64**, 035002 (2001), hep-ph/0012100.

[59] L. Randall and R. Sundrum, A Large mass hierarchy from a small extra dimension, Phys. Rev. Lett. **83**, 3370 (1999), hep-ph/9905221.

[60] K. Agashe, A. Delgado, and R. Sundrum, Grand unification in RS1, Ann. Phys. **304**, 145 (2003), hep-ph/0212028.

[61] K. Agashe, A. Delgado, M. J. May, and R. Sundrum, RS1, custodial isospin and precision tests, JHEP **0308**, 050 (2003), hep-ph/0308036.

[62] M. E. Peskin and T. Takeuchi, Estimation of oblique electroweak corrections, Phys. Rev. **D46**, 381 (1992).

[63] M. Goebel, Tests of the electroweak standard model and measurement of the weak mixing angle with the atlas detector, PhD thesis, University Hamburg, 2011.

[64] F. James and M. Roos, Minuit: A system for function minimization and analysis of the parameter errors and correlations, Comput. Phys. Commun. **10**, 343 (1975).

[65] A. Hoecker *et al.*, Tmva: Toolkit for multivariate data analysis, (2007), CERN-OPEN-2007-007, physics/0703039.

[66] R. Brun and F. Rademakers, ROOT: An object oriented data analysis framework, Nucl. Instrum. Meth. **A389**, 81 (1997).

[67] A. Hoecker, H. Lacker, S. Laplace, and F. Le Diberder, A new approach to a global fit of the ckm matrix, Eur. Phys. J. **C21**, 225 (2001), hep-ph/0104062.

[68] CKMfitter Group, J. Charles *et al.*, CP violation and the CKM matrix: Assessing the impact of the asymmetric B factories, Eur. Phys. J. **C41**, 1 (2005), hep-ph/0406184.

[69] J. Erler, Global fits to electroweak data using GAPP, (1999), 8 pages, Contribution to the Fermilab Workshop on QCD and Weak Boson Physics at the Tevatron Run II Report-no: UPR-885-T, hep-ph/0005084.

[70] J. Erler and P. Langacker (in: Review for Particle Data Group), Review of particle physics, J. Phys. **G37**, 075021 (2010).

[71] Electroweak working group, D. Y. Bardin *et al.*, Electroweak working group report, (1997), Prepared for Workshop Group on Precision Calculations for the Z Resonance (2nd meeting held Mar 31, 3rd meeting held Jun 13), Geneva, Switzerland, 14 Jan 1994, CERN-YELLOW-95-03A, hep-ph/9709229.

[72] V. Novikov, L. Okun, A. N. Rozanov, and M. Vysotsky, LEPTOP, (1995), hep-ph/9503308.

[73] G. Montagna, F. Piccinini, O. Nicrosini, G. Passarino, and R. Pittau, TOPAZ0: A Program for computing observables and for fitting cross-sections and forward - backward asymmetries around the Z0 peak, Comput.Phys.Commun. **76**, 328 (1993).

[74] G. Montagna, O. Nicrosini, F. Piccinini, and G. Passarino, TOPAZ0 4.0: A New version of a computer program for evaluation of deconvoluted and realistic observables at LEP-1 and LEP-2, Comput.Phys.Commun. **117**, 278 (1999), `hep-ph/9804211`.

[75] D. Y. Bardin *et al.*, Zfitter v.6.21: A semi-analytical program for fermion pair production in e+ e- annihilation, Comput. Phys. Commun. **133**, 229 (2001), `hep-ph/9908433`.

[76] A. B. Arbuzov *et al.*, Zfitter: A semi-analytical program for fermion pair production in e+ e- annihilation, from version 6.21 to version 6.42, Comput. Phys. Commun. **174**, 728 (2006), `hep-ph/0507146`.

[77] The LEP Electroweak Working Group, `http://lepewwg.web.cern.ch/LEPEWWG/`.

[78] The ALEPH, DELPHI, L3, OPAL, SLD Collaborations, the LEP Electroweak Working Group, the SLD Electroweak and Heavy Flavour Working Groups, Precision Electroweak Measurements on the Z Resonance, Phys. Rept. **427**, 257 (2006), `hep-ex/0509008`.

[79] Tevatron Electroweak Working Group and CDF and D0 Collaborations, Updated Combination of CDF and D0 Results for the Mass of the W Boson, (2009), `arxiv:0908.1374`.

[80] Tevatron Electroweak Working Group, Combination of CDF and D0 Results on the Width of the W boson, (2010), `arxiv:1003.2826`.

[81] P. Skands and D. Wicke, Non-perturbative QCD effects and the top mass at the Tevatron, Eur. Phys. J. **C52**, 133 (2007), `hep-ph/0703081`.

[82] D. Wicke and P. Z. Skands, Non-perturbative QCD Effects and the Top Mass at the Tevatron, (2008), `arxiv:0807.3248`.

[83] A. H. Hoang, A. Jain, I. Scimemi, and I. W. Stewart, Infrared Renormalization Group Flow for Heavy Quark Masses, (2008), `arxiv:0803.4214`.

[84] A. H. Hoang and I. W. Stewart, Top Mass Measurements from Jets and the Tevatron Top-Quark Mass, (2008), `arxiv:0808.0222`.

[85] M. Davier, A. Hoecker, B. Malaescu, and Z. Zhang, Reevaluation of the Hadronic Contributions to the Muon g-2 and to $\alpha(M_Z^2)$, Eur. Phys. J. **C71**, 1515 (2011), `1010.4180v2`.

[86] CDF and D0 Collaborations, Combined CDF and D0 Upper Limits on Standard Model Higgs- Boson Production with up to $6.7\,\mathrm{fb}^{-1}$ of Data, (2010), `arxiv:1007.4587`.

[87] CDF and D0 Collaborations, T. Aaltonen *et al.*, Combined CDF and D0 Upper Limits on Standard Model Higgs Boson Production with up to $8.2\,\mathrm{fb}^{-1}$ of Data, (2011), `arxiv:1103.3233`.

[88] ATLAS Collaboration, Limits on the production of the Standard Model Higgs Boson in pp collisions at $\sqrt{s} = 7\,\mathrm{TeV}$ with the ATLAS detector, (2011), CERN-PH-EP-2011-076 (2011), `arxiv:1106.2748`.

[89] CMS Collaboration, S. Chatrchyan *et al.*, Measurement of WW Production and Search for the Higgs Boson in pp Collisions at $\sqrt{s} = 7\,\mathrm{TeV}$, Phys. Lett. **B699**, 25 (2011), `arxiv:1102.5429`.

[90] C. P. Burgess, S. Godfrey, H. Konig, D. London, and I. Maksymyk, A Global fit to extended oblique parameters, Phys. Lett. **B326**, 276 (1994), hep-ph/9307337.

[91] R. Barbieri, A. Pomarol, R. Rattazzi, and A. Strumia, Electroweak symmetry breaking after LEP-1 and LEP-2, Nucl. Phys. **B703**, 127 (2004), hep-ph/0405040.

[92] G. Altarelli, R. Barbieri, and F. Caravaglios, Nonstandard analysis of electroweak precision data, Nucl. Phys. **B405**, 3 (1993).

[93] G. Altarelli, R. Barbieri, and F. Caravaglios, Electroweak precision tests: A concise review, Int. J. Mod. Phys. **A13**, 1031 (1998), hep-ph/9712368.

[94] C. P. Burgess, The Effective use of precision electroweak measurements, Pramana **45**, S47 (1995), hep-ph/9411257.

[95] H. E. Haber, Introductory low-energy supersymmetry, (1993), hep-ph/9306207.

[96] H. E. Haber and H. E. Logan, Radiative Corrections to the $Z \to b\bar{b}$ Vertex and Constraints on Extended Higgs Sectors, Phys. Rev. **D62**, 015011 (2000), hep-ph/9909335.

[97] C. D. Froggatt, R. G. Moorhouse, and I. G. Knowles, Leading radiative corrections in two scalar doublet models, Phys. Rev. **D45**, 2471 (1992).

[98] O. Deschamps *et al.*, The Two Higgs Doublet of Type II facing flavour physics data, Phys. Rev. **D82**, 073012 (2009), hep-ph/0907.5135.

[99] ALEPH Collaboration, A. Heister *et al.*, Search for Charged Higgs Bosons in e^+e^- Collisions at Energies up to $\sqrt{s} = 209\,\text{GeV}$, Phys. Lett. **B543**, 1 (2002), hep-ex/0207054.

[100] DELPHI Collaboration, P. Abreu *et al.*, Search for Charged Higgs bosons in e^+e^- Collisions at $\sqrt{s} = 189 - 202\,\text{GeV}$, Phys. Lett. **B525**, 17 (2002), hep-ex/0201023.

[101] L3 Collaboration, P. Achard *et al.*, Search for charged Higgs bosons at LEP, Phys. Lett. **B575**, 208 (2003), hep-ex/0309056.

[102] OPAL Collaboration, G. Abbiendi *et al.*, Search for Higgs bosons in e^+e^- Collisions at $\sqrt{s} = 183\,\text{GeV}$, Eur. Phys. J. **C7**, 407 (1999), hep-ex/9811025.

[103] LEP Higgs Working Group for Higgs boson searches, Search for charged Higgs bosons: Preliminary combined results using LEP data collected at energies up to $\sqrt{s} = 209\,\text{GeV}$, (2001), hep-ex/0107031.

[104] S. Casagrande, F. Goertz, U. Haisch, M. Neubert, and T. Pfoh, Flavor Physics in the Randall-Sundrum Model: I. Theoretical Setup and Electroweak Precision Tests, JHEP **0810**, 094 (2008), hep-ph/0807.4937.

[105] A. Delgado and A. Falkowski, Electroweak observables in a general 5D background, JHEP **05**, 097 (2007), hep-ph/0702234.

[106] M. S. Carena, A. Delgado, E. Ponton, T. M. P. Tait, and C. E. M. Wagner, Precision Electroweak Data and Unification of Couplings in Warped Extra Dimensions, Phys. Rev. **D68**, 035010 (2003), hep-ph/0305188.

[107] C. Csaki, J. Erlich, and J. Terning, The effective Lagrangian in the Randall-Sundrum model and electroweak physics, Phys. Rev. **D66**, 064021 (2002), hep-ph/0203034.

[108] The D0, V. M. Abazov *et al.*, Search for Randall-Sundrum gravitons in the dielectron and diphoton final states with $5.4\,\mathrm{fb}^{-1}$ of data from ppbar collisions at $\sqrt{s} = 1.96\,\mathrm{TeV}$, Phys. Rev. Lett. **104**, 241802 (2010), hep-ex/1004.1826.

[109] CDF, T. Aaltonen *et al.*, Search for Randall-Sundrum Gravitons in the Diphoton Channel at CDF, Phys. Rev. **D83**, 011102 (2011), hep-ex/1012.2795.

[110] CDF, T. Aaltonen *et al.*, Search for New Dielectron Resonances and Randall-Sundrum Gravitons at the Collider Detector at Fermilab, (2011), hep-ex/1103.4650.

[111] CMS Collaboration, Search for a RS graviton decaying to diphotons in pp collisions at $\sqrt{s} = 7\,\mathrm{TeV}$, CMS-EXO-10-019 (2011).

[112] ATLAS Collaboration, Search for dilepton resonances in pp collisions at $\sqrt{s} = 7\,\mathrm{TeV}$ with the ATLAS detector, Phys. Rev. Lett. **107**, 272002 (2011), 1108.1582.

[113] ATLAS Collaboration, Search for Extra Dimensions using diphoton events in 7 TeV proton-proton collisions with the ATLAS detector, Phys. Lett. **B710**, 538 (2012), 8 pages plus author list (20 pages total), 2 figures, 3 tables, matches published version in Physics Letters B, 1112.2194.

[114] Search for mass dilepton resonances with $5\,\mathrm{fb}^{-1}$ of pp collisions at $\sqrt{s} = 7\,\mathrm{TeV}$ with the atlas experiment, Mar, 2012.

[115] M. S. Carena, E. Ponton, J. Santiago, and C. E. Wagner, Light Kaluza Klein States in Randall-Sundrum Models with Custodial SU(2), Nucl. Phys. **B759**, 202 (2006), hep-ph/0607106.

[116] J. A. Cabrer, G. von Gersdorff, and M. Quiros, Improving Naturalness in Warped Models with a Heavy Bulk Higgs, (2011), hep-ph/1104.3149.

[117] L. Evans and P. Bryant, LHC Machine, JINST **3**, S08001 (2008).

[118] O. S. Brüning *et al.*, *LHC Design Report V1* (CERN, Geneva, 2004).

[119] CERN, http://public.web.cern.ch/public/Objects/Research/AccComplex0700829.gif, 2012.

[120] A. Achilli *et al.*, Total and inelastic cross-sections at LHC at $\sqrt{s} = 7\,\mathrm{TeV}$ and beyond, Phys.Rev. **D84**, 094009 (2011), 1102.1949.

[121] ATLAS Collaboration, Luminosity Public Results, https://twiki.cern.ch/twiki/bin/view/AtlasPublic/LuminosityPublicResults#2011_pp_Collisions.

[122] ATLAS Collaboration, The ATLAS Experiment at the CERN Large Hadron Collider, JINST 3 S08003 (2008).

[123] A. Yamamoto *et al.*, Progress in atlas central solenoid magnet. progress in atlas central solenoid magnet., (1999).

[124] G. Aad *et al.*, ATLAS pixel detector electronics and sensors, JINST **3**, P07007 (2008).

[125] A. Abdesselam *et al.*, The barrel modules of the ATLAS semiconductor tracker, Nucl.Instrum.Meth. **A568**, 642 (2006).

[126] ATLAS TRT Collaboration, E. Abat *et al.*, The ATLAS TRT barrel detector, JINST **3**, P02014 (2008).

[127] E. Abat *et al.*, The ATLAS TRT end-cap detectors, JINST **3**, P10003 (2008).

[128] ATLAS Collaboration, ATLAS Calorimeter Performance, Technical Design Report, CERN/LHCC 97-40 (1997).

[129] ATLAS Collaboration, ATLAS liquid argon calorimeter: Technical design report, (1996).

[130] M. Aharrouche *et al.*, Energy linearity and resolution of the ATLAS electromagnetic barrel calorimeter in an electron test-beam, Nucl. Instrum. Meth. **568, no.2**, 601 (2006).

[131] A. Artamonov *et al.*, The ATLAS forward calorimeters, JINST **3**, P02010 (2008).

[132] ATLAS Level-1 Trigger Group, Level-1 Trigger, Technical Design Report, ATLAS TDR 12 (1998).

[133] ATLAS Collaboration, Performance of the ATLAS Trigger System in 2010, Eur.Phys.J. **C72**, 1849 (2012), 1110.1530.

[134] ATLAS HLT/DAQ/DCS Group, ATLAS High-Level Triggers, DAQ and DCS, Technical Proposal, CERN/LHCC 2000-17 (2000).

[135] ATLAS, Luminosity Determination in pp Collisions at $\sqrt{s} = 7\,\text{TeV}$ using the ATLAS Detector in 2011, (2011), http://cdsweb.cern.ch/record/1376384.

[136] *PROSPINO2*, http://www.thphys.uni-heidelberg.de/~plehn/index.php?show=prospino.

[137] F. E. Paige, S. D. Protopopescu, H. Baer, and X. Tata, ISAJET 7.69: A Monte Carlo Event Generator for pp, $\bar{p}p$, and e^+e^- Reactions, (2003), hep-ph/0312045.

[138] M. Bahr *et al.*, Herwig++ Physics and Manual, Eur. Phys. J. **C58**, 639 (2008), hep-ph/0803.0883v3.

[139] W. Beenakker, R. Hopker, M. Spira, and P. Zerwas, Squark and Gluino Production at Hadron Colliders, Nucl. Phys. **B492**, 51 (1997), hep-ph/9610490.

[140] W. Beenakker, M. Kramer, T. Plehn, M. Spira, and P. M. Zerwas, Stop Production at Hadron Colliders, Nucl. Phys. **B515**, 3 (1998), hep-ph/9710451.

[141] W. Beenakker *et al.*, The Production of Charginos / Neutralinos and Sleptons at Hadron Colliders, Phys. Rev. Lett. **83**, 3780 (1999), hep-ph/9906298.

[142] M. Spira, Higgs and SUSY Particle Production at Hadron Colliders, PSI-PR-02-19 , 217 (2002), hep-ph/0211145.

[143] T. Plehn, Measuring the MSSM Lagrangian, Czech. J. Phys. **55**, B213 (2005), hep-ph/0410063.

[144] D. Stump *et al.*, Inclusive Jet Production, Parton Distributions, and the Search for New Physics, JHEP **10**, 046 (2003), hep-ph/0303013.

[145] J. Butterworth *et al.*, Single Boson and Diboson Production Cross Sections in pp Collisions at $\sqrt{s} = 7\,\text{TeV}$, ATL-PHYS-INT-2011-078, Aug, 2011.

[146] M. L. Mangano, M. Moretti, F. Piccinini, R. Pittau, and A. D. Polosa, ALPGEN, a Generator for Hard Multiparton Processes in Hadronic Collisions, JHEP **0307**, 001 (2003), hep-ph/0206293.

[147] J. Pumplin *et al.*, New generation of parton distributions with uncertainties from global QCD analysis, JHEP **0207**, 012 (2002), hep-ph/0201195.

[148] S. Frixione and B. R. Webber, Matching NLO QCD computations and parton shower simulations, JHEP **0206**, 029 (2002), hep-ph/0204244.

[149] S. Frixione, P. Nason, and B. R. Webber, Matching NLO QCD and parton showers in heavy flavor production, JHEP **0308**, 007 (2003), hep-ph/0305252.

[150] S. Frixione, E. Laenen, P. Motylinski, and B. R. Webber, Single-top production in MC@NLO, JHEP **0603**, 092 (2006), hep-ph/0512250.

[151] P. M. Nadolsky *et al.*, Implications of CTEQ global analysis for collider observables, Phys. Rev. **D78**, 013004 (2008), hep-ph/0802.0007.

[152] G. Corcella *et al.*, HERWIG 6: An Event Generator for Hadron Emission Reactions With Interfering Gluons (Including Supersymmetric Processes), JHEP **0101**, 010 (2001), hep-ph/0011363.

[153] J. Butterworth, J. R. Forshaw, and M. Seymour, Multiparton interactions in photoproduction at HERA, Z. Phys. **C72**, 637 (1996), hep-ph/9601371.

[154] ATLAS Collaboration, First Tuning of HERWIG/JIMMY to ATLAS Data, ATL-PHYS-PUB-2010-014, Oct, 2010, http://cdsweb.cern.ch/record/1303025.

[155] S. Jadach, Z. Was, R. Decker, and J. H. Kuhn, The Tau Decay Library TAUOLA, Version 2.4, Comput. Phys. Commun. **76**, 361 (1993).

[156] P. Golonka *et al.*, The Tauola-Photos-F Environment for the TAUOLA and PHOTOS Packages, Release II, Comput. Phys. Commun. **174**, 818 (2006).

[157] E. Barberio and Z. Was, PHOTOS - a Universal Monte Carlo for QED Radiative Corrections: Version 2.0, Comput. Phys. Commun. **79**, 291 (1994).

[158] T. Sjostrand, S. Mrenna, and P. Skands, PYTHIA 6.4 Physics and Manual, JHEP **0605**, 026 (2006), hep-ph/0603175.

[159] ATLAS Collaboration, Charged Particle Multiplicities in pp Interactions at $\sqrt{s} = 0.9$ and 7 TeV in a Diffractive Limited Phase Space Measured with the ATLAS Detector at the LHC and a New PYTHIA6 Tune, ATLAS-CONF-2010-031, July, 2010, http://cdsweb.cern.ch/record/1277665.

[160] A. Sherstnev and R. S. Thorne, Parton Distributions for LO Generators, Eur. Phys. J. **C55**, 553 (2008), hep-ph/0711.2473.

[161] GEANT4, S. Agostinelli *et al.*, GEANT4: A simulation toolkit, Nucl. Instrum. Meth. **A506**, 250 (2003).

[162] J. Allison *et al.*, Geant4 developments and applications, IEEE Trans. Nucl. Sci. **53**, 270 (2006).

[163] ATLAS Collaboration, The ATLAS Simulation Infrastructure, Eur. Phys. J. **C70**, 823 (2010), physics.ins-det/1005.4568.

[164] M. Böhler, private communication.

[165] ATLAS Collaboration, Luminosity Determination in pp Collisions at $\sqrt{s} = 7\,\text{TeV}$ Using the ATLAS Detector at the LHC, Eur. Phys. J. **C71**, 1630 (2011), hep-ex/1101.2185.

[166] Pileup Reweighting, https://twiki.cern.ch/twiki/bin/viewauth/AtlasProtected/PileupReweighting, 2011, Pileup Reweighting-00-00-15.

[167] Susy tools, https://twiki.cern.ch/twiki/bin/view/AtlasProtected/SUSYD3PDSnippets, 2011, SUSYTools-00-00-34.

[168] M. Cacciari, G. P. Salam, and G. Soyez, The anti-kt jet clustering algorithm, JHEP **04**, 063 (2008), hep-ph/0802.1189.

[169] Y. L. Dokshitzer, G. Leder, S. Moretti, and B. Webber, Better jet clustering algorithms, JHEP **9708**, 001 (1997), hep-ph/9707323.

[170] M. Wobisch and T. Wengler, Hadronization corrections to jet cross-sections in deep inelastic scattering, (1998), hep-ph/9907280.

[171] S. D. Ellis and D. E. Soper, Successive combination jet algorithm for hadron collisions, Phys. Rev. **D48**, 3160 (1993), hep-ph/9305266.

[172] ATLAS Collaboration, Performance of the Reconstruction and Identification of Hadronic Tau Decays with ATLAS, ATLAS-CONF-2011-152, Nov, 2011, http://cdsweb.cern.ch/record/1398195.

[173] T. Barillari *et al.*, Local hadronic calibration, ATL-LARG-PUB-2009-001-2, 2009.

[174] Determination of the tau energy scale and the associated systematic uncertainty in proton-proton collisions at $\sqrt{s} = 7\,\text{TeV}$ with the atlas detector at the lhc in 2011, ATLAS-CONF-2012-054, Jun, 2012.

[175] ATLAS Collaboration, Reconstruction, energy calibration, and identification of hadronically decaying tau leptons, May, 2011.

[176] ATLAS Collaboration, Expected electron performance in the ATLAS experiment, ATL-PHYS-PUB-2011-006, Apr, 2011.

[177] ATLAS Collaboration, Electron Performance Measurements with the ATLAS Detector using the 2010 LHC Proton-Proton Collision Data, (2011), Submitted to Eur. Phys. J. C, hep-ex/1110.3174.

[178] ATLAS Collaboration, Muon Reconstruction and Identification: Studies with Simulated Monte Carlo Samples, ATL-PHYS-PUB-2009-008, Mar, 2009.

[179] S. Hassani *et al.*, A Muon Identification and Combined Reconstruction Procedure for the ATLAS Detector at the LHC using the (MUONBOY, STACO, MuTag) Reconstruction Packages, Nucl. Instrum. Meth. **A572**, 77 (2007).

[180] R. Nicolaidou *et al.*, Muon identification procedure for the ATLAS detector at the LHC using Muonboy reconstruction package and tests of its performance using cosmic rays and single beam data, J.Phys.Conf.Ser. **219**, 032052 (2010).

[181] ATLAS Collaboration, Searches for Supersymmetry with the ATLAS Detector using Final States with Two Leptons and Missing Transverse Momentum in $\sqrt{s} = 7\,\text{TeV}$ Proton-Proton Collisions, (2011), Accepted by Phys. Lett. B, hep-ex/1110.6189.

[182] ATLAS Collaboration, Performance of Missing Transverse Momentum Reconstruction in Proton-Proton Collisions at 7 TeV with ATLAS, Eur. Phys. J. **C72**, 1844 (2012), hep-ex/1108.5602.

[183] D. Adams *et al.*, The ATLFAST-II performance in release 14 - particle signatures and selected benchmark processes, ATL-PHYS-INT-2009-110, Dec, 2009.

[184] E. Torró Pastor, D. Côté, and X. Portell Bueso, Validation of the ATLFAST-II Package for the Simulation of Supersymmetry Events, ATL-COM-PHYS-2011-1181, Sep, 2011.

[185] G. Corcella *et al.*, HERWIG 6.5 release note, (2002), hep-ph/0210213.

[186] ATLAS Collaboration, Expected Performance of the ATLAS Experiment - Detector, Trigger and Physics, (2009), CERN-OPEN-2008-020.

[187] ATLAS Collaboration, Prospects for SUSY and UED discovery based on inclusive searches at a 10 TeV centre-of-mass energy with the ATLAS detector, ATL-PHYS-PUB-2009-084, 2009.

[188] J. T. Linnemann, Measures of significance in HEP and astrophysics, (2003), Published in proceedings of PHYSTAT2003: *Statistical problems in particle physics, astrophysics, and cosmology*, Menlo Park, California, 2003., physics/0312059.

[189] ATLAS Collaboration, Search for Events with Large Missing Transverse Momentum, Jets, and at Least Two Tau Leptons in 7 TeV Proton-Proton Collision Data with the ATLAS Detector, ATLAS-CONF-2012-002, Feb, 2012.

[190] ATLAS Collaboration, Search for Supersymmetry with Jets, Missing Transverse Momentum and at least One Hadronically Decaying Tau Lepton in Proton-Proton Collisions at $\sqrt{s} = 7\,\text{TeV}$ with the ATLAS Detector, Phys. Lett. **B714**, 197 (2012), hep-ex/1204.3852.

[191] Atlas Collaboration, Search for new phenomena in final states with large jet multiplicities and missing transverse momentum using $\sqrt{s} = 7\,\text{TeV}$ pp collisions with the ATLAS detector, JHEP **1111**, 099 (2011), hep-ex/1110.2299.

[192] Atlas Collaboration, Search for squarks and gluinos using final states with jets and missing transverse momentum with the ATLAS detector in $\sqrt{s} = 7\,\text{TeV}$ proton-proton collisions, Phys. Lett. **B710**, 67 (2012), hep-ex/1109.6572.

[193] Atlas Collaboration, Search for supersymmetry in pp collisions at $\sqrt{s} = 7\,\text{TeV}$ in final states with missing transverse momentum and b-jets with the ATLAS detector, (2012), hep-ex/1203.6193.

[194] Atlas Collaboration, Search for scalar bottom pair production with the ATLAS detector in pp Collisions at $\sqrt{s} = 7\,\text{TeV}$, (2011), hep-ex/1112.3832.

[195] S. Asai *et al.*, Search for squarks and gluinos using final states with jets and missing transverse momentum with the ATLAS experiment in $\sqrt{s} = 7\,\text{TeV}$ proton-proton collisions: supporting documentation, ATL-PHYS-INT-2011-055, Jun, 2011.

[196] Susy grl, http://atlasdqm.web.cern.ch/atlasdqm/grlgen/Susy/Susy_v01/data11_7TeV.periodAllYear_DetStatus-v28-pro08-07_CoolRunQuery-00-04-00_Susy.xml, Sep, 2011.

[197] ATLAS, Luminosity Determination in pp Collisions at $\sqrt{s} = 7\,\text{TeV}$ using the ATLAS Detector in 2011, ATLAS-CONF-2011-116, http://cdsweb.cern.ch/record/1376384.

[198] How to clean jets, TWIKI: https://twiki.cern.ch/twiki/bin/view/AtlasProtected/HowToCleanJets2011, 2011.

[199] G. Cowan, K. Cranmer, E. Gross, and O. Vitells, Asymptotic formulae for likelihood-based tests of new physics, Eur. Phys. J. **C71**, 1554 (2011), arXiv:1007.1727.

[200] ATLAS Collaboration, Searches for supersymmetry with the ATLAS detector using final states with two leptons and missing transverse momentum in $\sqrt{s} = 7\,\text{TeV}$ proton-proton collisions, Phys. Lett. **B709**, 137 (2012), hep-ex/1110.6189.

[201] ATLAS Collaboration, Search for Diphoton Events with Large Missing Transverse Momentum in $1\,\text{fb}^{-1}$of 7 TeV Proton-Proton Collision Data with the ATLAS Detector, Phys. Lett. **B710**, 519 (2012), hep-ex/1111.4116.

[202] ATLAS Collaboration, Search for neutral MSSM Higgs bosons decaying to $\tau^+\tau^-$ pairs in proton-proton collisions at $\sqrt{s} = 7\,\text{TeV}$ with the ATLAS detector, ATLAS-CONF-2011-132, Sep, 2011.

[203] LEPSUSYWG, ALEPH, DELPHI, L3 and OPAL Experiments, Combined LEP GMSB stau/smuon/selectron Results, 189-208 GeV, LEPSUSYWG/02-09.2, 2002, http://lepsusy.web.cern.ch/lepsusy/.

[204] OPAL, G. Abbiendi *et al.*, Searches for Gauge-Mediated Supersymmetry Breaking Topologies in e^+e^- Collisions at LEP2, Eur.Phys.J. **C46**, 307 (2006), hep-ex/0507048.

[205] ALEPH, A. Heister *et al.*, Search for Gauge Mediated SUSY Breaking Topologies in e^+e^- Collisions at Center-of-mass Energies up to 209 GeV, Eur.Phys.J. **C25**, 339 (2002), hep-ex/0203024.

[206] DELPHI Collaboration, J. Abdallah *et al.*, Search for supersymmetric particles in light gravitino scenarios and sleptons NLSP, Eur.Phys.J. **C27**, 153 (2003), hep-ex/0303025.

[207] ATLAS Collaboration, Jet Energy Scale and its Systematic Uncertainty in Proton-Proton Collisions at $\sqrt{s} = 7\,\text{TeV}$ in ATLAS 2010 Data, ATLAS-CONF-2011-032, Mar, 2011, https://cdsweb.cern.ch/record/1337782.

[208] JES Uncertainty Provider, https://twiki.cern.ch/twiki/bin/viewauth/AtlasProtected/JESUncertaintyProvider, 2011.

[209] ATLAS Collaboration, Close-by Jet Effects on Jet Energy Scale Calibration in pp Collisions at $\sqrt{s} = 7\,\text{TeV}$ with the ATLAS Detector, ATLAS-CONF-2011-062, Apr, 2011.

[210] Multi-jet JES Uncertainty Provider, https://twiki.cern.ch/twiki/bin/viewauth/AtlasProtected/MultijetJESUncertaintyProvider, 2011.

[211] ATLAS Collaboration, Jet Energy Resolution and Selection Efficiency Relative to Track Jets from In-situ Techniques with the ATLAS Detector Using Proton-Proton Collisions at a Center of Mass Energy $\sqrt{s} = 7\,\text{TeV}$, ATLAS-CONF-2010-054, Jul, 2010, https://cdsweb.cern.ch/record/1281311.

[212] G. Romeo, A. Schwartzman, R. Piegaia, T. Carli, and R. Teuscher, Jet Energy Resolution from In-situ Techniques with the ATLAS Detector Using Proton-Proton Collisions at a Center of Mass Energy $\sqrt{s} = 7\,\text{TeV}$, ATL-COM-PHYS-2011-240, Mar, 2011.

[213] Jet Energy Resolution Provider, https://twiki.cern.ch/twiki/bin/viewauth/AtlasProtected/JetEnergyResolutionProvider, 2011.

[214] D. Stump *et al.*, Inclusive jet production, parton distributions, and the search for new physics, JHEP **0310**, 046 (2003), hep-ph/0303013.

[215] Z. Sullivan, Fully Differential W-prime Production and Decay at Next-to-leading Order in QCD, Phys. Rev. **D66**, 075011 (2002), hep-ph/0207290.

[216] H.-L. Lai *et al.*, Uncertainty Induced by QCD Coupling in the CTEQ Global Analysis of Parton Distributions, Phys. Rev. **D82**, 054021 (2010), hep-ph/1004.4624.

[217] M. Hohlfeld, M. Lungwitz, C. Meyer, and T. Mueller, Estimating theory uncertainties in w/z+jets and ttbar+jets events using the alpgen generator, ATL-COM-PHYS-2012-070, Jan, 2012.

[218] S. Asai *et al.*, Search for Supersymmetry with jets and missing transverse momentum and one lepton at $\sqrt{s} = 7\,\text{TeV}$ (supporting INT note), ATL-PHYS-INT-2011-008, Feb, 2011.

[219] M. Hohlfeld, private communication.

[220] ATLAS Collaboration, http://atlas.web.cern.ch/Atlas/GROUPS/PHYSICS/PAPERS/SUSY-2011-18/, Plots published along with [2].

[221] S. Schaepe, private communication.

[222] ATLAS Collaboration, Constraining the Gauge-Mediated Supersymmetry Breaking Model in Final States with two Leptons, Jets and Missing Transverse Momentum with the ATLAS Experiment at $\sqrt{s} = 7\,\text{TeV}$, ATLAS-CONF-2011-156, Nov, 2011, https://cdsweb.cern.ch/record/1398247.

[223] M. Baak and A. Hoecker, Mass Reach Summary of ATLAS Searches for New Phenomena - Status: March 2012, ATL-COM-PHYS-2012-284, Mar, 2012.

[224] CMS Collaboration, Search for new physics with same-sign isolated dilepton events with jets and missing transverse energy at the LHC, JHEP **1106**, 077 (2011), hep-ex/1104.3168.

[225] CMS Collaboration, Search for new physics with same-sign isolated dilepton events with jets and missing energy, CMS-PAS-SUS-11-010, 2011.

[226] CMS Collaboration, Search for supersymmetry in all-hadronic events with tau leptons, CMS-PAS-SUS-11-010, 2011.

[227] CMS Collaboration, Search for Physics Beyond the Standard Model Using Multilepton Signatures in pp Collisions at $\sqrt{s} = 7\,\text{TeV}$, Phys. Lett. **B704**, 411 (2011), hep-ex/1106.0933.

[228] SUSY Working Group Collaboration, R. L. Culbertson *et al.*, Low scale and gauge mediated supersymmetry breaking at the Fermilab Tevatron Run II, (2000), Part 3 of physics at Run II SUSY/Higgs report, hep-ph/0008070.

[229] P. Meade, N. Seiberg, and D. Shih, General Gauge Mediation, Prog. Theor. Phys. Suppl. **177**, 143 (2009), 0801.3278.

[230] Y. Kats, P. Meade, M. Reece, and D. Shih, The Status of GMSB After $1\,\mathrm{fb}^{-1}$ at the LHC, (2011), 1110.6444.

[231] A. L. Read, Presentation of search results: The CL_s technique, J. Phys. **G28**, 2693 (2002).

[232] ATLAS Statistics Forum, The CL_s method: Information for conference speakers, https://twiki.cern.ch/twiki/pub/AtlasProtected/StatisticsTools/CLsInfo.pdf, 2011.

[233] ATLAS Collaboration, Setting exclusion limits in atlas supersymmetry searches with a likelihood ratio based method, ATL-PHYS-INT-2011-032, Apr, 2011.

[234] Combination package, https://svnweb.cern.ch/trac/atlasgrp/browser/Physics/SUSY/Analyses/Combination/, 2012, Combination-00-00-20.

[235] H.-J. He, N. Polonsky, and S. Su, Extra families, Higgs spectrum and oblique corrections, Phys. Rev. **D64**, 053004 (2001), hep-ph/0102144.

[236] The Tau Slice Trigger Group, Tau Trigger Performance with 2011 data, ATL-COM-DAQ-2011-065 (2011).

Danksagung

Ich möchte die Gelegenheit nutzen und an dieser Stellen allen danken, die mir bei der Entstehung dieser Arbeit geholfen haben, die mich unterstützt, konstruktiv kritisiert und motiviert haben. Allen, ohne die diese Arbeit nicht möglich gewesen wäre. Danken möchte ich besonders

I would like to take this opportunity to thank everyone who supported me in writing this thesis or any other way, who gave me constructive criticism or motivated me. I would like to thank everyone without whom this thesis would not have been possible. I would like to thank especially

Prof. Dr. Johannes Haller für die Möglichkeit in seiner Grupper meine Doktorbarbeit zu schreiben; für zahlreiche Anregungen, hilfreiche Diskussionen, viel konstruktive Kritik vor allem in den letzten Wochen und für die Möglichkeit an zahlreichen Konferenzen aktiv mit Vorträgen teilnehmen zu dürfen.

Prof. Dr. Klaus Desch für seine Bereitschaft, meine Arbeit als Zweitgutachter zu bewerten und das Interesse an meiner Arbeit.

Prof. Dr. Peter Schleper für sein Interessen an meiner Arbeit und seine Einwilligung, meiner Disputation als Zweitgutachter beizuwohnen.

Prof. Dr. Caren Hagner für zahlreiche anregende Diskussionen auch über die Physik hinaus und den Prüfungsvorsitz.

The Gfitter Group for all that I have learned by working with them and for giving me the opportunity to present our work at various occasions.

Dr. Fabrizio Salvatore, Steffen Schaepe, Anthony Rose, Dr. Wolfgang Ehrenfeld for making the analysis happen! For fruitful discussions, and bringing us safely to the other side of the ATLAS approval process; for being wonderful hosts to me in Brigthon and in Bonn. It was great to be part of the team!

Dr. Wolfgang Ehrenfeld für all die Unterstützung in den letzten Jahren, sowohl in technischer Hinsicht als auch auf physikalischer sowie persönlicher Ebene.

Dr. Mark Terwort für seine Freundschaft, seinen kritischen Blick, seine Fragen und seine Antworten auf meine Fragen.

Dr. Michael Böhler für das Lesen grosser Teile meiner Arbeit und die konstruktive Kritik; für das gemeinsame Überstehen des Studiums vom ersten bis zum letzten Tag. Für die letzten neun Jahre.

Martin Wildt für die sehr abwechslungsreiche und interessante Zeit im gemeinsamen Büro, für anregende Diskussionen rund um die Physik und das Leben im Allgemeinen und Speziellen. Ich werde beides vermissen.

Dr. Martin Goebel, Dr. Karl-Johan Grahn, Dr. Takanori Kono, Dr. Sergei Gleyzer, Dr. Michael Medinnis for reading parts of my thesis and giving me helpful suggestions; for being my colleagues and creating a nice working atmosphere.

Kristin Heine für ein tolles Jahr als Kolleginnnen und eine neue Freundin.

Dr. Thomas Schörner-Sadenius für sein offenes Ohr und seine weisenden Worte zum richtigen Zeitpunkt.

Dr. David Grellscheid und Carsten Schneemann für eine unvergessliche Zeit auf der DSA 2002, auf der sie mich mit der Teilchenphysik bekannt gemacht haben und mich so auf die Idee gebracht und ermutigt haben, Physik zu studieren.

Annegret Süß für ein ausgesprochen nettes Zusammenleben und viel Unterstützung in der doch manchmal anstrengenden Zeit.

David Kennedy for believing in me every step of the way. For accompanying me for the past few years and for making my life better as it would have been without him. And I would like to thank Dorothy and Jim Kennedy for welcoming me so warmly in their home and lives.

The Zabriskies for their warmth and love, for their endless support and confidence in my abilities. I would like to thank them greatly for giving me a home and for being a wonderful family to me. It means the world to me.

Katy und Jörg Lenke für ihre Unterstützung und ihr Interesse an mir und meiner Arbeit. Dafür, dass sie mich immer wilkommen geheissen haben, meine Paten wurden und für ihre Herzlichkeit.

Silke Ludwig für die Fähigkeit vieles anders zu sehen als ich und mich daran teilhaben zu lassen. Dafür, dass sie meine Schwester ist, die ich um nichts in der Welt in meinem Leben missen wollen würde.

Meinen Eltern für die letzten 30 Jahre. Für ihre Unterstützung, ihren Glauben an mich und meine Fähigkeiten. Dafür mir so vieles in meinem Leben ermöglicht zu haben. Für das Öffnen der Tür zur Welt.

Ich bedanke mich bei allen, die ich hier vergessen haben sollte, die mich ein Stück durch mein Leben begleitet haben.